Optimisation of the Particle Detection Efficiency for Scintillation Detectors with SiPM Readout

von

Paul Papacz

Diplomarbeit in Physik

vorgelegt der

Fakultät für Mathematik, Informatik und Naturwissenschaften
der Rheinisch-Westfälischen Technischen Hochschule Aachen

im März 2010

angefertigt im

III. Physikalischen Institut A
Prof. Dr. Thomas Hebbeker

Zweitgutachter
Prof. Dr. Christopher Wiebusch

Abstract

The proposed upgrade of the LHC[1] to SLHC[2], planned for the period after about 10 years of LHC operation at design parameters and an integrated luminosity of about 500 fb^{-1}, will increase the peak luminosity of the collider by a factor of 10 to 10^{35} $cm^{-2}s^{-1}$.
To keep the amounts of data, resulting especially from the increased muon rates at these luminosities, manageable, a new 2D detector component for the CMS detector has been suggested, the *Muon Track fast Tag*.

This thesis presents studies of a scintillator-based, two-dimensional muon detector fulfilling the requirements of an MTT.
The studies base upon a GEANT4 simulation of light production and propagation inside a plastic scintillator. For the readout of the optical photons, the properties of small semiconducting photo detectors, called SiPMs[3], are simulated in detail.

The results of these studies show that the chosen materials and geometries of the setup promise a good signal-to-noise ratio and a readout timing that allows coping with the event rates of the SLHC environment.

Additionally a construction according to the specifications of the simulation is presented. This setup is read out by Silicon Photomultipliers, in analogy to the setups in the simulations.

[1] **L**arge **H**adron **C**ollider
[2] **S**uper **LHC**
[3] **Si**licon **P**hoto **M**ultipliers

Zusammenfassung

Die vorgeschlagene Aufrüstung des LHC zum SLHC, geplant für den Zeitraum nach ca. 10 Betriebsjahren des LHC bei Entwurfsparametern und einer integrierten Luminosität von ungefähr 500 fb^{-1}, wird eine Erhöhung der Spitzenluminosität des Beschleunigers um einen Faktor 10 auf 10^{35} $\text{cm}^{-2}\text{s}^{-1}$ mit sich bringen.
Um die Datenmengen, die insbesondere durch die erhöhten Myonraten bei diesen Luminositäten entstehen, handhabbar zu halten, wurde eine neue 2D-Detektorkomponente für den CMS-Detektor vorgeschlagen, der *Muon Track fast Tag*.

Diese Arbeit zeigt Studien eines szintillatorbasierten, zweidimensionalen Myondetektors, der die Anforderungen eines MTT erfüllt.
Die Studien basieren auf einer GEANT4 -Simulation der Lichterzeugung und -ausbreitung innerhalb eines Plastikszintillators. Für die Auslese der optischen Photonen werden die Eigenschaften von kleinen Halbleiter-Lichtdetektoren (SiPMs) im Detail simuliert.

Die Ergebnisse dieser Studien zeigen, dass die gewählten Materialien und Geometrien des Aufbaus ein gutes Signal-zu-Rausch-Verhältnis versprechen und eine Auslesegeschwindigkeit erlauben, mit der die Ereignisraten des SLHC bewältigt werden können.

Des Weiteren wird ein der Simulation entsprechender Detektor-Aufbau vorgestellt. Die Auslese innerhalb dieses Aufbaus wird, wie in der Simulation, mit Silizum-Photomultipliern durchgeführt.

Contents

Chapter 1

Introduction

History of Particle Physics

The way to modern particle physics starts way back in ancient Greece, where in ca $500 - 400$ BC Demokritos and his teacher Leukippos stated that everything is composed of different kinds of *atoms*[4] which were supposed to be the smallest and indestructible parts of all materials with nothing but empty space between them [Bro78a; Bro79].
This was only one of many competing theories of the ancient world.

For many centuries there was no scientific evidence of this or any other theory, not even serious attempts have been made.
In the very early 19^{th} century J. Dalton picked up the idea of Demokritos and used it to explain the "law of multiple proportions". He claimed that there is one sort of atoms of each (known) element and those atoms can be combined to molecules, but the atoms were still assumed to be indivisible [Bro78a].

After a series of experiments at the end of the 19^{th} century, J. J. Thomson found a particle with a mass to charge ratio that was more than a thousand times lower than that of a H^+ ion, the *electron*. He could also show that hydrogen holds exactly one electron [Bro80a].
At the same time Marie Curie proved that heavy elements could convert into lighter ones by "radioactive decay" [Bro78b].
Thus, more than 100 years ago it was clear that atoms, the smallest units, that matter was thought to be made of, were not as indivisible as imagined.

In the following years different models were considered to describe how atoms are built. And in 1911 E. Rutherford showed experimentally that most of the matter of the atom must be concentrated in its innermost centre, the (positively charged) nucleus. He could also identify the *proton*[5] and show that it was a part of other nuclei [Bro80b].
Soon it was clear that the nuclei of most elements are heavier than the sum of their proton (and electron) masses and so another (electrically neutral) constituent of matter was found, the *neutron*.

Many theoretical attempts have been made to understand atoms in a proper way but only the theory of *quantum mechanics* has been able to describe states of atoms in a satisfying way, at the price of abandoning many classical concepts like "the determinism of measurement".

The journey continues as in the middle of the 20^{th} century many new heavy particles have been found in collision experiments. These particles (called *hadrons*[6]) could be grouped by several quantum numbers like *spin* or *isospin*.
To describe this system, M. Gell-Mann, G. Zweig and later R. Feynman developed the concept

[4] ἄτομος: indivisible, uncuttable
[5] πρῶτον: first
[6] ἁδρός: stout, thick

that hadrons consist of smaller units called *quarks* or *partons* [GM64; Fey69]. A few years later it was clear, that partons are not just theoretical objects but physical constituents of hadrons and in particular of protons and neutrons, the "building blocks" of well-known matter.

Today partons can be subdivided into groups of 6 *quarks* (plus antiparticles) and *gluons*, providing the exchange force between the quarks. The heaviest of the quarks has been discovered in the 1990's at the TEVATRON Collider [D095; CDF95].

On the other hand during the 20^{th} century, several particles have been discovered that do not behave like hadrons, the *leptons*[7]. Unlike hadrons all leptons have the same spin ($\frac{1}{2}$) and seem not to consist of smaller units. Starting from the electron, the first known lepton, in the year 2000 the latest member of the lepton family, the τ *neutrino*[8], has been detected in the DONUT experiment [DON01].

Modern Particle Physics

Today, quarks and leptons can each be subdivided into three families each containing two particles (plus antiparticles). Along with the *gauge bosons* they build up the foundation of the very successful *Standard Model of particle physics* (SM).
Many measurements of different quantities have been performed to confirm (or falsify) the SM, and so lots of parameters are known with high precision, e. g. the magnetic moment of the electron, or the number of colours.

But we are still far away from the end of the road. The better the SM works, the more questions come up why it works. For example theories like QED[9], describing the electroweak interactions, can be formulated completely without regarding the masses of the involved particles, although providing theoretical predictions of high quality! Thus the existence of massive particles in the SM has to be explained. One attempt to do this is done by the Higgs mechanism (see also sec. 2.4.3 and 2.4.4).
Until present days it is not clear whether quarks and leptons are point-like particles or if they possess a substructure. Best measurements show that the electron radius is smaller than 10^{-22} m (depending on the underlying model) [Deh88].

One more hint for physics reaching beyond the SM is the standard model itself. It does not contain a theoretical description of the gravity and thus fails to describe physics at the *Planck Scale* ($E_{\text{Planck}} \approx 10^{19}$ GeV) at which gravity is expected to become as strong as the other forces.

Recent Approaches

The last decades have shown that it is possible to find evidence for many theoretical predictions and to find new physics with help of collider experiments. In doing so it becomes inevitable to go to higher and higher collision energies and luminosities, e. g. to find processes that are predicted to be very rare.
Moreover Heisenberg's uncertainty principle - one of the fundamental principles of quantum mechanics - says that certain properties, like location and momentum, cannot be known exactly, mathematically:

$$\Delta x \cdot \Delta p \geq \frac{\hbar}{2} \tag{1.1}$$

[7] λεπτός: small, thin, delicate
[8] from ital. "small neutron"
[9] **Q**uantum **E**lectro **D**ynamics, see also sec. 2.4.1.

This also means that in order to resolve smaller structures one needs to go to higher momenta and therefore to higher energies.

The long-term research and experience in collider and detector physics peak in two grand experiments: TEVATRON at *Fermilab* (Chicago, USA) and LHC at *CERN*[10] (Geneva, Switzerland/France).
TEVATRON was the first hadron collider reaching the TeV scale[11] and was able to discover the top quark after a few years of collisions.
In 2010 the LHC with its four detectors: CMS, ATLAS, ALICE, LHCb will supersede TEVATRON and will open a window to the energy scale of more than 10 TeV with a luminosity that has never been reached before at a hadron collider.

Future Plans

Although the LHC has not yet reached its design parameters, there are important plans to improve the collider's performance and, associated with this, of the detectors used to analyse the collisions.
The most probable upgrade considered at the moment is an increase of the LHC-luminosity by a factor of 10 to 10^{35} $cm^{-2}s^{-1}$, thus bringing much higher particle rates inside the detectors. A more detailed description of the planned upgrade of the LHC to the SLHC can be found in chapter 4.

[10] former: **C**onseil **E**uropéen pour la **R**echerche **N**ucléaire
[11] TEVATRON reaches a centre of mass energy of 1.96 TeV

Chapter 2

Theoretical Background

In this work, natural units are used. This means:

$$\hbar = c = 1. \tag{2.1}$$

This increases clarity without loss of information. One consequence of this definition is that the dimensions of many important quantities can be written in powers of eV, e. g.:

$$[\text{energy}] = [\text{momentum}] = [\text{mass}] = [\text{length}]^{-1} = [\text{time}]^{-1}. \tag{2.2}$$

According to common conventions in relativistic physics, Greek indices will be used to label time and space coordinates. For example, x^μ stands for x^0, x^1, x^2, x^3.
One further abbreviation in this context is:

$$x = (x^\mu) = (ct, \boldsymbol{x}) \overset{c=1}{=} (t, \boldsymbol{x}). \tag{2.3}$$

Further, γ^μ denotes the gamma or Dirac matrices.
Two widely used quantities are:

$$\beta = \frac{v}{c} \overset{c=1}{=} v, \qquad \gamma = \frac{1}{\sqrt{1 - \frac{v^2}{c^2}}} = \frac{1}{\sqrt{1 - \beta^2}}. \tag{2.4}$$

In natural unit these quantities are also:

$$\beta = \frac{p}{E}, \qquad \gamma = \frac{E}{m}, \tag{2.5}$$

with: $E, p, m =$ energy, momentum, mass of the particle.
In these units, the relativistic mass-energy-relation is simply given by:

$$E^2 = \boldsymbol{p}^2 + m^2. \tag{2.6}$$

2.1 Particles of the Standard Model

As mentioned in the introduction, after many years of research, it is possible to identify and classify twelve particles, all with spin=$\frac{1}{2}$ (*fermions*), which can be used to describe all the visible matter in the universe. Additionally, the theory provides a way to describe the fundamental forces by the exchange of (virtual) particles with spin=1 (*bosons*).
The fermions can be grouped according to their participation in different interactions. All fermions take part in the electroweak interaction. The first group considered here are the leptons. This group consists of the electron, the *muon* and the *tauon*, and the corresponding neutrinos:

$$\begin{pmatrix} e^- \\ \nu_e \end{pmatrix} \quad \begin{pmatrix} \mu^- \\ \nu_\mu \end{pmatrix} \quad \begin{pmatrix} \tau^- \\ \nu_\tau \end{pmatrix}.$$

As electron, muon and tauon have a charge of one elementary charge[12] e, they take part in the electromagnetic interactions. The neutrinos, being electrically neutral, can only participate in weak interactions. Therefore it is very hard to detect them because it is possible for them to travel long distances in matter without any interaction.
The other group, the six known quarks (*up*, *down*, *charm*, *strange*, *top*, *bottom*), can be arranged in three generations:

$$\begin{pmatrix} u \\ d \end{pmatrix} \quad \begin{pmatrix} c \\ s \end{pmatrix} \quad \begin{pmatrix} t \\ b \end{pmatrix}.$$

All quarks carry *colour charge* (that has three aspects) enabling them to interact via the strong force.
The 'up-type' quarks (u, c, t) have an electrical charge of $+\frac{2}{3} \cdot \mathrm{e}$, the 'down-type' quarks (d, s, b) have a charge of $-\frac{1}{3} \cdot \mathrm{e}$. Hence, the quarks can interact via electromagnetic, strong and weak force.
Because of the special properties of colour charge and thus of the strong interaction, quarks cannot be observed as isolated particles. Interactions with quarks always end up in the formation of hadrons that are colourless (hadronisation). Because of the 'strength' of the strong force the resulting bound states have a size in the order of a proton ($d_\mathrm{P} \approx 1.7 \cdot 10^{-15}$ m).
As one can see, the fermions are arranged in doublets, called generations. This grouping indicates their role in weak interactions. Only the weak interaction is able to convert a member of one doublet into the other and vice versa[13].
Additionally, quarks have finite probabilities to convert into quarks of other generations. For example the decay:

$$s \longrightarrow u + l + \overline{\nu}_l \tag{2.7}$$

is allowed and has a measurable probability. Many other combinations are possible and the transition probabilities can be summarized in the CKM-matrix [14].

For every particle mentioned above there exists an antiparticle with opposite sign for all additive quantum numbers like charge, baryon number or lepton number, and with same sign for non-additive quantum numbers like mass or spin.

Gauge theories like QED, QCD[15] and the electroweak 'unification' provide the possibility to describe the three forces by the exchange of bosons[16]. The electroweak theory shows that the electromagnetic and weak interactions can be described by the exchange of photons, W^+, W^-, and Z^0 bosons.
QCD provides eight *gluons* that mediate the strong interactions of quarks. The photon is massless and uncharged. W^- and W^+ have a mass of 80.40 GeV and an electrical charge of $\pm 1 \cdot \mathrm{e}$. The Z^0 boson has a mass of 91.20 GeV and is uncharged [PDG08]. The gluons are assumed as carrying a combination of colour and anticolor charge. The theory predicts the gluons to be massless. Direct measurements are difficult, but a rough estimate based on observations leads to a conservative value of $m_g < 1.3$ MeV [Ynd95].
A summary of all known particles is given in tab. 2.1.

[12] Unit of elementary charge ($\mathrm{e} = 1.602176487(40) \cdot 10^{-19}$ C)
[13] respecting the conservation laws, like lepton number or charge conservation
[14] **C**abibbo–**K**obayashi–**M**askawa matrix or quark mixing matrix
[15] **Q**uantum **C**hromo **D**ynamics, see also sec. 2.4.2.
[16] called "gauge bosons"

Table 2.1: Summary of the particles of the standard model. I_3 stands for the third component of the *weak isospin*. All values are taken from [PDG08].

Fermions (spin = 1/2)				
leptons:	$\boldsymbol{e}$	$\boldsymbol{\mu}$	$\boldsymbol{\tau}$	
	$q = -1$	$q = -1$	$q = -1$	$I_3 = +\frac{1}{2}$
	$m_e = 0.511$ MeV	$m_\mu = 105.7$ MeV	$m_\tau = 1776.8$ MeV	
	$\boldsymbol{\nu}_e$	$\boldsymbol{\nu}_\mu$	$\boldsymbol{\nu}_\tau$	
	$q = 0$	$q = 0$	$q = 0$	$I_3 = -\frac{1}{2}$
	$m_{\nu_e} < 2$ eV	$m_{\nu_\mu} < 0.2$ MeV	$m_{\nu_\tau} < 18$ MeV	
quarks:	$\boldsymbol{u}$	$\boldsymbol{c}$	$\boldsymbol{t}$	
	$q = +\frac{2}{3}$	$q = +\frac{2}{3}$	$q = +\frac{2}{3}$	$I_3 = +\frac{1}{2}$
	$m_u \approx 2.6$ MeV	$m_c \approx 1.3$ GeV	$m_t \approx 171.2$ GeV	
	$\boldsymbol{d}$	$\boldsymbol{s}$	$\boldsymbol{b}$	
	$q = -\frac{1}{3}$	$q = -\frac{1}{3}$	$q = -\frac{1}{3}$	$I_3 = -\frac{1}{2}$
	$m_d \approx 5.0$ MeV	$m_s \approx 104$ MeV	$m_b \approx 4.2$ GeV	

Bosons (spin = 1)				
$\boldsymbol{\gamma}$	$\boldsymbol{g}$	$\boldsymbol{Z}^0$	$\boldsymbol{W}^-$	$\boldsymbol{W}^+$
$q = 0$	$q = 0$	$q = 0$	$q = -1$	$q = +1$
$m_\gamma < 10^{-18}$ eV	$m_g < 1.3$ MeV	$m_Z = 91.2$ GeV	$m_W = 80.4$ GeV	

$\boldsymbol{H}$ (spin = 0)
$q = 0$
(hypothetical particle)

2.2 Formalism of Quantum Field Theory

Similar to classical mechanics, where equations of motion can be derived from the principle of stationary actions by demanding

$$\delta S = \delta \int_{t_1}^{t_2} \mathrm{d}t\, L(q, \dot{q}) \stackrel{!}{=} 0, \tag{2.8}$$

in quantum (field) theory a corresponding approach leads to:

$$\delta S = \delta \int_{t_1}^{t_2} \mathrm{d}t \int \mathrm{d}^3x \underbrace{\mathcal{L}(\phi(x), \partial_\mu \phi(x))}_{\text{Lagrangian (density)}} \stackrel{!}{=} 0 \tag{2.9}$$

$$\Rightarrow \partial_\mu \frac{\partial \mathcal{L}}{\partial(\partial_\mu \phi(x))} - \frac{\partial \mathcal{L}}{\partial \phi(x)} = 0, \tag{2.10}$$

with the field $\phi(x)$ and its (four dimensional) gradient $\partial_\mu \phi(x)$.
One major theoretical challenge is to find Lagrangians $\mathcal{L}$ that satisfy this equation and describe the propagation of particles. For example the Lagrangian:

$$\mathcal{L} = \overline{\psi}(x)(i\gamma^\mu \partial_\mu - m)\psi(x). \tag{2.11}$$

leads to the Dirac equation for free fermions.

2.3 Dirac Equation

Since Schrödinger's equation cannot be used to describe relativistic particles, in 1928 Dirac developed his equation to allow it and thus was able to predict the existence of a "positively charged electron", the *positron*.
The Dirac equation with the four-component column vector $\psi(x)$, called *Dirac-Spinor*, and the mass m of the fermion, reads:

$$(i\gamma^\mu \partial_\mu - m)\psi(x) = 0. \tag{2.12}$$

2.4 Gauge Principle

In classical electrodynamics the electric and magnetic fields can be described by a scalar potential φ and a vector potential $\boldsymbol{A}$. Further it can be shown that the physical solutions for the fields do not change, if the following transformations are applied:

$$\boldsymbol{A}(\boldsymbol{r}, t) \longrightarrow \boldsymbol{A}' = \boldsymbol{A}(\boldsymbol{r}, t) + \boldsymbol{\nabla}\chi(\boldsymbol{r}, t) \tag{2.13}$$

$$\varphi(\boldsymbol{r}, t) \longrightarrow \varphi' = \varphi(\boldsymbol{r}, t) - \dot{\chi}(\boldsymbol{r}, t), \tag{2.14}$$

with the gradient ($\boldsymbol{\nabla}\chi$) and time derivation ($\dot{\chi}$) of one and the same scalar gauge field χ [Nol04].

In non-relativistic quantum mechanics, the solutions of the Schrödinger equation are invariant under a **global** transformation:

$$\psi(x) \longrightarrow \psi'(x) = \mathrm{e}^{iq\chi}\psi(x). \tag{2.15}$$

Therefore, the resulting probability densities and expectation values of operators are not changed by such a transformation.

These examples show that phase transformations are an important principle in different fields. This principle can be used to describe the interaction between particles when looking at **local** phase transformations, i. e.

$$\psi(x) \longrightarrow \psi'(x) = \mathrm{e}^{i\chi(x)}\psi(x). \tag{2.16}$$

But the Dirac equation is not invariant under such a transformation. In order to make this equation invariant under local transformations, one has to introduce a new "covariant derivative" that can be written as:

$$D_\mu \equiv \partial_\mu + iqA_\mu, \tag{2.17}$$

with a vector field A_μ. This field transforms under (2.16) as:

$$A_\mu \longrightarrow A'_\mu = A_\mu - \partial_\mu \chi. \tag{2.18}$$

With this, the Dirac equation can be written as:

$$(i\gamma^\mu D_\mu - m)\psi(x) = 0 \quad \Rightarrow \quad (i\gamma^\mu \partial_\mu - m)\psi(x) = q\gamma^\mu A_\mu \psi(x). \tag{2.19}$$

The *gauge field* A_μ can be identified with the photon field coupling to a fermion with charge q.

2.4.1 Quantum Electrodynamics (QED)

If local phase invariance of the Dirac equation is claimed, it is needed to introduce a field that can be identified with the electromagnetic field, through which this particle interacts [Sch95]. The complete Lagrangian of QED is:

$$\mathcal{L} = \psi(i\gamma^\mu D_\mu - m)\psi - \frac{1}{4}F_{\mu\nu}F^{\mu\nu}, \tag{2.20}$$

with the kinetic term of the photon:

$$F_{\mu\nu} = \partial_\mu A_\nu - \partial_\nu A_\mu. \tag{2.21}$$

Gauge transformations can be described mathematically by *gauge groups*. In this case the group is the $U(1)$ (unitary group). The attempt to describe the strong and the weak force in a comparable way turns out to be more complicated because a 'simple' $U(1)$ group has not the adequate properties.
The solution is to use higher symmetry groups and thus it is e. g. possible to model the symmetry properties of (strong) colour interactions by $SU(3)$[17].

2.4.2 Quantum Chromodynamics (QCD)

In Quantum Chromodynamics, quarks are described by the quantum mechanical states Ψ that can be seen as a direct product of a state depending on time and space and another state describing the colour charge properties, i. e.:

$$\Psi = \psi(x) \otimes \chi_{\text{colour}} \tag{2.22}$$

($\psi(x)$ = Dirac spinor).
All known strong interactions can be described if three different colour charges (plus anti-colour charges for anti-particles) are assumed. Formally, the colour parts of the wave function can be written as:

$$\chi_{\text{red}} = \begin{pmatrix}1\\0\\0\end{pmatrix} \qquad \chi_{\text{green}} = \begin{pmatrix}0\\1\\0\end{pmatrix} \qquad \chi_{\text{blue}} = \begin{pmatrix}0\\0\\1\end{pmatrix}. \tag{2.23}$$

The Dirac equation is required to be invariant under local $SU(3)_{\text{C}}$[18] transformations. These transformations can be written as:

$$\Psi \longrightarrow \Psi' = \mathrm{e}^{i\frac{g_s}{2}\beta_a(x)\,t^a}\Psi \tag{2.24}$$

(sum over all $a \in [1, 8]$).
The operators t^a are the eight generators of $SU(3)_{\text{C}}$.
To fulfil the postulated invariance, eight vector fields must be introduced. This leads to the Lagrangian of QCD:

$$\mathcal{L} = \overline{\Psi}(i\gamma_\mu\, D^\mu - m)\Psi - \frac{1}{4}G^a_{\mu\nu}G^{\mu\nu}_a, \tag{2.25}$$

with:

$$G^a_{\mu\nu} = \partial_\mu G^a_\nu - \partial_\nu G^a_\mu - g_s f_{abc} G^b_\mu G^c_\nu, \tag{2.26}$$

[17] special unitary group, $U^\dagger U = \mathbf{1}$, $\det U = 1$
[18] The subscript C indicates that this group is meant to describe the transformation in the 'colour space' in contrast to the also used $SU(3)_{\text{F}}$ for transformations in the "flavour space"

where f_{abc} are structure constants. This Lagrangian contains all possible QCD interactions. The fields G^a_μ can be combined to represent eight colour carrying gluons. One usual method to do this is:

$$R\overline{G}, \quad R\overline{B}, \quad G\overline{B}, \quad G\overline{R}, \quad B\overline{R}, \quad B\overline{G}, \quad R\overline{R} - G\overline{G}, \quad R\overline{R} + G\overline{G} - 2B\overline{B}. \tag{2.27}$$

One major difference to QED is the fact that gluons have a colour charge and are able to interact with other gluons. Fig. 2.1 summarises the possible interactions in QCD:

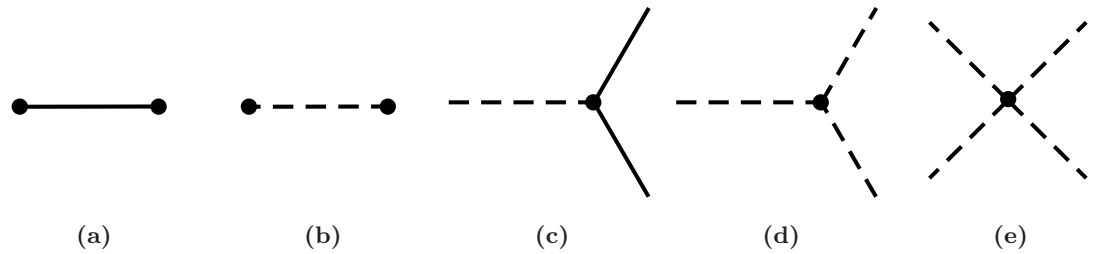

Figure 2.1: Summary of possible QCD interactions. (a) shows a 'pure' quark, (b) a pure gluon, (c) is the 'normal' quark-gluon vertex, (d) is one of the possible gluon-gluon interactions, (d) the other one. The solid line represents quarks, the dashed line stands for gluons. Adapted from [HM84].

The gluon-gluon interactions cause QCD to behave completely different from QED. One major difference is the *anti-screening* property of QCD leading to a coupling constant α_S, that become large at low energies. This results in the confinement of quarks in hadrons. For example, at the electroweak energy scale of $\alpha_S(M_{Z^0}) \approx 0.11$, while at lower energies, $\alpha_S(1\text{ GeV}) \lesssim 1$, making a perturbative approach impossible.

2.4.3 Electroweak Interactions

To describe the properties of weak interactions, a more sophisticated approach must be considered. It turns out that a combination of two symmetry groups $SU(2)_\mathrm{L} \times U(1)_\mathrm{Y}$ leads to a theoretical description in agreement with observations. The subscript 'L' denotes that only left handed fermions participate in weak interactions, 'Y' stands for "weak hypercharge" that is defined as $\mathrm{Y} = 2(Q - T_3)$ (with Q = charge, T_3 = third component of the weak isopin). In a way this theory unifies the electromagnetic and weak interactions which is reflected in the fact that the gauge boson fields can be written as linear combinations:

$$W^\pm_\mu = \frac{1}{\sqrt{2}}(W^1_\mu + iW^2_\mu) \tag{2.28}$$

$$Z_\mu = -B_\mu \sin\theta_W + W^3_\mu \cos\theta_W \tag{2.29}$$

$$A_\mu = B_\mu \cos\theta_W + W^3_\mu \sin\theta_W, \tag{2.30}$$

where the W^a stand for the three gauge fields of the $SU(2)$ and B for the gauge field of $U(1)$. The angle θ_W is called *Weinberg angle* and needs to be determined by experiment. Z_μ describes a boson field that allows to predict the existence of neutral currents (Z^0).
One property of this theory is that all gauge bosons mentioned above are assumed to be massless. This is correct for the photon as the force carrier of the electromagnetic force, but $W^\pm$ and Z^0 do have non-negligible masses, and it is not possible to simply add mass terms to the Lagrangian to describe the masses. One way to handle this issue is to introduce an additional Lagrangian depending on four scalar fields (ϕ^i) that result in a symmetry breaking[19]. This leads to additional

[19] in the ground state

terms that can be interpreted as a particle coupling to the $W^{\pm}$ and Z^0 bosons generating their masses. The attempt is called the *Higgs mechanism* [HM84].
The complete Lagrangian of the electroweak interaction including the *Higgs boson* can be written as:

$$\mathcal{L} = -\frac{1}{4}\boldsymbol{W}_{\mu\nu}\cdot\boldsymbol{W}^{\mu\nu} - \frac{1}{4}B_{\mu\nu}B^{\mu\nu} \qquad \begin{cases} W^{\pm},\ Z^0,\ \gamma \text{ kinetic} \\ \text{energies and self-interaction} \end{cases}$$

$$+ \overline{L}\gamma^{\mu}\left(i\partial_{\mu} - g\frac{1}{2}\boldsymbol{\tau}\cdot\boldsymbol{W}_{\mu} - g'\frac{Y}{2}B_{\mu}\right)L \qquad \begin{cases} \text{lepton and quark kinetic energies} \\ \text{and their interactions} \\ \text{with } W^{\pm},\ Z^0,\ \gamma \end{cases}$$

$$+ \overline{R}\gamma^{\mu}\left(i\partial_{\mu} - g'\frac{Y}{2}B_{\mu}\right)R$$

$$+ \left|\left(i\partial_{\mu} - g\frac{1}{2}\boldsymbol{\tau}\cdot\boldsymbol{W}_{\mu} - g'\frac{Y}{2}B_{\mu}\right)\phi\right|^2 - V(\phi) \qquad \begin{cases} W^{\pm},\ Z^0,\ \gamma, \text{ Higgs} \\ \text{masses and coupling} \\ \text{and the Higgs potential} \end{cases}$$

$$-\left(G_1\overline{L}\phi R + G_2\overline{L}\phi_c R + \text{h. c.}\right). \qquad \begin{cases} \text{lepton and quark masses} \\ \text{and coupling to Higgs} \end{cases}$$

Here L represents the left handed fermion doublet and R the right handed fermion singlet, g and g' are the coupling constants of electroweak interactions. ϕ and ϕ_c are Higgs fields and G_1, G_2 mass coupling constants. This Lagrangian shows the massless bosons, their interaction with the fermions, the Higgs mechanism, attaching the mass to the bosons, and finally the mass terms of the fermions.

2.4.4 Higgs Boson

The new particle called Higgs boson[20] must have spin=0 and charge=0. It has not been observed yet and searches (especially at LEP[21]) could only exclude the Higgs boson with a mass below $m_H \leq 114.4$ GeV [PDG08]. More recent results from TEVATRON exclude a Higgs boson with a mass in the range $162 - 166$ GeV [CD10]. Fits of the experimental results and corresponding predictions from electroweak calculations favour a Higgs boson with $m_H \lesssim 180$ GeV.
As mentioned above, this particle could explain the masses of the gauge bosons and of the fermions and, in a certain manner, it would make the standard model complete.
The discovery potential for the Higgs boson of the CMS detector is shown in fig. 2.2. The plot shows the significance in units of standard deviations from the SM vs. the Higgs mass for 30 fb^{-1}. This integrated luminosity can be accumulated within only a few months of LHC operation at design luminosity. The search for the Higgs boson is one of the primary goals of the LHC and it will be possible to find or exclude a standard model Higgs with its help.

2.4.5 Supersymmetry

As mentioned introductory, the standard model cannot describe all phenomena in particle physics (e. g. the hierarchy problem).
One favoured extension of the standard model that could solve this and other problems, has been developed in the 1970s and is called supersymmetry (SUSY). In this theory to every particle of the SM a new one is assigned with exactly the same quantum numbers, but with a difference in

[20] after its inventor P. Higgs
[21] **L**arge **E**lectron **P**ositron Collider

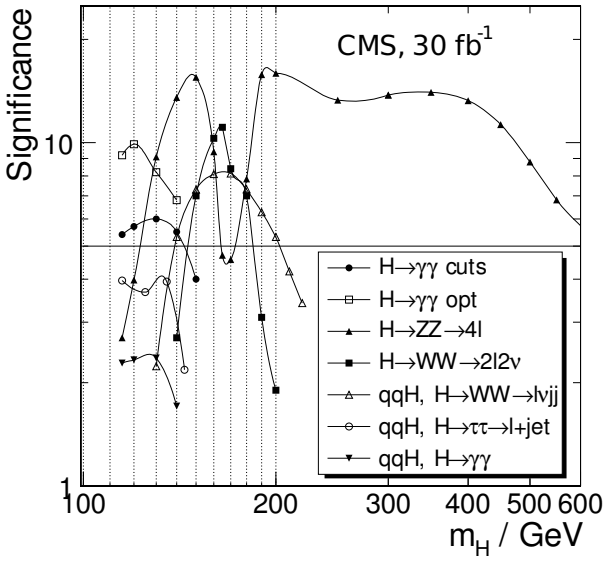

Figure 2.2: Signal significance as a function of the Higgs mass for 30 fb^{-1} for different production/decay channels at $\sqrt{s} = 14$ TeV [CMS06b].

spin of $\frac{1}{2}$. Nevertheless this symmetry must be broken in some way because the SUSY particles have not been observed until today. Thus they must be much heavier than their SM counterparts. By introducing these new particles, SUSY allows to solve some problems of particle physics like the hierarchy problem, unification of couplings and possibly even the existence of dark matter, known from astrophysics.

One SUSY scenario, the *minimal supersymmetric extension of the standard model* (MSSM), allows to solve these problems but unfortunately, this model needs more than 100 free parameters that have to be determined experimentally. A simplification, known as mSUGRA[22] allows a reduction of free parameters to five. The LHC provides the possibility to scan this parameter space in a wide range. One example for the discovery reach of the CMS detector with respect to a certain parameter plane is shown in fig. 2.3.

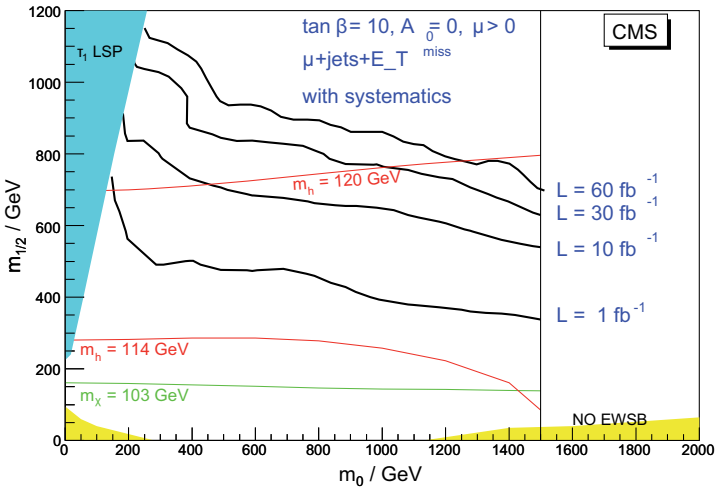

Figure 2.3: Discovery reach of CMS in the $m_0 - m_{1/2}$-plane of the MSSM for different integrated luminosities for fixed parameters $\tan\beta, A_0, \mu$, $\sqrt{s} = 14$ TeV [CMS06b].

[22] **m**inimal **SU**per **GRA**vity

Chapter 3

LHC and the CMS Detector

In the search for new physics there are several theories that predict the existence of new particles with masses from several hundred GeV up to some TeV. Producing these new particles in collider experiments requires correspondingly high centre-of-mass energies. Since the energy of electron-positron storage rings is limited due to the synchrotron radiation losses ($\Delta E \sim \frac{1}{R}\left(\frac{E}{m}\right)^4$, R the bending radius of the accelerator, E, m energy and mass of the particle), heavier particles are used to reach higher beam energies. When using protons and anti-protons as collision partners, the luminosity of the collider is limited due to the challenging production of anti-protons. The desired centre-of-mass energies can be reached by using protons because they are about 2000 times heavier than electrons and thus do not suffer dramatically from synchrotron radiation losses as electrons do and they are much easier available than anti-protons. Therefore, instead of using protons and anti-protons, the LHC[23] is a proton-proton collider with a design centre-of-mass energy of $\sqrt{s} = 14$ TeV.

3.1 The Large Hadron Collider (LHC)

The LHC is built in the tunnel of the former e^+/e^--collider LEP[24] close to Geneva, Switzerland. It has a circumference of 26.7 km and is located between 45 m and 170 m below surface as demonstrated in fig. 3.1a. The protons inside the beam are bent by 1232 dipole magnets that

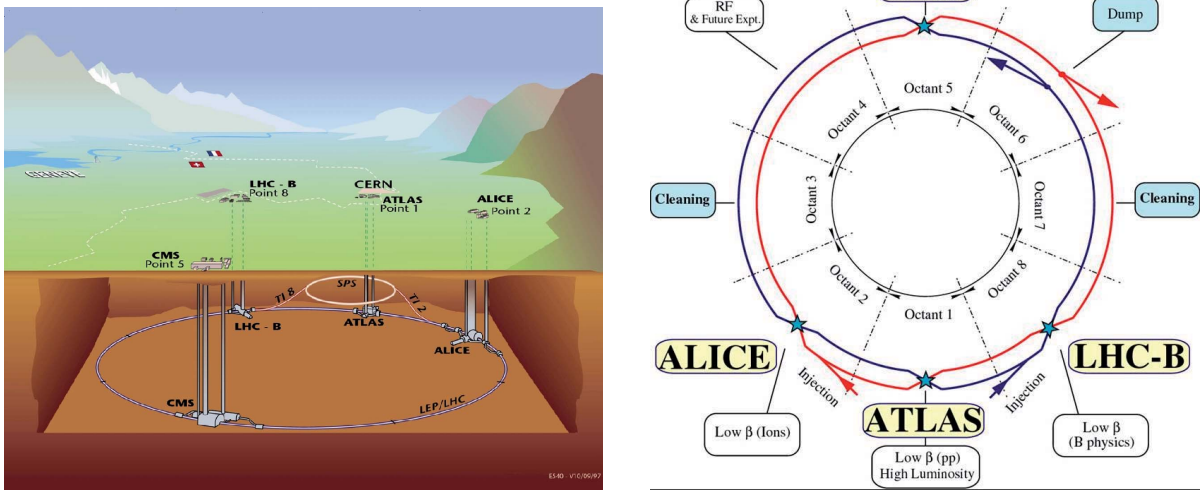

(a) Underground view of the LHC and SPS[25] with the four major experiments [CER09].

(b) Layout of the LHC beams [CER09].

Figure 3.1: Sketch of the LHC storage ring and of the proton beams inside the ring.

[23] **L**arge **H**adron **C**ollider
[24] **L**arge **E**lectron **P**ositron Collider

each create a peak dipole field of about 8.4 T requiring the usage of special superconducting materials that need cooling down to 1.9 K. The bending power of these magnets limits the beam energy to 7 TeV.
Due to the fact that no particle/anti-particle combination is used inside the LHC, the acceleration and deflection of the beams must take place in two separate rings as is shown in fig. 3.1b. Because of this and the limited space inside the beam pipe, a 'two-in-one' solution for the dipoles has been chosen that is illustrated in fig. 3.2. One disadvantage of this solution is the magnetic coupling of both rings that complicates maintenance and reduces flexibility.

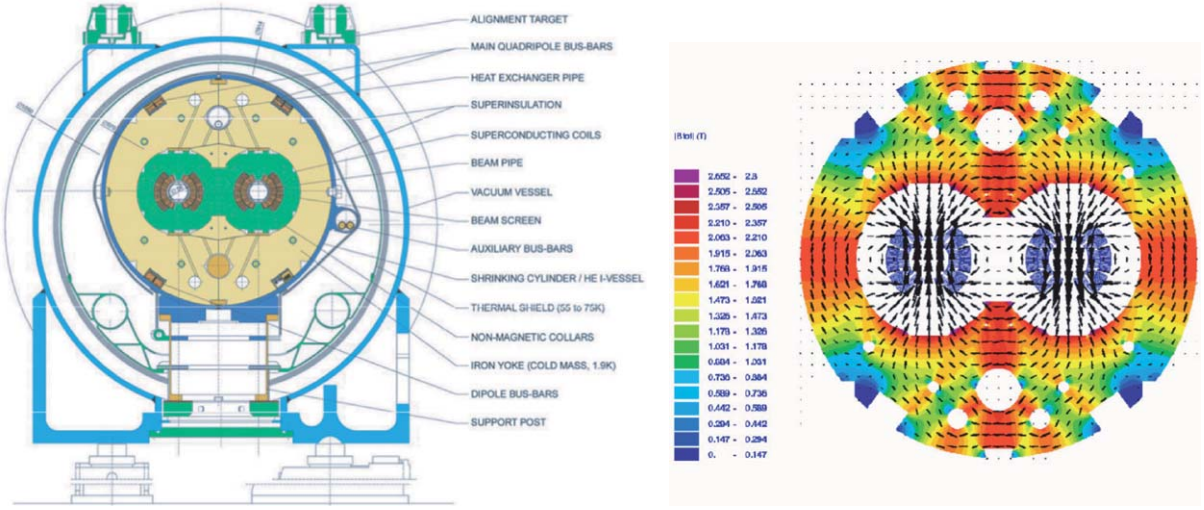

(a) Schematics of the dipole cross-section.

(b) Computation of the magnetic flux within the dipole. The peak magnetic field of more than 8 T is reached inside the innermost part of the dipole and is not shown here.

Figure 3.2: Sketch of the twin bore dipole magnets used in LHC [Eva07b].

One important property of a particle collider is its (instantaneous) luminosity. The number of events per time of a specific process with cross section σ_{event} is given by [PDG08]:

$$\dot{N}_{\text{event}} = \mathsf{L} \cdot \sigma_{\text{event}}.$$

Here the luminosity L is approximately:

$$\mathsf{L} = f \frac{N_{\text{b}}^2 \, n_{\text{b}}}{4\pi \, \sigma_x \, \sigma_y}, \tag{3.1}$$

where n_{b} is the number of bunches within the proton beam and is intended to be 2808 (per beam). N_{b} is the number of particles per bunch which will be in the order of 10^{10} in design operation and f the revolution frequency with intended 40 MHz. σ_x and σ_y denote the widths of the beam which is assumed to be Gaussian distributed in both directions.
The peak luminosity is expected to be as high as 10^{34} cm^{-2}s^{-1} at the interaction points where the two all-purpose detectors ATLAS[26] and CMS[27] are placed and 10^{32} cm^{-2}s^{-1} for the LHCb[28]-experiment and even lower (10^{27} cm^{-2}s^{-1}), for heavy ion collision, for the ALICE[29]-detector. Before injected into the main storage ring, the proton beams are accelerated in several steps as shown in figure 3.3.

[25] **S**uper **P**roton **S**ynchrotron
[26] **A** **T**oroidal **L**HC **A**pparatu**S**
[27] **C**ompact **M**uon **S**olenoid
[28] for **b**-physics
[29] **A** **L**arge **I**on **C**ollider **E**xperiment

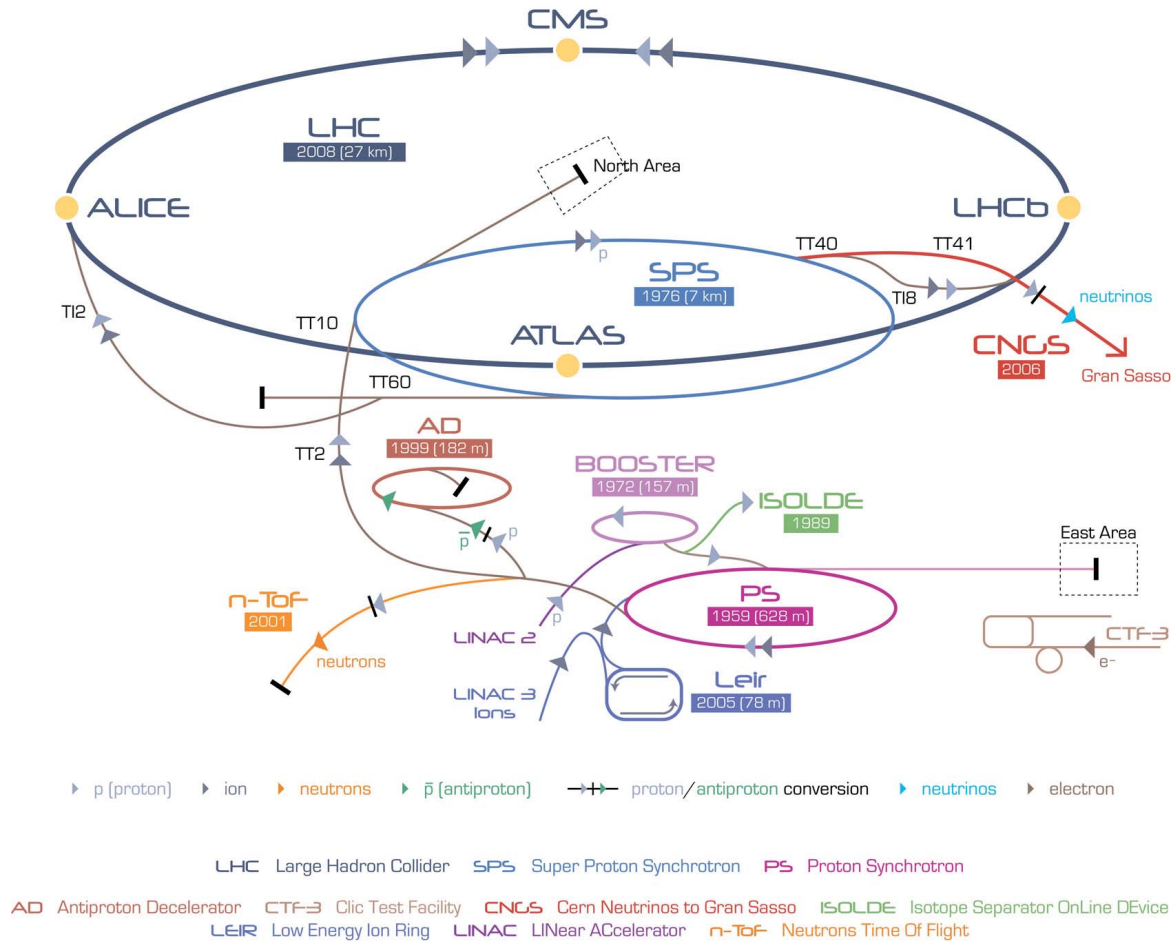

Figure 3.3: The injection and acceleration chain of the LHC [CER09].

After being created by ionisation of hydrogen, the protons are accelerated to 50 MeV in the *Linac2*, a linear proton accelerator. Then the PSB[30] is filled and the protons are accelerated to 1.4 GeV and the bunches are compressed to 190 ns. Thereafter the bunches are injected into the PS[31], split up and further accelerated to 25 GeV. Before the bunches are filled into the SPS, they are compressed to a length of 4 ns. Here the protons are accelerated up to the LHC injection energy of 450 GeV per beam. Finally, in the LHC, they are accelerated to the design beam energy.
The expected lifetime of the proton beams inside the LHC is in the order of 15 h.

More details on the LHC can be found in [Eva07b; EB08; Brü04a; Brü04b; Brü04c; PDG08].

3.2 CMS and its Components

The Compact Muon Solenoid has been constructed as a multi-purpose detector particularly for proton-proton collisions at the LHC at CERN. It has been first built on the surface and was then lowered and installed in a cavern about 100 m underground at *Point 5* (see fig. 3.1a). It is a challenge for the construction of all detector components to handle the expected particle flux after a proton-proton collision at the design collision energies and luminosities. At a bunch crossing rate of up to 40 MHz it is essential to be able to clearly distinguish the products of the interaction of one bunch crossing from another. For this purpose a detector with high granularity

[30] **P**roton **S**ynchrotron **B**ooster
[31] **P**roton **S**ynchrotron

and good time resolution is needed, resulting, among other things, in the need of a vast number of readout channels and a very good synchronisation. A coverage of nominally the whole solid angle is important to have a good resolution for the missing transverse momentum where new physics could show up.
Due to the fact that the centre-of-mass system of the collision partners is approximately at rest in the laboratory frame, a spherical design of the detector would be preferred because the reaction products are expected to leave the interaction point in all directions (not isotropically). However the beams have to pass the detector, so a cylindrical structure surrounding the beam axis has been chosen that allows the coverage of approximately $4\,\pi$ of solid angle around the interaction point. The detector is constructed of five wheel-like structures called the *barrel* region and two *endcaps*. Each *wheel* has a diameter of 14.6 m and in total the detector has a length of 21.6 m and a weight of 12500 t. A schematic view of the detector with its components is given in fig. 3.4
The CMS coordinate system is as follows:

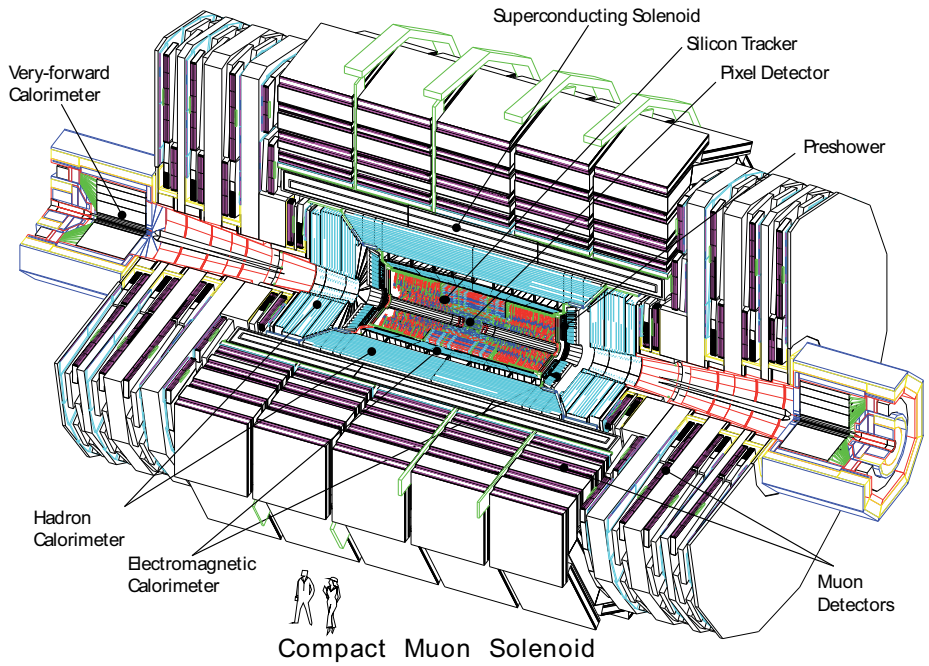

Figure 3.4: Sketch of the CMS detector with its major components [CMS08].

The centre lies in the (nominal) interaction point with the y-axis pointing vertically upwards. The z-axis points along the beam pipe while the x-axis points to the centre of the LHC collider ring. The azimuthal angle ϕ is measured in the $x-y$-plane from the x-axis. The polar angle is translated into the pseudorapidity η by:

$$\eta = -\ln\tan\left(\frac{\theta}{2}\right) \tag{3.2}$$

Here θ denotes the angle between the particle momentum and the beam axis. η has the range $[-\infty, \infty]$ and has the advantage to be closely related to the (invariant) rapidity y in special relativity.
The main detector components are described in the following sections starting from the interaction point going outwards. Further details on CMS can be found in [CMS08; CMS06a; CMS98; CMS00a; CMS97b; CMS97a; CMS00b].

3.2.1 The Tracking System

To handle the many different particles leaving the interaction point, a detector with high granularity is needed that also has a very good time and space resolution. Due to the high particle rates

expected in this region and the accompanied radiation damages, the choice of proper materials of the components for the Tracker is crucial to ensure a lifetime that is as long as possible. Silicon is the material of choice in this case. To increase the lifetime further, the cooling of the Tracker to $-10°C$ is necessary. Nevertheless, the first Tracker parts will have to be replaced after a period of about 3 years of collisions at design luminosity.
The working principle of a silicon tracker is illustrated in fig. 3.5a. A silicon layer works like a semi-conductor diode with reverse voltage applied. A traversing ionising particle creates electron-hole pairs inside the depleted silicon volume which leads to a measurable electric pulse at the diode terminals. The readout anodes (upper part in the figure) are typically sub-divided into pixels or strips. This fine segmentation allows a very fast and precise position determination. The figure additionally shows the deflection of the electrons (and holes) in a magnetic field. The deflection angle (Lorentz angle) must be taken into account when reconstructing tracks. A complete schematic of the Tracker and its components can be found in fig. 3.6.

The Pixel Detector

The *Pixel Detector* is the detector component which is closest to the interaction point. It consists of three cylindrical barrel layers and is completed by two disk-like modules at both ends. These components are shown in fig. 3.5b. The 48 million pixels in this arrangement cover the wide region of $|\eta| < 2.5$. Each pixel having a size of $100 \times 150\ \mu m^2$ allows for a spatial resolution in the range of $15 - 20\ \mu m$. The major advantage of pixels is their ability to measure three coordinates simultaneously, one big disadvantage is the huge amount of readout channels needed.

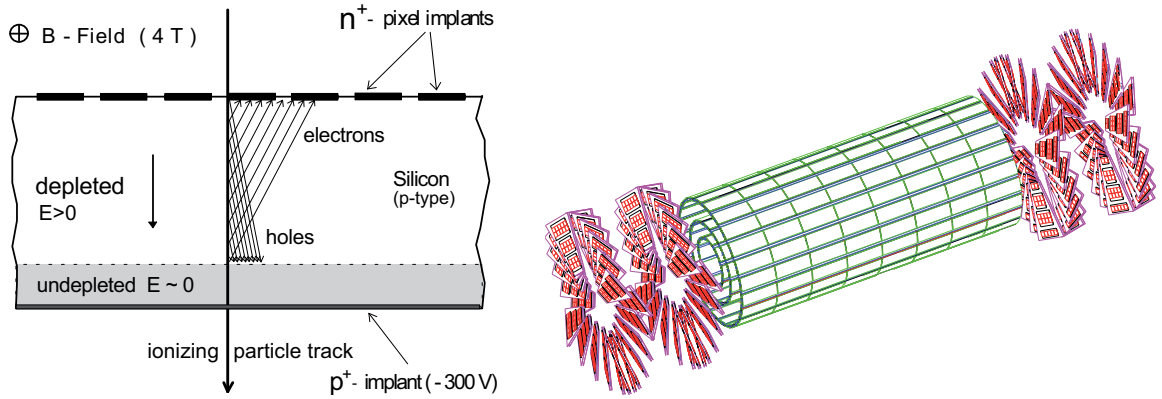

(a) Cross section view of a silicon layer of the tracker. A traversing particle creates electron hole pairs that drift to the terminals causing an electrical signal. The charge carriers are deflected by the magnetic field [CMS98].

(b) Layout of the three barrel layers and endcaps of the innermost pixel detector [CMS06a].

Figure 3.5: Working principle of a Tracker layer and a schematic view of the Pixel Tracker.

The Silicon Strip Tracker

The remaining (outer) parts of the Tracker are composed of silicon micro-strip devices. This reduces the number of readout channels and also the construction costs. By mounting the different layers under a well-known angle to each other it is possible to measure both coordinates of a traversing particle with high precision. The remaining Tracker components are:

- **Tracker Inner Barrel (TIB) / Tracker Inner Disks (TID)**:
  The *Inner Barrel* part is situated directly outside the Pixel Detector again in cylindrical

shape and is complemented by the *Tracker Inner Disks* which are located at both ends of this cylinder. The strip pitch of $80 - 120$ µm allows a single hit resolution of $23 - 35$ µm and a two-track separation of better than 200 µm.

- **Tracker Outer Barrel (TOB)**:
  The *Tracker Outer Barrel* consists of six detection layers. Due to the reduced particle flow, with respect to the inner most part of the detector, a bigger strip pitch can be chosen what allows to further reduce the number of readout channels. Still a single hit resolution of $35 - 53$ µm can be reached.

- **Tracker End Caps (TEC)**:
  The Tracker is closed by the two *Tracker End Caps*, each containing nine disks carrying the modules with the silicon readout.

The overall transverse momentum resolution of the Tracker can be written as[32] [CMS98]:

$$\frac{\Delta p_{\mathrm{T}}}{p_{\mathrm{T}}} \approx a \, \frac{p_{\mathrm{T}}}{\mathrm{TeV}} \oplus b \tag{3.3}$$

With $a = 15\,\% - 60\,\%$ depending on the η-region and a constant $b = 0.05\,\%$.

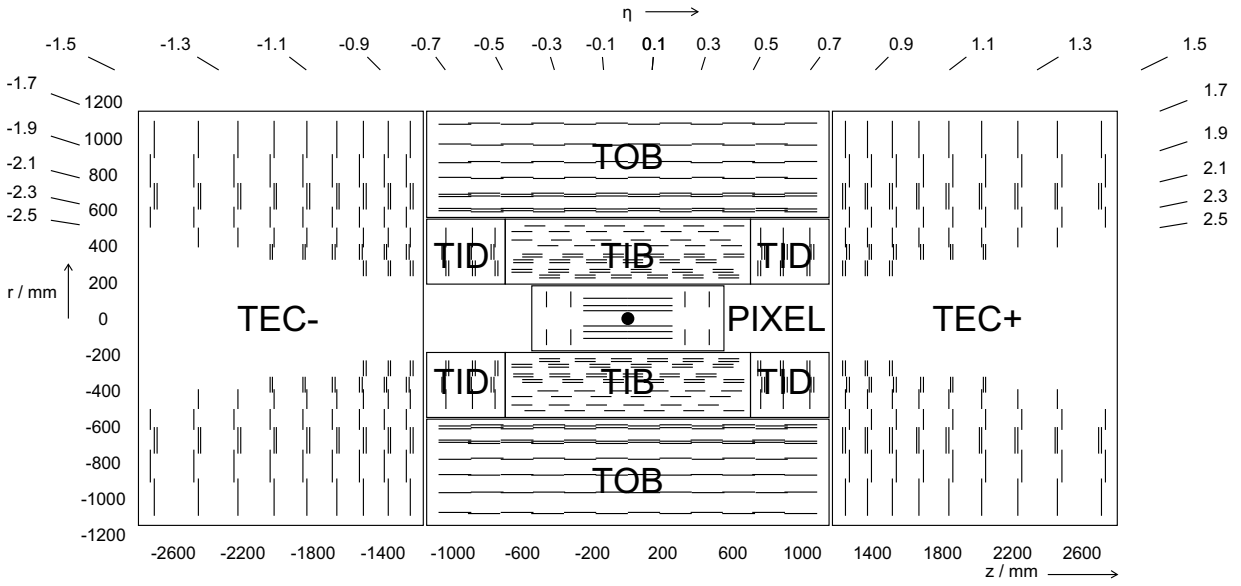

Figure 3.6: Drawing of the Tracker cross section with all its components [CMS08].

3.2.2 Electromagnetic Calorimeter (ECAL)

One way to measure the energy of electrons and (high energy) photons is to let them interact electromagnetically until they are absorbed in a specified volume and to count the optical photons created by scintillation within the material. To do this efficiently a material with a high proton number is preferred which should also be transparent to its own scintillation light.
In the CMS detector this is realised by 61200 lead tungstate ($PbWO_4$) crystals in the central barrel region of the detector and 7324 crystals in each endcap, all positioned directly outside the Tracker.
$PbWO_4$ is a fast inorganic scintillator[33] (decay time ≈ 10 ns) that has a high density, short

[32] With the notation: $\alpha \oplus \beta = \sqrt{\alpha^2 + \beta^2}$

[33] An inorganic scintillator has a completely different light creation mechanism as an organic scintillator. Details on this can be found in [Bir64].

radiation length[34] of 8.9 mm and a small Molière radius[35] (22 mm). It has a high mass fraction of metal (about 85 %) and is nevertheless transparent to (visible) light. The components of the ECAL are:

- **Barrel region (EB)**:
  The crystals in the barrel region of the ECAL have a face cross-section of $\approx 22 \times 22$ mm^2 and a length of 230 mm. They are composed to form a hermetic and homogeneous calorimeter. Due to the low light output of the $PbWO_4$ ($\frac{N_\gamma}{E} \approx \frac{30}{\text{MeV}}$) and the very high magnetic field inside the detector, special photodetectors are needed. For the barrel region Avalanche Photo Diodes (APD, see also section 5.6.5) have been chosen which have a very high quantum efficiency (75 % at 430 nm) and are insensitive to magnetic fields.

- **Endcaps (EE)**:
  The ECAL Endcaps are positioned at the ends of the cylindrical ECAL structure and are readout by Vacuum Photo Triodes (VPT). These light sensitive devices can be described as photomultipliers with only one gain stage. They have comparably small gain but can be operated at high magnetic fields without major losses in signal quality. Nevertheless high voltage ($600 - 800$ V) is needed.

- **Preshower (ES)**:
  The motivation for the *Preshower* detector of the ECAL lies in the improvement of identifying π^0's that can decay into two photons and fake a high-energetic photon. The Preshower is constructed as a sampling calorimeter with two layers. Electromagnetic showers are initiated by incoming photons/electrons in the lead radiator and the deposited energy and shower profile are measured in a layer of silicon strip sensors after each radiator. The ES covers $1.653 < |\eta| < 2.6$.

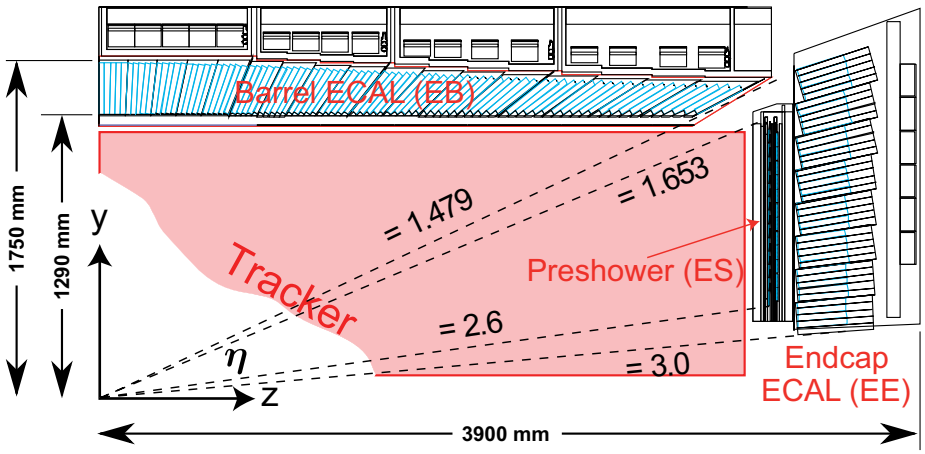

Figure 3.7: Section through one quarter of the ECAL. Adapted from [CMS06a].

All components together cover a range of $|\eta| < 3.0$.
The energy resolution of the ECAL is found to be [CMS06a]:

$$\frac{\Delta E}{E} = \frac{S}{\sqrt{E/\text{GeV}}} \oplus \frac{N}{E/\text{GeV}} \oplus C \tag{3.4}$$

[34] The radiation length is the distance an (high-energetic) electron travelled in matter where its energy has dropped to $1/e$ of its starting energy. More details in [Leo87].
[35] The Molière radius R_M is a measure for the energy deposit of a particle inside a volume. On average 90 % of the electromagnetic shower energy, caused by a traversing particle, is deposited in a cylindrical volume with the radius R_M. See also e. g. [Kle05].

where the stochastic term is $S \approx 2.8\,\%$, the noise term is $N \approx 12\,\%$ and constant the term $C \approx 0.3\,\%$.
An overview of all the components of the ECAL can be found in fig. 3.7.

3.2.3 Hadronic Calorimeter (HCAL)

The working principle of the HCAL is similar to that of the ECAL but the incoming particles loose energy by reactions of the strong force rather than electromagnetically. In these reactions new particles are produced resulting in a hadronic shower inside the absorber material. The read-out and the measurement of the energy deposit are done with help of scintillation light caused by the created charged particles.
Hadronic calorimeters are crucial to measure the energy of hadron jets and together with the electromagnetic calorimeters to determine the missing energy of a process caused by e. g. neutrinos or new particles that do not interact inside the detector.
The calorimeter is hermetic and covers a total of $|\eta| < 5.0$ surrounding the whole ECAL. An overview of the calorimetric system of CMS can be found in 3.8.

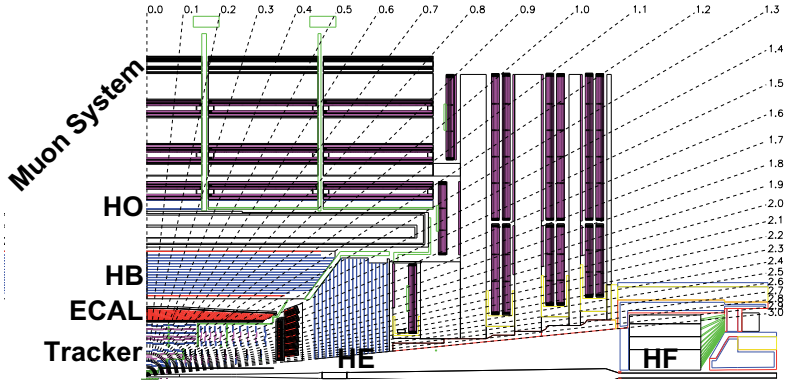

Figure 3.8: Cross-section view of the CMS detector to show the components of the HCAL. Adapted from [CMS06a].

The components of the HCAL are:

- **Hadron Barrel (HB)**:
  The *Hadron Barrel* is a sampling calorimeter that is built to have layers of 50.5 mm brass each followed by a layer of 4 mm scintillating material read out with scintillating fibres. Brass has a short nuclear interaction length and is not magnetic. The shower particles produced in the brass create scintillation light that is detected by multi-channel HPDs[36]. Basically the HPD is a vacuum photodiode tube where the collection electrode (anode) is replaced by a reverse-biased silicon diode. It is also only weakly sensitive to magnetic fields [DeS97].
  The HB is cylindrical and situated in the radial range 1777 mm $< r <$ 2877 mm, resulting in up to 10.6 interaction lengths, and it covers $|\eta| < 1.3$.

- **Hadron Endcap (HE)**:
  The calorimeters in the endcaps work in a similar way as those in the barrel region and have a thickness of about 9 interaction lengths.

- **Hadron Forward (HF)**:
  To handle the very high particle rates and with it the high radiation doses in the very forward region, the *Hadron Forward* calorimeter uses steel absorbers and quartz fibres as

[36] **H**ybrid **P**hoto**D**iode

active medium. Particles passing this material generate Cherenkov light that can be detected by conventional PMTs. These can be used at this place due to the much lower magnetic filed in the outer region of the detector.
The HFs are located 1120 mm away from the interaction point with a coverage of $2.9 < |\eta| < 5.0$.

- **Hadron Outer (HO)**:
  Since the ECAL and the HB do not provide enough material to stop all the incoming hadrons, an additional layer, the *Hadron Outer*, is needed. All the components described in the sections above are located inside the magnetic coil. The HO is situated directly outside the magnet. The tiles consist basically of scintillating material and are read out by wavelength shifting fibres. Modules of the HO are only placed in the five wheels and not in the endcaps.

With the HO the whole calorimetric system (ECAL + HCAL) of CMS has a minimum of 11.8 interaction lengths and is expected to have a resolution of [CMS97b]:

$$\frac{\Delta E}{E} \approx \frac{1\ \text{GeV}}{E} \oplus 4.5\ \% \tag{3.5}$$

in the energy range $30\ \text{GeV} < E < 1\ \text{TeV}$.

3.2.4 Superconducting Magnet

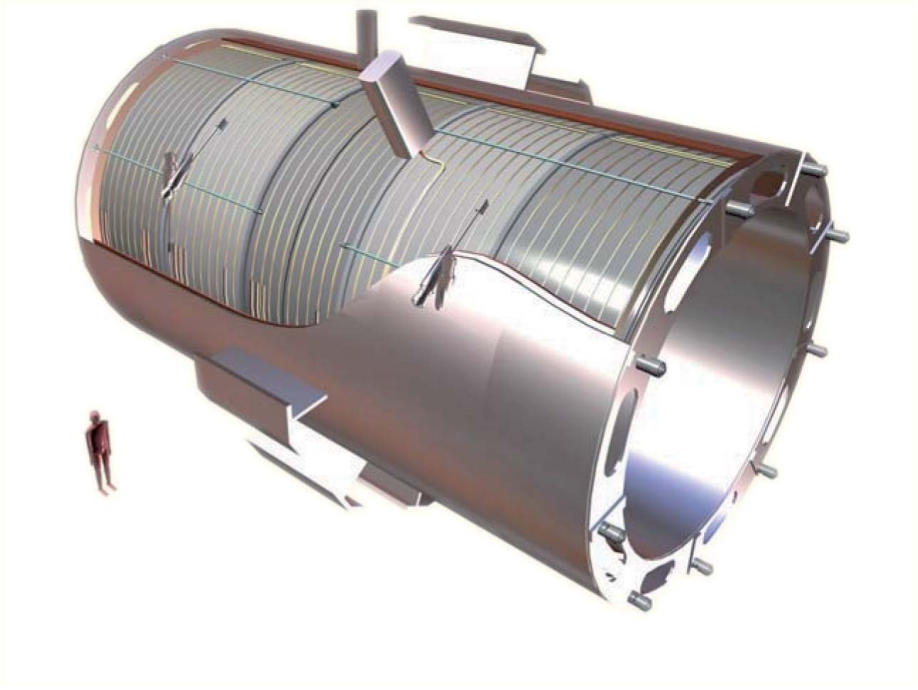

Figure 3.9: Artistic view of the magnet of the CMS detector [CMS08].

The 'heart' of the CMS detector is a superconducting magnet that is located directly outside the Hadron Barrel and in front of the Hadron Outer calorimeter. This layout has the advantage that particles have to pass less material before reaching the calorimeters. To create the magnetic field of nearly 4 T a large superconducting *Solenoid* magnet is needed. This results in a cylindrical coil with a diameter of 6 m and a length of 12.5 m that is able to store 2.6 GJ of energy at full operation current. Nevertheless, it is 'thin', i. e., $\frac{\Delta R}{R} \approx 0.1$. To return the magnetic flux a 10000 t iron yoke in form of the five wheels and 2 endcaps is needed (see also fig. 3.9).

3.2.5 Muon System

One big goal of CMS is to clearly identify the charge and precisely measure the momentum of muons coming from the interaction point over a wide momentum range. Many promising theories predict reactions with high energetic muons in the final state. For example, the Higgs production and decay via the process:

$$pp \to H \to ZZ^{(*)} \to \mu^+\mu^-\mu^+\mu^-$$

is called "the golden channel" because of its clean signature and the well detectable muons. For this and other purposes a powerful muon detection system is needed.

Drift Tube (DT) chambers

In the barrel region of the detector the muon momenta are measured by *Drift Tube* chambers. The DT chambers are mounted inside the iron return yoke wheels and thus form concentric cylinders with different diameters. Due to the return yokes, the magnetic field here is much weaker than in the inner region ($\lesssim 2$ T). A cross section view of one wheel is shown in 3.10. Each DT chamber

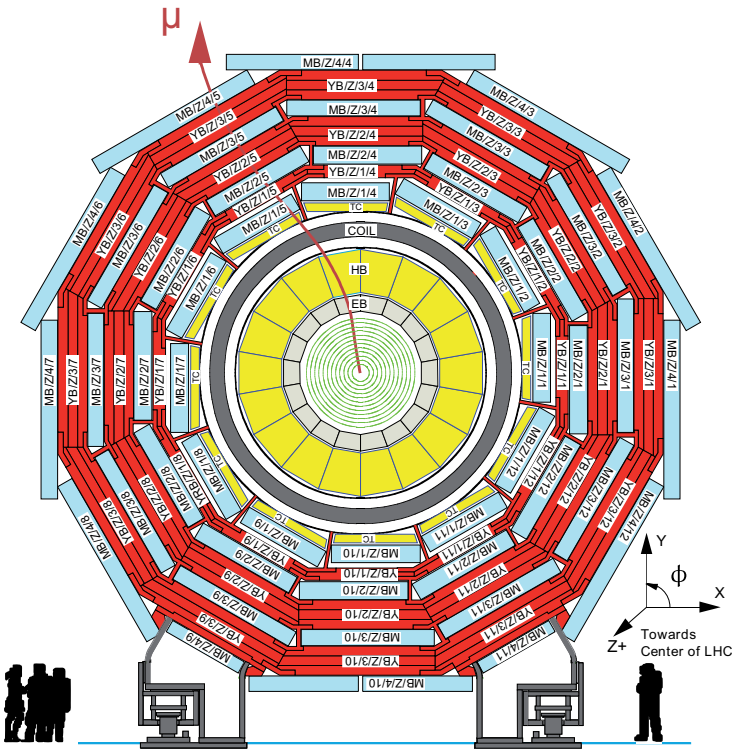

Figure 3.10: Schematical view of one of the CMS wheels. Special focus is given here to the DT chambers. They are labelled according to: MB/wheel/station/sector. The return yokes are also clearly visible here (adapted from [CMS08]).

consists of three *Superlayers* (SL), except of the outermost chambers labelled MB4 where only two SLs are built in. In every DT the middle SL is rotated by 90° to make a measurement in two dimensions possible. That is the reason why they are called ϕ- and θ-superlayer. An overview of an SL and its parts can be found in fig. 3.11. The superlayers are made of four layers of drift cells/tubes. The drift cells are the actual sensitive detectors in this setup. Each cell has a width of 42 mm, a height of 13 mm and a length between 1990 mm and 3020 mm. Each cell is filled with a mixture of 85 % Ar and 15 % CO_2. A 50 µm anode wire made of gold-plated stainless-steel is mounted in the middle of each cell where a voltage of +3600 V is applied. The voltage applied to the cathodes that are glued to the 'I'-shaped aluminium beams is −1200 V.

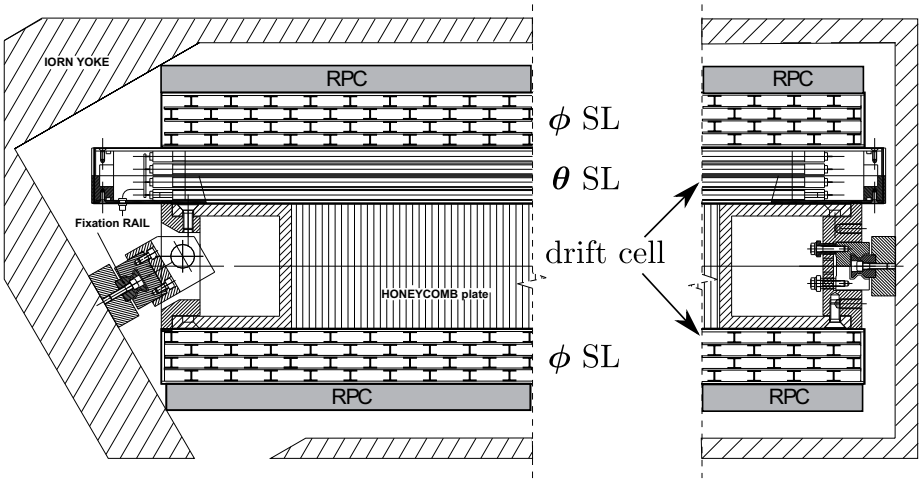

Figure 3.11: Sketch of one Drift Tube chamber. The three superlayers (SL) with their drift cells are shown. The RPCs are described in sec. 3.2.5. Adapted from [CMS08].

Additionally there are field forming electrodes mounted on the upper and lower side of the cell at +1800 V. A drawing of a drift cell can be found in fig. 3.12.
To minimise the non-sensitive volume of the system and to handle the left-right ambiguities, the drift cell layers are displaced by half a drift cell width with respect to the neighbouring layers. Charged particles (especially muons) passing the gas volume ionise the gas molecules. The electrons and ions cannot recombine because of the high electrical field, and the electrons are accelerated towards the anode wire, the ions towards the cathode strips. When the electrons reach the anode wire, the acceleration due to the very dense field causes them to ionise further gas atoms/molecules and so on causing an avalanche effect, so that the number of electrons reaching the anode wire becomes large enough to create a measurable electrical signal. The gas composition

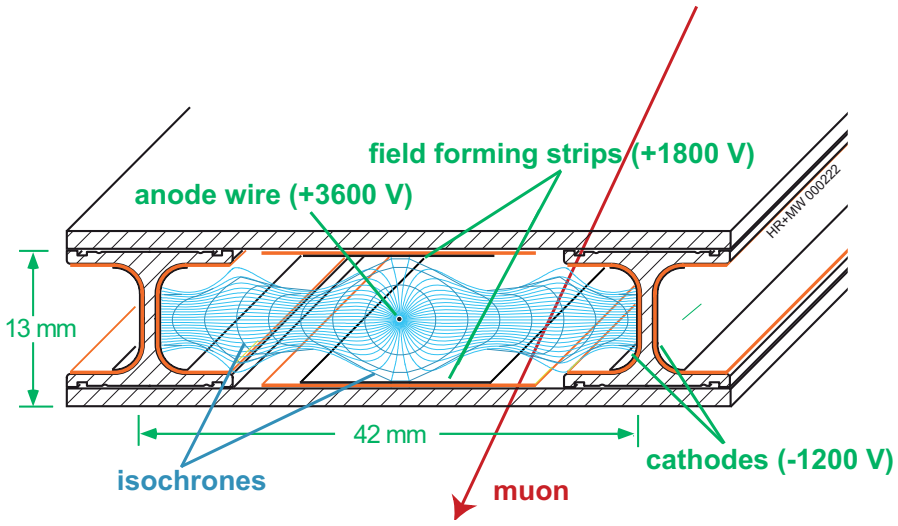

Figure 3.12: Schematics of one drift cell. The field lines and isochrones are a result of a corresponding simulation. A traversing muon ionises the gas inside the volume what creates an electrical signal at the anode. Adapted from [CMS08].

and the cell size were chosen to limit the drift time inside a cell to maximally 380 ns. There is a linear correlation between time and drift-path length. A drift velocity of about 55 µm/ns is reached.
The DT chambers cover the region of $|\eta| < 1.2$ and reach a spatial resolution of 100 µm.

Cathode Strip Chambers (CSC)

The environment of the forward regions, i. e. in the endcaps of the detector, is a bit more challenging. Due to the highly inhomogeneous and strong magnetic field and the expected high particle fluxes, it is mandatory to use a different kind of muon detector. For these purposes *Cathode Strip Chambers* have been chosen. These are trapezoidal multiwire proportional chambers made of seven anode wire planes with gaps of 9.5 mm in between that are filled with a mixture of 40 %Ar + 50 %CO_2 +10 %CF_4. The size of the chambers is up to $3400 \times 1500\ \text{mm}^2$. The chambers have cathode strips running fan-shaped in radial direction and anode wires in azimuthal direction. The anode wires are 50 µm in diameter and have a spacing of 3.2 mm. A schematic view and the operation principle are illustrated in fig. 3.13. There is a voltage of 3.6 kV applied

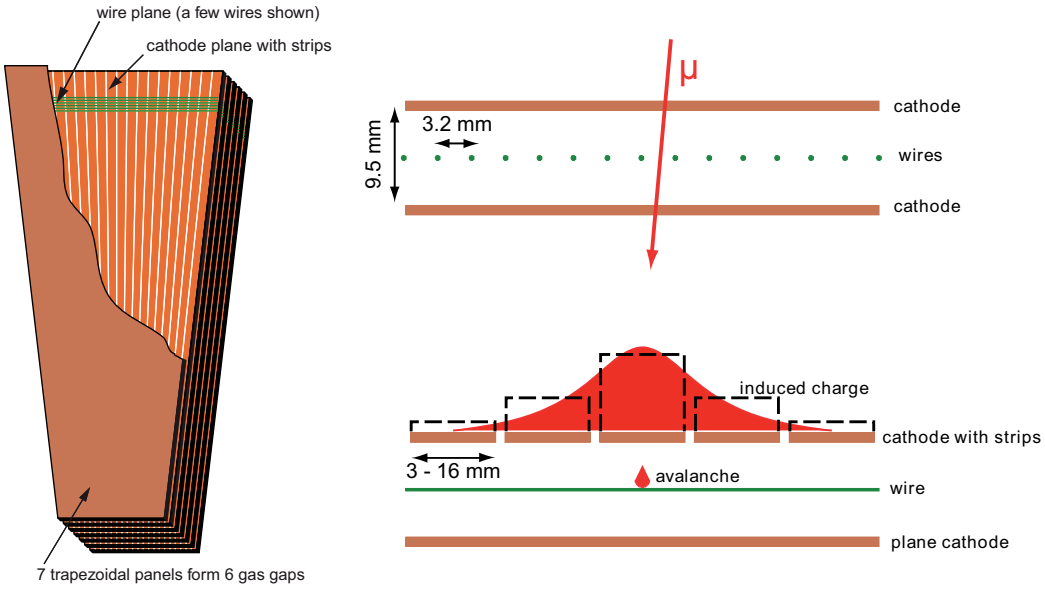

Figure 3.13: Schematics and operation principle of a CSC. On the left hand side the segmentation of the cathode and the anode wires are shown. On the right hand side, a traversing muon triggers an avalanche on the anode wire that induces charge on the cathodes. Due to this segmentation, a track can be reconstructed with high precision. Adapted from [CMS06a; CMS97a].

to the layers, so a minimal ionising particle passing the chamber volume ionises the gas and due to the high-voltage applied a gas gain in the order of $7 \cdot 10^4$ is reached.
In the inner part of the endcaps, where even higher rates and a magnetic field up to 4 T are expected, a slightly different chamber design has been chosen. The wires are thinner (30 µm) and the wire spacing is 2.5 mm. Also the voltage is lower, at about 2.9 kV. Due to the strong magnetic field, the wires of these chambers are tilted by an angle $\alpha = 29°$ to compensate the effects of the Lorentz force onto the drift electrons.
The electrons created in the gas ionisation develop an avalanche reaching the anode wires and induce a charge distribution on the cathode plane. Because of the segmentation of the cathodes it is possible to interpolate the track position from the collected charge fractions. This makes it possible to measure both coordinates with only one module.
The CSCs are positioned in the endcaps and cover the range $0.9 < |\eta| < 2.4$. The chambers reach a spatial resolution of better than 50 µm.

Resistive Plate Chambers (RPC)

The relatively slow muon system needs a fast component to assign muon tracks unambiguously to a particular bunch crossing (BX). Since a time interval of 25 ns between BX is expected, a device

with a time resolution better than this value is needed. Therefore *Resistive Plate Chambers* have been chosen. An RPC is made of two gas filled gaps with a high voltage, up to 12 kV, applied to each of them. The small gas gaps (2 mm) are positioned in between two bakelite plates that are directly attached to the high voltage electrodes. Between those gas gaps the common aluminium

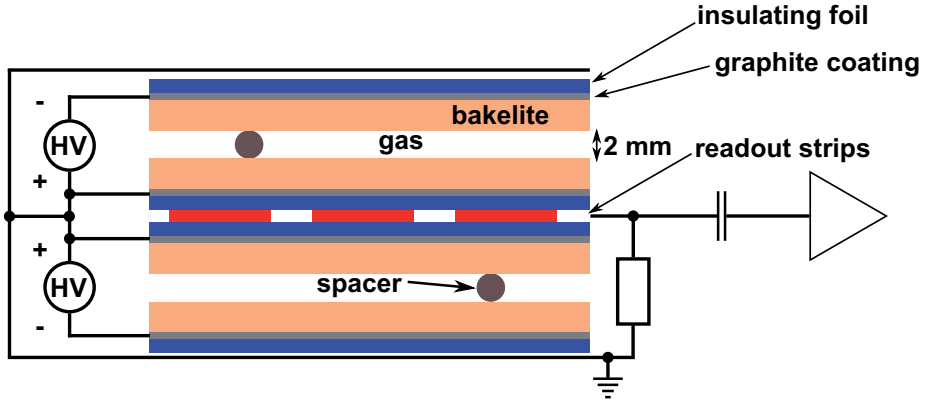

Figure 3.14: Cross-section of an RPC. Clearly visible are the two gas gaps. Adapted from [CMS06a].

readout strips are placed. An overview of the setup is shown in fig. 3.14.
The best results could be achieved with a mixture of: 96 % $C_2H_2F_4$ + 3.5 % i-C_4H_{10} + 0.3 % SF_6. An incoming particle ignites an avalanche inside the gas volume. The drift of the created charge carriers induces a "fast charge" on the pick up electrode that can be read out. The usage of double-gap RPCs allows to operate the single gaps at lower voltage with even better efficiency than single-gap RPCs.

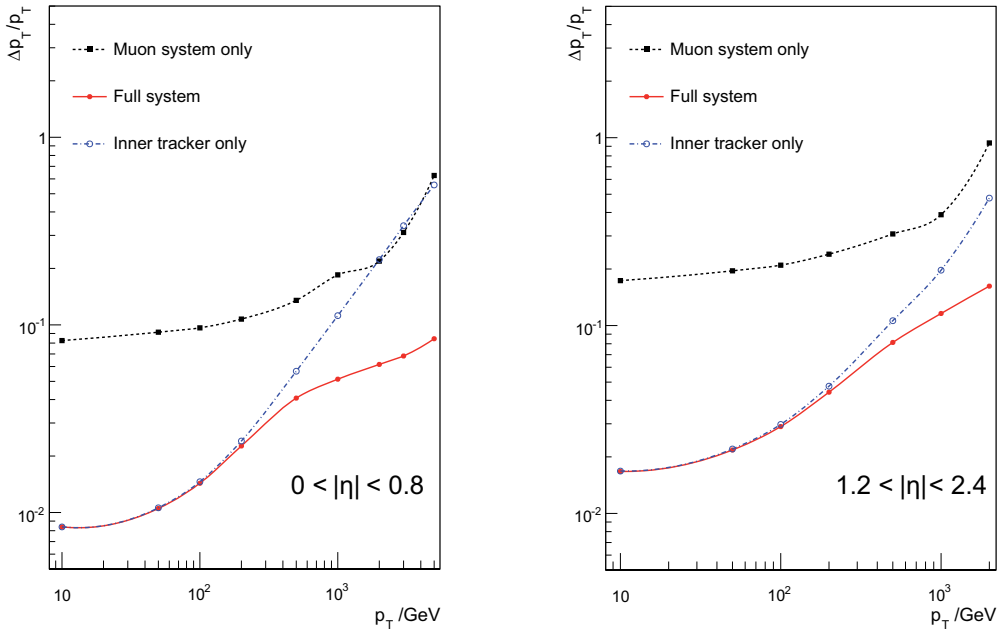

(a) (b)

Figure 3.15: Resolution of the muon transverse momentum as a function of the transverse momentum. (a) showing the region $0 < |\eta| < 0.8$, (b) showing $1.2 < |\eta| < 2.4$

RPCs reach a time resolution of better than 3 ns which is basically determined by the gap width. They are mounted in both the barrel and endcap region to trigger on muons. The alignment

is parallel to the beamline in the barrel and perpendicular in the endcap region. Depending on position they have a length of 250 mm up to 1200 mm.
The momentum resolution ($\frac{\Delta p_T}{p_T}$) of the whole muon system in the range of 10 GeV up to 1 TeV is expected to be $8-15$ % up to $20-40$ % depending on the η-region. It can be strongly improved in combination with the Tracker, as shown in fig. 3.15.

3.2.6 Trigger

As mentioned before, at design luminosity a bunch crossing rate of 40 MHz is expected with approximately 20 proton-proton collisions per BX resulting in about 10^9 events per second. Due to technical reasons, i. e. limited manageable data rates and storage capacities, this rate has to be reduced down to less than 100 Hz. The trigger systems are subdivided into basically two parts to manage this. The Level-1 Trigger (L1) is based on information provided directly by the detector readout electronics. The High-Level Trigger (HLT) consists of dedicated software using reconstruction algorithms to further reduce the rates in several steps. An overview of the L1 triggering system can also be found in fig. 3.16.

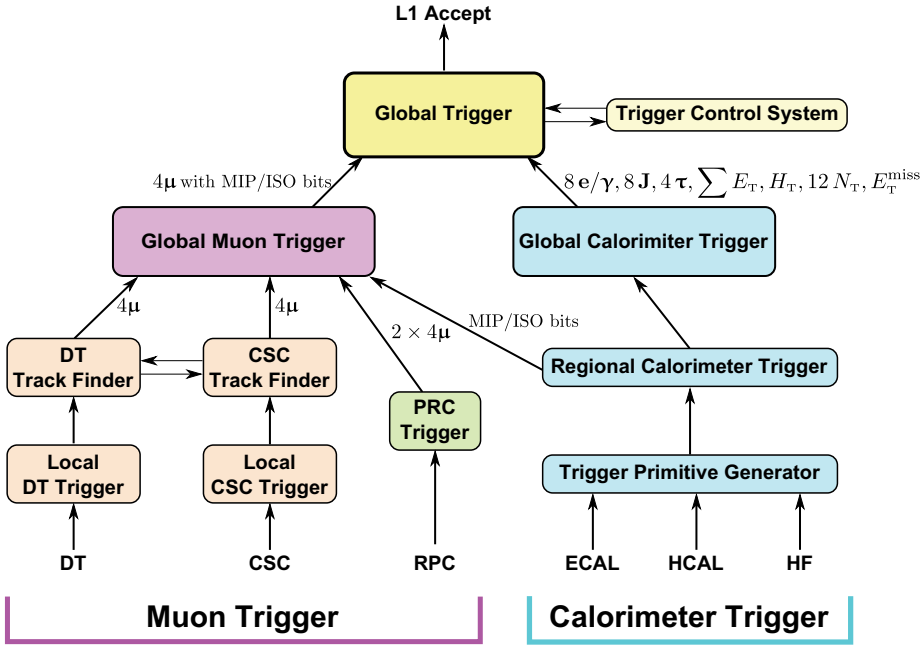

Figure 3.16: Architecture of the Level-1 Trigger. Adapted from [CMS08].

Global Muon Trigger (GMT)

In the GMT, all three muon systems (DT/CSC and RPC) take part.

- In the barrel region, the DT trigger information is generated in several steps. Entries in the drift chambers in different superlayers are assigned to the corresponding bunch crossing by the BTI[37]. Groups of BTI sets are combined to portions of a track with help of the TRACO[38]. It also improves the angular resolution and introduces a quality hierarchy. This data is passed to the *Trigger Server* which is composed of several sub-devices (TSS[39], TSM[40], TST[41]). This kind of assignment happens for each muon station of every sector and

[37] **B**unch and **T**rack **I**dentifier
[38] **Tra**ck **Co**rrelator
[39] **T**rack **S**orter **S**lave
[40] **T**rack **S**orter **M**aster
[41] **T**rack **S**orter **T**heta

is transmitted to the *Regional Muon Trigger* called DTTF[42] that connects track segments to a full track and assigns a transverse momentum to it with help of different mechanisms. The four tracks with the highest momentum are processed by the GMT. Some of these steps are also shown in fig. 3.17.

- In the endcaps the CSCs also produce trigger information. Due to the reduced magnetic bending for the measurement of p_T, spatial information of up to three stations is used to receive a similar resolution and efficiency as the DT system has. The data processing is done according to the specifications of the CSCs. The trigger information is created in a comparable way as in the DTs. Up to four muon candidates are sent to the GMT.
- In both regions the RPCs take the role of a redundant triggering system. They use the Pattern Comparator Trigger (PACT) that is based on spatial and time coincidences of hits in four RPC stations. Up to four found candidate tracks or hit patterns from barrel and also four from endcap region are sent to the GMT after some ghost-busting algorithms have been applied.
- Information from calorimeters about isolation and compatibility with minimal ionising particles is also considered in the muon trigger.

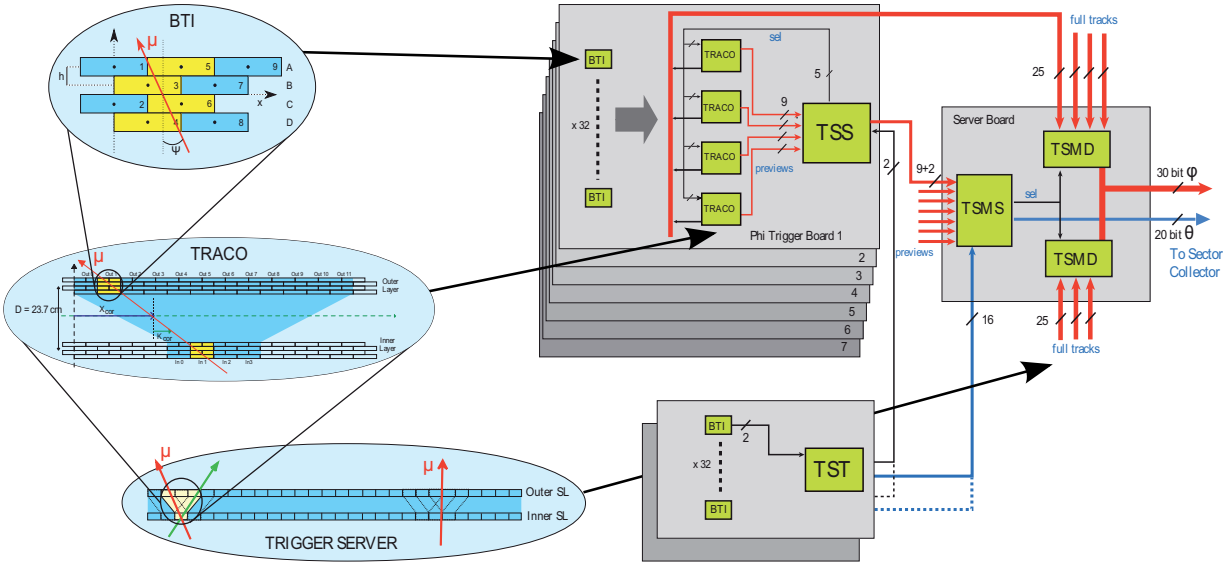

Figure 3.17: Scheme of the local trigger generation from one DT (from [CMS00b]).

Calorimeter Trigger

Calorimeter information is also considered in the L1 trigger, especially to identify 'interesting' electrons/photos, transverse energy sums, τ-vetos and also information relevant for muons.

Global Trigger

The Global Trigger combines the information from the GMT and from the calorimeters and makes a decision whether to accept or reject an event at L1. At Level-1 there is no Tracker information processed (see also fig. 3.16). This happens in the HLT for the first time.

High Level Trigger (HLT) and Data Acquisition (DAQ)

The architecture of the DAQ system of CMS is shown in fig. 3.18. The latency of the L1 trigger

[42] **D**rift **T**ube **T**rack **F**inder

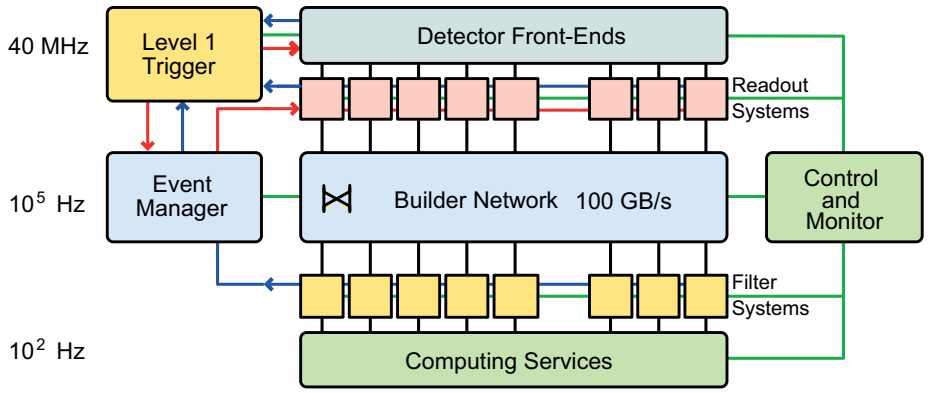

Figure 3.18: Architecture of the DAQ system of CMS. The processing units of the HLT are also indicated [CMS02].

is 3.2 µs. If there is no associated L1 trigger signal within this time interval the data from an event is discarded. Otherwise the data is passed to the *Readout Units* (in the *Readout System*) where they are buffered and interfaced to a large switched network, the *Builder Network*. The event rate at this point has already been reduced down to 100 kHz with help on the L1 trigger information. The remaining data flow of ≈ 100 GB/s is handled by the Builder Network that stands for the collection of networks that provide the connections between the Readout System and the Filter Systems. The data flow in the DAQ is controlled by the *Event Manager*. The *Filter Units* (in the *Filter System*) are the actual processing units of the HLT algorithms. Each unit contains several CPUs. With help of the HLT the event rate is reduced down to several 100 Hz before it can be stored to mass storage devices. After this the data is stored and archived for later offline data analysis.

Chapter 4

The SLHC Upgrade

New physics that could show up at LHC is expected to have very small cross-sections. If these cross-sections are even smaller than expected, detecting will require integrated luminosities far beyond the reach of LHC. This is one of the driving arguments to increase the peak luminosity up to 10^{35} cm^{-2}s^{-1} after a few years of LHC operation at design parameters.
The proposed project, called 'SuperLHC', foresees an upgrade in the acceleration and injection chain of the LHC beams. Several improvements and redevelopments are needed, like superconducting quadrupoles or studies of the radiation impact on the new components, to make the luminosity upgrade real. At present there are two proposals, one including a BX rate increase to 80 MHz (12.5 ns between BX), the other one a reduction to 20 MHz (50 ns between BX) (the design bunch crossing rate is 40 MHz). Both have advantages and disadvantages.
Due to the fact that many detector components will have taken much radiation damage potentially ending their lifetime after a few years of operation in the LHC environment, and in order to sustain the increasing particle rates, both all-purpose detectors, CMS and ATLAS, will need some upgrades. For more details see [Eva07a].

4.1 'Super'-CMS

In the scope of the upgrade of the luminosity, the CMS detector has to undergo some changes. This project is sometimes referred to as 'SuperCMS' or 'CMS2'. It seems clear that many

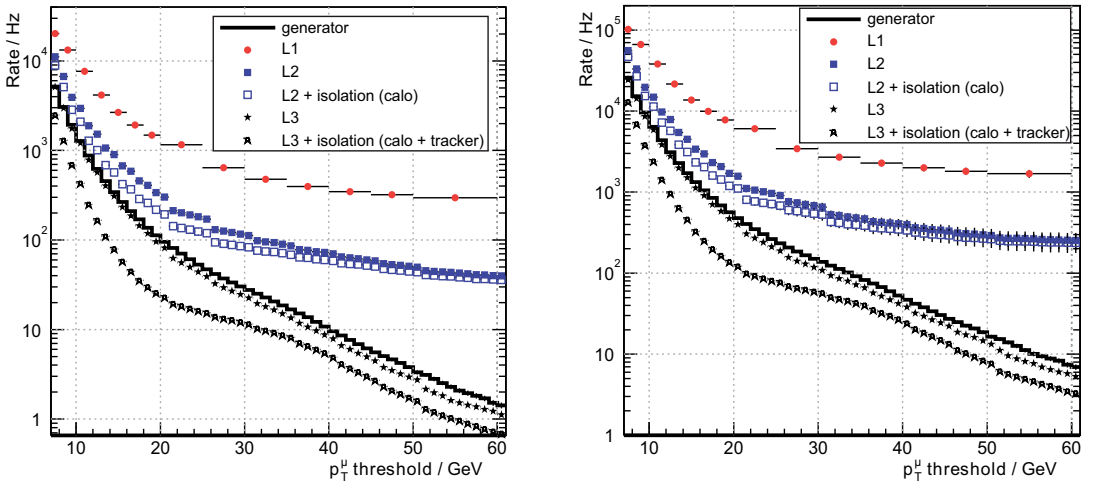

(a) Muon rates at low luminosity (10^{33} cm^{-2}s^{-1}) [CMS02].

(b) Muon rates at design luminosity (10^{34} cm^{-2}s^{-1}) [CMS02].

Figure 4.1: Single-muon trigger rates depending on the p_T-threshold for the different trigger steps. L1 stands for the Level-1 hardware/firmware trigger, L2 and L3 show (software based) high level trigger rates. See also sec. 3.2.6. (a) shows the rates for low luminosity and (b) for the LHC design luminosity.

detector components of the CMS detector will have to be replaced due to radiation damage, like e. g. the Inner Tracker that will have to be replaced completely. These upgrades will proceed in several steps, mostly independent of the accelerator upgrade, resulting in a nearly continuous research and development of components. Electronics will need upgrades due to radiation damage

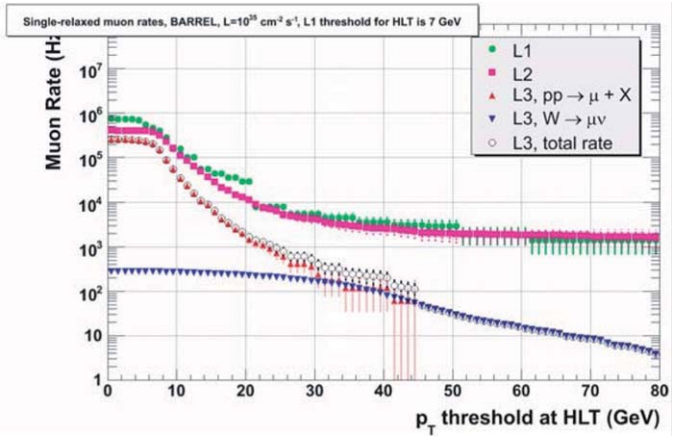

Figure 4.2: Study on muon rates at SLHC-luminosity (10^{35} cm^{-2}s^{-1}). From [MAB07] (courtesy of J. Alcaraz).

and the expected higher occupancy at the LHC. From today's point of view the calorimetric systems will need only minor upgrades. The muon systems are designed to sustain much higher rates than expected in the LHC and even the SLHC environment. Nevertheless an upgrade of the trigger system is needed to handle the higher muon rates especially to reduce the emerging data rates. Fig. 4.1 shows the muon trigger rates for the low and design luminosity at LHC and fig. 4.2 those for the SLHC luminosity.
The plans to keep the same L1 trigger bandwidth at SLHC (~ 10 kHz for single muons) as at LHC cannot be realised by increasing the p_T-threshold. One reason is, that new physics could show up in muons with momenta in the range of few tens of GeV. Another reason is, that even a higher p_T-threshold would not reduce the L1 rates significantly as can be seen in fig. 4.2.
The improvement of the transverse momentum resolution of the muon measurement would limit the number of low momentum muons mis-measured to higher momentum. One idea to do this is described in sec. 4.1.1. Further information about the CMS upgrade can be found in [CMS07].

4.1.1 Muon Track fast Tag (MTT)

Fig. 4.1 shows clearly that a luminosity increase by a factor of 10 is accompanied by a single muon trigger rate increase of one order of magnitude. In order to increase the momentum resolution, information from the Tracker needs to be processed in the L1 trigger. One approach to realise this is a new detector component (the MTT) just beyond the Calorimeters and the Solenoid. The working principle of that kind of detector is shown in fig. 4.3. A muon hitting the MTT defines a region of interest within the tracker. The 'width' of this region is given by the extensions of a bent 10 GeV-muon track. The corresponding *Tracker Layers* (TkLs) (at least two) are read out and the information is sent to the muon trigger system (fig. 4.4). The upgraded trigger is meant not to change the functionality and efficiency of the existing system.
The multiple scattering of the muons inside the calorimeters and the solenoid causes a spreading in both, the position, expressed by the position angle ϕ_p and the incoming angle, denoted as ϕ_p. The spread in dependency of the muon momentum is shown in fig. 4.5. The spread in the position angle may sum up to 14 mrad which corresponds to a position uncertainty of 50 mm just before the MB1. Thus the spatial resolution of the detector used as MTT should be of the same magnitude [Mon09]. More details on this proposal can be found in [MAB07].

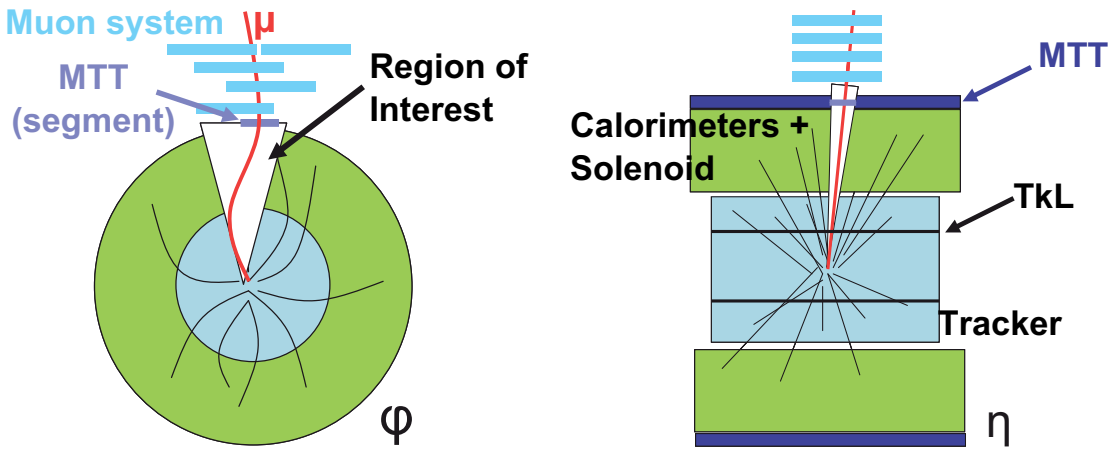

(a) Cross-section view of the CMS detector in the φ-plane. A muon passing one MTT segment is shown.

(b) Cross-section view of the CMS detector in the η-plane. The whole barrel region is covered by the MTT.

Figure 4.3: Schematic views of the CMS detector to illustrate the working principle of the MTT. Adapted from [MAB07].

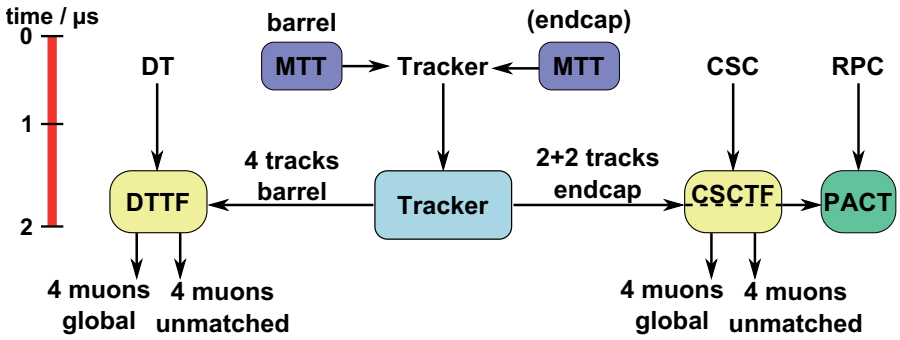

Figure 4.4: Proposed architecture of the upgraded Muon Trigger system. The time zero point is the collision. Adapted from [MAB07].

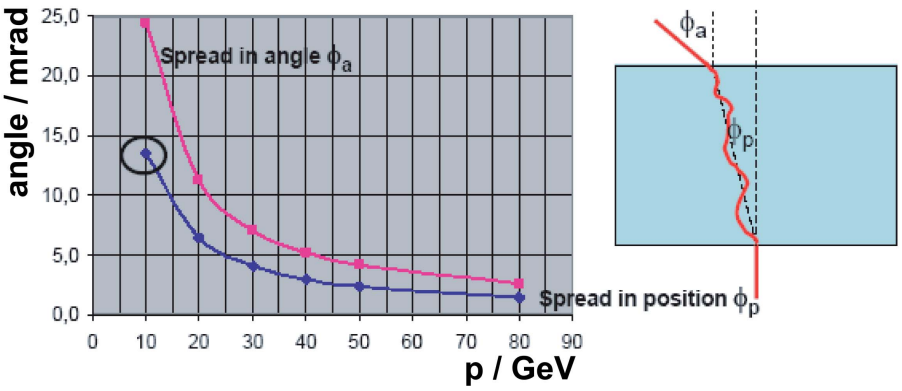

Figure 4.5: Developing of position angle and incoming angle of muons from the vertex to just beyond the Solenoid (caused by multiple scattering) [MAB07].

4.1.2 MTT in Detail

Several concepts are in discussion how to realise a device fulfilling the requirements needed for an MTT. One idea is to use upgraded double-gap RPC modules with readout strips in both directions in front of and behind MB1.

The approach pursued in the scope of this thesis lies in the study of a scintillator based MTT segment with SiPM readout fulfilling the mentioned requirements, especially the time and space resolution. Two basic setups are in focus here. One with a 'direct' SiPM readout, i. e. the SiPMs are mounted directly onto the surface of the scintillating material. In the other one a wavelength shifting fibre is embedded into the piece of scintillator to increase the photon yield at the SiPMs. Here straight fibres at different positions and also bent fibres with different bending radii are examined. In all cases the scintillator is meant to have a length and width of about $100 - 250$ mm and a height of about $5 - 10$ mm. An overview of the mentioned setups can be found in fig. 4.6. A muon traversing a piece of scintillator creates photons that propagate inside

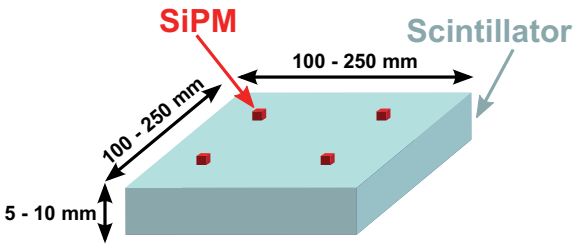

(a) "Direct readout". SiPMs mounted directly onto the surface.

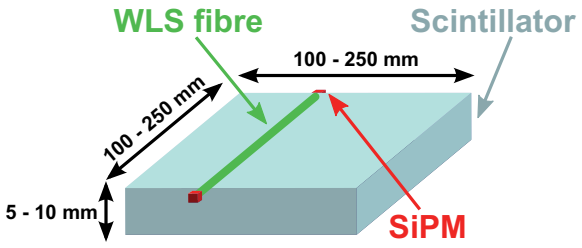

(b) Readout with straight fibre and SiPMs mounted to the fibre's ends.

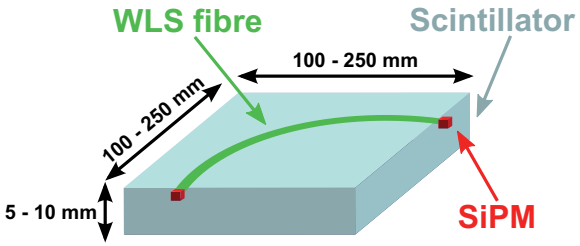

(c) Readout with bent fibre and SiPMs mounted to the fibre's ends.

Figure 4.6: Different scintillator setups with SiPM readout studied for MTT (not to scale). Fibres are embedded.

the material and can be detected by light sensitive detectors. The photons are subject to different processes inside the scintillator (see sec. 6.3.1) but are kept inside the material mainly by total internal (Fresnel) reflection at surface boundaries. One possibility to help to keep the photons inside the scintillating volume is to wrap the scintillator using a material with high reflectivity.
Important and interesting aspects of this type of detector are the photon yield at the photosensitive detector (SiPM) and/or at the WLS fibre, the timing properties, i. e. when do the photons arrive at the SiPMs related to the muon incoming point in time and other related quantities.
These values are expected to be dependent on geometric properties of the setup, like size of the scintillator or position of the fibre, as well as on material properties like surface roughness or wrapping reflectivity etc. These are the points of study in this thesis.
The space available between solenoid and the first muon station varies and can be estimated to be in the order of a few centimetres ([Mon09]) depending on the wiring of the different components. A final determination of the available space can be done in the planned detector shutdown after about two years of LHC operation.

Chapter 5

Particle Detector Basics

5.1 Passage of charged Particles through Matter

When considering a particle detector it is essential to know how a traversing particle will behave inside this detector. In many cases the interest is on the deposited energy or energy per path length inside the relevant detector material.
There are several physical processes by which particles interact with matter like inelastic scattering with atomic electrons, elastic scattering, emission of bremsstrahlung, emission of Cherenkov radiation or nuclear interactions.
The most important effects in "everyday particle detectors" are the inelastic interactions with electrons of matter, i. e. ionisation and atomic excitation. At higher particle energies bremsstrahlung becomes a non-negligible process of energy loss in matter.

5.1.1 Heavy Particles

The energy loss of most charged particles heavier than electrons and up to light nuclei (e. g. $^4_2$He) is described by the *Bethe-Bloch* formula:

$$\left.\frac{\mathrm{d}E}{\mathrm{d}x}\right|_{\text{Ion.}} = -K \cdot \frac{Z}{A} \cdot \rho \cdot \frac{1}{\beta^2} \cdot \left[\ln(\beta^2\gamma^2) + C\right], \tag{5.1}$$

with:

A = atomic mass of the material ($[A] = \mathrm{g/mol}$),
Z = atomic number,
ρ = density of the matter,
$C = \ln \dfrac{2m_\mathrm{e}c^2}{I_\text{eff}}$,
$K = \dfrac{4\pi N_\mathrm{A}\alpha^2\hbar^2}{m_\mathrm{e}} \approx 0.03 \dfrac{\mathrm{MeVm^2}}{\mathrm{kmol}}$,
m_e = mass of the electron,
$N_\mathrm{A} = 6.02 \cdot 10^{23}\ /\mathrm{mol}$ = Avogadro constant,
$I_\text{eff} \approx (10\ \mathrm{eV}) \cdot Z$ = effective ionisation energy,
$\alpha \approx \dfrac{1}{137}$ = fine-structure constant.

This equation can be derived from quantum mechanical considerations and can be used to determine the mean energy loss of a particle with high accuracy over a very wide range of particle energies [Bet30]. In this form the formula is valid for moderately relativistic particles and needs some corrections at very low and very high energies.
Nevertheless especially for particles with $0.1 \lesssim \beta\gamma \lesssim 1000$, corresponding to a muon in the energy range of 10 MeV $\lesssim E_\mu \lesssim$ 1 TeV, it describes the energy loss very well [PDG08].

5.1.2 Electrons and Positrons

The energy loss of electrons and positrons cannot be described by the Bethe-Bloch formula because in contrast to muons, they have the same mass as the collision partners, i. e. the shell electrons of the atoms of the matter they pass through. Another major difference is, that the collision partners are indistinguishable quantum mechanical objects, what also has to be considered.
The modified formula for energy loss of fast electrons and positrons with $\beta \approx 1$ results in:

$$\left.\frac{\mathrm{d}E}{\mathrm{d}x}\right|_{\text{ion.}} \approx -K \cdot \frac{Z}{A} \cdot \rho \cdot \frac{1}{2}\left[\ln(\gamma^2) + D\right], \tag{5.2}$$

with the same quantities as in (5.2) and D a term with a slight material and γ dependence [Leo87].

5.2 Fluctuations in Energy Loss

While the Bethe-Bloch formula describes the mean energy loss of a particle, it is clear that particles will suffer major fluctuations from this mean value due to the statistical nature of the interactions in matter, i. e. the losses by collisions or radiation.
For thick absorbers where the number of collisions is large, the fluctuations in energy loss will follow a Gaussian distribution and thus will read as:

$$f(x, \Delta E) \propto \exp\left(\frac{-(\Delta E - \overline{\Delta E})^2}{2\,\sigma^2}\right), \tag{5.3}$$

with:

x = thickness of absorber,
ΔE = energy loss in absorber,
$\overline{\Delta E}$ = mean energy loss,
σ = standard deviation.

When regarding non-relativistic heavy particles, the spread of this function ($\sigma_0 = \sigma(\text{non-rel.})$) can be expressed by [Leo87]:

$$\sigma_0^2 = K \cdot m_\mathrm{e} \cdot \rho \frac{Z}{A}\, x, \tag{5.4}$$

with the already known constants. For relativistic particles it becomes:

$$\sigma^2 = \frac{\left(1 - \frac{1}{2}\,\beta^2\right)}{1 - \beta^2}\,\sigma_0^2, \tag{5.5}$$

with $\beta = \frac{v}{c}$.
In many applications the materials used to detect (charged) particles, i. e. scintillation counters or gas volumes, cannot be treated as 'thick' in the sense mentioned above. In these materials the number of collisions is too small to describe the energy loss with help of the *Central Limit Theorem* in a Gaussian form. In thin absorbers, there is a non-negligible probability of a large energy transfer in one collision resulting in an asymmetric form of the distribution as shown in fig. 5.1. The expectation value and the variance of this asymmetric distribution, known as 'Landau-distribution', cannot be defined because all moments diverge. The *most probable value* is more interesting rather than the mean value. While the energy loss in collisions has always a maximum value, the mean can be calculated from the Bethe-Bloch formula, the most probable value is found to be [Leo87]:

$$\Delta E_\mathrm{mp} = \xi\left[\ln\left(\frac{\xi}{\epsilon}\right) + 0.198 - \delta\right], \tag{5.6}$$

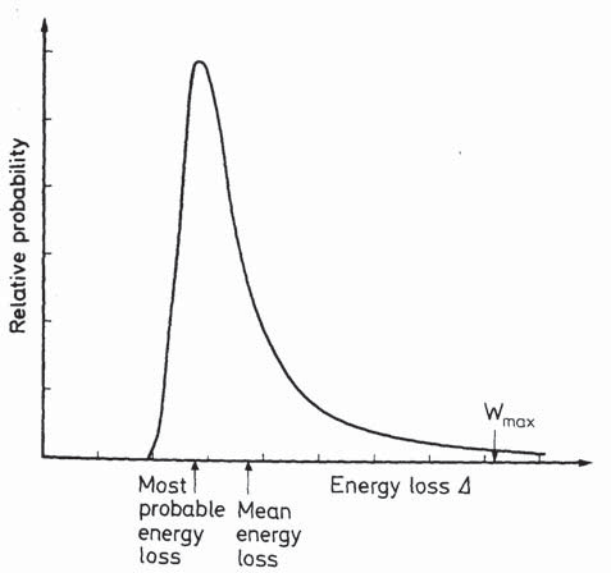

Figure 5.1: Example of a distribution of energy loss in a thin absorber [Leo87].

with:

$$\xi = \frac{1}{2}\, K \cdot \rho \, \frac{Z}{A} \, \frac{1}{\beta^2}\, x,$$

$$\ln \epsilon = \ln \left(\frac{(1-\beta^2) I^2}{2\, m\, c^2\, \beta^2} \right) + \beta^2,$$

δ = density corrections.

While the distribution developed by Landau uses some (limiting) assumptions in the calculation, there have been several attempts to improve the theory and make it fit better to experimental results [Leo87].

5.2.1 Multiple Scattering

Besides the (inelastic) interaction with electrons (in matter), charged particles traversing matter can experience one or more (elastic) Coulomb scatterings from nuclei (where each of these collisions is a Rutherford scattering).
Assuming that the number of scatterings is $\gtrsim 20$ and that the energy loss is negligible, the process can be treated statistically resulting in an approximation for the RMS of the net spatial deflection angle [PDG08]:

$$\sqrt{\langle \theta^2 \rangle} \approx \frac{20 \text{ MeV}}{p\, \beta\, c} \cdot Z \sqrt{\frac{x}{X_0}} \left(1 + 0.038 \, \ln \frac{x}{X_0} \right), \tag{5.7}$$

where X_0 is the radiation length of the material.

5.2.2 Radiative Energy Loss

A charged particle traversing matter can be deflected in the electric field of the nuclei of the atoms. This kind of radial acceleration leads to the emission of *bremsstrahlung*. For a traversing particle with mass m the contribution to the energy loss can be written as:

$$\left. \frac{\mathrm{d}E}{\mathrm{d}x} \right|_{\text{rad.}} \approx -\, 4 \cdot N_\mathrm{A} \cdot \frac{Z^2}{A} \, \frac{\alpha^2 \cdot \hbar^2}{m^2} \, \rho \cdot E \, \ln \left(\frac{183}{Z^{1/3}} \right) \tag{5.8}$$

$$= -\, \frac{K \cdot m_\mathrm{e}}{\pi} \, \frac{1}{m^2} \, \frac{Z^2}{A} \cdot \rho \cdot E \, \ln \left(\frac{183}{Z^{1/3}} \right), \tag{5.9}$$

and again the same notation as above applies [GS08].
This kind of energy loss strongly depends on the mass of the traversing particle. Most affected by radiation losses are the lightest particles, electrons and positrons, and at energies above several hundred GeV, muons.
In order to determine whether radiation losses must be taken into account, one can regard the critical energy. It is defined as the energy of the traversing particle, where bremsstrahlung losses become as strong as energy losses by ionisation and excitation. This energy depends on the material (i. e. gas, solid or liquid) and can be averaged to [Kle05]:

$$E_{\mathrm{c}}^{\mathrm{e}} \approx \frac{580\ \mathrm{MeV}}{Z}. \tag{5.10}$$

Above the critical energy the radiation losses dominate the energy loss of the traversing particle. Due to the strong mass dependence in most applications the bremsstrahlung losses must only be considered for electrons (and positrons) because for the next heavier particle, the muon, the critical energy is $\left(\frac{m_\mu}{m_e}\right)^2 \approx 40000$ times higher [Leo87].

5.3 Scintillators

One of the oldest devices to detect charged particles are scintillators. In these materials the atomic/molecular states are excited by the energy deposited by the traversing charged particle. This energy is freed e. g. in form of (optical) photons while the molecules de-excite to their ground states. In former times these photons where detected by the human eye but in the 1940s the development of (high voltage) photo multiplier tubes (PMT) began that allowed an automatisation of the readout process of the scintillators.
There are several different substances that have scintillating abilities, i. e. inorganic crystals, gases and liquids and also organic materials, all of them following a different scintillation principle.

5.3.1 Organic scintillators

Organic scintillators are built of aromatic compounds which are characterised by their carbon ring structure. One property of this kind of chemicals is the short decay time of excited electronic states which is an ideal property for a scintillator. Due to the hybridisation of the s and two p

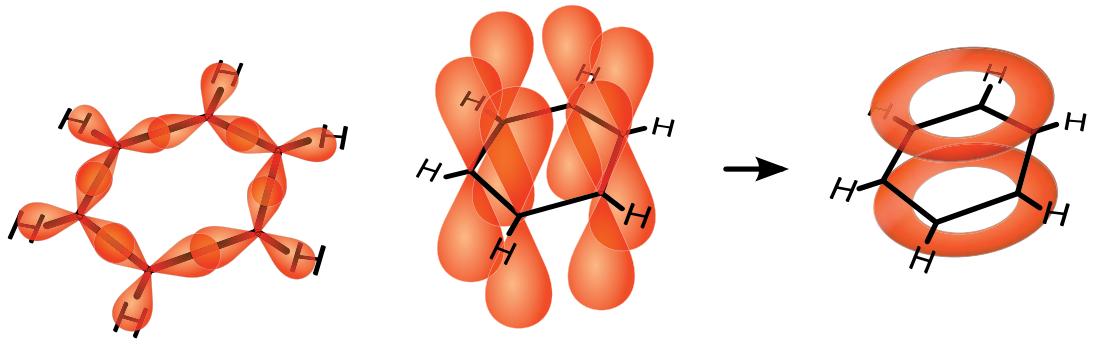

(a) (b)

Figure 5.2: Structure of σ-bonds (sp^2 hybridized orbitals) in the benzene molecule (a); left side of (b): the six (atomic) p_z-orbitals, right side: model of delocalized (molecular) π-orbital system [Wik09a].

orbitals the angles between the three resulting bondings of carbon compounds become 120° and lie in one plane. Thus it is possible for the C-C bondings to arrange in a hexagonal structure as

shown in fig. 5.2. In this molecule called benzene, the remaining non-hybridized p orbitals overlap to form a molecular orbital containing delocalized electrons which contribute to the bonding of the molecule. There are also molecules with more than one ring, sharing many properties with benzene, exemplarily shown in fig. 5.3. Within these orbitals the electrons fulfil boundary

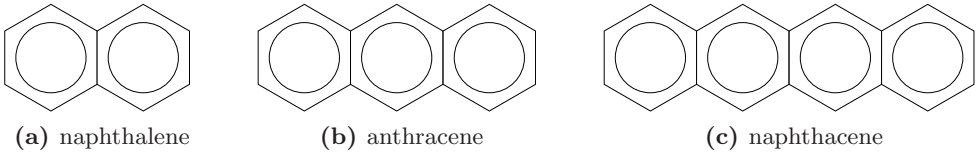

(a) naphthalene **(b)** anthracene **(c)** naphthacene

Figure 5.3: Representations of some aromatic molecules used as scintillators. The circles inside the hexagonal structure stand for the delocalized (π) electrons of the molecular orbitals.

conditions allowing the solution of the corresponding Schrödinger equation in form of standing waves with quadratically spaced energy levels. The orbitals described by these wave functions are called π-orbitals. Electrons in the π-orbitals can be excited by a traversing charged particle. The de-excitation of higher states of these π-electrons to the ground state are responsible for the luminescence of this kind of materials. The energy difference between the different states is typically of the order of a few eV which explains the production of visible light within the scintillator. A typical energy level diagram for the different molecular states is shown in fig. 5.4. The figure shows the singlet and triplet states of a molecule and the small substructure for every

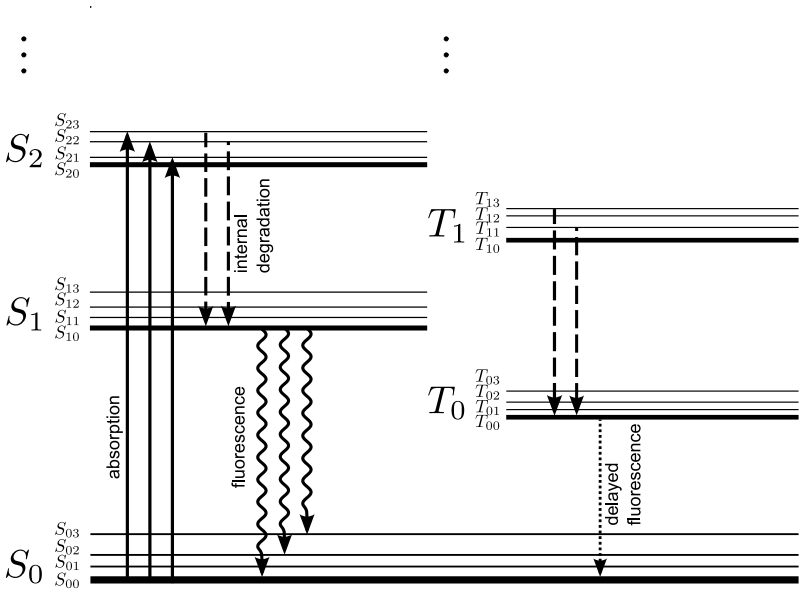

Figure 5.4: Typical energy levels of an organic (scintillator) molecule. The singlet states are denoted with S_{nk}, the triplet states with T_{nk}. For clarity the singlet and triplet states are separated spatially. Adapted from [Leo87] and [Bir64].

electron level caused by the excited vibrational modes of the molecule. The energy spacing of the fine structure is in the order of a few tenths of eV. A traversing particle excites the electrons and the vibrational levels as suggested by the figure. The decay of the excited singlet states S_{2k}, S_{3k} etc. to S_1 takes place within picoseconds and proceeds without the emission of radiation which is known as "internal degradation". From here the state decays with a high probability within a few nanoseconds to one of the S_{0k} states, emitting radiation with a wavelength corresponding to the energy difference of the states. These are in general excited vibrational states which is the reason for the scintillator being (partially) transparent to its own light.

While the triplet states cannot decay to S_{0k} due to multipole selection rules, they can decay by interaction with other excited T states in the manner of:

$$T_1 + T_1 \rightarrow S_1 + S_0 + \text{phonons}$$

The S_1 state decays in the same way as described above, though some time later. This causes some scintillators to have a *delayed* component in the radiation emission spectrum. However, this delayed component of the scintillation light is negligible in many materials.
Typical densities of scintillators used in high energy physics are in the range of 1.03 to 1.20 g/cm^3 and photon yields of $\mathcal{O}(1)$ per 100 eV energy deposit can be achieved.
In plastic scintillators, which are solely used in the scope of this thesis, there is a non-linearity in the light output of the scintillator that was first described by Birks' semi-empirical formula [Bir64]:

$$\frac{\mathrm{d}L}{\mathrm{d}x} = L_0 \frac{\frac{\mathrm{d}E}{\mathrm{d}x}}{1 + k_\mathrm{B} \frac{\mathrm{d}E}{\mathrm{d}x}} \tag{5.11}$$

Here $\frac{\mathrm{d}L}{\mathrm{d}x}$ is the light output of the scintillating material per distance, $\frac{\mathrm{d}E}{\mathrm{d}x}$ the energy loss per distance of the traversing particle, k_B is Birks' constant that has to be measured for every material and L_0 the luminescence at low specific ionisation density.
A summary of different measurements for specific luminescence vs. specific energy loss is given in fig. 5.5. For a minimum ionising particle, where $\frac{\mathrm{d}E}{\mathrm{d}x} \leq \mathcal{O}(2\ \mathrm{MeVcm^2/g} \cdot Z)$ the linear approxi-

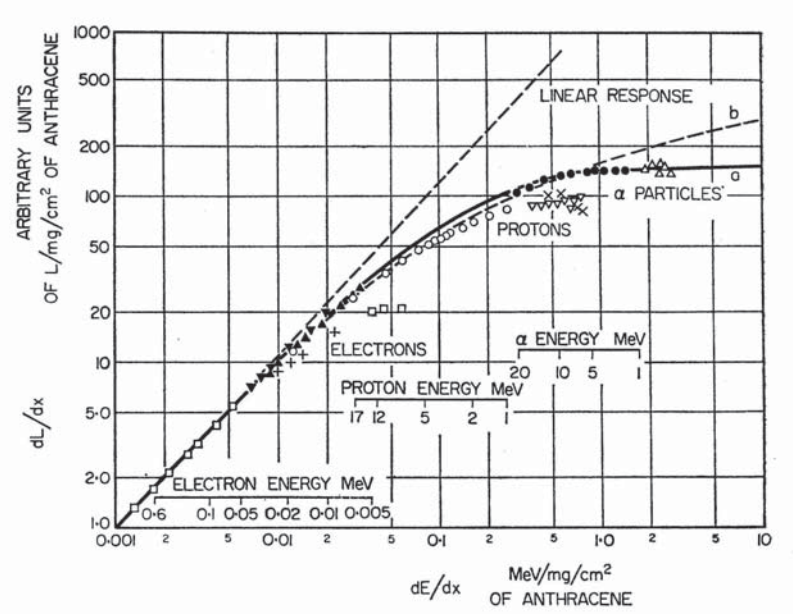

Figure 5.5: Variation of specific fluorescence with specific energy loss for anthracene crystals. (a) shows the theoretical curve described by (5.11), (b) shows a more complex approach [Bir64].

mation is correct within a few percent, i. e. $k_\mathrm{B} \approx 0$.
In order to decrease the decay time, there are fluorine compounds with a concentration of about 1 % mixed to the scintillating base material. The initial decay time that can be of the order 15 ns or more can be reduced to a few nanoseconds by a (radiationless) dipole-dipole interaction called Förster-process.
A very common way to increase the attenuation length within the scintillator, i. e. to decrease self-absorption is to solve a second fluorine compound in a small concentration (0.05 %) that absorbs the short wavelength photons and emits them at higher wavelengths [PDG08]. A summary of this concept with the corresponding attenuation lengths is given in fig. 5.6.

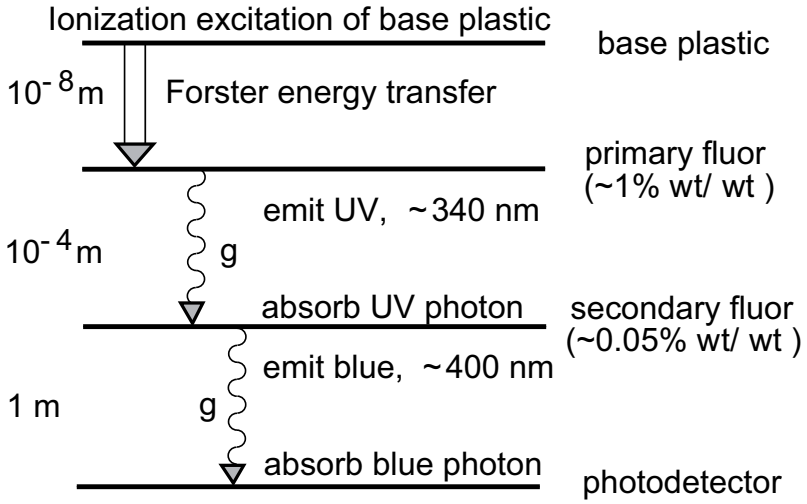

Figure 5.6: Schematical picture of the working mechanism of a plastic scintillator. The energy transfer distances and approximate fluorine concentrations (in weight percentage) are shown [PDG08].

5.4 Wavelength Shifting (WLS)

A common way to 'extract' photons from a piece of scintillator is to use wavelength shifting fibres that are connected to the scintillator. WLS materials absorb photons of a given wavelength spectrum and emit new photons with higher wavelengths, i. e. lower energies. These are typically organic materials that must be preferably sensitive to the given scintillation light.
Typical values of the attenuation length in the photon absorption range of the spectrum of a wavelength shifter are of the order of millimetres [Kle05].

5.5 Photomultiplier

A common device to detect light created by particles traversing matter is the photomultiplier tube (PMT). A schematic view of a PMT is shown in fig. 5.7. It consists of a photosensitive cathode that has a typical probability of $20 - 40\,\%$ to emit an electron when hit by a photon (photoelectric effect). Due to the applied high voltage, this electron is accelerated to the first

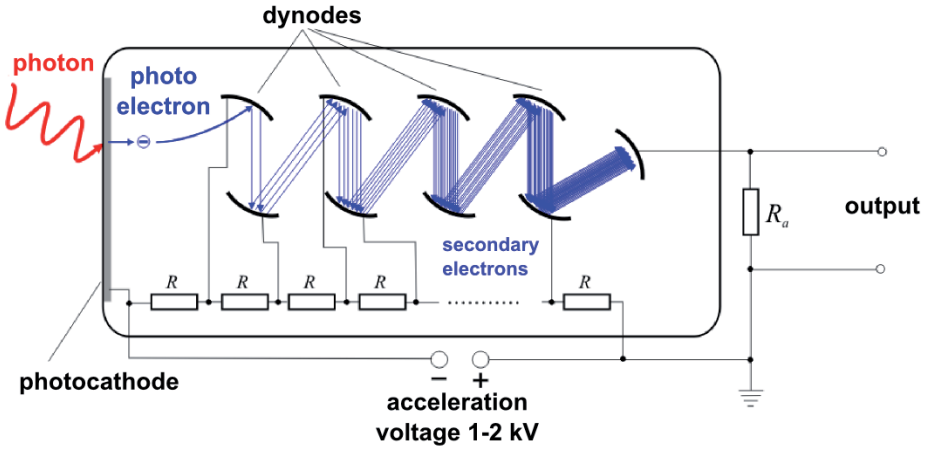

Figure 5.7: Schematical view of a PMT [Wik09b].

electrode. These electrodes are called *dynodes*. When an electron hits a dynode a number of new (secondary) electrons (typically of the order of 5) are emitted from this dynode. The dynode array builds a "potential ladder" with help of voltage dividers. Thus the electrons are accelerated from dynode to dynode by which they get 'multiplied'.

The electrons are collected at the last dynode (the anode) creating an electrical signal that can be amplified electrically and measured. Assuming a linear cathode - dynode - anode system, the resulting signal is proportional to the number of simultaneously incoming photons.
A big advantage of the PMT is its ability to detect even single photons with moderate efficiency. One major disadvantage is that a high magnetic field can prevent the photo electron from reaching the first dynode and thus spoil any measurement. Another disadvantage is the high voltage of typically several kV that has to be applied to the PMT to reach proper working conditions. Additionally, only a small fraction of the volume/surface of a PMT is sensitive to photons and the bigger part of the device is needed for amplification. This has to be considered because typical PMTs have lengths of some cm and diameters of mm up to few cm.

5.6 Solid State Detectors

The development of fast semi-conducting light detectors in the past years peaks in the production of so called “silicon photo multipliers” (SiPMs). To elucidate the working principle of this kind of devices, first of all diodes of semi-conducting materials are explained in more detail.

5.6.1 Semiconductors

A semiconductor is an element with the property of an increasing conductivity with the increase of temperature. This behaviour can be explained with help of the band structure of these elements. The energy gap between the valence band and the conduction band is typically in the order of 1 eV or less while the band gap of insulators is much bigger.

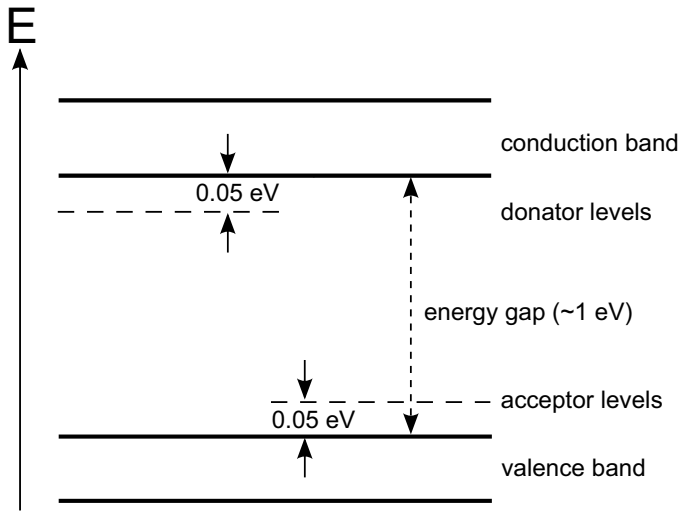

Figure 5.8: Schematical energy band structure of semiconductors. To represent the two possibilities in one image, both the donator and the acceptor levels are shown.

To improve the electrical properties of semiconductors the method of doping has been developed: Semiconductors can be found mostly in the 4th main group. Doping of a semiconductor means (controlled) introduction of a small amount of impurities into the crystal lattice of the (more or less) pure material. Most common types of doping are for example the introduction of a 3rd/5th group element into the lattice of a 4th group element. These dopants have the ability to accept/donate electrons from/to the surrounding lattice.
This results in a p-type in the first case and an n-type semiconductor in the second case.

Here one finds additional acceptor or donator levels within the energy band structure as illustrated in fig. 5.8.

5.6.2 The p-n Junction

When p-doped and n-doped materials are brought into mechanical contact, the electrons of the n-region diffuse into the p-region where they can be bound by acceptor ions, leaving positively charged donator ions in the n-region.
The regions close to the p-n interface become charged and because of this charge separation, a potential difference, called the built-in potential, appears and an electric field is created. See fig. 5.9.

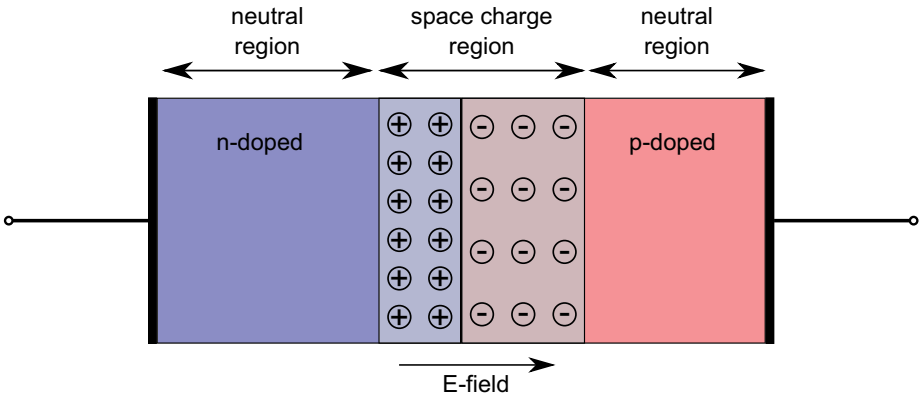

Figure 5.9: p-n junction in (thermal) equilibrium with no bias voltage applied. Red and blue regions are n- and p-doped regions respectively. The grey zone denotes the recombination region where a charged space region appears.

5.6.3 The pn-Photodiode

A p-n junction can be used as a photo detector. When a photon hits the diode material there is a probability that an electron-hole pair is produced within the material. The electron receives the energy of the incoming photon and is raised into the conduction band. The pair can only be created when the photon energy is bigger than the band gap:

$$E_{\text{phot}} = \hbar\,\omega_{\text{phot}} > E_{\text{g}}.$$

Figure 5.10 shows the two types of semi-conductors (direct and indirect) where optical charge carrier generation can take place. Photons that hit the space charge region can cause an inner photoelectric effect as described above. The electrical field attracts the “newly created” charge carriers and an electric (photo) current flows through the diode.
The efficiency of such a ‘simple’ photodiode is not very high because the penetration depth of photons depends on their wavelength and they cannot travel arbitrarily long distances within the diode material. It is possible that electron-hole pairs are not only produced in the space charge zone but also outside of it. These charge carriers first have to diffuse to the charged region where they are accelerated by the electrical field and contribute to the photocurrent. This part of the photocurrent is the diffusion photo current (I_{phot}).
One possibility to increase the photo sensitivity is to adapt the construction form of the diode as shown exemplarily in fig. 5.11. The diode is designed to have a transparent casing so the incoming light is less absorbed before reaching the pn-layer. The doped regions are arranged to allow a maximal size of the depletion zone when a reverse voltage is applied. Appling a reverse

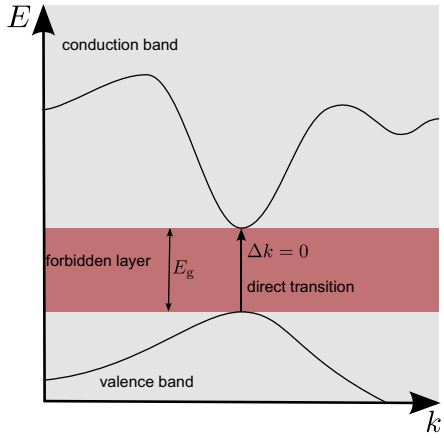

(a) Transition of an electron inside a direct semi-conductor. In this kind of transition the crystal momentum does not change.

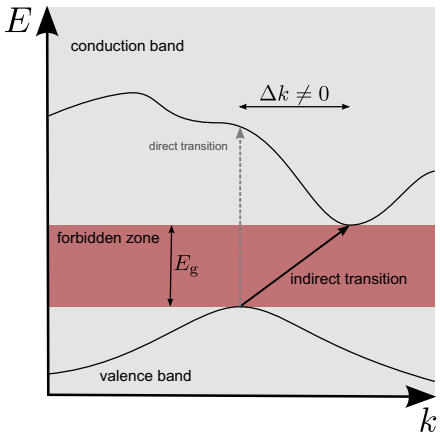

(b) Transition of an electron inside an indirect semi-conductor. The transition from the highest energy in the valence band to the lowest energy in the conduction band requires a change of the momentum which is mostly provided by a phonon.

Figure 5.10: Schematics of the band structure of direct and indirect semi-conductors. Adapted from [Wik09a].

voltage to the photodiode increases the space charge region and with it the sensitivity. The width d of the space charge region (of a normal diode) can be calculated to [Lut07]:

$$d(U) = \sqrt{\frac{2\,\epsilon_\mathrm{r}\,\epsilon_0}{e} \cdot \left(\frac{1}{n_\mathrm{A}} + \frac{1}{n_\mathrm{D}}\right) \cdot (U_\mathrm{bi} - U)}\,, \tag{5.12}$$

with:

n_D = doping concentration of donators,
n_A = doping concentration of acceptors,
U_bi = built-in potential.

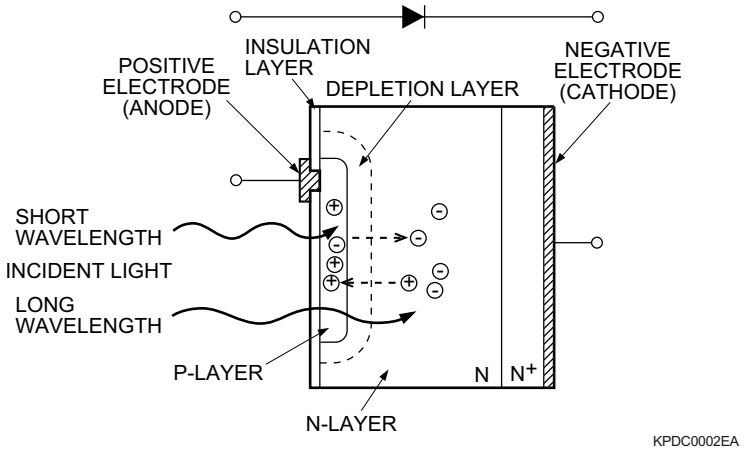

Figure 5.11: Example of the design of a common photodiode [Ham08b].

Due to the charge separation, the pn-junction also has a capacitance which is dependent on the voltage applied. It can be calculated to [Göb06]:

$$C_{pn}(U) = \frac{A\,\epsilon_\mathrm{r}\,\epsilon_0}{d(U)} \tag{5.13}$$

$$= \frac{C_{pn,0}}{\sqrt{1-\frac{U}{U_\mathrm{bi}}}}, \tag{5.14}$$

where $C_{pn,0} = C_{pn}(0)$ and A is the cross section area of the junction, respectively.
Additionally the frequency response and linearity of the diode can be improved. The application of a reverse voltage does not affect the signal current but one disadvantage is the increase of dark current and the possibility of damaging the device when a too high voltage is applied [Ham08b].
The most simple circuit to read out a photodiode is given in fig. 5.12a. The current inside the diode created by the incoming photons is modelled by a current source connected in parallel. A possible readout circuit of a diode with applied reverse voltage is given in fig. 5.12b. The photo

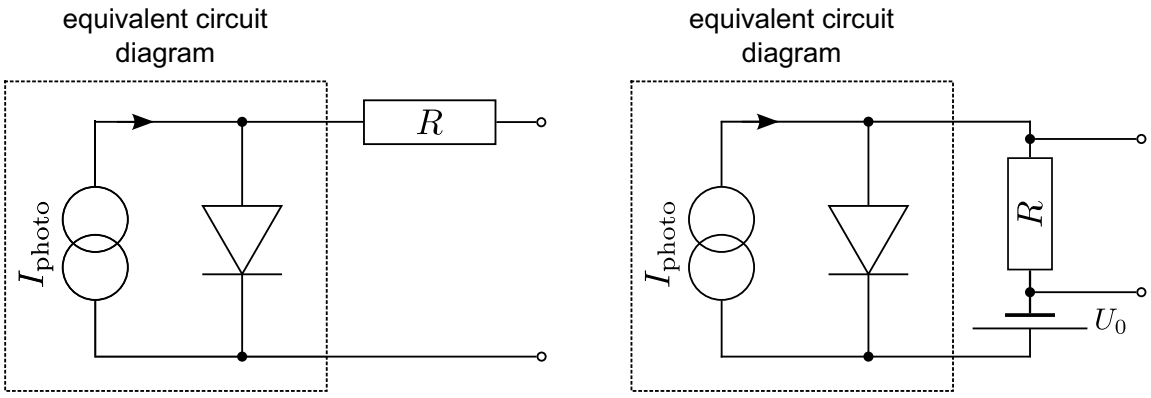

(a) Photodiode with no voltage applied. **(b)** Photodiode with reverse voltage applied.

Figure 5.12: Basic circuit diagrams of a diode used as a photo detector. The photodiode is represented by the given equivalent circuit diagram in the dashed box. One or more incident photons create a current pulse that is modelled by a current source here.

current (and with it the short circuit current I_sc as shown in fig. 5.13) rises linearly with the intensity of illumination over a wide range (typically several orders of magnitude). The diode characteristic curve of an illuminated diode can be written as [HBG01]:

$$I_\mathrm{D}(U_\mathrm{D}) = I_0 \cdot \left[\mathrm{e}^{\frac{U_\mathrm{D}}{U_\mathrm{T}}} - 1\right] - I_\mathrm{photo}, \tag{5.15}$$

with U_D = voltage at the diode (see also fig. 5.13), and [Sil97]: $I_\mathrm{photo} = I_{\text{photo drift}} + I_{\text{photo diff}}$.
Curves of a diode with different light input intensities are schematically shown in fig. 5.13.

5.6.4 pin-Photodiode

To increase the size of the depletion zone and to increase the frequency response an additional, lowly doped (intrinsic) layer is brought between the p- and the n-layer. Fig. 5.14a shows the basic setup and the electrical field inside the pin-diode [TS02; HBG01].
In this kind of diode the probability for a photon to create an electron-hole pair within the depletion zone is much higher. Also electron-hole pairs created outside this region can reach it very fast. Another advantage of pin-diodes is the reduced junction capacitance improving some timing properties of the diode [HBG01].

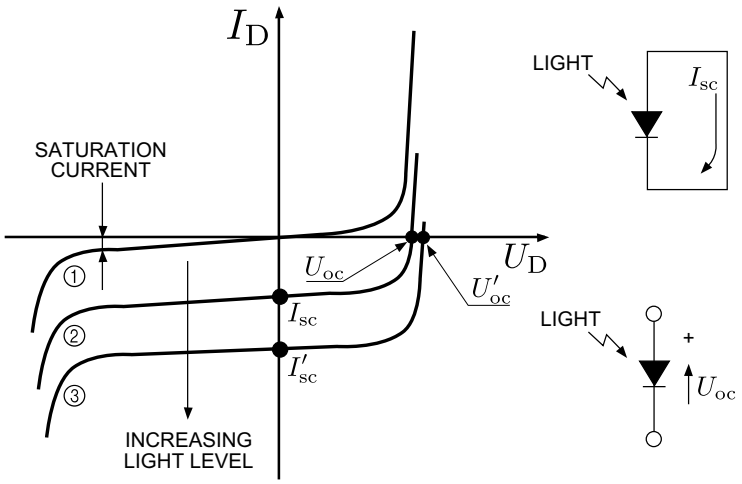

Figure 5.13: Characteristic curves of a photodiode with no light ①, little light input ②, even more light input ③. The two special cases where the diode is short-circuited and in open circuit, respectively, are also shown in the drawing [Ham08b].

5.6.5 Avalanche Photodiode (APD)

When going to lower intensities ($\lesssim 100\,\gamma$) and/or higher frequencies (several 10 GHz), the properties of the pin-diode does not suffice the requirements and a special type of diode (the avalanche photodiode) is needed [Sil97]. The APD has either a structure comparable to that of a pin-diode and is operated close to the breakdown voltage or has a special avalanche structure as is shown in fig. 5.14. When a photon creates charge carriers (absorption layer), they diffuse in direction

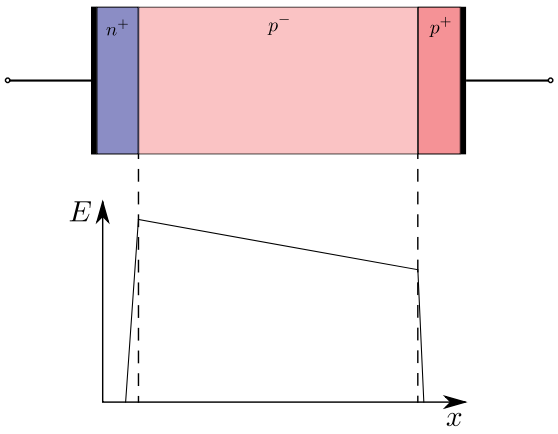

(a) Structure and electrical field of a pin-diode. The heavily doped regions are denoted with a plus (n^+ / p^+), the lightly doped region is denoted with a minus (p^-). An APD can also have a pin-like structure.

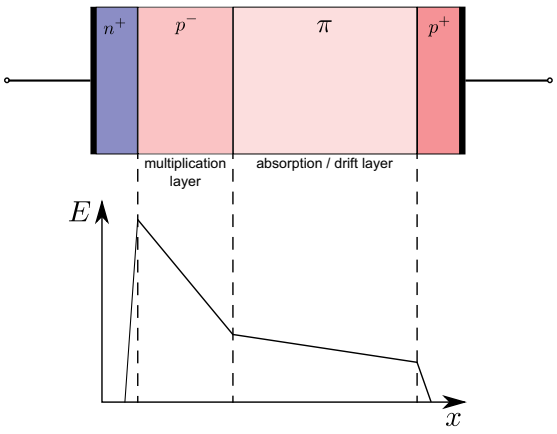

(b) Structure and electrical field of an APD. The region denoted with a π means a nearly completely intrinsic p-material. (The p^- layer is in practice much smaller than the π layer.)

Figure 5.14: Sketch of a pin (a) and an avalanche (b) photodiode. The depletion region expands over almost the whole intrinsic/lightly doped region.

of the multiplication layer where they are heavily accelerated by the electrical field. When the charge carrier, e. g. an electron, gains an energy $E_e > E_g$ there is a probability that this electron can produce more charge carriers by collision ionisation within the multiplication layer. Collision ionisation can be seen as the inverse process of the Auger effect. Those newly produced charge carriers are also accelerated by the field and can also produce new electron-hole pairs on their part. Depending on the width of the multiplication layer, this process can repeat several times

creating an avalanche of charge carriers [HBG01].
The amplification of the initial current I_{phot} can be written as [HBG01]:

$$I = I_{\text{phot}}\, M,$$

where M is the multiplication factor which is dependent on the applied diode voltage and can be approximated above some tens of volts by:

$$M = \frac{1}{1 - \left(\frac{U_{\text{R}} - I\, R_{\text{S}}}{U_{\text{br}}}\right)^{m}}. \tag{5.16}$$

Here U_{R} is the applied reverse voltage and U_{br} stands for the breakdown voltage of the diode. $I\, R_{\text{S}}$ is the voltage drop over the series resistor of the diode and m a parameter that has to be determined empirically and is in the order of 1 to 10 [HBG01].
One major disadvantage of this type of device is the high noise rate that is highly dependent on the applied voltage and on the ambient temperature [Sil97].

5.6.6 Geiger Mode APD / SiPM

While the nomenclature for Geiger mode APDs / SiPMs is not unambiguous in the literature, and while many different terms can be found to describe the same type of device ('MPPC[43]', 'SPM/SiPM[44]', 'PPD'[45] etc.), the function principle is always the same:
Because pin-diodes have no internal gain and they have a quite large noise, they are not suitable to detect light flashes of less than several hundred photons. The internal gain of the APDs admittedly improves the signal to noise ratio, but still there are more than some 20 photons needed to create a detectable pulse. To improve the photon detection efficiency even more,

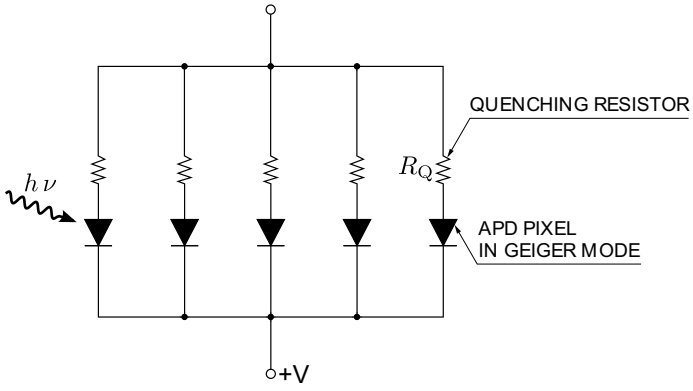

Figure 5.15: Schematics of one SiPM built of APDs (adapted from [Ham08a]).

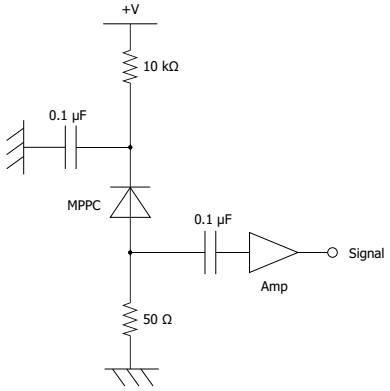

Figure 5.16: Very basic readout circuit for an SiPM [Ham09].

a special type of APDs has been developed that works in Geiger mode. Geiger mode means the operation of the APD slightly above the breakdown voltage causing the internal electrical field to become very large making a very high internal gain in the order of 10^6 possible. This kind of device has the possibility to detect single photons as a traditional PMT can do. When operated in Geiger mode the output pulse of the detector is *not* proportional to the number of incoming photons any more but has in contrast (theoretically) always the same height and shape. So the price for the high detection efficiency is the absence of a dynamic range of the device.
The electrical current caused by the avalanche in the diode has to be quenched by a dedicated resistor to prevent damage of the device and also to improve the frequency response of the diode.

[43] **M**ulti-**P**ixel **P**hoton **C**ounter
[44] **S**ilicon **P**hoto**M**ultiplier
[45] **P**ixelated **P**hoton **D**etectors

The solution to the problem of the dynamical range is to divide the diode into many sub-devices (called pixels) that are connected in parallel and which are each equipped with a quenching resistor, as is schematically shown in fig. 5.15. The final pulse is a sum of the pulses of the single pixels where each pixel was triggered by one or more incoming photons (and/or noise) [Ren06]. From now on devices subdivided into pixels are referred to as 'SiPMs' where each pixel is an APD in Geiger-mode. A simple readout circuit for an SiPM with reverse voltage applied is shown in fig. 5.16.
One of the characteristic quantities of an SiPM is the (intrinsic) gain G that can be calculated to [Sen07]:

$$G = \frac{C_{pn}\,(U - U_{\mathrm{br}})}{\mathrm{e}}.$$

The gain is temperature dependent (decreases with higher T) as most properties of a diode are. Another essential quantity of an SiPM is the photon detection efficiency (PDE or $\varepsilon_{\mathrm{PD}}$) that can be written as:

$$\varepsilon_{\mathrm{PD}} = \varepsilon_{\mathrm{quant}} \cdot \varepsilon_{\mathrm{geom}} \cdot P_{\mathrm{ava}}. \tag{5.17}$$

$\varepsilon_{\mathrm{quant}}$ is the quantum efficiency of the pn-junction, i. e. the probability that an incoming photon creates an electron-hole pair. The value for this quantity given by the manufacturer of the SiPMs used in the scope of this thesis (Hamamatsu) is $\varepsilon_{\mathrm{quant}} \gtrsim 70\,\%$ [Ham08a]. The geometrical fill factor $\varepsilon_{\mathrm{geom}}$ is the ratio of the effective and total pixel areas. Each pixel needs a quenching resistor and wiring that take some space[46], so the more pixels an SiPM has (for a constant SiPM area!), the smaller the fill factor becomes but the dynamical range increases. This is also shown in fig. 5.17a and 5.17b. Typical values of $\varepsilon_{\mathrm{geom}}$ for a 100 pixel device are found to be:

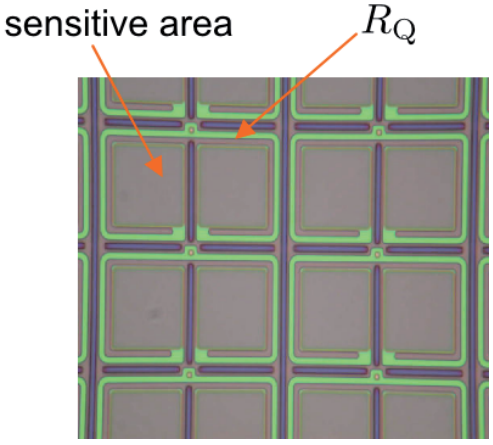

(a) Photograph of a typical silicon photomultiplier. The different components of the pixel (quenching resistor, wiring etc.) are clearly visible [Sen07].

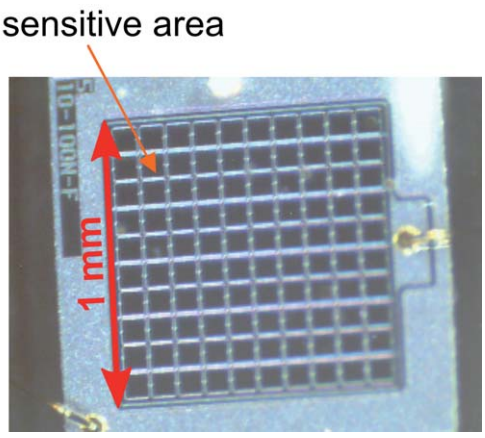

(b) Microscopic view of a Hamamatsu SiPM (`S10362-11-100C`) [Mer09].

Figure 5.17: Examples of the sensitive area of SiPMs.

$\varepsilon_{\mathrm{geom}} = 78.5\,\%$ ([Ham08a]). P_{ava} denotes the probability of an electron-hole pair to trigger an avalanche inside the SiPM. It is not unproblematic to measure this quantity since it is strongly dependent on the overvoltage applied. A determination of P_{ava} is described in [OMO08] and the results are shown in fig. 5.18. P_{ava} reaches values between 0.9 and 1.0 for a operation voltage of $\gtrsim 79$ V (for this particular device). The wavelength dependent $\varepsilon_{\mathrm{PD}}$ of a typical SiPM is shown in fig. 5.19. The number of pixels that were hit by a photon and fired (N_{fired}) can be characterised

[46] There are also approaches to use backilluminated SiPMs allowing a fill factor of basically 100 %. For more information, see [NHH07]

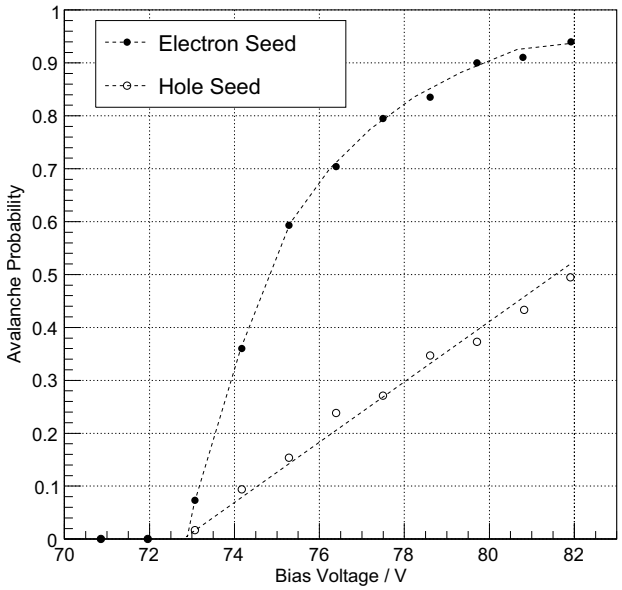

Figure 5.18: Simulation of the voltage dependence of the avalanche probability of electrons and holes in an SiPM. The breakdown voltage of the analysed device (`S10362-11-25`) lies at 73.5 V, the operation voltage is 75.0 V [OMO08].

(for a large number of incoming photons) by [Ham08a]:

$$N_{\text{fired}} = N_{\text{total}} \cdot \left(1 - \mathrm{e}^{-\frac{N_{\text{phot}}\,\varepsilon_{\text{PD}}}{N_{\text{total}}}}\right), \tag{5.18}$$

with the number of incident photons N_{phot} and the total number of pixels N_{total}. This relation clearly shows the dependence of the dynamical range on the total number of pixels.
The creation of electron-hole pairs and the triggering of the avalanche happen quite fast inside the SiPM. Drift times inside the material of 100 ps are typical [HBG01].

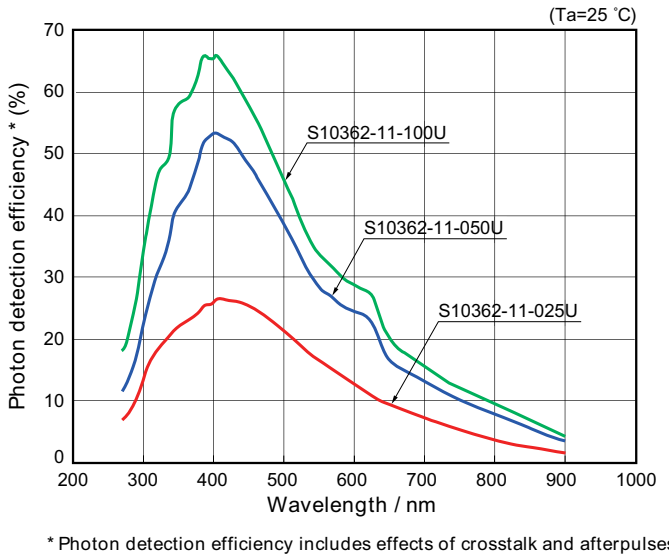

Figure 5.19: Photon detection efficiency vs. incident photon's wavelength for SiPMs with different pixel sizes [Ham08a].

Chapter 6

The GEANT4 Framework

GEANT4 stands for **Ge**ometry **an**d **T**racking and is a toolkit to simulate the passage of particles through matter with help of Monte-Carlo methods. The classes of the `C++`-framework are foreseen to create stand-alone simulations as well as to implement them into other applications.
The package provides methods to specify geometrical structures of the simulated detector, with all involved materials and their properties and to simulate the creation and tracking of most fundamental particles. A variety of many, sometimes competing, physical interaction models is provided to describe particle interaction in matter covering the wide energy range of 250 eV up to some PeV for electrons, photons, muons, hadrons and ions. It is also possible to access data of all particles, interactions, volumes and the response of sensitive detector components at most points of the simulation run. Particles can be tracked through simple applied electric and magnetic fields. The visualisation of the detector parts and some or all particle trajectories is possible.
Some components of the framework, relevant in the scope of this thesis, are described in the following sections in more detail. More information on the GEANT4 framework can be found in [Ago03; All06; G409; G408].

6.1 Overview

To illustrate the working structure of a programme designed with the GEANT4 framework, some implementation details shall be discussed here.
There are interfaces for eight user classes provided by the framework. Three of them are mandatory:

- `G4VUserDetectorConstruction`: In a derivation of this class the user has to provide information about the geometry of the detector (*DetectorConstruction*) that shall be simulated. There are no default geometries specified.
- `G4VPhysicsList`: Here the user defines the physics process classes (*PhysicsList*) to be used.
- `G4VUserPrimaryGeneratorAction`: The user also has to provide information about the kind, number and initial properties of the primary particles (*Primaries*).

Classes that are not mandatory but necessary to steer the simulation are:

- `G4UserRunAction`: Here the user can specify actions that shall be executed at every start and end of every *Run*.
- `G4UserEventAction`: The same as above but for every *Event*. Here information about the whole event can be gained.
- `G4UserStackingAction`: Tracks can be suspended or postponed if there are particle tracks with higher priority. (Mainly used for optimisation.)
- `G4UserTrackingAction`: Specifies actions at the creation and completion of every *Track*. Information about the particle track can be extracted here.

- `G4UserSteppingAction`: Customise the behaviour while going from *step* to *step* in the simulation. Detailed information from every *StepPoint* can be obtained here.

A Run represents one simulation procedure with a specified number of identical or different events, e. g. one Run can process 100 times one muon passing a piece of scintillator with each muon at another position. Every starting muon initialises an Event that ends when all primary and secondary particles have been tracked to the end, i. e. detected or absorbed or removed in another way.
A Track is always a momentary representation of the state of a particle, while a step carries the 'Delta'-information between two Track-points. Whole particle trajectories are usually not stored due to memory consumption.

6.2 Geometry

As mentioned above, in the DetectorConstruction class, the user has to define all components of the detector, especially every kind of volume, and their alignment that shall be simulated. This includes details about the chemical composition of the materials so that values for quantities like absorption length or corrections for the energy loss in matter (Bethe-Bloch formula) can be computed. Here also properties for optical processes, like refractive indices, attenuation lengths or reflectivity, can be set, especially optical surfaces and their properties.

6.2.1 Volumes

A volume in GEANT4 has to be defined in three steps:
First of all a *Solid* must be defined. It contains all the geometrical information, i. e. the dimensions and shape of the volume. Many different shapes (like simple boxes, spheres, twisted tubes etc.) are provided by the framework.
Then a *LogicalVolume* has to be created where a Solid and physical information, like its material, are merged.
Finally a *PhysicalVolume* is created when combining the information of the LogicalVolume with a rotation and position in a mother volume. This can be done by a *Placement* or a *Parameterisation* inside a mother volume.
A LogicalVolume can be declared as a *SensitiveDetector* to create *Hits* that are collections of the particle's properties at the detection point. A short overview is also shown in fig. 6.1.
The geometry information is used by the GEANT4 kernel while tracking particles. Material information is of course used to determine interaction lengths.

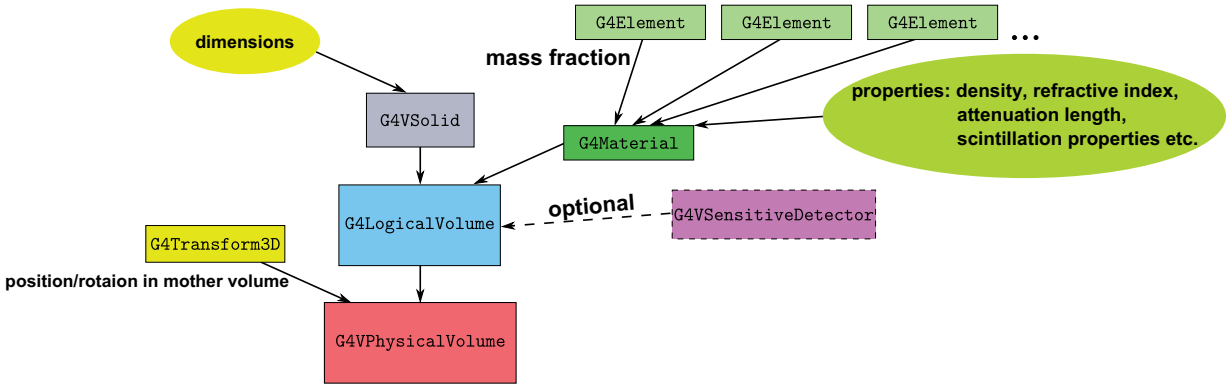

Figure 6.1: Shortened overview of the logic of volume building and placing in the GEANT4 DetectorConstruction. All volumes must have a mother volume, except of the *world volume* which is the (only) basic volume. Particles leaving the world volume are removed immediately.

6.3 Physics

In the PhysicsList all relevant processes can be activated and also production cuts can be set. This class is modular so that only the processes needed in particular or only processes of a defined energy range have to be implemented. All particles that can occur within the simulation have to be registered here, otherwise they cannot be created.
A production cut is a length, set by the user, that is used to decide whether a secondary particle (e. g. an δ-electron or a bremsstrahlung photon) shall be produced or not. If, within the current volume, a secondary particle would travel (in the momentary material) less than the length given by the cut, its production is inhibited. The corresponding energy loss is counted as a continuous energy loss.

6.3.1 Optical Processes

A special group of physical processes are those that create and invoke optical photons[47].

Creation

Three processes can be implemented that create optical photons: The *CerenkovProcess*, the *TransitionRadiation* and the *ScintillationProcess*. The number of optical photons created in transition radiation processes is negligibly small. For the number of optical Cherenkov photons N_γ created per length L a particle travelled through a dielectric material one finds [Kle05]:

$$\left(\frac{\mathrm{d}N_\gamma}{\mathrm{d}L}\right)_{\text{Cherenkov}} < \sin^2\theta_\mathrm{C} \cdot \frac{49}{\mathrm{mm}} \tag{6.1}$$

where $\theta_\mathrm{C} = \arccos\frac{1}{n\,\beta}$ denotes the Cherenkov angle. For a 1 GeV muon traversing a typical scintillator with refractive index[48] $n = 1.6$ this number becomes: $\frac{\mathrm{d}N_\gamma}{\mathrm{d}L} \approx 30/\mathrm{mm}$ which is very few compared to the number of scintillation photons that is of the order of $\left(\frac{\mathrm{d}N_\gamma}{\mathrm{d}E}\right)_{\text{scinti}} \approx 10000 - 20000\ /\mathrm{MeV}$ with typically[49] $\left(\frac{\mathrm{d}E}{\mathrm{d}L}\right)_{\text{scinti}} \approx \frac{0.2\ \mathrm{MeV}}{\mathrm{mm}}\,\frac{\varrho}{\varrho_0}$ for a minimal ionising particle. So the Cherenkov process can also be neglected in this case.
In GEANT4 the scintillation process is characterised by several parameters:
The first important parameter is the *scintillation yield*. This is the effective mean number of photons created per energy deposit of the traversing particle. This number follows a Poissionian distribution. There can be material dependent effects that broaden or narrow this distribution, this is considered by the *resolution scale*. This parameter is basically interesting for inorganic scintillators and is not used here (i. e. set to $1 \Leftrightarrow$ no broadening).
Other important parameters are the *time constants*. The decay time of most scintillating materials can be described by a superposition of two exponentials. One that is shorter (typically $\mathcal{O}(\tau_\text{short}) = 1$ ns) and one that is longer (typically $\mathcal{O}(\tau_\text{long}) = 10$ ns). The contribution of the two terms is considered with the *yield ratio*. For fast organic scintillators, that are regarded here, only the fast time component is relevant.
Furthermore an emission spectrum of photons must be provided in the form of a list of points (photon energy, relative emission).

[47] In GEANT4 an optical photon is treated in a different way as a high energy photon (`G4Gamma`). From here on a photon or 'gamma' always means an optical photon when not specified in a different way.
[48] In general, the value of the refractive index depends on the material condition, e. g. water will have a different refractive index than ice or water vapour and for vapour the refractive index will vary with density or pressure etc.
[49] ϱ is the density of the material and $\varrho_0 = 1\ \mathrm{kg/dm^3}$

Invocation

The processes invoking optical photons are *bulk absorption*, *Rayleigh scattering*, *reflection* and *refraction* at medium boundaries, *wavelength shifting* (WLS).

- Absorption:
  Once a photon has been created it can be absorbed inside a medium (if an attenuation length has been specified for this medium). The probability to travel a certain length is distributed exponentially with the attenuation length as parameter. See also sec. 6.5 for more details.
- Rayleigh scattering:
  Just changes the direction of a photon in the well-known way. It is mainly interesting for photons travelling though a gas-filled volume.
- Reflection/Refraction:
  A photon has several possibilities to interact at a medium boundary. More details can be found in sec. 6.6.
- WLS:
  Wavelength shifting materials can absorb photons of a certain wavelength range and emit new photons isotropically with a different wavelength. For this kind of materials, an absorption and an emission spectrum must be provided. In this implementation of the WLS process, only one new photon per absorbed photon can be emitted.

6.4 Primary Particles

The user has to set the number and the starting properties, i. e. the position, direction and momentum (eventually polarisation) of the primary particle(s) and of course its type and charge. All intrinsic properties of the particles used in GEANT4 are taken from the PDG[50]-Database. This information is processed by an instance of the `G4ParticleGun`.

6.5 Tracking/Stepping

Despite the name (Geometry and Tracking), particles in GEANT4 are not tracked directly but 'transported' from StepPoint to StepPoint. The *SteppingManager* brokers information between the particle within a step, the geometry, the physical interactions in matter etc. and decides about the step length depending on the received information. Each physical process proposes a step length and the SteppingManager selects the process with the shortest step length, with respect to the geometric extension of the momentary material.

6.5.1 Step Length

A particle travelling through matter is subject to many different processes. It can also pass different regions consisting of different materials inside the detector. The determination of the proper interaction length is done in the following way:
The point of an interaction (e. g. the decay of a particle or absorption of a photon) is characterised by the mean free path $\lambda(l)$. The probability to travel the length l is:

$$P(l) = \mathrm{e}^{-n_\lambda}, \tag{6.2}$$

[50] **P**article **D**ata**G**roup

with: $n_\lambda = \int_0^l \frac{\mathrm{d}l}{\lambda(l)}$.
Because the probability distribution as a function of n_λ is a simple exponential, its value for each process is set to:

$$n_\lambda = -\ln \eta, \tag{6.3}$$

where η is a random number uniformly distributed in $(0, 1)$ that is being diced for every process independently at the point of production of the particle. Form this value the step length is computed and returned to the SteppingManager.
There are several different processes that can limit the step length like decay, interaction, geometrical boundary or a user-given maximum length. Values for n_λ are computed independently for every of these processes. The SteppingManager picks the shortest of the according lengths and invokes the process's *post step action*. If the particle still exists (i. e. no decay or interaction has happened) the n_λ's of the different processes are decremented by the value corresponding to the travelled path length and new step lengths are computed. See [Ago03] for more details.

6.6 Reflection/Transmission at optical Surfaces/Boundaries

One important topic that has to be considered when dealing with optical photons is their behaviour at surface boundaries that is basically characterised by:

- the reflection or refraction angle,
- the probability that the photon is reflected or refracted: this is the quantum mechanical effect that has to be considered when photons shall be treated as particles rather than waves.

There are three kinds of boundaries a photon can encounter.

Case: dielectric → black metal

This case is trivial in the sense that the photon is immediately absorbed when reaching the black metal.

Case: dielectric → dielectric

The reflection/transmission probability is determined with help of the classical description of electromagnetic waves with $\boldsymbol{E} = \boldsymbol{E}_0\, \mathrm{e}^{\mathrm{i}(\boldsymbol{k}\cdot\boldsymbol{x}-\omega\, t)}$ and $\boldsymbol{B} = \sqrt{\mu\,\epsilon}\,\frac{\boldsymbol{k}\times\boldsymbol{E}}{|\boldsymbol{k}|}$.
The photon properties (incoming wave-vector $\boldsymbol{k}$, polarisation etc.) are used to determine the reflection (R) and the transmission ($\mathsf{T} = 1-\mathsf{R}$) *coefficient* and with it the reflective and refractive angles. This results in the well-known Fresnel equations including the special case of total internal reflection.
For photons the values for the classical parameters T and R are interpreted as transmission and reflection *probabilities* respectively.

Case: dielectric → metal

In this case it is not possible for the photon to be transmitted. It can be reflected with respect to the local normal of the medium boundary (see also sec. 6.6.1) or absorbed according to the (user-specific) absorption probability of the material. Any material, independent of its composition, can be specified to have a 'metal-like' surface, it only affects the reflection properties and not the material properties.

6.6.1 Surface Boundaries

The reflection processes described above are significantly dependent on the *surface roughness* where the reflection takes place. There are different approaches to describe the roughness of a surface. In GEANT4 there are two different models used named GLISUR and UNIFIED.
In both models a local surface normal is diced once for every reflection of every photon according to different parameters. This local surface normal (*facet normal*) is used for all further calculations.

GLISUR

In this model the surface roughness is parameterised by only one parameter $0 \leq p \leq 1$.
To find the facet normal, $\boldsymbol{n}_{\text{loc}}$ is computed as $\boldsymbol{n}_{\text{loc}} = \boldsymbol{n}_{\text{glob}} + (1-p) \cdot \boldsymbol{n}_{\text{smear}}$ with:

$$\boldsymbol{n}_{\text{smear}} = \begin{pmatrix} \eta' \\ \eta'' \\ \eta''' \end{pmatrix} \tag{6.4}$$

where η', η'', η''' are uniformly distributed random numbers $\in [0,1]$. Some other constraints ensure a physically reasonable result.

UNIFIED

As described in detail in [NIK89] another approach than that in GLISUR is supposed to be chosen to reach results compatible with measurements. One major point here is to make reflection properties dependent on the angular distribution of the (local) micro-facets rather than of their height distribution.
The assumption is that the angle α between a micro-facet and the average surface is normally distributed with a standard deviation σ_α. The value of σ_α has to be determined experimentally (see also sec. 7). Thus, in the simulation of the surface, the normals are diced according to this distribution. The micro facets are regarded to be smooth at scales comparable to the considered photon wavelengths (see also sec. 7.3.3).
In order to account for the various reflection possibilities at medium boundaries a few more considerations have been pursued ([LM96]). Fig. 6.2 shows the distribution of the radiant intensity in this model. A photon coming in under the angle θ_{i} to the average surface can be subject to different boundary processes:

- It can be reflected specularly with the same angle: The probability is given by the *specular spike constant* C_{ss}.
- It can be reflected at the micro facets resulting in a spread of the distribution dependent on σ_α with a probability given by the *specular lobe constant* C_{sl}.
- The photon can be subject to internal Lambertian reflection, the probability is given by the *diffuse lobe constant* C_{dl}.
- In some materials there is a possibility that a photon is reflected backwards in the same direction where it came from. This is controlled by the *backscatter spike constant* C_{bs}.
- The photon can also be transmitted under the refraction angle θ_{r}.

These constants have to be determined by experiment. The radiant intensity (photon flux per solid angle) $J = \frac{\mathrm{d}\Phi}{\mathrm{d}\omega}$ is in good approximation [LM96]:

$$\begin{aligned} J_{\mathrm{U}}(\theta_{\mathrm{i}}, \theta_{\mathrm{r}}, \phi_{\mathrm{r}}) \quad &\approx \quad \mathsf{R}(\theta'_{\mathrm{r}}, n_1, n_2)\,[C_{\mathrm{sl}}\, g(\alpha_{\mathrm{r}}; 0, \sigma_\alpha) \\ &+ \quad C_{\mathrm{ss}}\, \delta(\theta_{\mathrm{i}} - \theta_{\mathrm{r}})\delta(\phi_{\mathrm{r}}) + C_{\mathrm{bs}}\, \delta(\theta_{\mathrm{i}} + \theta_r)\delta(\phi_{\mathrm{r}}) \\ &+ \quad C_{\mathrm{dl}}\, \cos(\theta_{\mathrm{r}})] \\ &+ \quad \mathsf{T}(\theta'_{\mathrm{t}}, n_1, n_2)\, g(\alpha_{\mathrm{t}}; 0, \sigma_\alpha), \end{aligned} \tag{6.5}$$

with:
ϕ_{r}: the angle between the projection of the reflected or refracted photon onto the average surface,
θ'_{r}: angle of reflection with respect to the micro-facet normal,
$g(\alpha; 0, \sigma_\alpha)$: a gaussian with mean 0 and standard deviation σ_α with the restriction $\alpha \in [0, \pi/2]$.
As shown in [NIK89], a surface can be considered as highly polished when the distribution of a

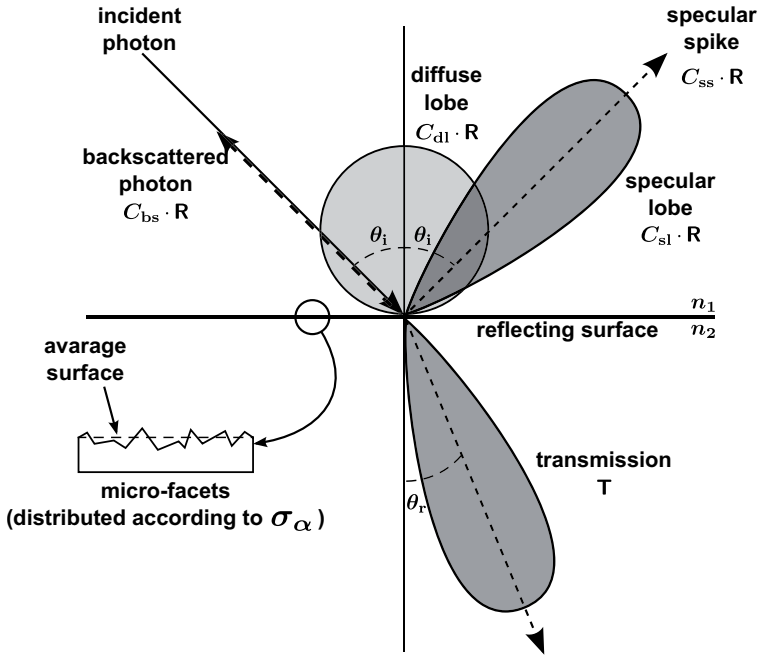

Figure 6.2: Polar plot of the radiant intensities in the UNIFIED model. The constants C_i are described in the text. Adapted from [LM96; NIK89].

sample of measured heights of a pieces of scintillator, that is typically Gaussian with mean at zero and a variance σ_{h}, is found to be: $\frac{\sigma_{\mathrm{h}}}{\lambda_{\mathrm{phot}}} \leq 0.025$. In this case σ_α can be set to 0 and the specular lobe part vanishes.
In the case where $\frac{\sigma_{\mathrm{h}}}{\lambda_{\mathrm{phot}}} > 1.5$ the specular spike part can be neglected and the specular lobe is dominant. This material is highly rough.

6.7 Wrapping Materials

Because the UNIFIED model is meant to replace GLISUR and because it provides more flexibility, it is the only model that will be used in all simulations in the scope of this thesis.
A wrapping can be simulated as a volume where the inner part has been 'removed' thus leaving a shell of the material representing the wrapping material. All reflection properties mentioned above can be applied here.
Besides this the UNIFIED model provides the possibility to simulate a diffuse reflector with an (infinitesimally small) air gap in between the material surface and the coating. In UNIFIED this coating can only be a diffuse reflector (at the moment). All reflections and refractions in the different boundaries are applied in one step to increase performance.

Chapter 7

Roughness of the Scintillator

As mentioned in sec. 6.6 there are several parameters in GEANT4 that are used to describe the properties of an optical surface. The roughness of the surface in the UNIFIED model is characterised in particular by the value of σ_α, that can be determined by measuring the profile of the surface, e. g. by using a stylus probe.
In order to find the value of σ_α for a typical piece of scintillator, a surface scan with help of an atomic force microscope (see sec. 7.1) has been performed by the II$^{\text{nd}}$ Physics Institute A (RWTH Aachen University)[51]. The scanned scintillator (`BC-404`) is identical with the one that shall be used for first test setups/measurements and, of course, in the simulations. It has been cut into pieces of $5 \times 5 \times 8\,\text{mm}^3$, so it could fit into the specimen holder of the atomic force microscope, and hand-polished by our mechanics workshop.

7.1 Atomic Force Microscope (AFM)

An AFM is a scanning microscope that measures the interatomic forces, i. e. van der Waals forces, while scanning the surface of a material and translates these into height information. A schematic view of an AFM is shown in fig. 7.1a. The AFM consists of a nanoscopic needle (*Tip*) that is mounted on a cantilever. With this Tip the surface of a specimen is scanned. At different positions, the Tip is attracted differently by the surface and the cantilever is bent accordingly to the attracting force. This can by measured as a spring force. The bending of the cantilever is typically read out with help of capacitive or optical sensors.
This technique allows a detailed surface analysis with a spatial resolution of better than 20 nm. The height resolution can reach even smaller values ($\Delta h < 0.4$ nm [Anf09]). More details can be found in [BQ86].

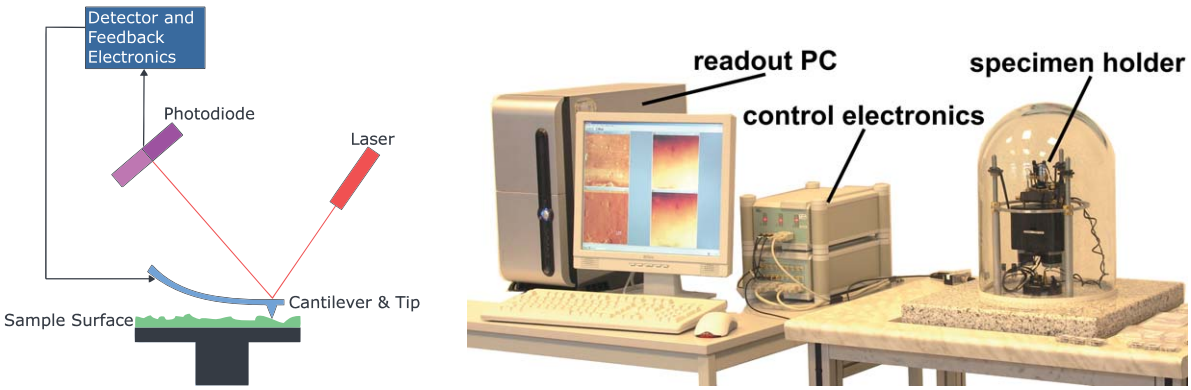

(a) Illustration of the working principle of an AFM [Wik09c].

(b) The device used to scan the scintillator surface [Anf09]. The piece of scintillator is mounted on the specimen holder located under the bell jar.

Figure 7.1: Working principle and example of an AFM.

[51] Many thanks to Dr. Marcus Liebmann at this point.

7.2 View of the Surface

The visualisation of the scan can be performed with help of the free software WSxM[52] [Nan09]. It is a dedicated scanning probe microscope software with analysis and visualisation methods. One scanning example is shown in fig. 7.2. The figure shows scans of one area with increasing spatial resolution and, with it, decreasing size from 40×40 µm^2 down to 10×10 µm^2. Typical

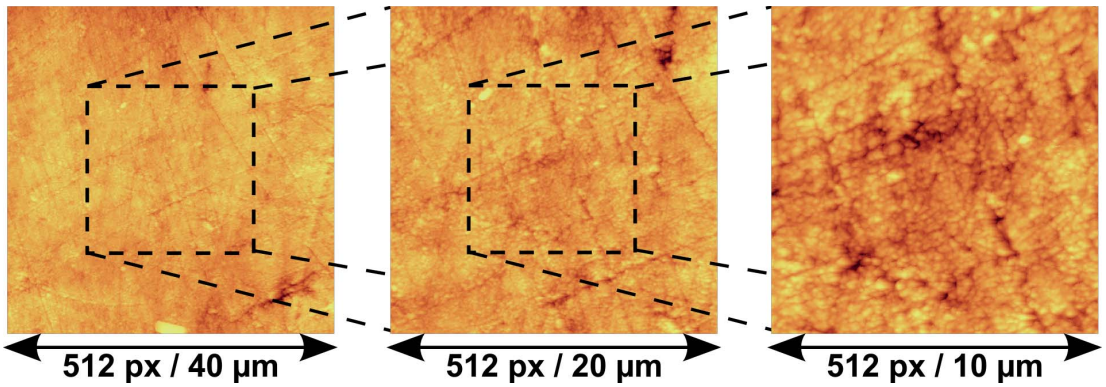

Figure 7.2: Scans of the surface of a piece of scintillator. The scintillator has been hand-polished by the mechanics workshop of the IIIrd Physics Institute A before performing the scan. The three scanning steps of one and the same area are shown.

structures appearing in all scanned specimen are small channels and less frequently larger rifts. At some points there are larger specks that could be residuals from the polishing paste or dust. The surface view (fig. 7.3), created with help of the analysis framework ROOT, shows the typical height differences of this sample. Fig. 7.3b shows additionally one section of this surface scan with an area of 400×400 nm^2 what can be regarded as a typical surface that an incoming photon with a wavelength in the order of 400 nm will experience.

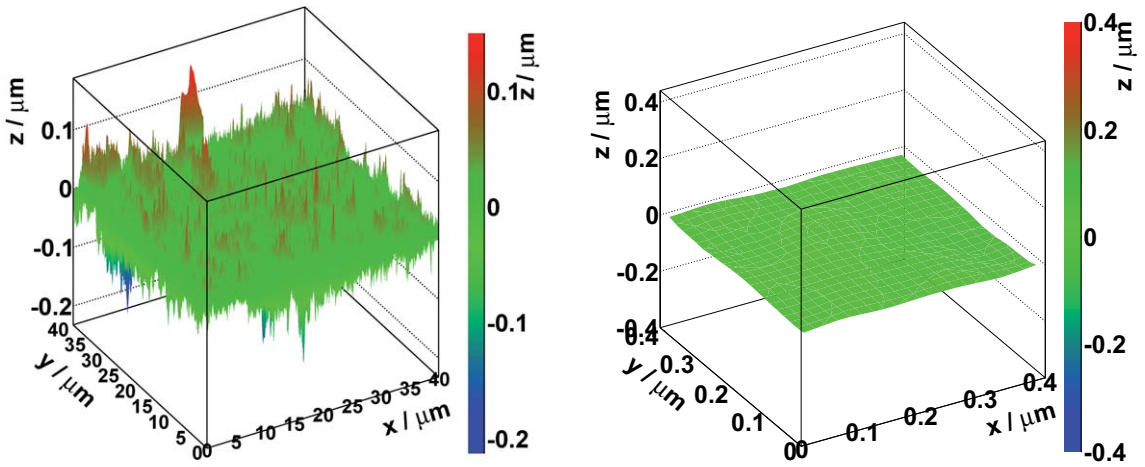

(a) The same surface as in 7.2 right but with height information coded by colour. Take note: The scaling of the z-axis is much smaller than of the other axes.

(b) One section of the scan from (a). Here the scalings are all in the same order of magnitude. The surface appears much smoother.

Figure 7.3: Surface scans with height information.

[52] **W**indows **S**canning **x** (= Force, Tunnelling, Near Optical, ...) **M**icroscope

7.3 Analysis of the Surface

The distance between two points of the scan is ≈ 20 nm with the best resolution. The optical photons appearing in the simulation will have a wavelength range of roughly $300 - 600$ nm (see also sec. 8.1). Thus the distribution of the surface quantities in this resolution range is of interest. This is the reason why the analysis has been performed at different *length scales*. In particular that means that there has been a mask applied to the data so that only data points with a certain distance are taken into account in the analysis. This fakes a lower resolution which is relevant to photons with comparable wavelengths.

7.3.1 Height Distributions

The first point in the analysis of the surface is the distribution of the heights of the scanning points around the mean surface (h). The stylus scans the surface from left to right and from

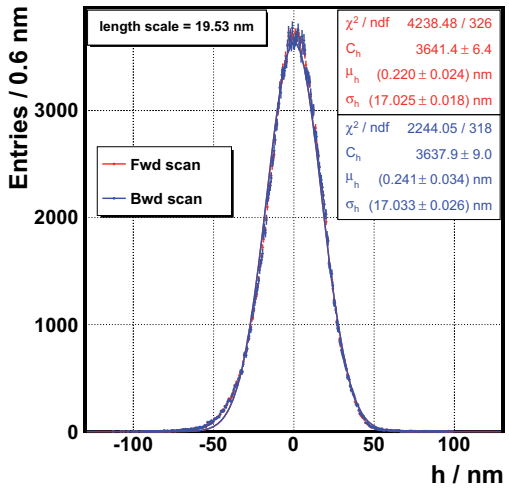

(a) Scanned with highest resolution. The Gaussian fit matches only approximately. The red and the blue curve lie on top of each other, i. e. forward and backward scan are nearly identical.

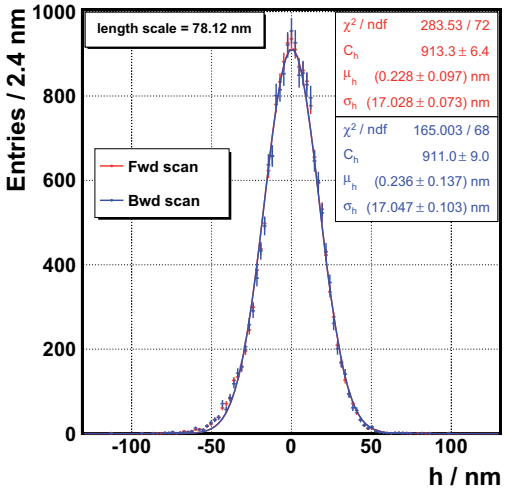

(b) Same scan as in (a) but with an increasing length scale. The fit matches better because the uncertainties are bigger.

Figure 7.4: Height distributions of one 10×10 µm^2 area scanned with a point distance of ≈ 20 nm.

right to left, called *forward* and *backward* scan respectively. Some examples of the distributions are shown in fig. 7.4 (the 10 µm^2 scan) and in fig. 7.5 (the 40 µm^2 scan). The heights are only approximately Gaussian distributed which can be explained by the fact that there are grooves with basically the same height, forcing the height distributions to values close to zero. Some larger specks can explain the deviations in the tails of the distributions. Fits become better ($\frac{\chi^2}{\text{ndf}}$ becomes smaller) with higher length scale but this is just due to the lack of statistics, causing larger uncertainties, for this sample at this length scale.
The distributions and fits resulting from the forward and the backward scans are always almost identical. The mean values (μ_h) of the fits are close to zero and the widths (σ_h) differ in the range of one per cent or less. For all further analyses the average of these distributions is used.
As mentioned in [LM96] and [NIK89], the width of the height distribution (σ_h) over the wavelength of the incoming photon can be used as a measure of the roughness of the surface. If $\frac{\sigma_\text{h}}{\lambda} \leq 0.025$ the surface can be treated as highly polished and the simulation can be done with pure specular reflection/transmission. In other cases the distribution of the local micro-facets has be taken into account to simulate the surface in an according way. The two scanned areas provide

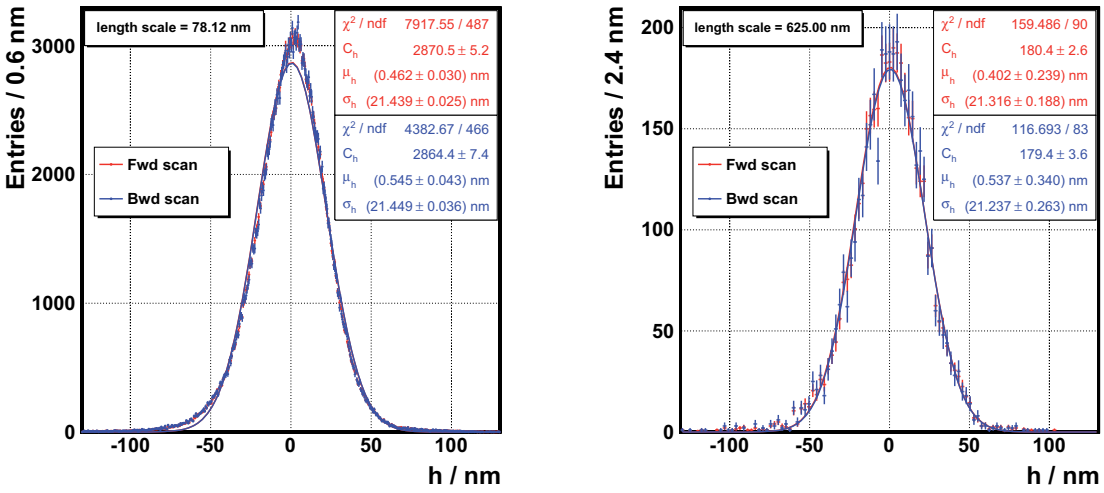

(a) At this resolution, at the same length scale the fit matches worse as compared to fig. 7.4b.

(b) The height distribution at the length scale of an optical photon. Compare also fig. A.1.

Figure 7.5: Height distributions of 40×40 μm^2 area (containing the smaller area from fig. 7.4). Scanned point distance ≈ 80 nm.

very similar distributions as can be seen in a comparison between fig. 7.5b and fig. A.1. The height distributions of the scans with all resolutions and for two different areas are summarised in fig. 7.6. There seems to be a correlation between the sample size (and with it the actual resolution) and the measured height distribution, especially for area 2. The scans performed with high resolution show only $\frac{1}{16}$ of the area of a scans with lower resolution. So it is possible, that the smaller areas show only "a part of the truth" and in the larger scan a broader variety of height distributions can be seen. The more relevant quantity is the width over the wavelength. It has

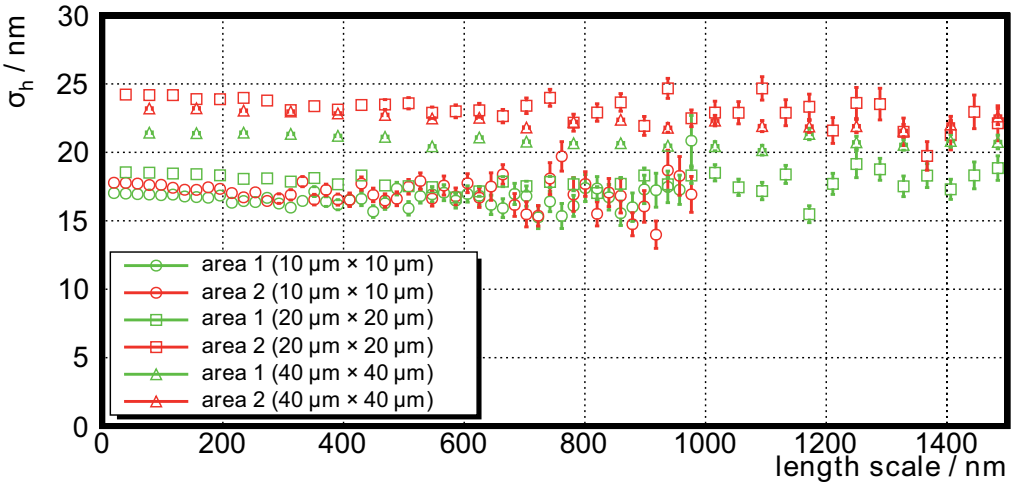

Figure 7.6: Distribution of the heights vs. the length scale.

been assumed, that the length scale can be identified with the wavelength of an optical photon. The results are shown in fig. 7.7. The behaviour for all areas and resolutions is very similar. The dashed line shows the edge mentioned above (0.025) and it is clear that in the relevant wavelength region ($300 - 600$ nm) the scintillator cannot be treated as highly ('perfectly') polished but the angular distribution of the facet normals has to be taken into account.

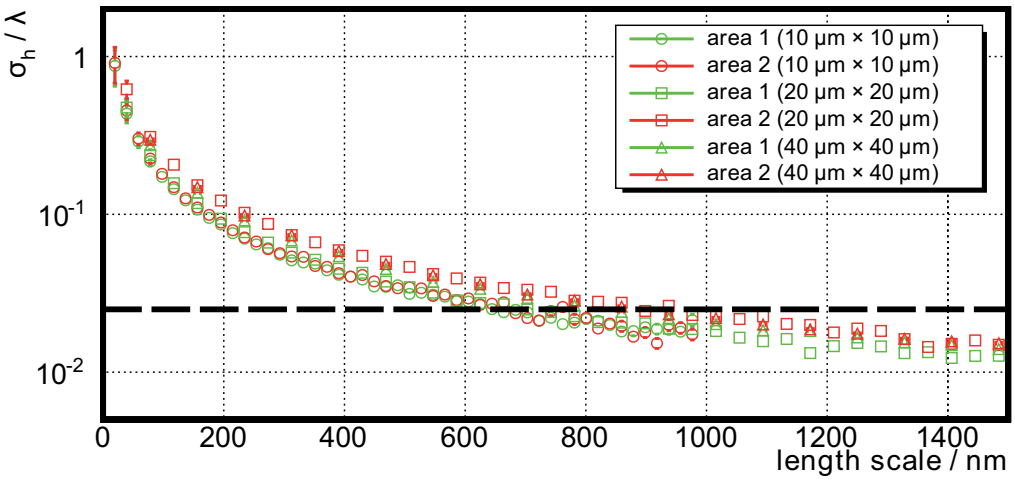

Figure 7.7: Width of the height distributions over the wavelength of an optical photon. The dashed line indicates the breaking point: $\frac{\sigma_h}{\lambda} \leq 0.025$.

7.3.2 Slope Distributions

As shown in the section before, the distribution of surface normals with respect to the average surface normal has to be taken into account. As for the height distributions, the angle distributions are extracted from forward and backward scans. As these are almost identical, again the averaged distributions are used to retrieve the parameters. The angles are retrieved by converting the slopes by "angle = arctan(slope)". The slope is defined by the line between two adjacent scanning points. Another issue comes up when looking at slopes. Adjacent points in x and y

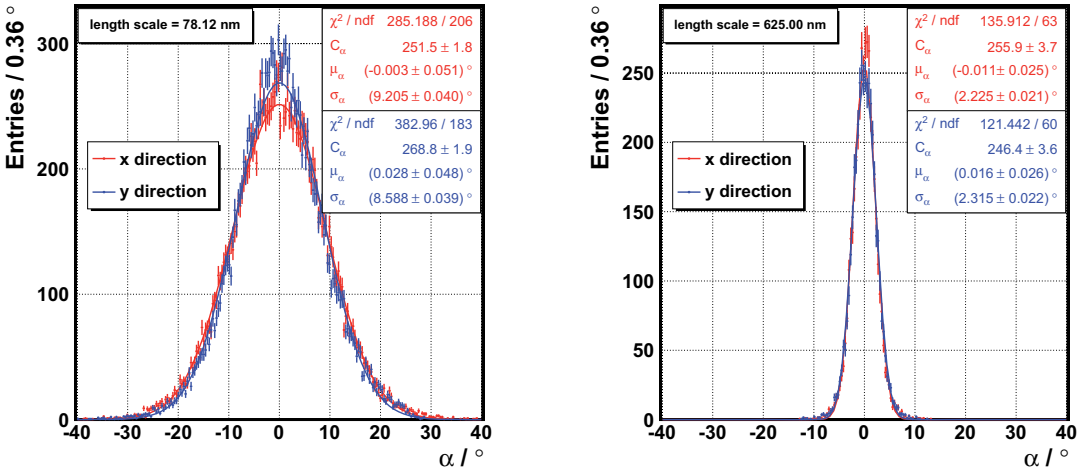

(a) Distribution of angles for a 10×10 µm^2 area.

(b) Distribution of angles of another area (40×40 µm^2) and with lower resolution as in (a).

Figure 7.8: Distributions of the slopes converted to angles with respect to the average surface normal. The distributions in x and in y direction are shown.

direction respectively are used to compute the slopes, examples are shown in fig. 7.8. Again the Gaussian fits match only approximately. The distributions in x and in y are very similar. Once again the most important quantity is the width of this distributions σ_α which is obtained from the Gaussian fits. A summary plot with widths resulting for the different length scales is shown in

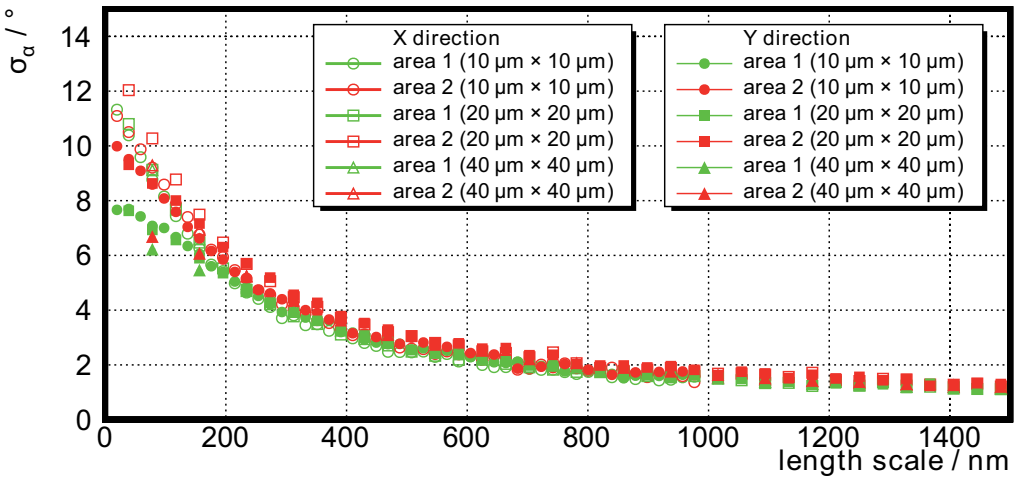

Figure 7.9: Summary of the widths of the distributions of angles, i. e. slopes.

fig. 7.9. In this case the deviations between results from areas scanned with different resolutions are very small (cf. sec. 7.3.1). Area 1 appears to be smoother when looking in y-direction while in area 2 the widths are approximately equal. Systematic errors resulting from the scan cannot be excluded. The AFM takes data line by line in x-direction and moves after each line one step in y-direction. So that a information in x direction is received in a different way than in y direction. All in all area 2 seems to be rougher than area 1. The differences in σ_α are of the order of 20 %. As expected, the surface becomes smoother with increasing wavelength.
In the relevant region ($330 - 600$ nm) σ_α turns out to be $2.0° - 4.5°$, however depending on the area, the resolution and the direction.

7.3.3 Further Considerations

The assumption made in the preceding sections is that the distribution of the slopes is the crucial parameter to define the reflection properties of an incoming photon. This means, between two measured (or rescaled) points the surface is treated as perfectly plain. In order to justify this assumption, a cross check has been made.

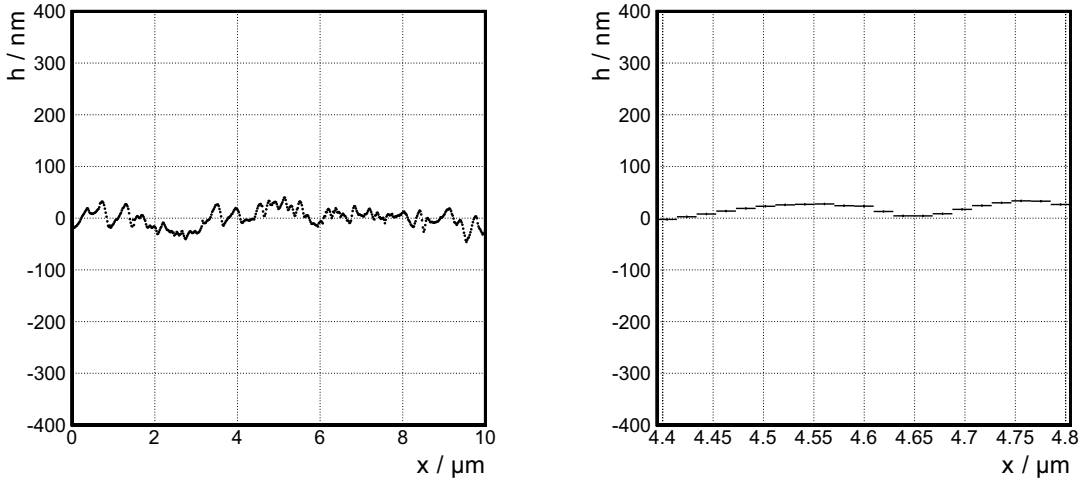

(a) Height profile in x-direction. Take note of the different scaling of the axes (compare fig. 7.3a).

(b) Same height profile as in (a) but with other axis scaling (compare fig. 7.3b).

Figure 7.10: Typical height profile of the scintillator surface.

A typical height profile of the scintillator surface is shown in fig. 7.10. An incoming photon of a typical wavelength of 400 nm is assumed to interact with a piece of the surface that is exemplarily shown in fig. 7.10b. A linear fit is performed and the distance of each point to the line is extracted. This is performed point by point for all profiles retrieved from the scan. The fitting range is adapted to the relevant wavelength, i. e. $200 - 800$ nm. An illustration of the method is shown in fig. 7.11a. A typical distribution of the distances to the line is shown in

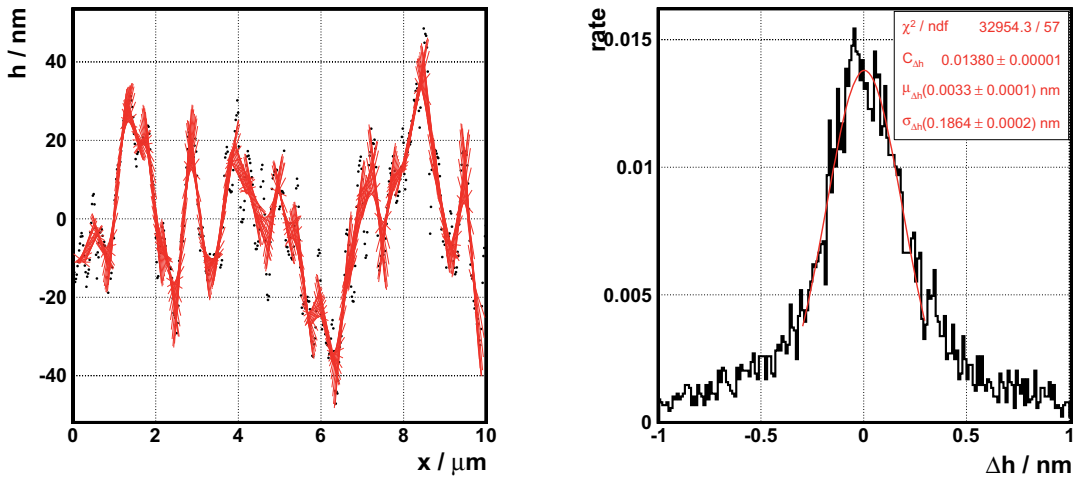

(a) Height profile with fitted curves. Fitting range: 400 nm.

(b) Typical distribution of the point differences to the linear fit. The quality of the Gaussian fit is poor but provides information about the width of the distribution.

Figure 7.11: Height profiles of the scintillator and their analysis.

fig. 7.11b. The distribution shows long tails and is narrow in the inner region. Nevertheless a Gaussian fit in the inner region is performed to quantify the distribution and especially to estimate the width. The fit quality is very low, but sufficient for this simplified analysis.

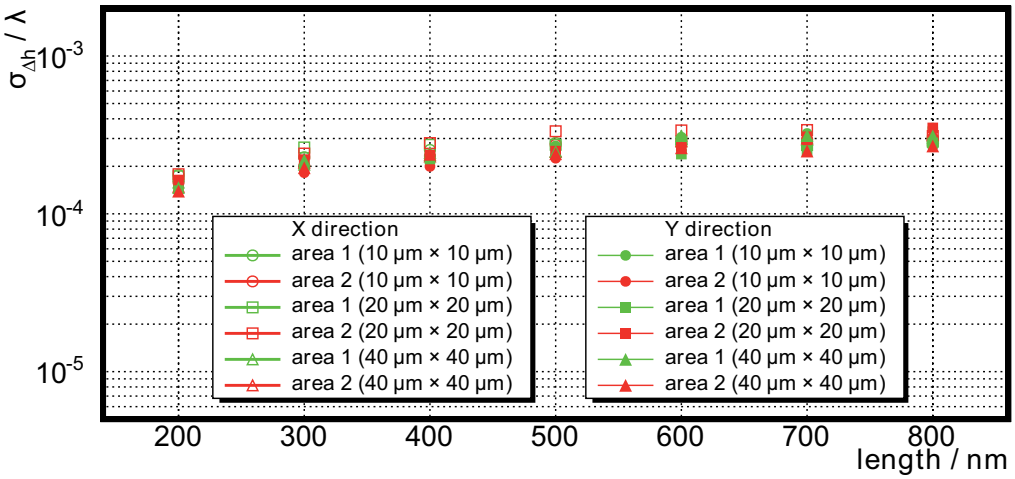

Figure 7.12: Width of the distance distributions over the wavelength for different wavelengths.

The same quantity as in sec. 7.3.1 ($\frac{\sigma_h}{\lambda}$) is used to gain information about the quality of this newly obtained surface. The summary of the fitted widths over the wavelength is shown in fig. 7.12. It is clearly visible that all values for all scans and surfaces are way below the critical number

$\frac{\sigma_h}{\lambda} = 0.025$ and can be treated as very smooth at this length scales. These means that geometrical optics can be applied to the photons at these length scales as it happens in the GEANT4 model reflection model UNIFIED.

Chapter 8

Simulated Setups

The setups simulated in the scope of this thesis have already been mentioned in sec. 4.1.2 and shall be discussed in more detail now.
The concept of using a piece of scintillator as an MTT unit provides several difficulties. The fact that the magnetic field directly outside the calorimeters is one of the strongest inside CMS, forbids the use of conventional PMTs. Therefore another kind of light sensitive detector has to be found. In this approach SiPMs are used as readout devices. As described in sec. 5.6.6 those are light sensitive semiconductor detectors that typically have a sensitive area in the order of few mm^2. Since the number of photons per SiPM is expected to be low, a detailed simulation of the different considered detector setups and geometries is needed. Using more SiPMs would result in a higher number of readout channels and corresponding electronics which is disfavoured due to the highly limited available space.
Another aspect is the timing of the detector element. The MTT must be able to distinguish unambiguously between two bunch crossings. Despite the fact that organic scintillators are very fast, i. e. have a very short decay time, the photons must propagate through the material to reach the photo detector. When using direct readout, the photons have to hit the relatively small sensitive area, eventually making them travel a long path inside the scintillator before getting detected. When using a WLS fibre, the photon collection area (i. e. the fibre surface) is larger but the decay time of the WLS material has to be taken into account in addition.
In the following sections the geometric setup and all used material properties are described in detail.

8.1 Material Properties

To make accurate predictions of the detector behaviour by simulation, one has to consider the properties of the different materials that are used to model the prototypes.

8.1.1 Scintillator

In all simulations the scintillator properties of the `BC-404` from "Bicron/Saint-Gobain" are used. This scintillator has an emission spectrum located in the visible range reaching from ≈ 380 nm to ≈ 500 nm with a peak at 408 nm (see fig. 8.1a). This fits very well to the absorption spectrum of the used SiPMs (see sec. 5.6.6) and the used WLS fibre (see sec. 5.4). The attenuation length of the scintillator is 1600 mm and the refractive index is 1.58. It has a very short decay time of 1.8 ns [BIC98; SG05b]. Another important quantity of the scintillator is its light output that is 8000 photons per MeV energy deposit according to [SG05b]. A comparison between the manufacturer's specified spectrum and the digitised one is shown in fig. 8.1. In Geant4 photon wavelengths are expressed in terms of energies. So fig. 8.1c shows the read-in distribution converted to energies, while fig. 8.1d shows the output distribution as computed by the simulation according to the given spectrum. The distributions match very well.

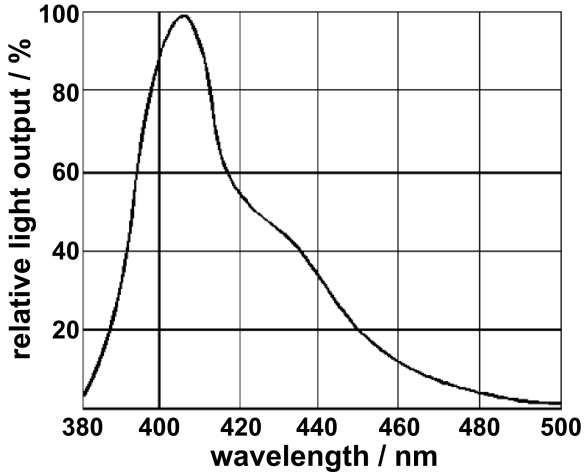

(a) Photon emission spectrum of scintillator BC-404 as given by the manufacturer [BIC98; SG05b].

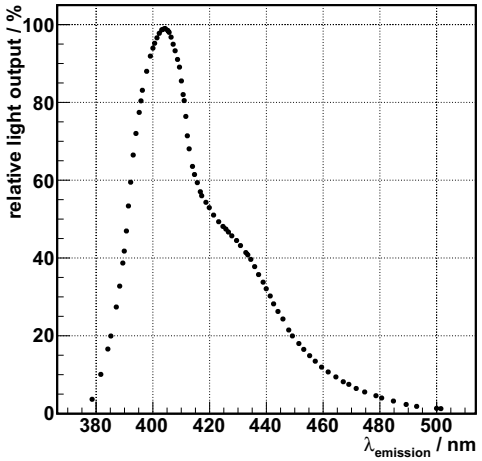

(b) The spectrum read in point-by-point.

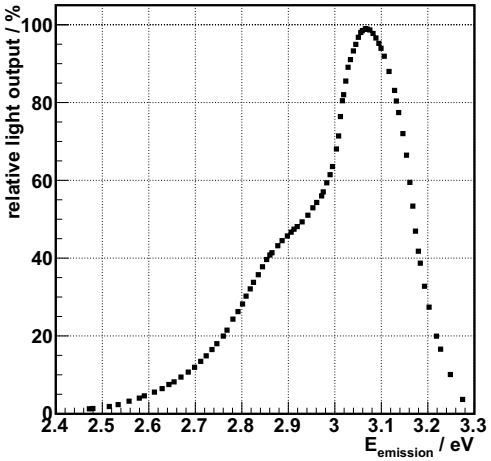

(c) The same spectrum as in (b) but converted to energies.

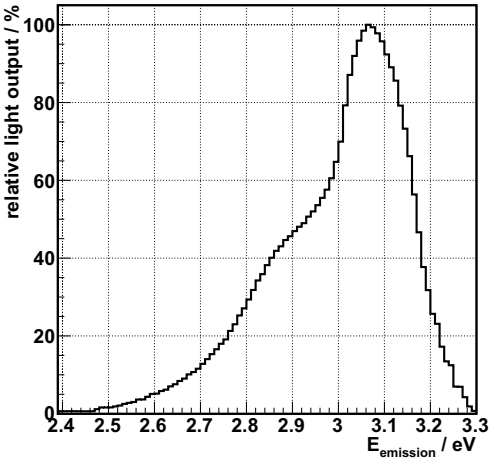

(d) Photon energy distribution computed by the simulation.

Figure 8.1: The light emission spectrum of scintillator BC-404.

8.1.2 SiPMs

Due to the fast development in the semi-conductor manufacturing in the last few years, a vast variety of silicon photomultipliers became available. The most important quantity of a light sensitive detector is its photon detection efficiency ($\varepsilon_{\mathrm{PD}}$). In many applications Hamamatsu SiPMs became a kind of standard device because they reach a $\varepsilon_{\mathrm{PD}}$ of up to 75 %. In the scope of this thesis the S10362-11-100C type (1×1 mm^2 sensitive area, 100×100 µm^2 pixel size) is used as a benchmark unit. The wavelength dependent detection efficiency of this device (fig. 8.2a) has been read in point-by-point and is shown in fig. 8.2b. As mentioned above, all quantities of photons are expressed as a function of their energy, so in fig. 8.2c the detection efficiency is shown as a function of the photon energy. Finally in fig. 8.2d the spectrum is shown as computed by the simulation. To perform a more realistic behaviour, a linear interpolation between the read-in points is performed. When reaching the edges of the given spectrum, additionally a linear extrapolation to the left and right has been implemented with the attempt to make the spectrum more realistic. It is very unlikely that a detection spectrum will fall off abruptly to zero, thus

the extrapolation happens in the range between the first/last sampled energy $\mp 10\,\%$. This is an arbitrary value and so, to further improve the simulation conditions, the spectrum should be modelled of values achieved from measurement.

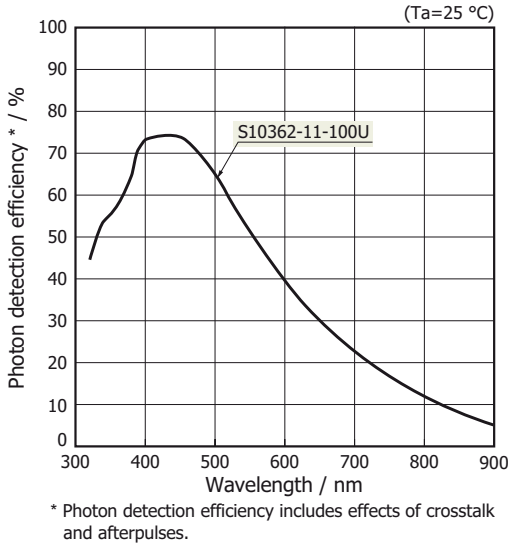

(a) Wavelength dependent photon detection efficiency of the S10362-11-100C SiPM as given by the manufacturer [Ham09].

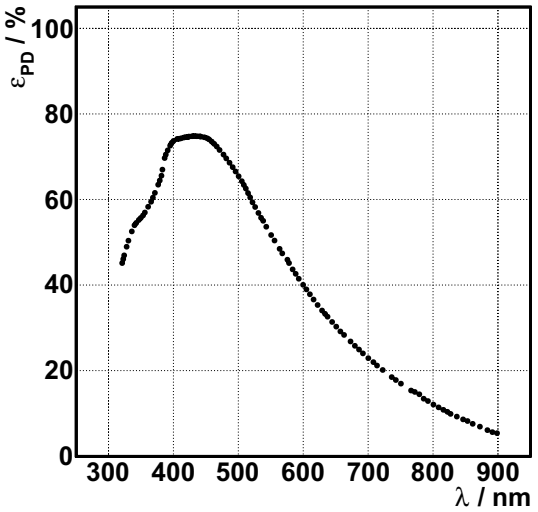

(b) The spectrum from (a) read in point-by-point

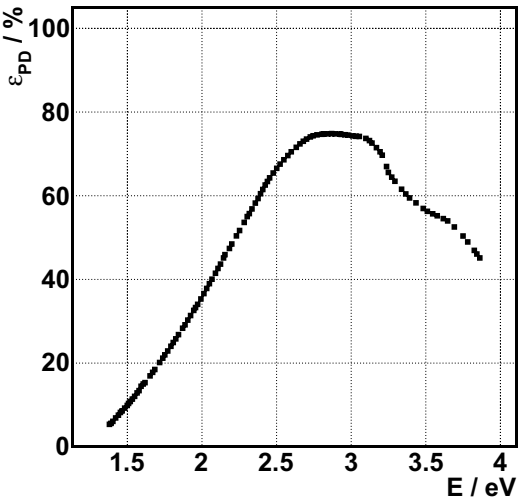

(c) The same spectrum as in (b) but converted to photon energies.

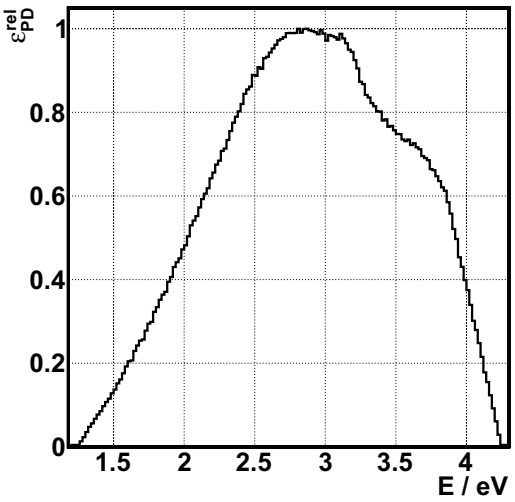

(d) Relative efficiency spectrum as computed by the simulation (with extrapolation).

Figure 8.2: Photon detection efficiency of the S10362-11-100C SiPM.

8.1.3 Wavelength Shifting Fibre

In all WLS simulation setups, the properties of the BCF-92 fibre are used. This kind of fibre has a core of polystyrene with a refractive index $n_{\text{core}} = 1.60$, an acrylic inner cladding (typically made of PMMA[53] with refractive index $n_{\text{inner}} = 1.49$ and an outer cladding made of a fluor-acrylic material (fPMMA) called EMA[54] with a refractive index $n_{\text{outer}} = 1.42$ [SG05c].

[53] **P**oly(**M**ethyl **M**eth**A**crylate)
[54] **E**xtra **M**ural **A**bsorber

This fibre has a short decay time $\tau_{\text{fibre}} = 2.7$ ns and a large attenuation length for its own light of $X_0 > 3.5$ m. The emission spectrum peaks at 492 nm and is shown in fig. 8.3a. In GEANT4 the emission spectrum can be handled basically independent of the absorption spectrum. The

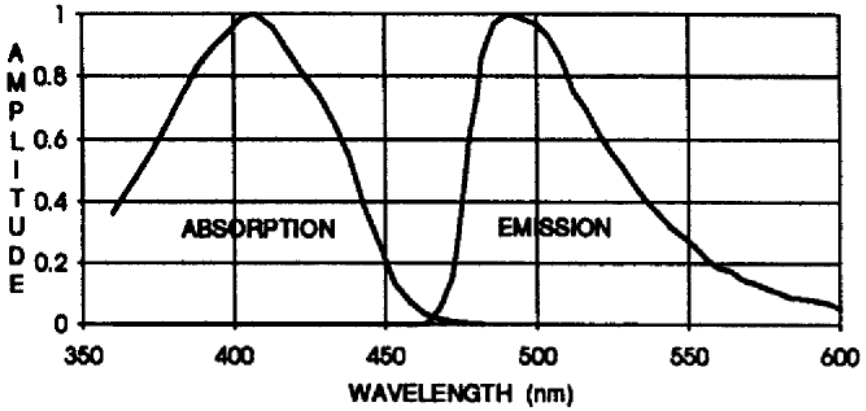

(a) Absorption and emission spectrum of BCF-92 [SG05c].

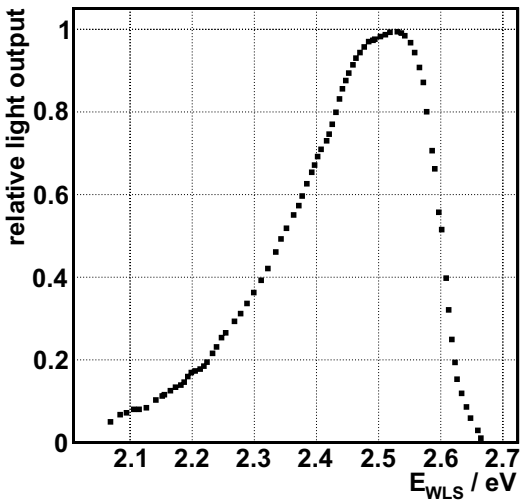

(b) The emission spectrum from (a) sampled and converted to energies.

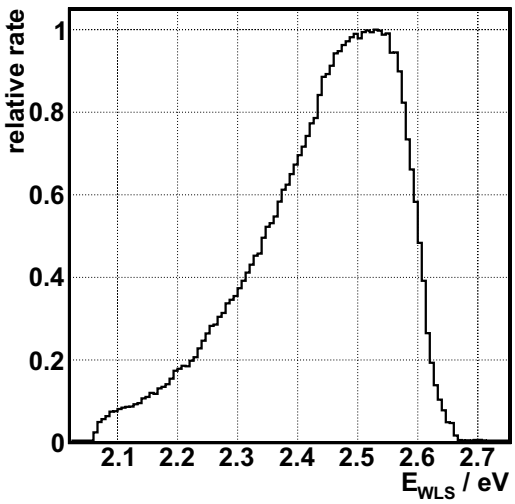

(c) The rate of WLS photons computed by the simulation.

Figure 8.3: Absorption and emission spectra of BCF-92.

handling of the absorption spectrum turns out to be more complicated. In GEANT4 the absorption spectrum can only be implemented by providing the attenuation lengths for the different wavelengths. Only relative absorption efficiencies are available and provide details on attenuation lengths only in the emission region. So the only conclusion that can be drawn from the absorption spectrum (fig. 8.3a left) is that the fibre absorption has its maximum in the emission range of the scintillator (BC-404) (compare fig. 8.1a and fig. 8.3a).
Nevertheless, to simulate the behaviour of the fibre, an absolute "attenuation length spectrum" has to be provided. Due to the lack of information, two assumptions have been made:

- In the relevant region the absorption is uniform, i. e. happens with the same probability for every wavelength. This is an optimization in the sense, that more photons will be absorbed in the fibre compared to a more realistic case.
- The attenuation length in the absorption region is smaller than the fibre diameter. This is a heuristic assumption but can be motivated by the following reasons: In [KKP81] the measurement of WLS bars results in an attenuation length of (5.2 ± 0.2) mm. The measured

material is not directly comparable to the fibre used here but the results are a first hint. Aside from this the fibres are available with diameters from 0.25 mm to 5.00 mm [SG05c]. In a fibre with a higher attenuation length than its diameter the overall probability for photons to be absorbed in the fibre would be very small and they would have to cross the fibre several times or with high angles, with respect to the fibre surface, to be absorbed making the use of a fibre pointless.

These reasons suggest to use an attenuation length that is in the order of 1 mm. The benchmark point in this study will be 0.5 mm which corresponds to the fibre radius.

8.1.4 Optical Cement

To maximise the number of photons arriving at the fibre it is advisable to have an optical coupling between the fibre and the scintillator. Typically this is done with help of optical cement. Commercial products for this application are `BC-600` and `EJ-500`. These are equivalent ([Elj09]) but the latter will be used in simulations because more information about its properties (e. g. the transmission spectrum) is provided by the manufacturer. The transmission spectrum is shown in fig. 8.4a.
In the simulations the absorption probability of photons is computed according to the attenuation length that must be provided. The transmission spectrum ($T_\lambda(x)$) in fig. 8.4a can be converted to attenuation lengths by:

$$T_\lambda(x) = \mathrm{e}^{-\frac{x}{X_\lambda}} \tag{8.1}$$

$$T_\lambda(d) = \mathrm{e}^{-\frac{d}{X_\lambda}} \tag{8.2}$$

$$\Leftrightarrow X_\lambda = -\frac{d}{\ln T_\lambda} \tag{8.3}$$

X_λ is the attenuation length for light of wavelength λ and $d = 0.125$ mm is the sample thickness where the transmission has been measured; the refractive index is $n_{\mathrm{OC}} = 1.57$ [Elj07] (see also [SG05a]). This has been done in fig. 8.4c for wavelengths and in fig. 8.4d for energies of the photons. The relevant optical spectrum is also denoted in the plot.

8.2 Simulated Geometry

The geometry of the particular components used in the simulations shall be described.
The coordinate system in all simulations is as follows:
The origin lies in the middle of the simulated world volume and will be in all cases in the middle of the scintillator. The y-axis always points upwards. The x-axis is the 'width-axis' and the z-axis is the 'length-axis'. Absolute coordinates are always given relative to the origin of this coordinate system.

8.2.1 Scintillator

The piece of scintillator used in the simulations is a simple cuboid with quadratic footprint. Footprint size and height will be in the order of 100×100 mm^2 and 10 mm respectively. A sketch created with help of the GEANT4 simulation is shown in fig. 8.5.

8.2.2 SiPMs

The SiPMs used in the simulations are always quadratic with a pixel density of 100/mm^2. The top view of an SiPM in the simulation is shown in fig. 8.6a. The fill factor for this kind of SiPM is $\varepsilon_{\mathrm{geom}} = 0.785$ ([Ham09]) resulting in a sensitive pixel area of 0.886×0.886 mm^2. In fig. 8.6b

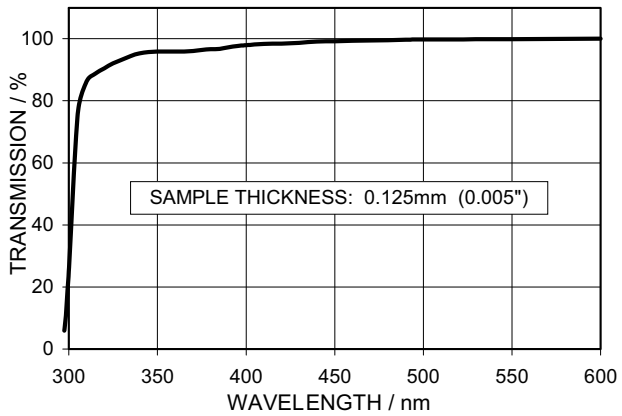

(a) Wavelength dependent transmission spectrum of the optical cement EJ-500. The transmission has been measured relative to that in air [Elj07].

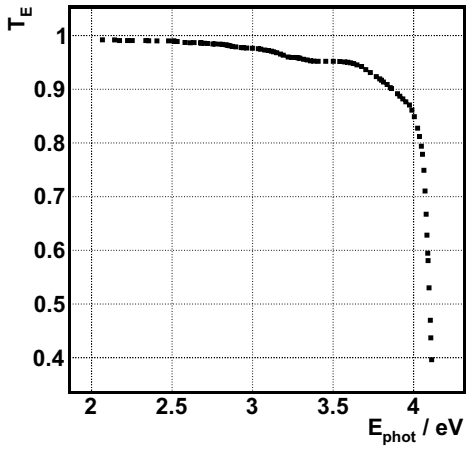

(b) Sampled spectrum from (a) and converted to energies.

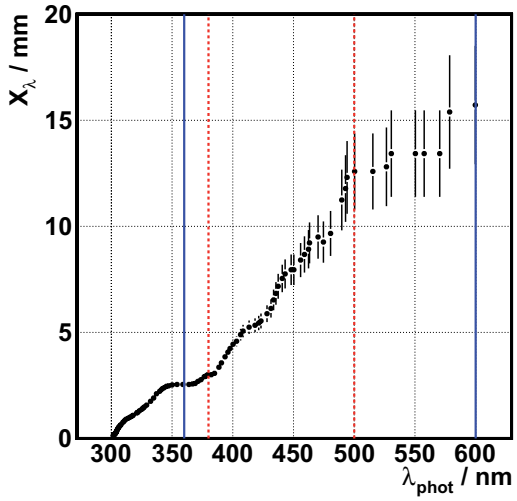

(c) Transmission probabilities converted to attenuation lengths according to eq. 8.1. The scintillator emission spectrum lies between the dashed lines. The complete possible emission spectrum lies between the solid lines. Attenuation lengths are between 2.5 mm and ≈ 15 mm. The uncertainties are a consequence of the read-off accuracy of the actual spectrum.

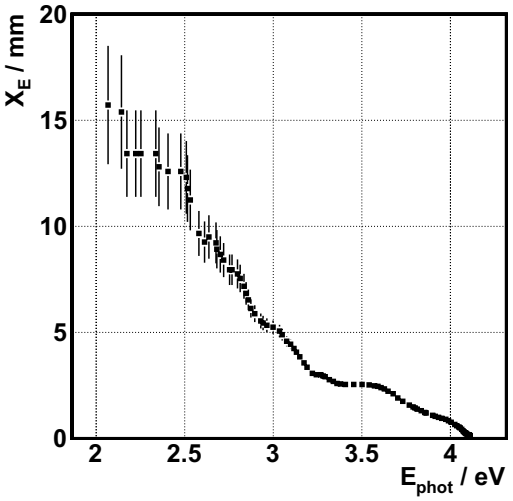

(d) Same as (c) but converted to energies.

Figure 8.4: Transmission spectrum of optical cement EJ-500.

the side view of an SiPM is shown. A height of 50 µm has been chosen which is of no real importance because arriving photons are absorbed immediately in the SiPM, but it has to be set to a particular value due to GEANT4 volume logics. The small gap between the SiPM and the scintillator or fibre is due to the fact that there will never be a perfect mechanical coupling between the two. It has to be filled with a material (optical gel or cement) with an appropriate refractive index and good transmission to maximise the light yield at the SiPM. In the simulations the SiPMs will be coupled with the EJ-500 cement.

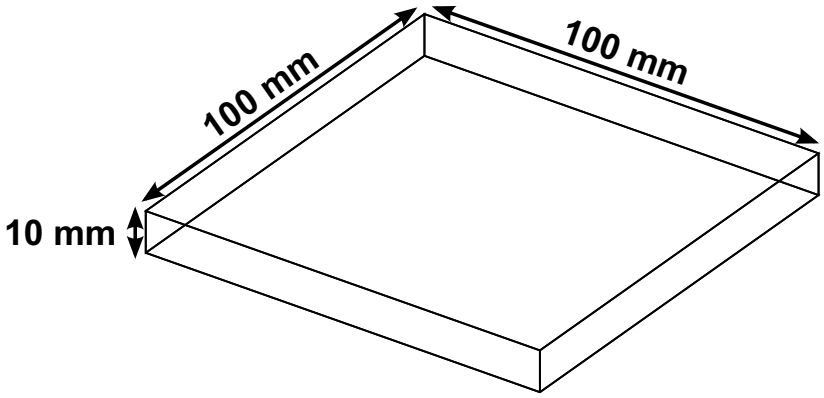

Figure 8.5: Example of a piece of scintillator visualised by GEANT4.

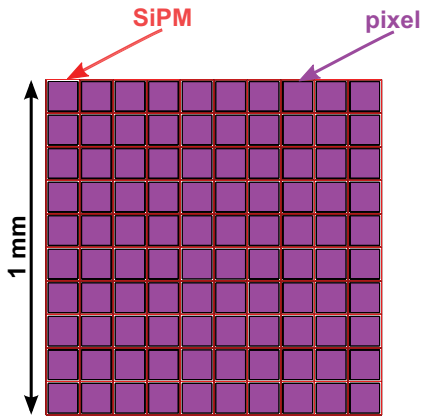

(a) Top view: Silicon Photomultiplier modelled according to [Ham09]. The red lines denote the pixel contours. The magenta squares show the sensitive parts of the pixels. Fill factor according to [Ham09].

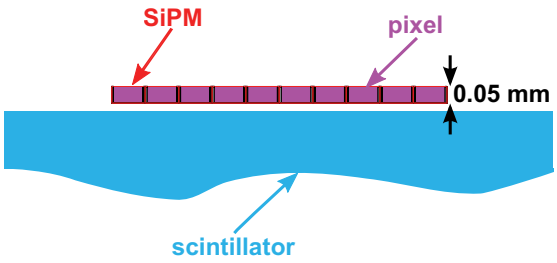

(b) Side view: The height of the SiPM is arbitrary but necessary due to GEANT4 volume logics. The gap between SiPM and scintillator has been chosen to be 25 µm.

Figure 8.6: Visualisation of an SiPM modelled according to [Ham09].

SiPM Setup

The direct readout setup considered in the scope of this thesis, i. e. SiPMs mounted on the 'top' (one of the sides with the larger area) of the scintillator, is easily feasible and prevents large amount of dead space between the scintillator tiles in a possible MTT setup where the segments (consisting of these scintillator tiles) will be close-packed, surrounding the Solenoid (see also [MAB07]). The saved space at the sides of the scintillator has the advantage that several scintillator tiles can be placed abreast in a final detector design. Read-out electronics and power supply can be directly attached to the SiPMs and also mounted on the top of the device. One reasonable arrangement is to place four SiPMs at $(x_{\mathrm{SiPM}}, z_{\mathrm{SiPM}}) = \left(\pm\frac{1}{3}\cdot w_{\mathrm{scinti}}, \pm\frac{1}{3}\cdot l_{\mathrm{scinti}}\right)$ as shown in fig. 8.7.

8.2.3 WLS Fibre

There are basically two different types of fibres that are regarded here: fibres with quadratic and with round cross sections. Both kinds of fibres are multi-cladding fibres with one inner and one outer cladding. For the quadratic/round fibre the inner cladding has a width of 4 %/3 % and the outer cladding 2 %/1 % of the fibre width/diameter [SG05c].
To obtain a most realistic situation, the fibre is embedded into a groove that is filled with optical

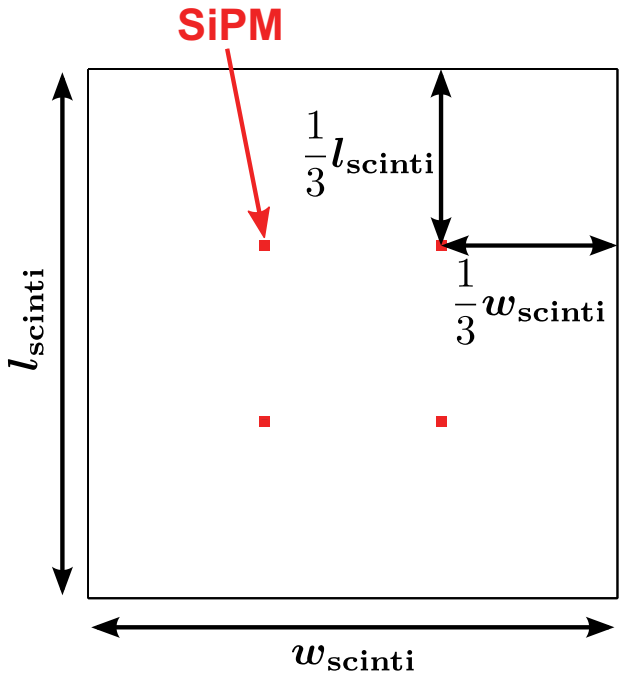

Figure 8.7: Example of the positioning of four SiPMs on a quadratic scintillator with a footprint of 100×100 mm^2 and arbitrary height.

cement. The fibre has a width/diameter of 1 mm and the groove has a width of 1.1 mm. The fibre is centred inside the groove. So on every side there are $l_{\text{cement}} = 50$ µm cement between fibre and scintillator and there is also cement on the top of the fibre so that the groove is always completely filled. This setup is shown in fig. 8.8.

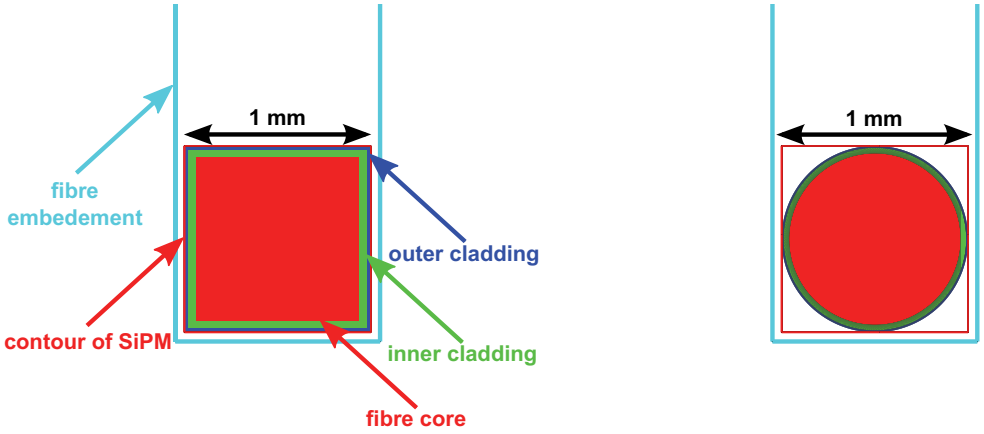

(a) Cross section of the quadratic fibre in embedment. Cleary visible the different fibre layers.

(b) Cross section of the round fibre in embedment.

Figure 8.8: Different fibre cross sections in embedment. The embedment groove is 'milled' directly into the scintillator. For comprehension the contour of an SiPM, mounted directly on the fibre's end, is shown.

Fibre Setups

To find the optimal light yield, the fibres (quadratic and round) will be positioned at different places within the scintillator. Additionally the effectivity of bent fibres will be analysed. These setups are shown in fig. 8.9. To be able to describe the fibre position with respect to the scintillator

size, it will be always given in relative coordinates. For the straight fibre the coordinate vector $\boldsymbol{x}$

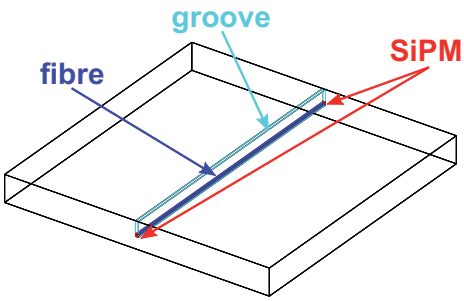

(a) 'Default' position of the fibre in the scintillator: $x_{\text{rel}} = 0$, $y_{\text{rel}} = 0$. This is called the *middle position*.

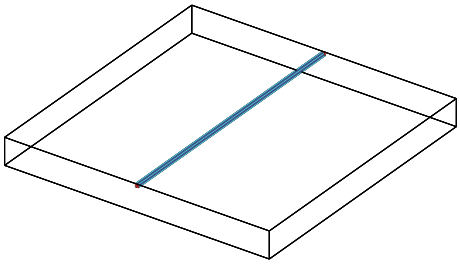

(b) The fibre in *top position*, $x_{\text{rel}} = 0$, $y_{\text{rel}} = 1$.

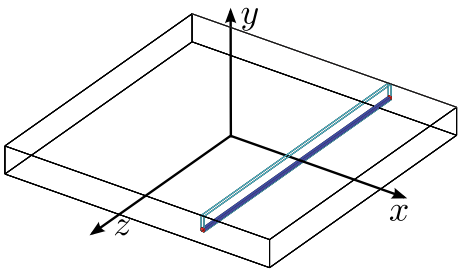

(c) The fibre shown exemplarily in an intermediate position, $x_{\text{rel}} = 0.5$, $y_{\text{rel}} = 0$. The origin of the coordinate system lies in the centre of the scintillator.

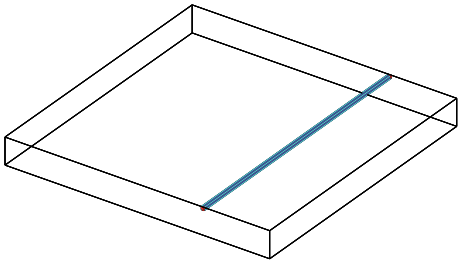

(d) The fibre shown in another intermediate position, $x_{\text{rel}} = 0.5$, $y_{\text{rel}} = 1$.

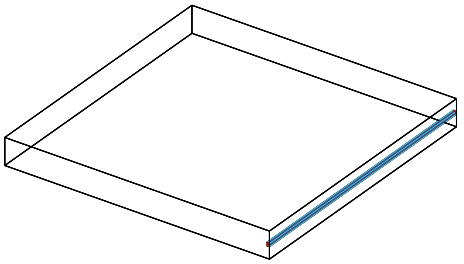

(e) The fibre in one most outer position ($x_{\text{rel}} = 1$, $y_{\text{rel}} = 0$). The groove is milled from the side rather than from the top. This setup is called *edge position*.

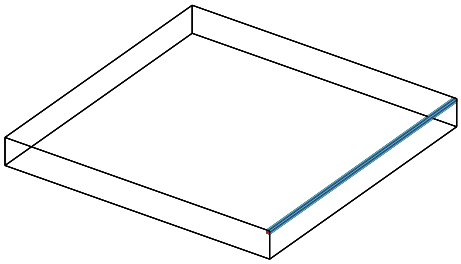

(f) The fibre in one of the 'corners': $x_{\text{rel}} = 1$, $y_{\text{rel}} = 1$.

Figure 8.9: Illustration of the coordinate system and the fibre positioning. The cyan-coloured volume always denotes the embedment of the WLS fibre (typically filled with optical cement or air); z_{rel} is always zero. Shown is an example of a scintillator with $100 \times 10 \times 100\,\text{mm}^3$ and a quadratic fibre.

points to the middle of the fibre volume and considers the different components to compute the right position:

$$\boldsymbol{x} = \begin{pmatrix} x \\ y \\ z \end{pmatrix} = \begin{pmatrix} x_{\text{rel}} \cdot \frac{1}{2}\,(w_{\text{scinti}} - w_{\text{fibre}} - l_{\text{cement}}) \\ y_{\text{rel}} \cdot \frac{1}{2}\,(h_{\text{scinti}} - h_{\text{fibre}} - l_{\text{cement}}) \\ z_{\text{rel}} \cdot 0 \end{pmatrix} = \boldsymbol{x}_{\text{rel}} \cdot \frac{1}{2} \begin{pmatrix} w_{\text{scinti}} - w_{\text{fibre}} - l_{\text{cement}} \\ h_{\text{scinti}} - h_{\text{fibre}} - l_{\text{cement}} \\ 0 \end{pmatrix}. \quad (8.4)$$

Here w_{scinti} and h_{scinti} are the width and height of the scintillator, respectively. w_{fibre} and h_{fibre} are the width and height of the fibre, respectively, and in case of a round fibre both become the fibre diameter. The orientation in this setup is such that the fibre is always parallel to the z-axis. All variations in the position of the fibre are handled with help of the relative position vector $\boldsymbol{x}_{\text{rel}}$. The z-position is always zero what means that the fibre is always positioned in the middle of the scintillator and extends by the same ratio in both directions of the scintillator's length and will typically have the same length as the scintillator. The range of x_{rel} and y_{rel} is $[-1, +1]$ where $|x_{\text{rel}}| = 1$ (see fig. 8.9e, 8.9f) and $|y_{\text{rel}}| = 1$ (see fig. 8.9b, 8.9d, 8.9f) is equivalent to the fibre being positioned adjacent to the left(right) and upper(lower) scintillator surface, respectively. $x_{\text{rel}} = 0$ (see fig. 8.9a, 8.9b) and $y_{\text{rel}} = 0$ (see fig. 8.9a, 8.9c, 8.9e) stand for the fibre placed in the middle of the scintillator.

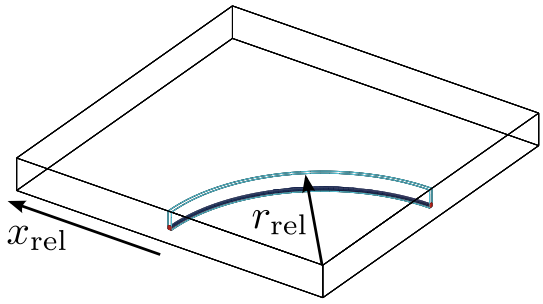

(a) Bent fibre in middle position at $r_{\text{rel}} = 0.5$. After conversion: $x_{\text{rel}} = 0.5$; $y_{\text{rel}} = 0$

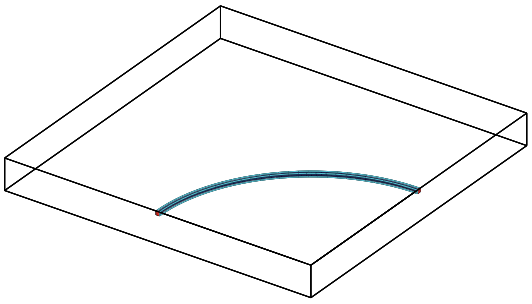

(b) Bent fibre in top position. $r_{\text{rel}} = 0.5$, $x_{\text{rel}} = 0.5$, $y_{\text{rel}} = 1$.

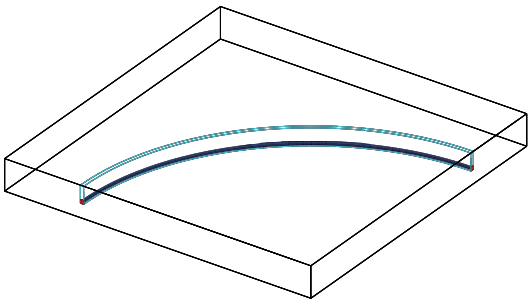

(c) Bent fibre in middle position. $r_{\text{rel}} = 0.75$, $x_{\text{rel}} = 0.75$, $y_{\text{rel}} = 0$.

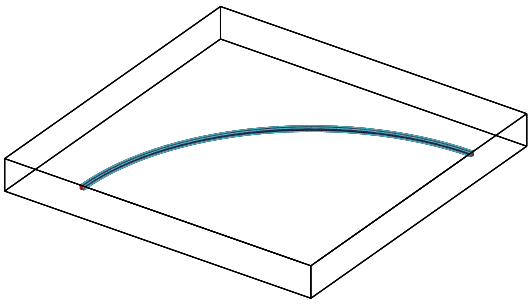

(d) Bent fibre in top position. $r_{\text{rel}} = 0.75$, $x_{\text{rel}} = 0.75$, $y_{\text{rel}} = 1$.

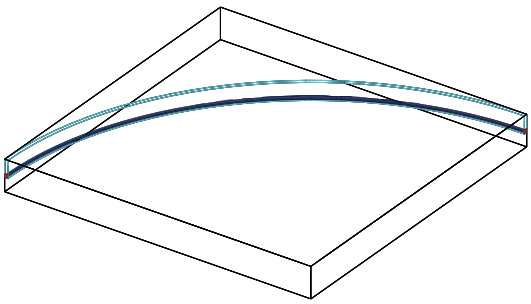

(e) Bent fibre in middle position. $r_{\text{rel}} = 1$, $x_{\text{rel}} = 1$, $y_{\text{rel}} = 0$.

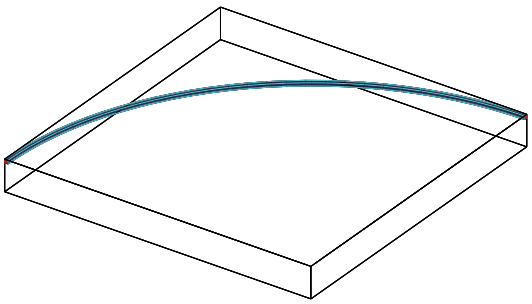

(f) Bent fibre in top position. $r_{\text{rel}} = 1$, $x_{\text{rel}} = 1$, $y_{\text{rel}} = 1$.

Figure 8.10: Different examples of a bent fibre in a groove. Here for a $100 \times 10 \times 100\ \text{mm}^3$ scintillator and a round fibre cross section.

When looking at bent fibres, the more relevant variable is the bending radius in the middle of the fibre r_{middle}. It is calculated depending on the relative bending radius r_{rel}:

$$r_{\text{middle}} = r_{\text{rel}} \cdot (w_{\text{scinti}} - w_{\text{fibre}}/2 - l_{\text{cement}}/2) + \frac{1}{2} \cdot (w_{\text{fibre}} + l_{\text{cement}}) \tag{8.5}$$

The arc taken by the semicircle is always 90°. The origin (x- and z-coordinate) of this semicircle is fixed and lies in one of the scintillator corners. The y-coordinate is determined in the same way as in eq. (8.4).
r_{rel} lies in $[0, 1]$ where $r_{\text{middle}}(0) = \frac{1}{2}\ (w_{\text{fibre}} + l_{\text{cement}}) > 0$ is the smallest possible bending radius. To be able to compare the results of different fibres and positions, the relative bending radius can be converted into a relative x-coordinate. This can be done by:

$$x_{\text{rel}} \mathrel{\widehat{=}} x_{\text{rel}}^{\text{bent}} = 2 \cdot \left(r_{\text{rel}} - \frac{1}{2} \right) \tag{8.6}$$

Different bent fibre setups are shown exemplarily in fig. 8.10.
As mentioned above the SiPMs have to be coupled to the fibre. To simulate a most realistic situation, a small gap between fibre and SiPM is simulated. The gap can be filled with an appropriate material, i. e. air or optical cement in this case. An example is shown in fig. 8.11.

8.2.4 External Reflector

The wrappings provided by the implemented UNIFIED model (see also sec. 6.7) are only able to handle diffuse reflectors. To investigate the behaviour of a specular reflector, there will be an additional volume modelled to represent the reflecting foil with variable reflectivity. This foil will always be made of aluminium with a thickness of 1 mm and a distance to the scintillator of 100 µm. The material of the foil is only relevant to the energy loss of the traversing charged particle (i. e. the muon) and has no influence on the propagation of the photons. The visualisation of the setup is shown in fig. 8.12.

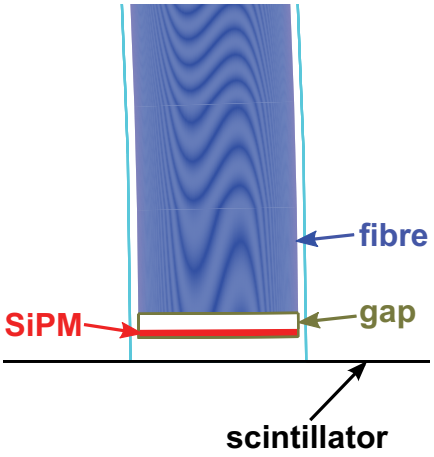

Figure 8.11: Example of an SiPM coupled to a bent fibre. The gap is variable in size and will be typically filled with optical cement or air.

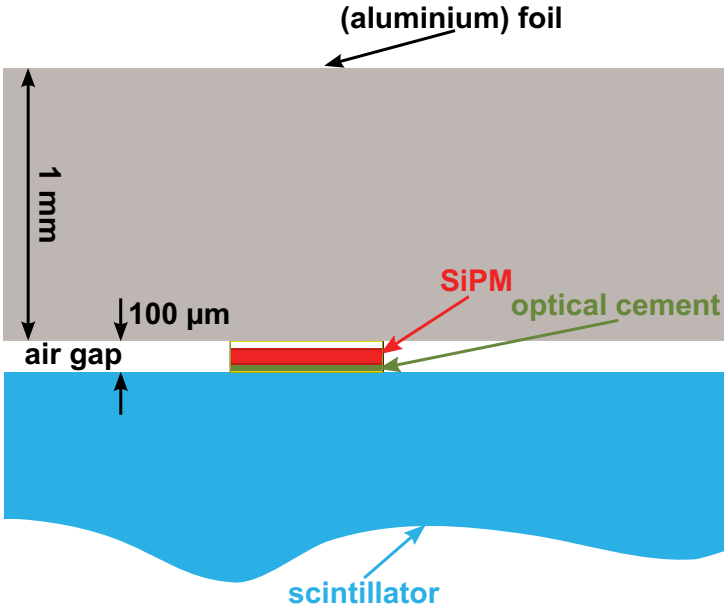

Figure 8.12: Visualisation of the scintillator wrapped by an aluminium foil.

Chapter 9

Results

For the different setups, described in detail in sec. 8, the photon yield under different parameter settings has been studied.
Unless explicitly denoted, in the following sections, there will be positively and negatively charged muons with a momentum of 2 GeV passing the scintillator. These muons simulate cosmic muons and will pass the scintillator perpendicularly and uniformly distributed over the whole scintillator area. Fig. 9.1 shows several muons passing the scintillator at random positions. Red colour denotes muons with negative charge and blue colour those with positive charge.

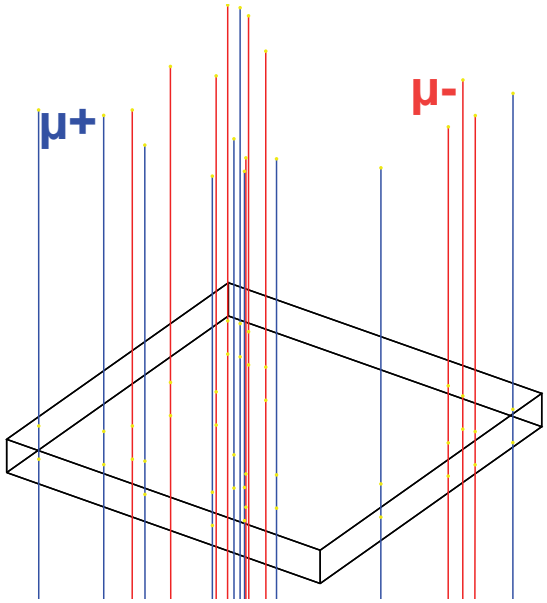

Figure 9.1: 20 muons passing a scintillator at random positions. Blue lines denote positively charged muons, red lines stand for negatively charged muons.

9.1 First Overview

To clarify the quantities of interest, some initial considerations shall be presented.

9.1.1 Energy Loss

The energy loss of incoming muons should follow a Landau distribution (as described in sec. 5.2) especially for a material like a piece of organic scintillator with a thickness in the order of a few millimetres and a muon with a momentum in the order of GeV (minimum ionising particle). The simulation meets these demands with high accuracy as is shown in sec. B.1.

9.1.2 Optical Photons

There are several constraints on the creation of optical photons within the scintillator to reproduce realistic conditions. These are described in the following paragraphs.

Number of Photons

Highly correlated to the energy loss is the number of created photons inside the scintillator. One has to distinguish between the photons created by the 'direct' energy deposit of the traversing muon and the 'indirect' energy deposit caused by secondary particles (e. g. δ-electrons or bremsstrahlung photons) inside the scintillator. While the total number of photons created is proportional to the energy deposit of the muon (fig. 9.2a), the direct number of photons per energy loss follows a Poissonian distribution with mean at 8000/MeV and is approximately Gaussian distributed for this mean value, as can be seen in fig. 9.2b for different scintillator thicknesses.

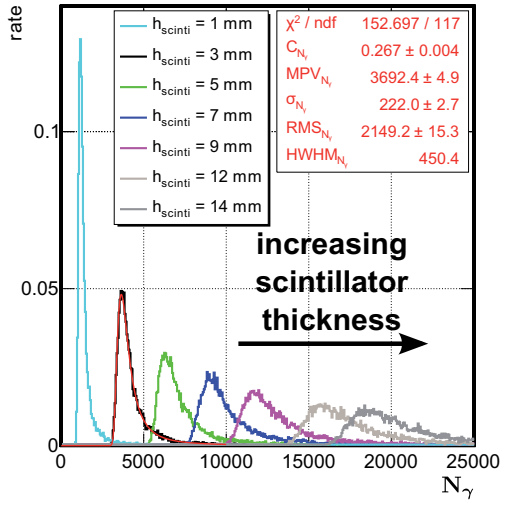

(a) Distributions of the total number of photons produced by a muon traversing a scintillator with different thicknesses. The red line shows a Landau fit to one of the distributions.

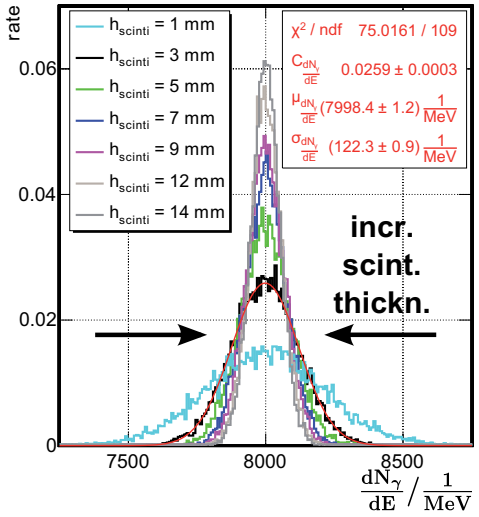

(b) Distributions of the number of photons per energy loss of traversing muon in a scintillator with different thicknesses. The red line shows a Gaussian fit to one of the distributions.

Figure 9.2: Total photon number, and number of photons per energy loss of the muon.

The evaluation of Landau distributed quantities turns out to be complicated because all moments of the distribution diverge (see also sec. 5.2) and thus expectation value and variance cannot be defined. In addition, the more interesting parameter of a Landau distribution is the MPV[55] rather than the mean value. Anyhow, a program package to handle Landau distributed variables has been developed as described in [KS83]. This method is designed to truncate the integration range, thus allowing to determine parameters that are used to find an approximate mean and variance of a Landau distributed quantity by a χ^2-fit. The truncation and with it the fitting parameters, are dependent on the analysed data set. It turns out that the fitting routine used in the analysis framework `ROOT` is very capable of finding the MPV. The other fitting parameter provided by this routine (confusingly enough called σ) is not the variance but the stretching parameter of the original Landau distribution (called a_x in [KS83]). This parameter does not give an obvious description of the distribution as the variance would. So additionally the RMS ($\sum x_i^2 - \mu^2$, μ = mean value) and a simply determined HWHM[56] value are provided (see also fig. 9.2a). The extraction of the HWHM happens by finding the two histogram entries on each

[55] **M**ost **P**robable **V**alue
[56] **H**alf **W**idth at **H**alf **M**aximum

side of the peak that are next to the half maximum and to interpolate linearly between them. From this interpolation the two values on the abscissa with height = half height are determined. The half of the difference of these two 'x-values' is used as HWHM.

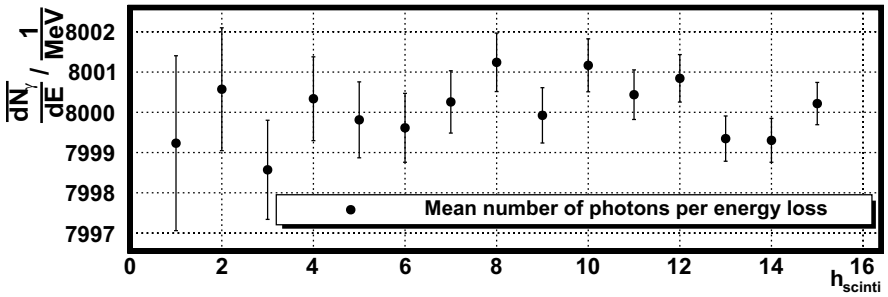

(a) Mean number of photons per energy loss of a muon versus increasing scintillator thickness.

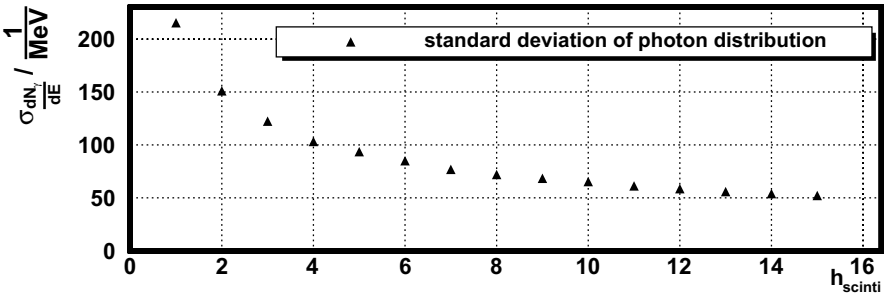

(b) The relative width of the distributions for different scintillator thicknesses. The decrease of the width with increasing thickness can be explained with the increase of the total energy loss and with it the total number of photons created in a thicker scintillator.

Figure 9.3: Number of photons per energy loss in scintillator.

Fig. 9.3 shows the mean number of photons per energy loss and the width of the fitted distribution for different scintillator thicknesses. They all meet the expected distributions for this kind of material. With increasing scintillator thickness the Gaussian distributions become narrower because of the higher total number of photons produced in an event with larger thickness and thus more statistics.

Starting Conditions of the Photons

To follow realistic conditions, the photons created in the scintillating material must fulfil some constraints concerning their creation position and direction. This means, they have to be created uniformly along the track of the charged particle (y-axis) and their initial directions must be distributed uniformly within the solid angle. The latter implies, they are uniformly distributed in azimuth angle φ and uniformly distributed in the cosine of the polar angle ϑ. All distributions are as expected and are shown in the appendix (fig. B.6).

9.2 Direct readout

The first setup considered here is the one with direct readout where the SiPMs are mounted directly onto the scintillator surface, as has been shown in fig. 8.7 (see also sec. 8.2.2). An example event for this kind of setup is shown in fig. 9.4. Each muon creates about 10^4 photons that propagate inside the scintillator. One of these photons has been picked to illustrate a typical propagation behaviour in a perfectly polished piece of scintillator. The photon is reflected many times until it hits one of the SiPMs and is absorbed.

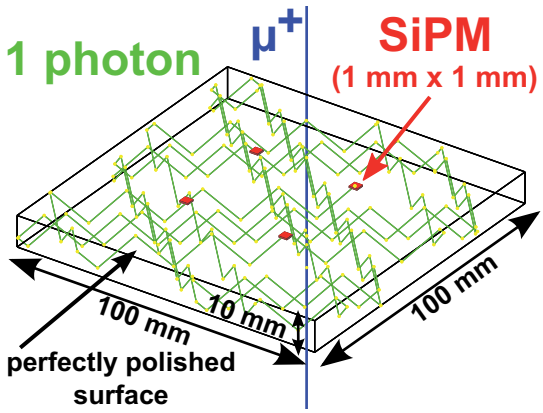

Figure 9.4: Muon traversing a piece of scintillator with *one* example photon propagating inside the scintillator and hitting one of the SiPMs. (SiPMs not to scale.)

9.2.1 Photons on the Scintillator Surface

When considering a direct readout of the scintillator, the first interesting property of the setup is the expected number of photons per SiPM area. To get an overview of this number, the photons 'touching' the scintillator surface, i. e. photons getting reflected or transmitted on the surface, are counted. Fig. 9.5 shows the distribution for a perfectly polished scintillator surface. The

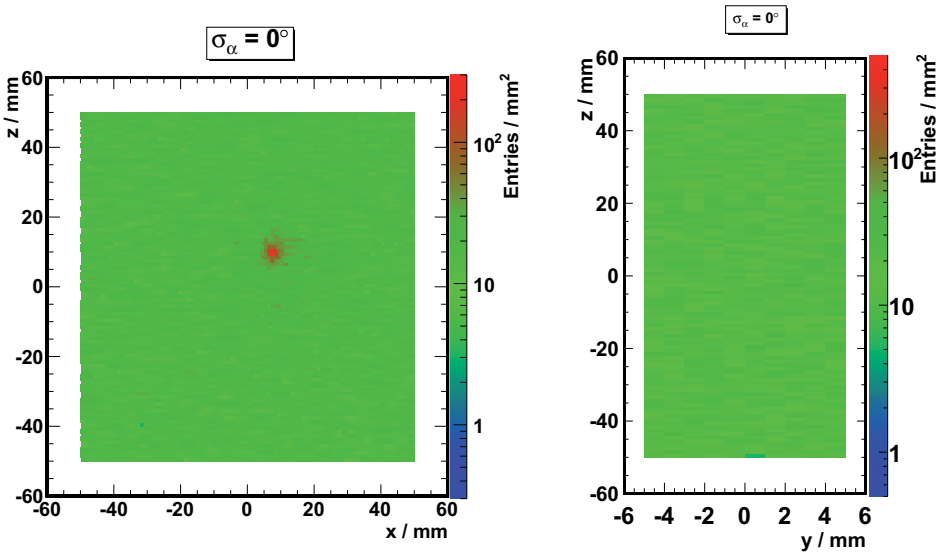

(a) Photon distribution on the $x-z$-, i. e. 'upper', plane of the scintillator. Clearly visible is the muon incoming point.

(b) The same event as in (a) but showing the $y-z$-plane. For clarity the same scaling as in (a) has been chosen.

Figure 9.5: Photon distributions on the different scintillator planes for a perfectly polished scintillator with $100 \times 10 \times 100\ \text{mm}^3$. The binning has been chosen to fit a "default" SiPM area, i. e. $1 \times 1\ \text{mm}^2$. The distribution on the $x-y$-plane looks very similar to that on the $y-z$-plane.

'upper' and one side plane are shown, the distributions for the other planes look very similar. On the upper plane the muon traversing point is clearly visible. Since photons are created uniformly along the muon track in the scintillator, many of them have an initial momentum pointing parallel to the muon track and thus the track's footprint on the surface is clearly visible.
To study the influence of the scintillator's surface roughness on the photon propagation, the parameter σ_α is varied over a wide range. Some results for a scintillator with $100 \times 10 \times 100\ \text{mm}^3$

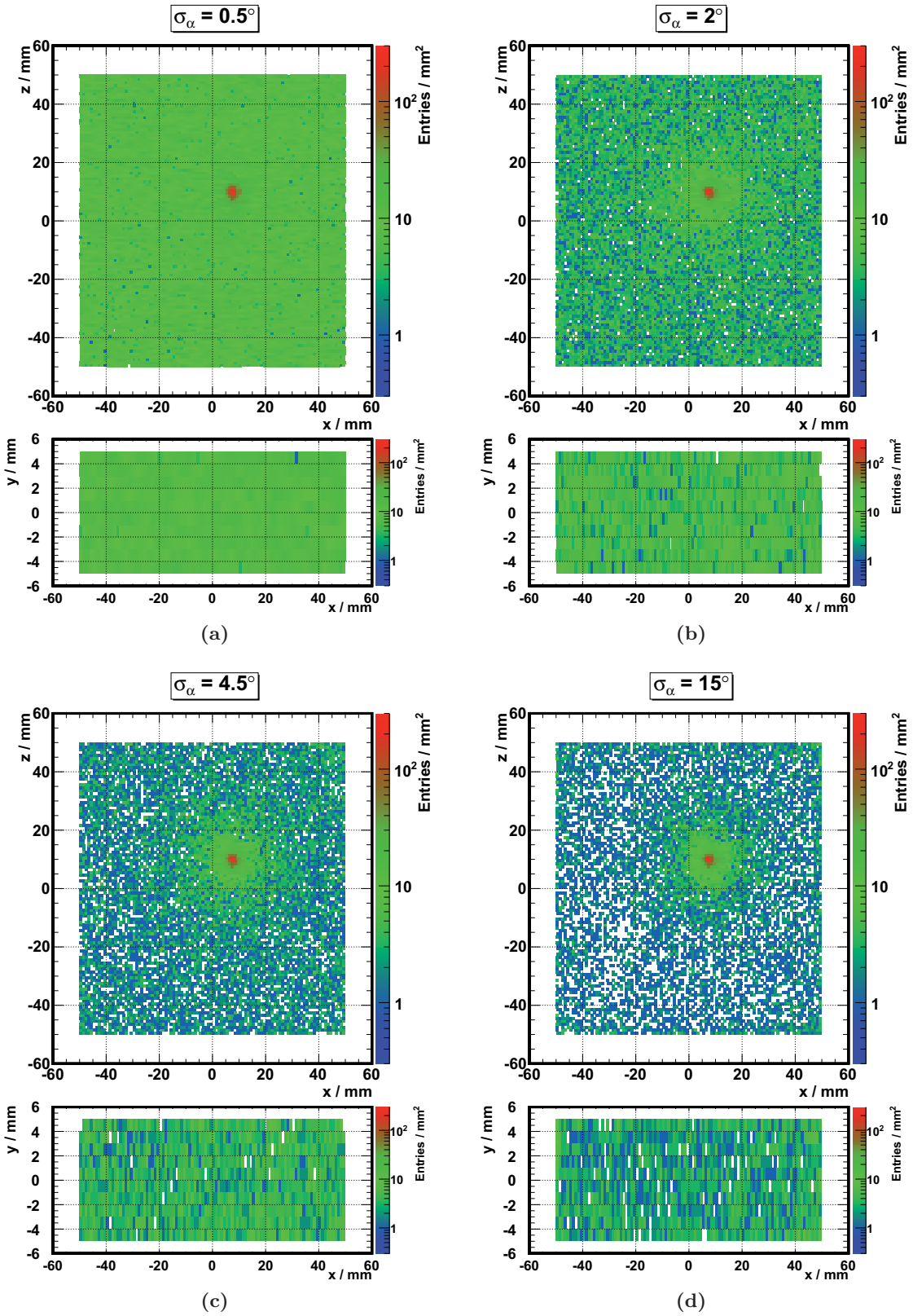

Figure 9.6: Photons at scintillator surface for different surface roughness parameters for a muon with constant incoming point. The number of contacts decreases visibly with increasing roughness. The same colour coding applies in all figures.

are shown in fig. 9.6. It is clear that an increase in roughness has a major impact on the number of surface contacts. This can be explained by the fact that photons do not get 'trapped' in special modes inside the volume, allowing them to get reflected many times before getting absorbed in the scintillator (this is also visible in fig. 9.4). Besides this the probability to leave the scintillator becomes much higher at every reflection point with increasing roughness.

9.2.2 Photons at SiPM

The number of photons arriving at one particular SiPM should be rather independent of its distance to a traversing muon to ensure the homogeneity of the detector. The correlation plots

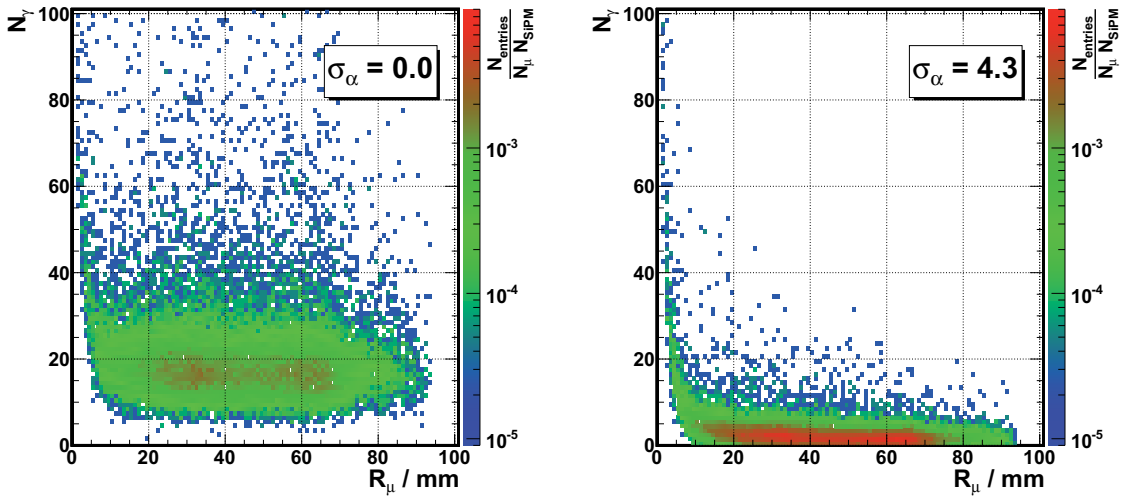

(a) Number of photons at SiPM for a scintillator with $\sigma_\alpha = 0°$.

(b) Number of photons at SiPM for a scintillator with $\sigma_\alpha = 4.3°$.

Figure 9.7: Number of photons arriving at SiPM vs. distance of the muon to the SiPM (summarised for all SiPMs).

in fig. 9.7 show that the number of photons at an SiPM is basically independent of the muon distance. One exception is made by muons traversing the scintillator very close to one SiPM. As suggested by the distributions in fig. 9.6 the number of photons increases for these muons which is even more obvious for a scintillator with higher roughness, as shown in fig. 9.7b.
Since the number of muons traversing the scintillator at the SiPM position is very small (for four SiPMs with 1×1 mm^2 and a scintillator with 100×100 mm^2 only 0.4 ‰) these events have only a very small influence on the distributions.
The number of photons arriving at one SiPM does not exactly follow a Landau distribution as can be seen in fig. 9.8a. Neither does the mean number of photons averaged over the number of SiPMs (see fig. 9.8b). This can be explained by the fact, that it is possible that one SiPM is not hit at all in an event. The geometry of the scintillator is also convoluted into these distributions in a non-trivial way.
To be able to quantify these distributions, the peak value is extracted and the half width at half maximum (HWHM) (as described in sec. 9.1.1) is used. The determination of the peak value, i. e. the MPV, is done by fitting a Landau distribution in a gradually decreasing fitting range that is located symmetrically around the maximum value of the distribution. The fit is considered as successful when $\frac{\chi^2}{\mathrm{ndf}} < 3$. The MPV of this fit is regarded as the peak value. One example of the result of this method is shown in fig. 9.9 along with the determined peak value and the HWHM of the distribution.
From the distributions shown in fig. 9.6 it is already clear that the typical number of photons

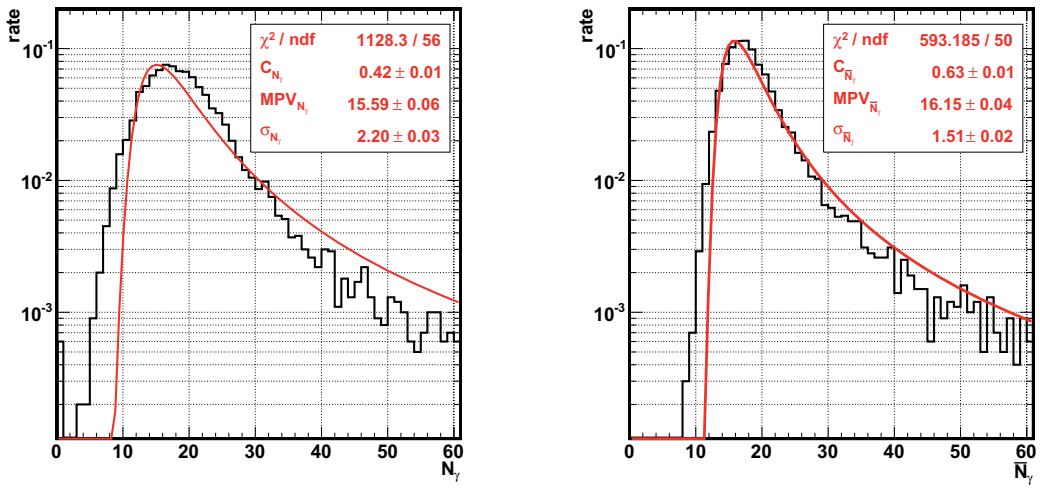

(a) Number of photons arriving at SiPM. The Landau fit is poor.

(b) Number of photons arriving at SiPM averaged over four SiPMs. The Landau fit is better but does not describe the distribution very well.

Figure 9.8: Number of photons arriving at SiPM. Examples for a $100 \times 10 \times 100$ mm^3 scintillator and an SiPM with a footprint of 1×1 mm^2.

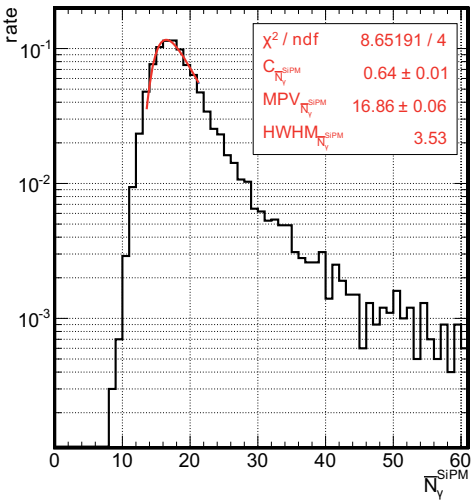

Figure 9.9: Fit to find the peak of the distribution (mean number of photons at SiPM). Same setup as in 9.8b.

per square millimetre is limited to the order of 20. This number stands for all photons that had contact with the surface. Most of them did not leave the scintillator at this point but were reflected back into it.

When considering realistic conditions there will always be a small air gap in between scintillator surface and SiPM. Thus there is always the possibility for the photon to get reflected back due to total internal reflection if the SiPM is not optically coupled to the surface. To illustrate this behaviour, fig. 9.10 shows the comparison between the number of photons arriving at the SiPMs with only an air gap between the scintillator and the SiPM, and for SiPMs coupled with optical cement to the scintillator. As the number of photons at SiPM is very small in the case of no optical coupling, and the MPV is always zero in this case, the mean value of these distributions is shown in the plot instead. The simulations have been performed for two different gap thicknesses: 50 µm and 100 µm.

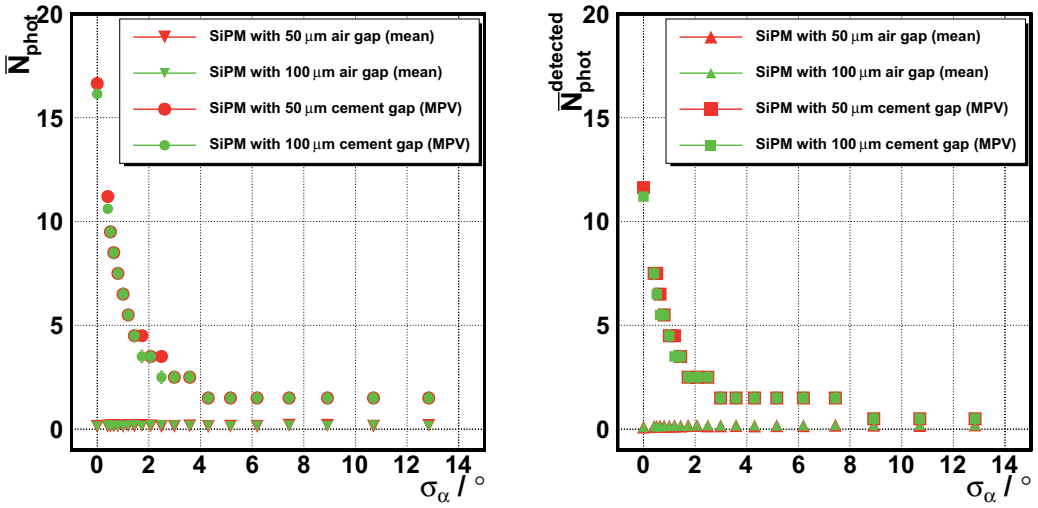

(a) Photons hitting the SiPM.

(b) Photons detected in Pixel.

Figure 9.10: Photon numbers for setups with an air gap between the scintillator and the SiPM and those with optical cement. The thickness of the gap has only a minor impact on the photon numbers.

This demonstrates, that the optical coupling of the SiPMs is very important and so the following simulations are always performed with a volume between the SiPMs and the scintillator surface that represents the optical cement (EJ-500).
When looking at photons arriving at the SiPM several aspects have to be considered. The first question is if the number of photons arriving at one SiPM is comparable to that at another one. It turns out that this number is the same within statistical fluctuations as shown exemplarily in fig. 9.11 for two different roughness parameters of the scintillator surface. The result justifies the usage of the mean values of photons in SiPM for the further analysis.

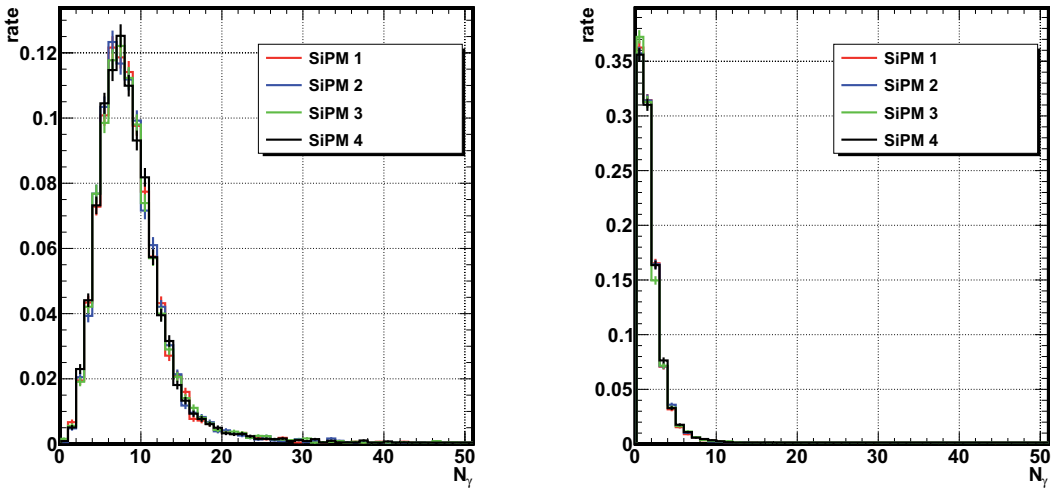

(a) Comparison between the number of photons arriving at four SiPMs in the same setup with $\sigma_\alpha = 0°$ (direct readout).

(b) Comparison between the number of photons arriving at four SiPMs in the same setup with $\sigma_\alpha = 8.9°$ (direct readout).

Figure 9.11: Comparison between four SiPMs in the same setup. The distributions are identical within statistical fluctuations. The SiPM positions are as shown in fig. 8.7.

Another issue is the detection efficiency of the SiPM. As mentioned in sec. 5.6.6 the detection

efficiency is a product of different efficiencies and probabilities. It is possible to simply extract the geometrical efficiency $\varepsilon_{\text{geom}}$ from the total efficiency by dividing by the value given by the manufacturer and to reduce the sensitive area of one pixel of the SiPM accordingly (as described in sec. 8.2.2). The remaining part of eq. 5.17 is the overall detection probability. So the number

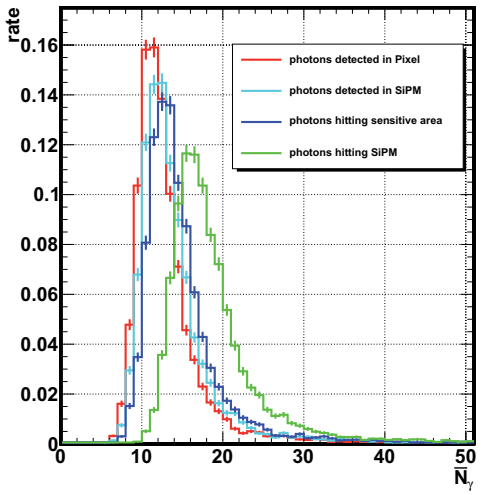

(a) Mean number of photons at SiPM for $\sigma_\alpha = 0°$ (direct readout).

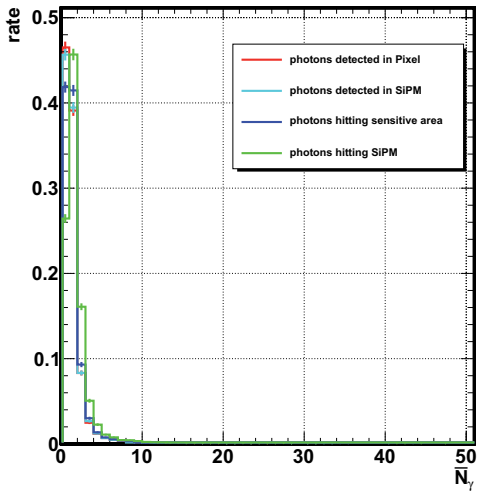

(b) Mean number of photons at SiPM for $\sigma_\alpha = 8.9°$ (direct readout).

Figure 9.12: Mean number of photons at SiPM for the different detection stages.

of photons at the SiPM can be split into those arriving at the SiPM, those hitting the sensitive area and those that really get detected. Example distributions are shown in fig. 9.12. The last part of the "detection path" is the fact that SiPMs work in Geiger mode and thus the output is independent of the number of photons that hit one pixel (as long as it is > 0). To consider this issue only the first detected photon per pixel is counted. In fig. 9.12 this number is denoted as the "photons detected in Pixel".

9.2.3 Reflections

With increasing roughness, i. e. larger value of σ_α, the number of contacts with the scintilla-

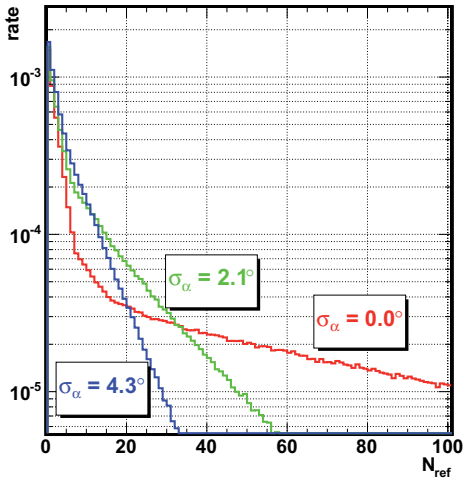

Figure 9.13: Example of the number of reflections per photon for three values of σ_α.

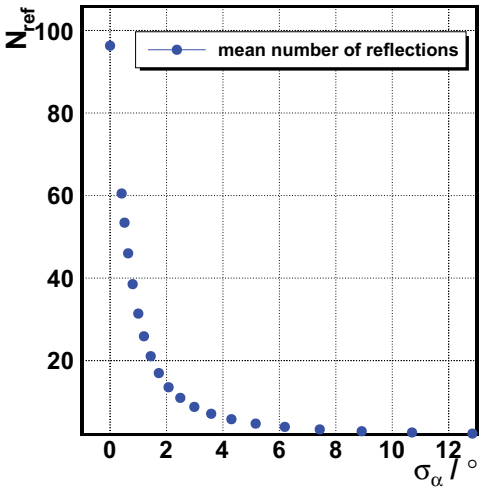

Figure 9.14: Mean number of reflections per photon before hitting SiPM.

tor surface decreases, and with it, especially the number of reflections, as shown in fig. 9.13 for different roughness parameters. The number of reflections is approximately exponentially distributed with a significant deviation close to zero. This means, it is very likely for a photon to be reflected only few times or even not at all before leaving the scintillator (or getting absorbed). The number of reflections decreases dramatically with increasing roughness of the scintillator. It becomes more and more difficult for the photons to be reflected back into the scintillator several times because the effective reflection angle is always different and does not allow the photon to be trapped inside the scintillator. This is clearly correlated to the number of reflections a photon experiences before hitting an SiPM as illustrated in fig. 9.14. The number of photons hitting the SiPM is also reduced as already shown in fig. 9.10.

9.2.4 External Reflectors

As described in sec. 8.2.4 in GEANT4 there are different ways to simulate a wrapping of the scintillator. In the scope of this thesis the following types of wrappings have been chosen:

- For comparison, the first setup uses no reflector at all.
- There are two setups using the 'intrinsic' reflectors of the UNIFIED model. Denoted as "G4 diffuse reflector" with and without air gap. These are always diffuse reflectors. In the former the reflection behaviour of an incoming photon at the air gap and afterwards at the wrapping is simulated in one step.
- Another possibility to simulate a diffuse reflector is to place an air filled volume between the scintillator and the reflector. It is possible to adjust the reflection properties of this wrapping. The first of two settings with this kind of reflector is a pure diffuse reflector ("diffuse reflector with air gap") and the second one is:
- a pure specular reflector ("specular reflector with air gap"). These are the extreme adjustments in the simulation model.

The simulations have been performed with two reflectivities that are typical for reflective foils, i. e. 80 % and 95 %. An additional simulation with a specular reflector at 98 % reflectivity has

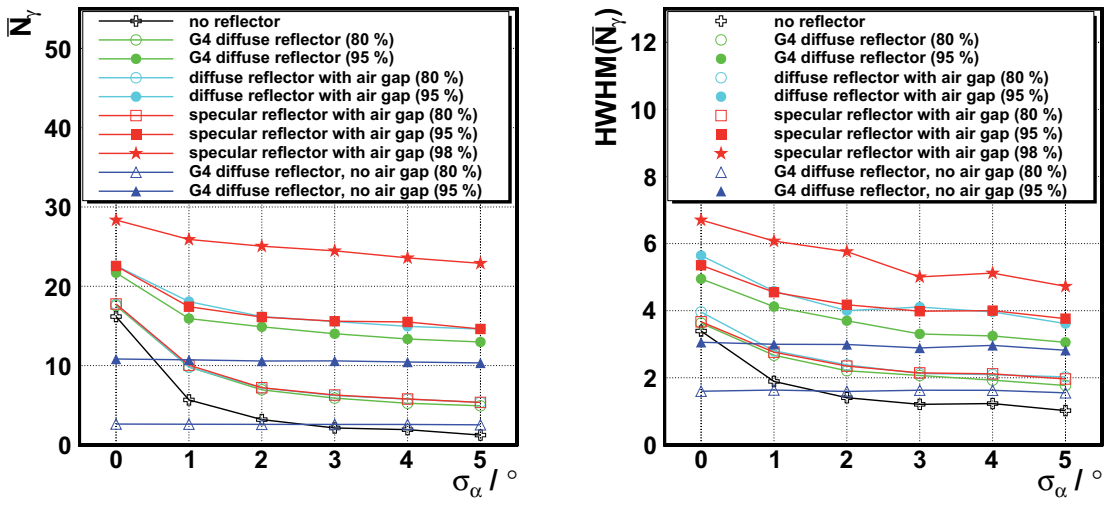

(a) MPV of the number of photons arriving at the SiPM.

(b) HWHM of the number of photons arriving at the SiPM.

Figure 9.15: Summary of the number of photons arriving at the SiPM and the width of the distributions for different types of reflectors.

also been performed. A summary of the results is shown in fig. 9.15.
It turns out that the reflector without air gap comparably gives the worst results. With low reflectivity (80 %) the yield is partially even worse than for a scintillator with no reflector. This shows the importance of the total reflection between the scintillator and the air gap.

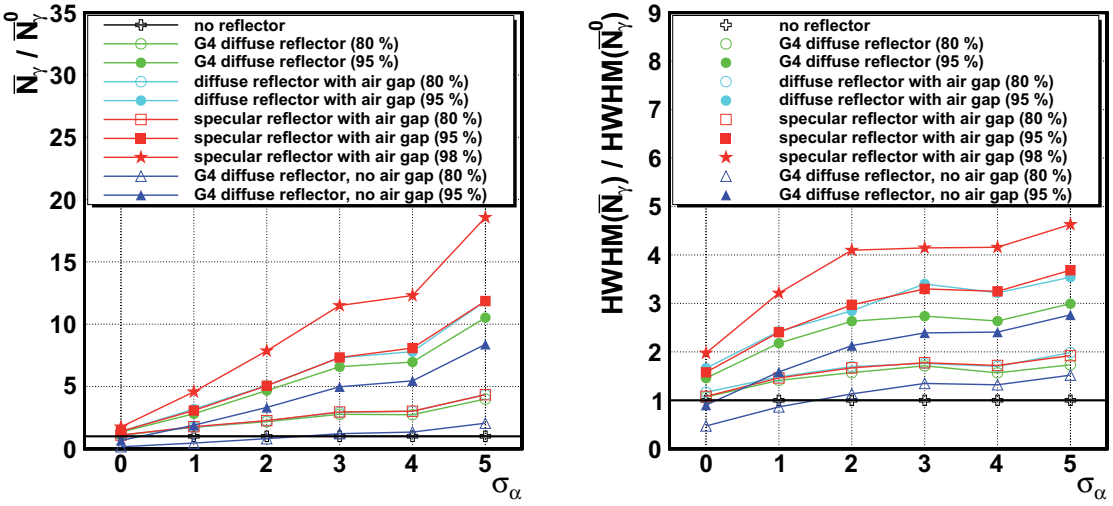

(a) MPV of the number of photons arriving at the SiPM normalised to the case with no reflector.

(b) HWHM of the number of photons arriving at the SiPM normalised to the case with no reflector.

Figure 9.16: Number of photons arriving at the SiPM and the width of the distributions for different types of reflectors normalised to the setup with no reflector. N_γ^0 denotes the number of photons in a setup with no reflector.

The results for diffuse and specular reflectors with the same reflectivity are very similar and it is clear that the GEANT4 modelling of an air gap leads to a slightly smaller amount of photons at the SiPMs. Reflectors with higher reflectivity make the distributions become broader because it is more probable that a higher number of photons arrive at the SiPM. As expected, the setup with the reflector with the highest reflectivity leads to a photon yield of about five to 20 times better than with no reflector, with only a small increase in width. These results normalised to the setup with no reflector are shown in fig. 9.16.
The figure shows clearly the increase in photon yield with basically every kind of reflector. Also the width increases but with a much smaller factor. The results have to be compared to the number of photons that is really detected in the SiPM. The summary plots are shown in fig. 9.17. Only photons detected in the pixel are shown here and only one photon per pixel can be detected per event. Also here it becomes clear that a wrapping with high reflectivity leads to photon yields several times bigger than without a reflector or one with smaller reflectivity. It also becomes clear that a good reflector can allow photons yields that are comparable with those for a highly polished scintillator ($\sigma_\alpha \to 0°$) and even higher.

9.2.5 Timing

Another important issue is the timing, i. e. the arrival time of photons at the SiPM and with it correlated the time resolution of the whole detector system. The first overview of the timing of the detector with direct readout is shown in fig. 9.18. The figures show clearly that the timing is basically independent of the muon distance to the SiPM. As shown above (fig. 9.7) the number of photons arriving at the SiPMs is basically independent of the distance of the muon traversing point, and so the shape of these distributions is basically given by the probability of a muon to pass the scintillator in a particular distance to the SiPMs. One exception is made by muons that traverse very close to the SiPMs ($R_\mu \lesssim 5$ mm). In these cases the number of photons arriving

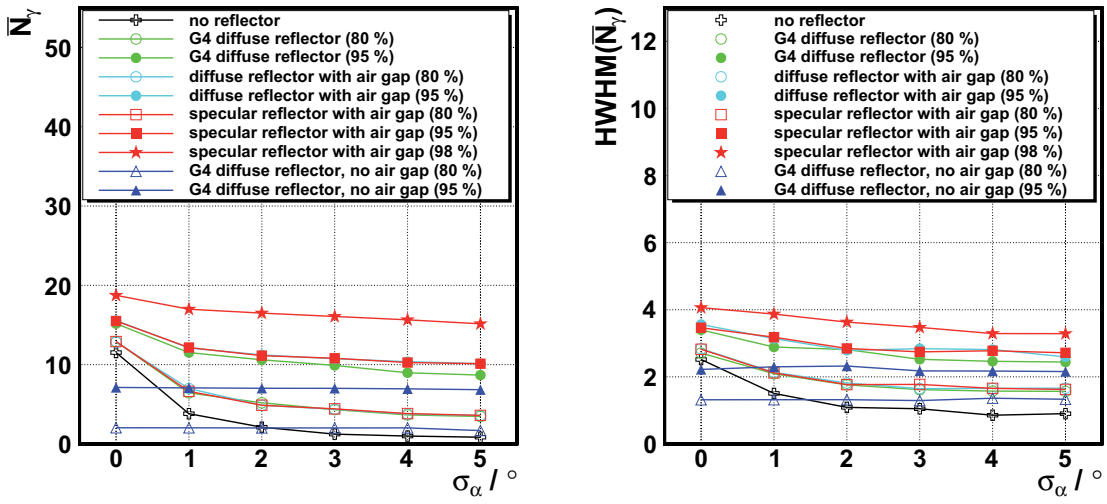

(a) MPV of the number of photons detected in a pixel.

(b) HWHM of the number of photons detected in a pixel.

Figure 9.17: Number of photons detected in a pixel and the width of the distributions for different types of reflectors.

at the SiPMs increases heavily which is the explanation of the accumulation of entries close to zero in these distributions. The distributions become narrower with increasing roughness. This means, it becomes more and more unlikely for the photons to arrive later at the SiPMs because less reflections are possible.

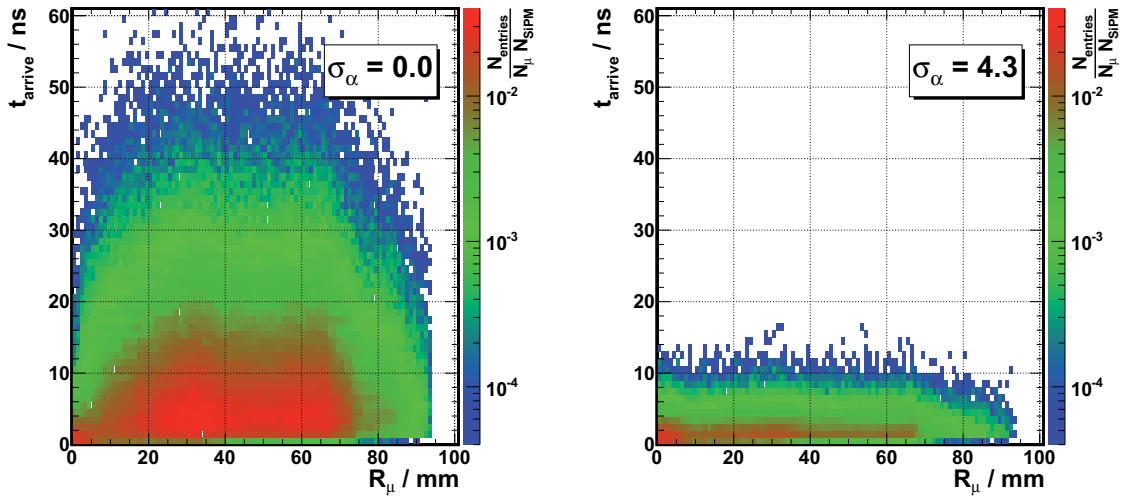

(a) Arrival time of photons for $\sigma_\alpha = 0°$.

(b) Arrival time of photons for $\sigma_\alpha = 4.3°$.

Figure 9.18: Arrival time of photons vs. muon distance to the SiPM for two different roughness parameters.

Fig. 9.19 shows that the distribution of arrival times of the photons at different SiPMs is basically identical. So again only the mean distribution is used to quantify the timing behaviour.
As mentioned in sec. 9.2.2 there are different detection stages of the photons. Most important is the moment when the photons hit the SiPM and when they are detected inside a particular pixel. Two examples are shown in fig. 9.20. It is clear that the shape of the distributions does not change at the different detection stages. The peak and the HWHM stay basically the same. From fig. 9.20 it is already clear that the peak value and the HWHM will change with increasing

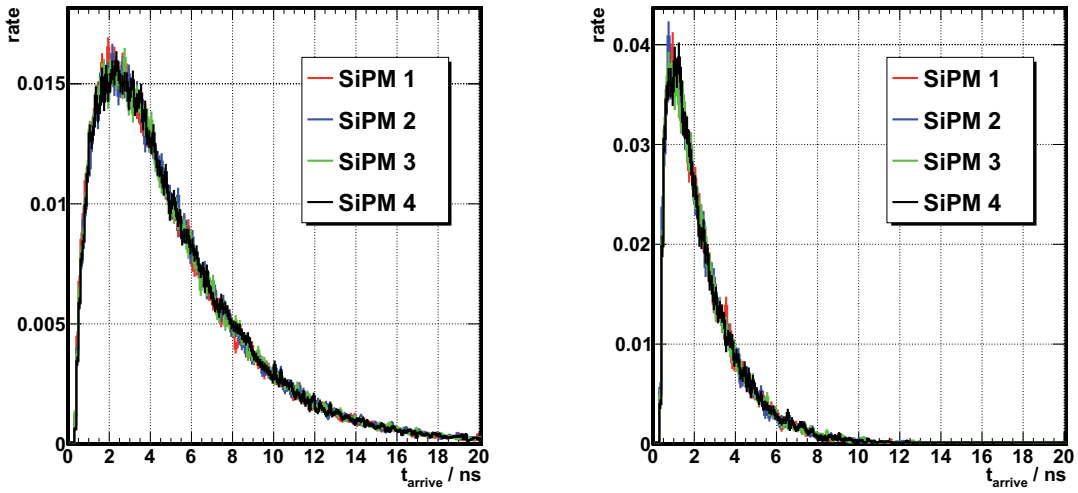

(a) Timing distributions of a perfectly polished scintillator ($\sigma_\alpha = 0°$).

(b) Timing distributions of a scintillator with $\sigma_\alpha = 8.9°$.

Figure 9.19: Timing distributions for four SiPMs in the same setup shown for two different surface roughness parameters.

roughness of the scintillator (for a setup without reflector). To be able to quantify the distributions a similar method as described in sec. 9.2.2 is used. A Gaussian fit with gradually decreasing fitting range around the maximum value of the distribution is performed until $\frac{\chi^2}{\text{ndf}} < 3$. In some

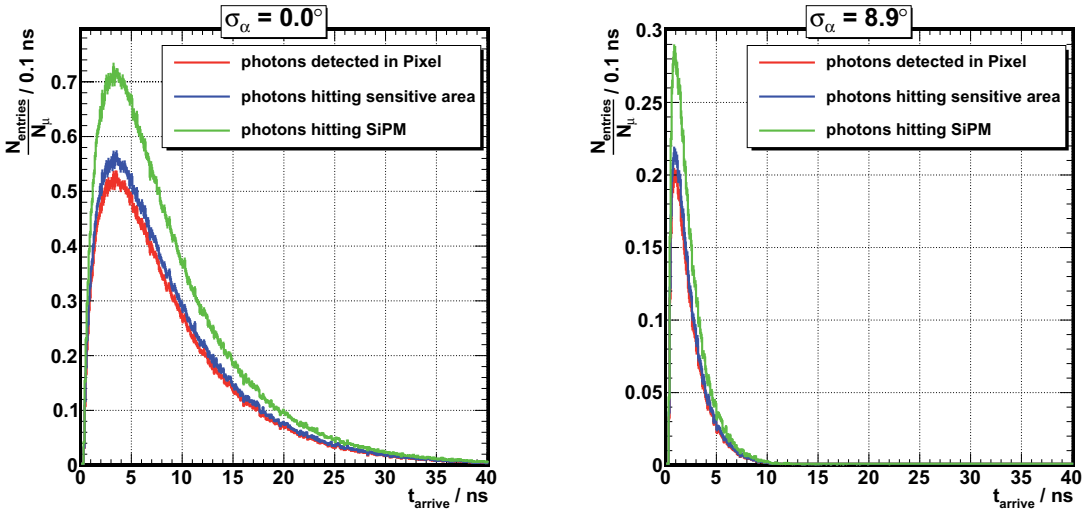

(a) Arrival time of the photons for different detection stages ($\sigma_\alpha = 0°$).

(b) Arrival time of the photons for different detection stages ($\sigma_\alpha = 8.9°$).

Figure 9.20: Distribution of the arrival time of photons in the SiPM for different detection stages exemplarily shown for two different scintillator roughness parameters and without reflector.

cases the fit fails with this method because there is not enough statistics or the photon number is too small. It turns out that this fitting method works fine as long as the mean value of the photon distribution is bigger than ≈ 12. If the mean is below this value simply the abscissa value of the bin with the biggest content is treated as the MPV. Additionally the HWHM is extracted from this distribution. One example of the result of this method is shown in fig. 9.21.
When applying different reflectors the interest lies also on the behaviour of the timing of the scintillator. The method described before is used to extract peak and HWHM value from the

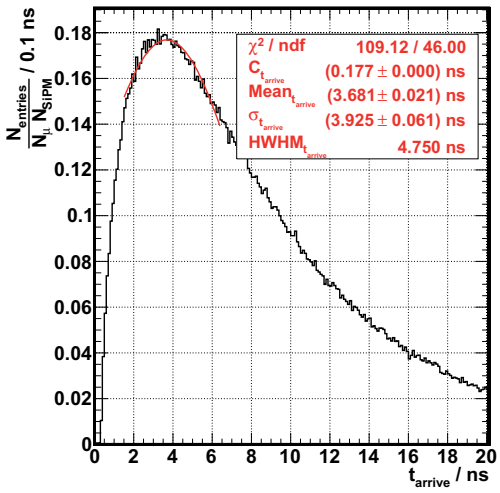

Figure 9.21: Example of the peak finding method described in the text.

distributions. The summary of the results against the scintillator roughness is shown is fig. 9.22 for different reflectors. Additionally the HWHM values are shown. It turns out that the timing properties of the setup are only weakly affected by the different reflector types. Peak value and HWHM are approximately constant and close to the values of a scintillator with no reflector and with small roughness ($\sigma_\alpha \leq 1°$) for wrappings with high reflectivity. Setups with lower reflectivity are more affected by the roughness.

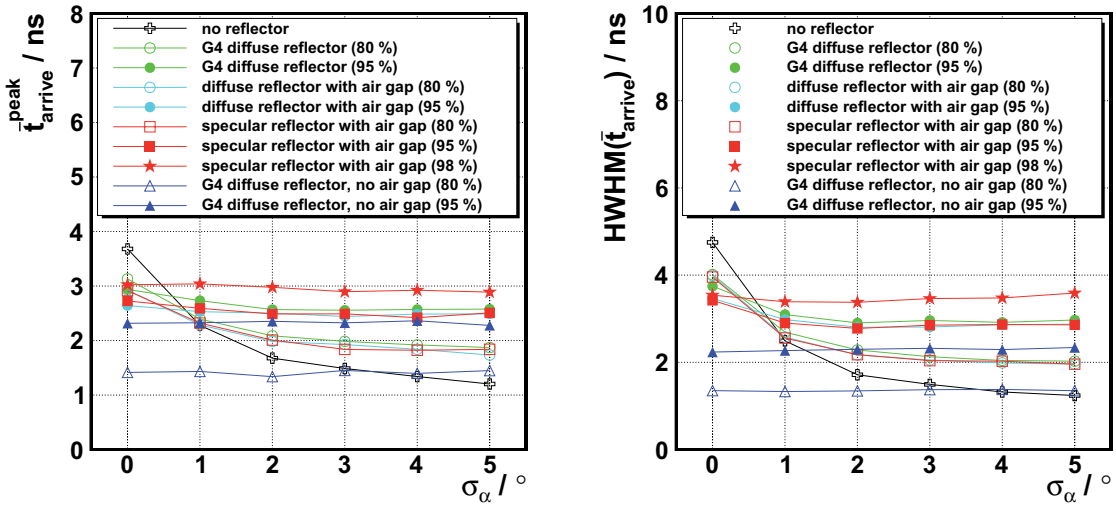

(a) Peak values of arriving time distribution of the photons.

(b) HWHM of arriving time distribution of the photons.

Figure 9.22: Peak and HWHM of photon distributions of arriving photons vs. scintillator roughness for different reflectors/reflectivities.

Other interesting quantities are the time of the first photon hit and the rise time of the distribution, i. e. the time difference between 10 % and 90 % of the maximum value of the distribution. These are shown in fig. 9.23. The arrival time of the first photons is constant for all setups and is at (0.35 ± 0.03) ns while the rise time varies slightly with increasing roughness and is typically between ≈ 1 ns and ≈ 1.5 ns.

Subsequently another issue of the photon timing is studied. Beside the rise time and the peak value of the photon arrival time the point in time when 90 % (or more) photons have been de-

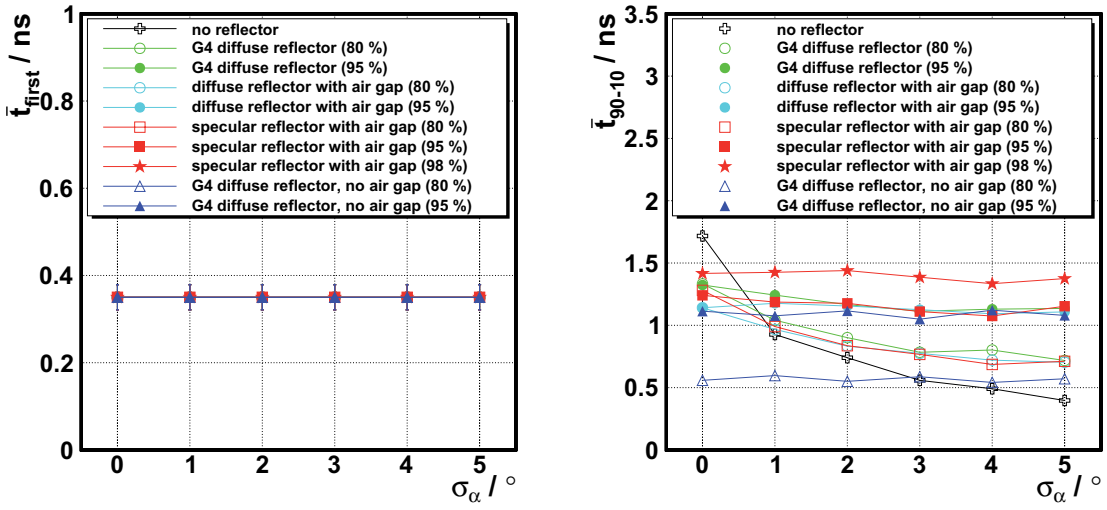

(a) Arrival time of the first photons at SiPM.

(b) Rise time ($t_{90\,\%} - t_{10\,\%}$) of the photon distribution.

Figure 9.23: Further timing properties of setups with different reflectors.

tected in the SiPM (i. e. the integrated number of photons) has been studied. This is shown for four favoured setups (fig. 9.24 and fig. 9.25) again with different values of σ_α. As it turned out that the type of the reflector (diffuse/specular) has only a minor influence on the behaviour of the setup, only the specular one has been chosen for this consideration.

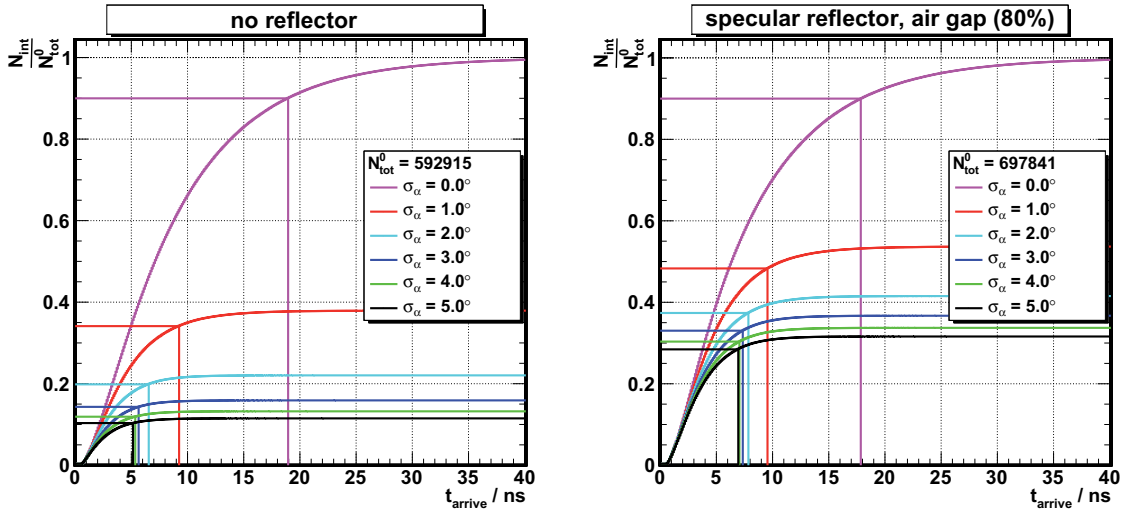

(a) Integrated number of photons vs. arrival time for a scintillator with no wrapping.

(b) Integrated number of photons vs. arrival time for a scintillator with a specular reflector with 80 % reflectivity.

Figure 9.24: Integrated number of photons normalised to the total number of photons arriving at SiPM for the setup with the smallest value of σ_α vs. arrival time for a scintillator with different wrappings.

The curves are normalised to the total number of photons arriving at the SiPM for the smallest shown value of σ_α (i. e. $\sigma_\alpha = 0°$) which is denoted by N^0_{int}.
The horizontal lines denote the height of the curve at 90 % of its maximum height. The vertical lines show the corresponding time values.
The figures show clearly that for different scintillator and reflector properties the 90 %-point

varies roughly between 5 ns and 20 ns. The spread becomes smaller with increasing reflectivity of the external reflector. Especially for a wrapping with 98 % reflectivity the 90 %-point lies within 1 ns for all considered $\sigma_\alpha > 0°$. This is one more point that suggests the usage of a reflector with high reflectivity.
When looking at SLHC conditions, there is one disadvantage that could appear in this approach. The higher the reflectivity, the longer the photons survive inside the scintillator, leading to long tails in the distributions, i. e. photons arriving very late at the SiPMs. This can cause the photons to hit the SiPM within the next bunch crossing period and thus obscuring a possible signal from the subsequent BX. This has to be considered in a final setup.

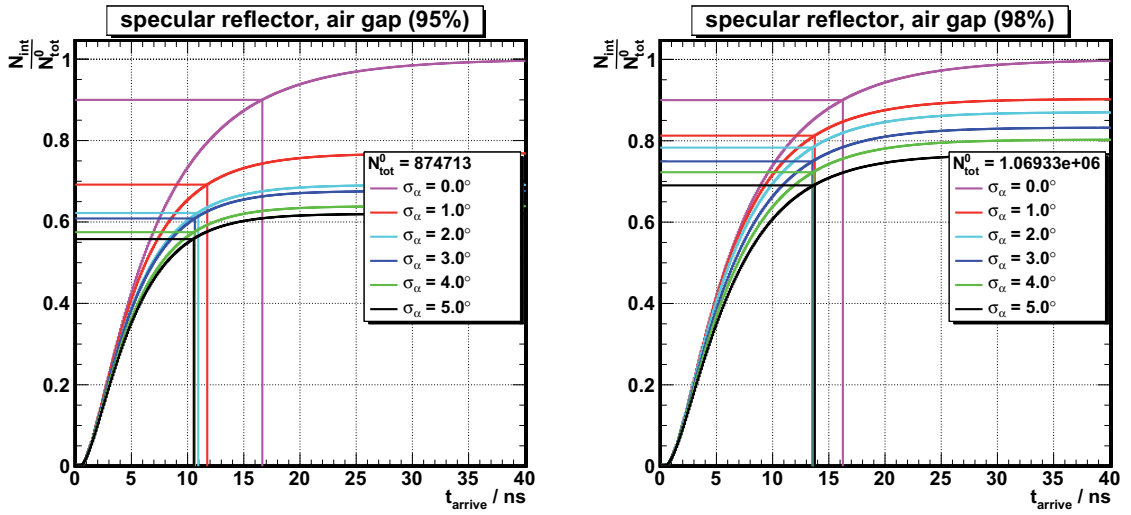

(a) Integrated number of photons vs. arrival time for a scintillator with a specular reflector with 95 % reflectivity.

(b) Integrated number of photons vs. arrival time for a scintillator with a specular reflector with 98 % reflectivity.

Figure 9.25: Integrated number of photons normalised to the total number of photons arriving at SiPM for the setup with the smallest value of σ_α vs. arrival time for a scintillator with different wrappings.

9.2.6 Other Geometries

There are also approaches considering a different scintillator geometry to realise the MTT. Two favoured setups are a $100 \times 6 \times 100$ mm^3 and a $250 \times 8 \times 250$ mm^3 piece of scintillator, respectively. The first one has the advantage that it needs less space and thus provides more room for the readout electronics. The second setup uses bigger scintillator tiles that allow reducing the number of readout channels but have a reduced spatial resolution.
For these two setups the simulation has been performed once without any reflector and once with a reflector with 95 % reflectivity that can be realised with typical reflective foils. The summary plots are shown in fig. 9.26.
It becomes clear that for the big scintillator ($250 \times 8 \times 250$ mm^3) the number of photons decreases dramatically while the small one ($100 \times 6 \times 100$ mm^3) suffers smaller losses compared to the default setup ($100 \times 10 \times 100$ mm^3). In the small scintillator there are less photons created because the height is 40 % smaller than in the basic setup but the photon yield at the SiPM is reduced only by about 20 %. In the big scintillator there is a reduction of the initial photon number by only 20 % but the surface is about six times larger and so the photon density at the scintillator surface drops significantly. There are almost always zero photons hitting the SiPMs in this scenario.
The timing properties have also been studied and are summaries in fig. 9.27. They are almost

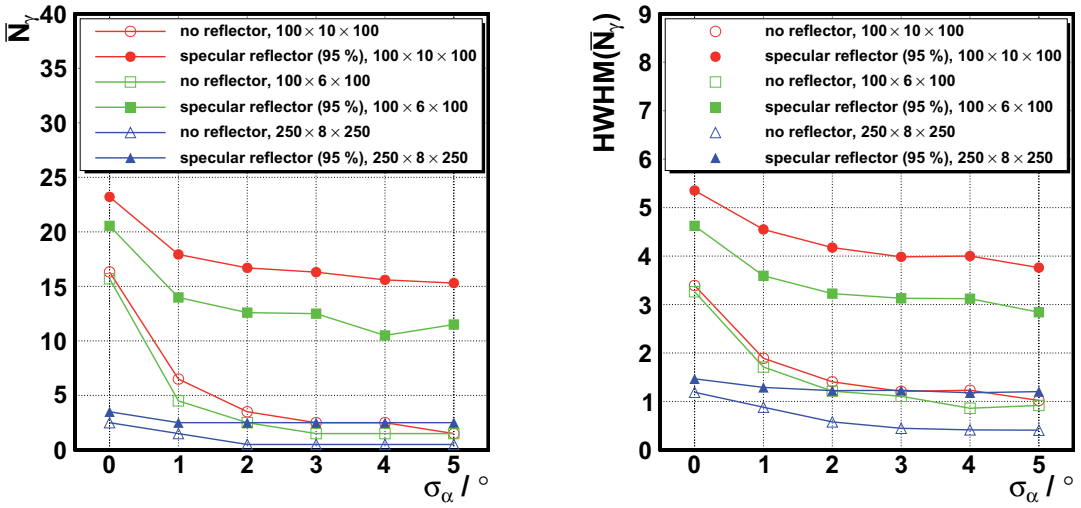

(a) MPV vs. σ_α for the different scintillator sizes. **(b)** HWHM vs. σ_α for the different scintillator sizes.

Figure 9.26: Summary of the MPV and HWHM of the photon distributions for different scintillator sizes. The reflector is always simulated with an air gap between scintillator and wrapping.

the same for the different scintillator sizes. The values have large spread because, especially for the big scintillator, there are only few photons arriving at all and thus there is only few statistics.

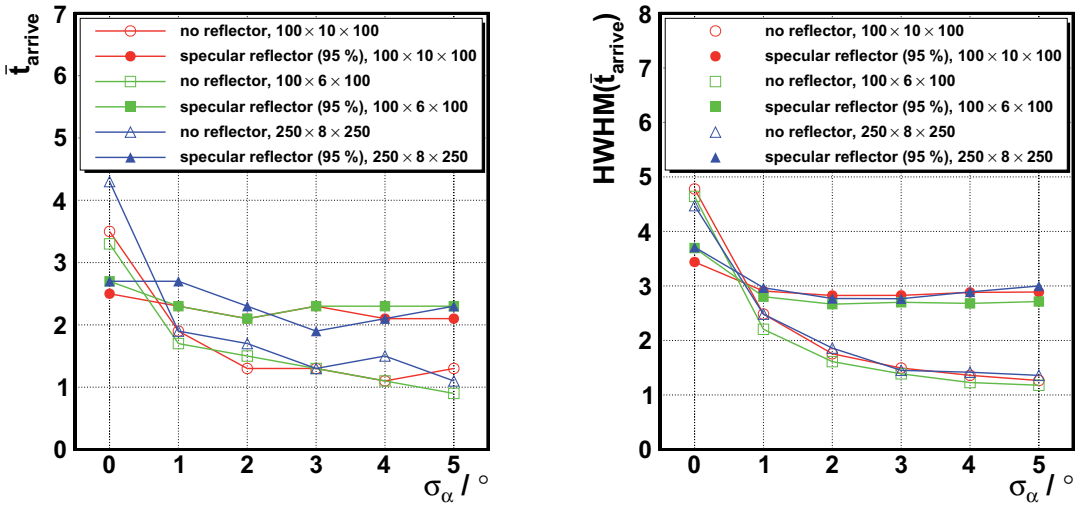

(a) Peak value of the photon arrival time vs. σ_α for different scintillator sizes. **(b)** HWHM value of the photon arrival time vs. σ_α for different scintillator sizes.

Figure 9.27: Timing properties of the different scintillators. The wrapping is always a specular reflector with an air gap.

9.3 WLS Readout

The WLS readout has been studied in detail. One example of a WLS event is shown in fig. 9.28 with one scintillator photon and one WLS photon. A traversing muon creates optical photons that propagate inside the scintillator. They can hit the fibre and get absorbed resulting in a newly created photon inside the fibre with a different wavelength.

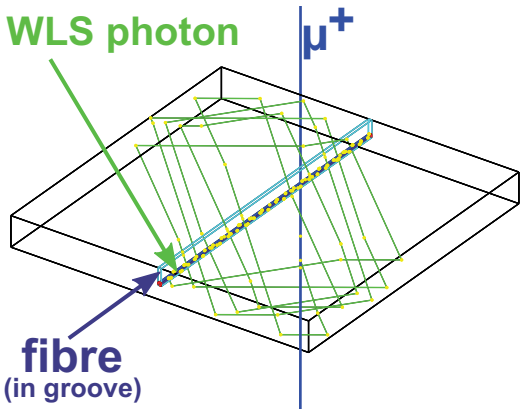

Figure 9.28: Example event with WLS fibre. One scintillator and one WLS photon are shown exemplarily.

9.3.1 Photons at Fibre

To get a first overview of the number of photons arriving at the fibre, the correlation plot 9.29 shows the number of photons absorbed in the WLS fibre against the distance of the traversing muon. There is basically no correlation visible, except where the muon distance is close to zero.

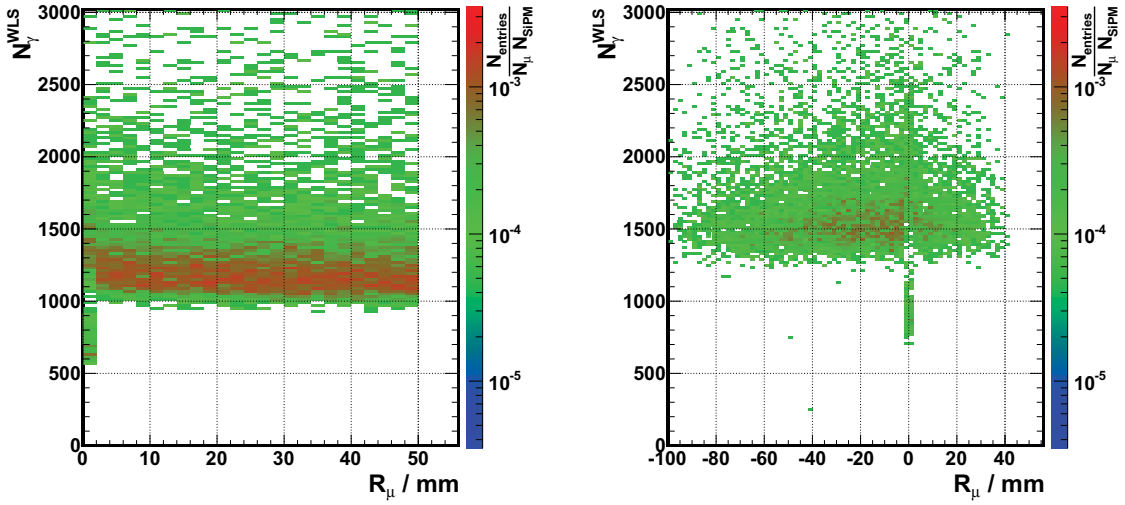

(a) Distance of the muon to the fibre vs. the number of photons absorbed in the fibre for a straight fibre in the middle position, as shown in fig. 8.9a.

(b) Distance of the muon to the fibre vs. the number of photons absorbed in the fibre for a bent fibre with $r_{\text{rel}} = 1$, as shown in fig. 8.10e.

Figure 9.29: Examples of the correlation between the distance of the traversing muon to the WLS fibre vs. the number of photons in the fibre for a scintillator with $\sigma_\alpha = 0°$.

Here the muon went through the fibre and so there was less scintillating material in its way. Negative distances mean that the muon went through the scintillator at the "inner side" of the fibre (only relevant for bent fibres).

Number of Photons

The number of photons arriving at and absorbed in the wavelength-shifting fibre also approximately follows a Landau distribution as can be seen in fig. 9.30a. The distribution is more Landau-like but still not ideally Landau distributed. To determine the peak value and the width the same methods as described in sec. 9.2.2 are applied. The results for the photons absorbed in the fibre are shown in fig. 9.30a. Also, anticipating, the number of photons arriving at the SiPMs

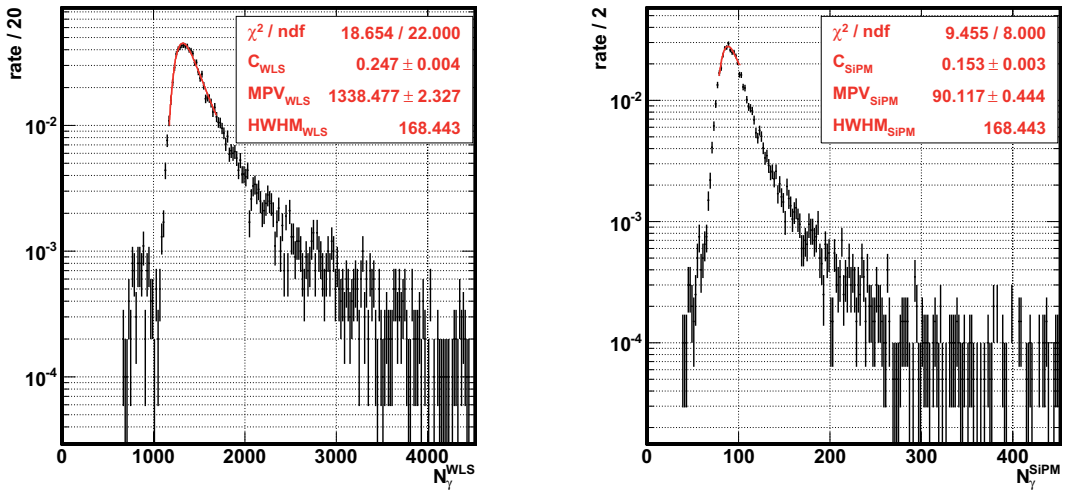

(a) Number of photons absorbed in the WLS fibre. Example for scintillator with $100 \times 8 \times 100$ mm^3. Determination of peak value as in sec. 9.2.2.

(b) Example of an averaged photon distribution at the SiPMs. Same setup as in (a).

Figure 9.30: Photon distributions in the WLS fibre and the coupled SiPMs.

is exemplarily shown in fig. 9.30b. A value of $\frac{\chi^2}{\text{ndf}} < 2$ can be demanded in this case.
The small bumps in the distributions at lower values ($N_\gamma^{\text{WLS}} \lesssim 1000$ and $N_\gamma^{\text{SiPM}} \lesssim 50$) are explained by the fact, that some of the muons (about 1 %) go through the fibre or the fibre embedment. Since both are non-scintillating materials, the muons will create less photons inside the scintillator.

Starting Conditions

The scintillator photons hitting the fibre are absorbed in the fibre according to the attenuation length for the given wavelength. As mentioned in sec. 8.1.3 this attenuation length cannot be determined without big effort and has been set to a reasonable and constant but uncertain value. The absorption point of the photon inside the fibre is dependent on this value but also on the angle under which the photon hits the fibre. Example distributions are shown in fig. 9.31 and 9.32. Fig. 9.31a/9.32a shows the projection of the creation points of the WLS-photons on the $x-y$-plane for a fibre with round/quadratic cross section. To be able to compare the fibres in the other planes, in spite of their different shapes, the distributions in fig. 9.31b and fig. 9.32b show the absorption points in the region $-25\ \mu\text{m} < y < +25\ \mu\text{m}$, i. e. every bin shows absorptions in a cube with $50 \times 50 \times 50\ \mu\text{m}^3$ where the fibres have a comparable thickness.
The creation points are identical with the absorption points of the scintillator photons inside the fibre. In fig. 9.31a it is visible that it is most probable for the photon to get absorbed in the outer region of the fibre. The same applies to the quadratic fibre. This can be explained by the fact that a photon will typically arrive with an angle > 0 with respect to the fibre normal and thus the projection of the travelled distance on this plane will be short.
Fig. 9.31b and 9.32b show that the probability to hit the fibre is almost uniformly distributed along the whole fibre. There is a slightly increased probability to get absorbed in the outer rims of the fibres, comparable to the $x-y$-plane. The drop of entries in the very outer cells is a pure binning effect because the fibre diameter is a non-integer multiple of the fibre core or cladding. Note: The relative cladding thickness is different for round and quadratic fibre.
Fig. 9.31a and 9.32a have slightly less entries at bigger y-values. This can be explained by the fact that the fibre is embedded from above and glued with the optical cement (as described in

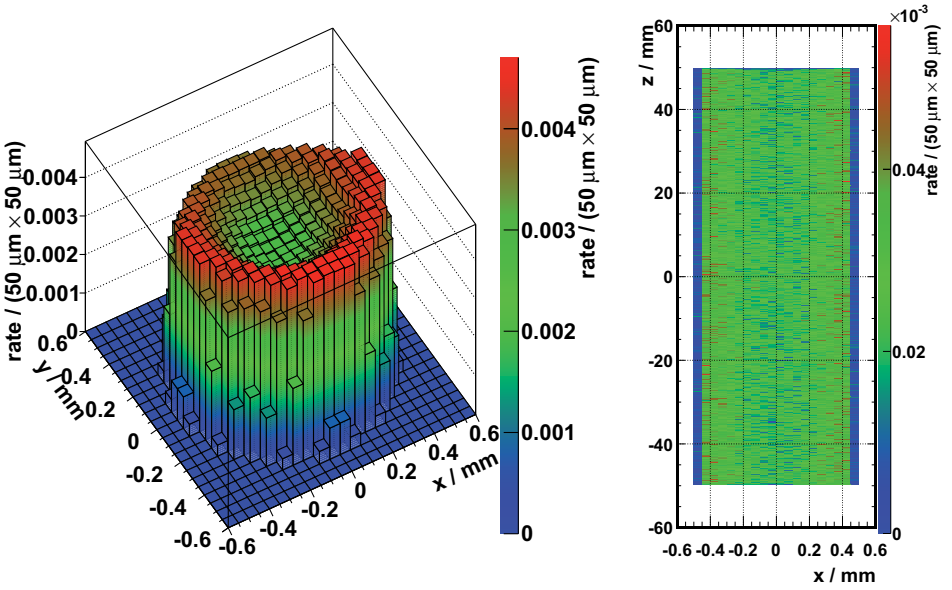

(a) Projection of the creation points on the $x-y$-plane.

(b) Slice of the creation points in -25 µm $< y < +25$ µm on the $x-z$-plane.

Figure 9.31: Projections of the creation points of WLS-photons on two of the three planes for a round fibre. The $y-z$-plane looks very similar to the $x-z$-plane. Note: the y-axis points upwards, the x-axis follows the width and the z-axis follows the length of the fibre (fibre at $x_{\text{rel}} = 0$, $y_{\text{rel}} = 0$). The histograms are normalised to the total number of photons absorbed.

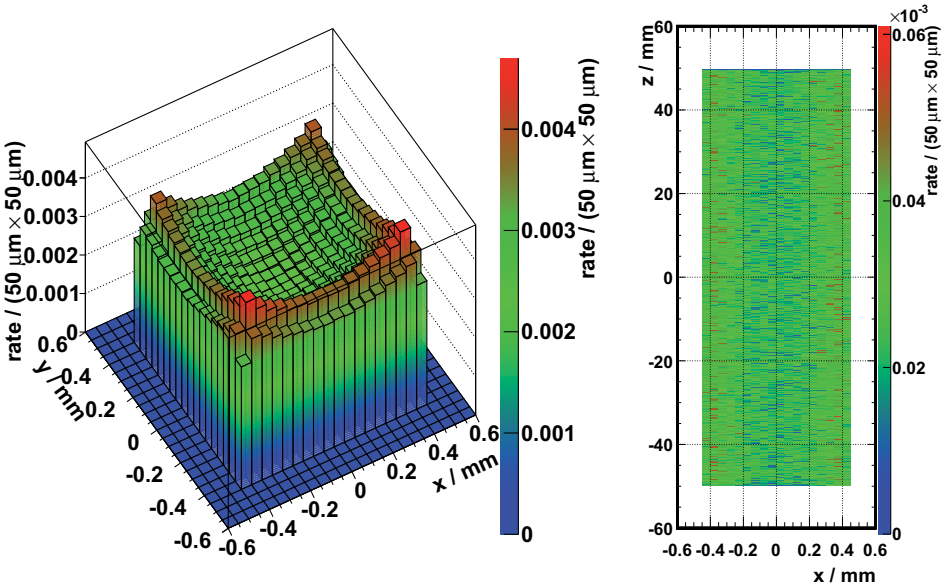

(a) Projection of the creation points on the $x-y$-plane.

(b) Slice of the creation points in -25 µm $< y < +25$ µm on the $x-z$-plane.

Figure 9.32: Projections of the creation points of WLS-photons on two of the three planes for a quadratic fibre. The $y-z$-plane looks very similar to the $x-z$-plane. Note: the y-axis points upwards, the x-axis follows the width and the z-axis follows the length of the fibre (fibre at $x_{\text{rel}} = 0$, $y_{\text{rel}} = 0$). The histograms are normalised to the total number of photons absorbed.

sec. 8.1.4) and so the probability is higher that photons coming from above are absorbed in the cement and do not reach the fibre.
The momenta of the newly created WLS-photons have to be isotropically distributed. The distributions of the momentum coordinates are shown in the appendix (fig. B.7). They match almost perfectly a uniform distribution in all coordinates.

Coupling of the Fibre

One interesting point is the number of photons that are absorbed if the fibre is not optically coupled to the scintillator. The results are shown in fig. 9.33.

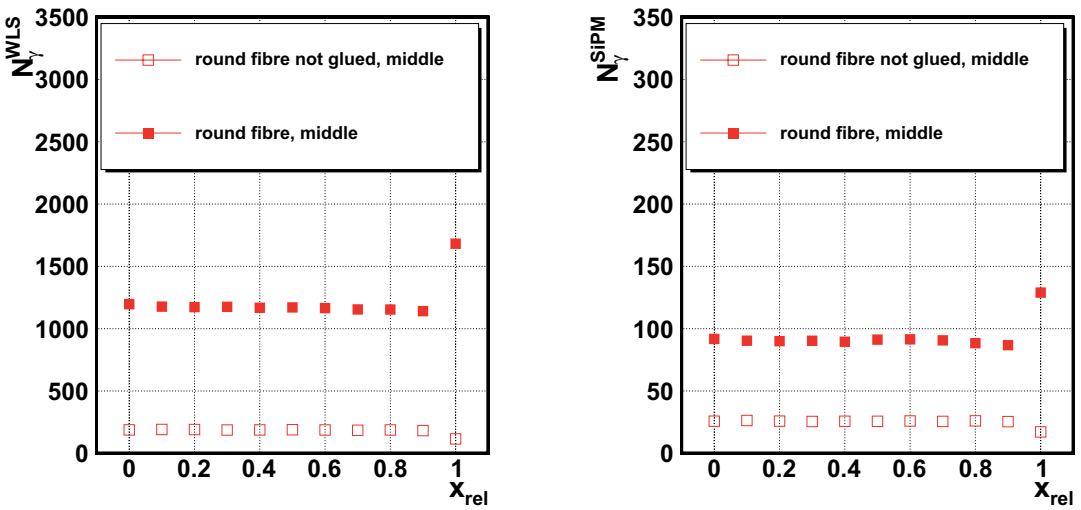

(a) MPV of the number of photons absorbed in the WLS fibre.

(b) MPV of the number of photons arriving at the SiPMs.

Figure 9.33: Number of photons at fibre and SiPM for a fibre with and without optical cement.

It is evident that a fibre with no surrounding optical cement has a light yield of only about 15 % of a glued fibre. Nevertheless the number of photons hitting the SiPM does not scale with the same factor. The photons that are created inside the fibre without optical cement are trapped easier inside the fibre because the ratio of the refractive indices of air and the outer fibre cladding is smaller than that of optical cement and the cladding, allowing a smaller critical angle at total internal reflection.
Besides this a setup with an uncoupled optical fibre is difficult in handling because the fibre has to be fixed in some way, e. g. to attach the SiPM to it. Furthermore already small impurities on the fibre surface lead to loss of light and so the number of photons at the SiPMs would be reduced.

Absorption in the Optical Cement

As described in sec. 8.1.4 the optical cement has an attenuation length in the order of a few cm. The attenuation in the cement has an impact on the number of photons arriving at the WLS fibre. This is exemplarily shown in fig. 9.34 for a fibre with round cross section at middle and top position for different values of x_{rel}. It is clear that, depending on the fibre position, the losses are in the order of up to 30 %. The increase of the photon number for the fibre in middle position at $x_{\mathrm{rel}} = 1$ can be explained by the fact that the fibre is positioned on the side of the scintillator as has been illustrated in fig. 8.9e. Here it is obvious that there is less optical cement where the photon could be absorbed. The decrease of the photon number for the fibre in top position at

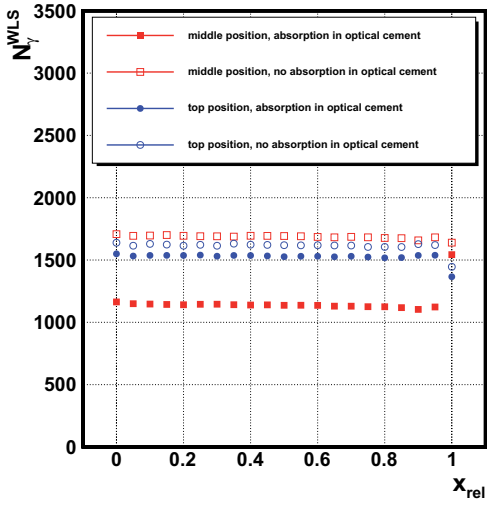

(a) MPV of the distribution of photons absorbed in the WLS fibre, with and without absorption in the optical cement.

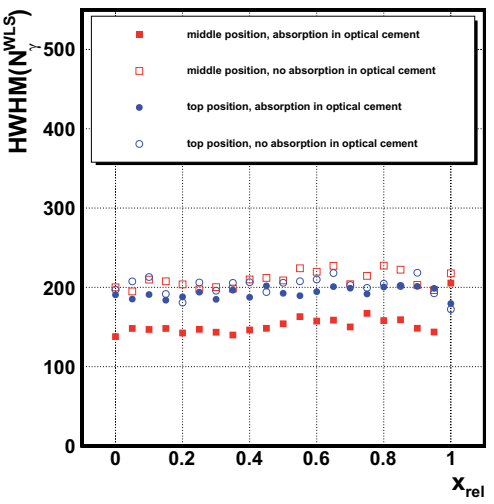

(b) HWHM of the distribution of photons absorbed in the WLS fibre, with and without absorption in the optical cement.

Figure 9.34: MPV and HWHM vs. x_{rel} of the number of photons absorbed in a round WLS fibre with and without absorption.

$x_{\text{rel}} = 1$ is explained by the fact that the fibre is embedded in one of the corner edges of the scintillator and thus has a smaller area heading towards the scintillator.

9.3.2 Photons at SiPM

There are always two SiPMs in a WLS setup, each at one end of the fibre. A first overview of the number of photons arriving at the SiPMs is given in fig. 9.35. Again there is no correlation

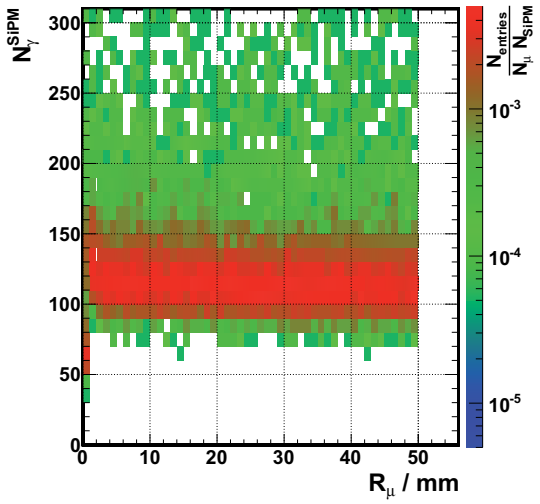

(a) Number of photons arriving at the SiPMs vs. the muon distance to the fibre for a straight fibre in the middle position.

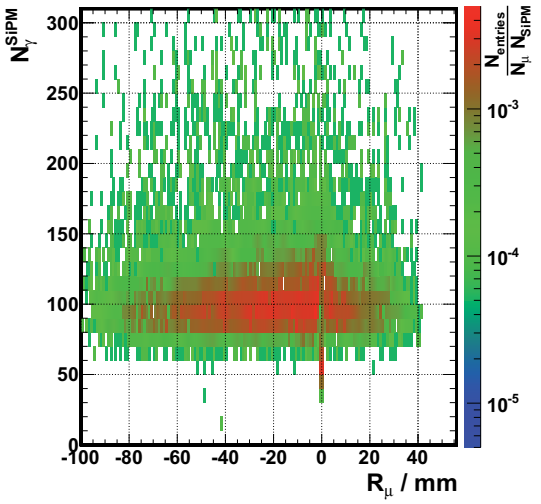

(b) Number of photons arriving at both SiPMs vs. the muon distance to the fibre for a bent fibre with $r_{\text{rel}} = 1$.

Figure 9.35: Number of photons arriving at the SiPMs vs. the muon distance R_μ for two different fibre setups for $\sigma_\alpha = 0$.

visible. Only the small dip close to zero where the muons went through the fibre.
To show that it is permitted to use the mean of the distribution of photons in the SiPMs, one

example of the photon distributions is shown in fig. 9.36a. The distributions are identical within statistical fluctuations.
From this example it is already clear that much more photons are expected at the SiPM in comparison with the direct readout scenario. As the occupancy of the SiPMs increases, it becomes more likely that one and the same pixel is hit multiple times within one event. Fig. 9.36b shows the number of photons in the different detection stages for two fibre positions. It is clearly visible that the number of photons is reduced after the application of the different efficiencies. All in all it is remarkable that the peak number of photons that are detected in the pixels is only about one half of the initial number that hit the whole SiPM. Another property is also visible: As there are 100 pixels in each SiPM there cannot be more than 100 photons detected per event. This is the reason why the overall detection distribution (red curve) stops at exactly 100.

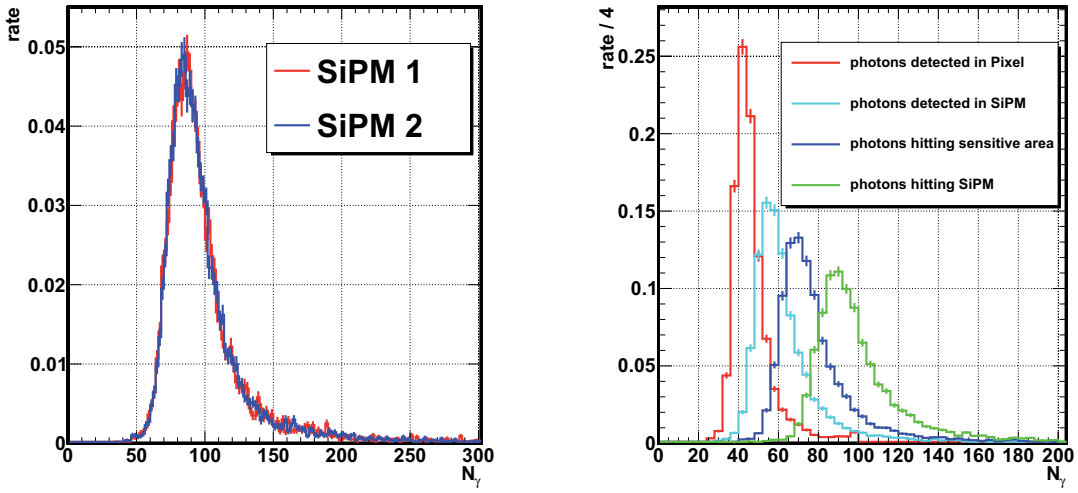

(a) Number of photons at the two SiPMs in the WLS setup. $x_{\text{rel}} = 0.0$.

(b) Number of photons at SiPM for the different detection stages ($x_{\text{rel}} = 0$).

Figure 9.36: Photon distributions for the two SiPMs in the WLS setup.

SiPM occupancy

As already mentioned in the sections before, the number of photons expected at the SiPMs is in the order of 100. As the number of pixels is in the same magnitude the occupancy of one SiPMs is of interest. Example distributions are shown in fig. 9.37 and 9.38.
The SiPM's occupancy for a fibre with quadratic cross section shows an approximately uniform distribution along the whole SiPM area. In a quadratic fibre there is no possibility for the photons to get trapped in special modes. In contrast to this is the distribution for a round fibre. A circular structure shows up when looking at the photons arriving at the SiPMs. Especially in the averaged plot it is clearly visible that in the central bin there are almost no entries. This is explained by the fact that photons are trapped in circular modes inside the fibre as is predicted theoretically in [SL00] and has been measured in [POF08]. Fig. 9.39 tries to illustrate the photon behaviour inside a round fibre.
The slightly reduced number of photons in the very outer rims of the distributions can be explained by the, i. e. photons travel preferred in the core of the fibre.

SiPMs and WLS

The coupling of the SiPM to the WLS fibre is another issue that has to be considered. In several applications that use WLS fibres the SiPMs are simply impressed onto the end of the fibre [RY09].

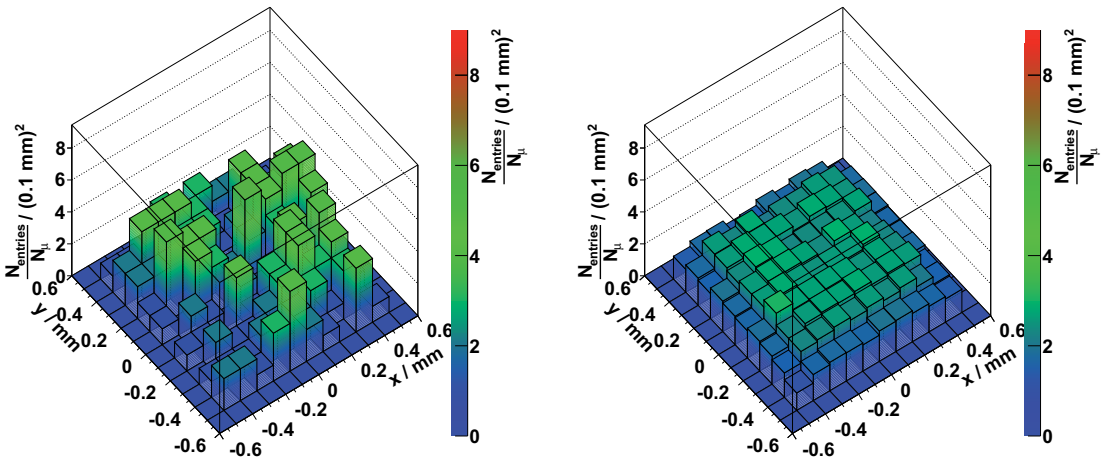

(a) Distribution of the optical photons at the SiPM for a quadratic fibre in one event.

(b) Distribution of the optical photons at the SiPM for a quadratic fibre in many events averaged over the number of events.

Figure 9.37: Distribution of optical photons on the SiPM for a quadratic fibre.

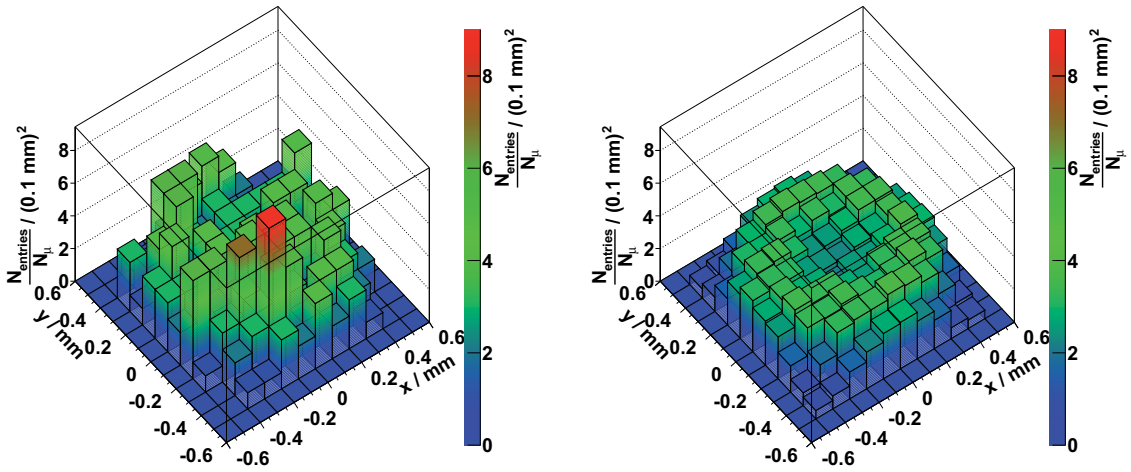

(a) Distribution of the optical photons at the SiPM for a round fibre in one event.

(b) Distribution of the optical photons at the SiPM for a round fibre in many events averaged over the number of events. Clearly visible the circular structure.

Figure 9.38: Distribution of optical photons on the SiPM for a round fibre.

It is clear that with this method it cannot be excluded that there will be a small air gap left between the fibre and the SiPM. Thus two possibilities are investigated in the scope of this thesis: The first one assumes that the SiPMs are stuck directly to the end of the fibre leaving an air gap of 100 µm, in the other one this gap is filled with optical cement (EJ-500), see also fig. 8.11. The results for the photon yield at the SiPMs are shown in fig. 9.40.
The results show that the photon yield is only slightly affected by the coupling of the SiPM to the fibre. About 15 % of the photons are lost in case of a round and only ≈ 10 % in case of a quadratic fibre. Nevertheless, the setup without the optical cement is easier to handle especially for prototype setups. Therefore in the following simulations the SiPMs will be always simulated

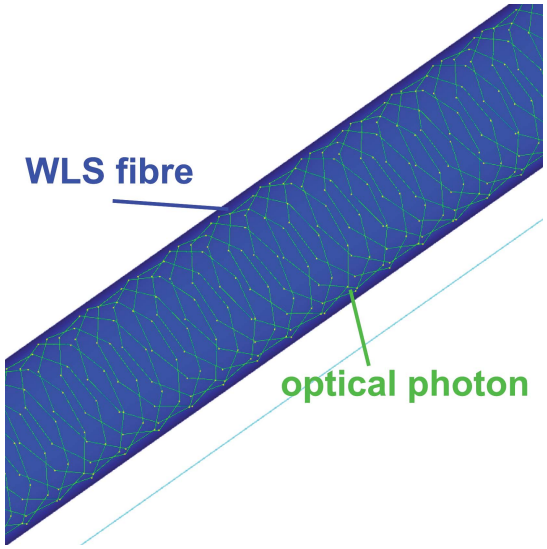

Figure 9.39: Sketch of an optical photon trajectory in a circular mode inside a WLS fibre.

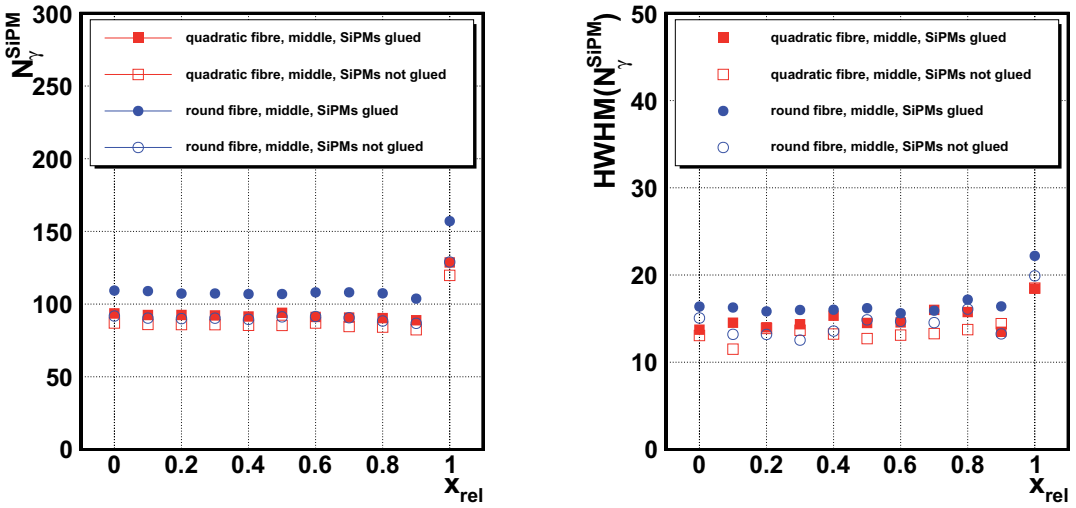

(a) MPV of photons for a glued an not glued SiPM.

(b) HWHM of photons for a glued an not glued SiPM.

Figure 9.40: Photon yield for SiPMs glued and not glued to the WLS fibre exemplarily shown for a fibre in the middle position.

with an air gap of 100 µm between them and the fibre. A final setup however, should take these effects into account and consider a coupling with optical cement or gel.

Surface Roughness

In the previous sections the surface of the scintillator has been treated as perfectly polished, but the surface roughness of the scintillator must be taken into account as has been shown in sec. 9.2. So the variation of x_{rel} for different values of σ_α has been studied. As the middle position of the fibre is disfavoured by the results shown in fig. 9.34, the focus is put on the fibre in the top position. A summary for three important values is shown in fig. 9.41.
The figure shows clearly that the x_{rel}-dependence of the photon numbers does not change with increasing roughness. Nevertheless the number of photons arriving at the fibre and at the SiPMs drops dramatically by $50 - 70$ % for values of σ_α as obtained from measurement. This shows again

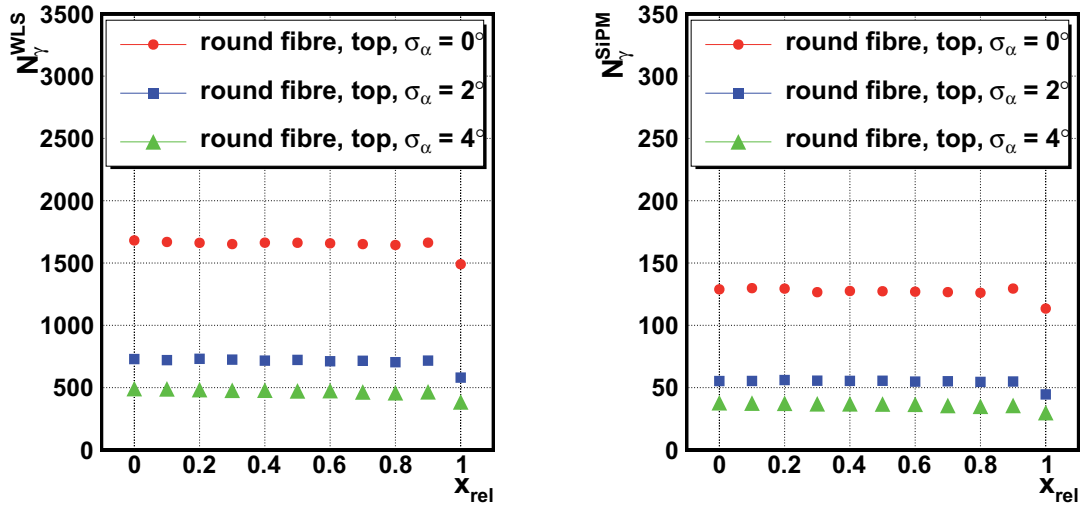

(a) MPV of the number of photons arriving at the fibre.

(b) MPV of the number of photons arriving at the SiPMs.

Figure 9.41: Number of photons arriving at the WLS fibre and SiPM, respectively, for different values of σ_α.

the importance of a well polished surface and the need of an additional reflector to maximise the photon yield (see sec. 9.3.4).

9.3.3 Bent Fibres

In many applications a bent fibre can be used to maximise the photon yield and increase homogeneity of the readout (one example can be found in [Kor04]). These setups have been studied in more detail for fibres with round and quadratic cross sections. The relative bending radius of the fibre is varied in the range of $0.5 \leq r_{\text{rel}} \leq 1$. These values are converted to x_{rel} as mentioned in sec. 8.2.3. The summary of the results for quadratic and round fibres is shown in fig. 9.42. The red vertical line shows the point where the bent and straight fibres have the same length.

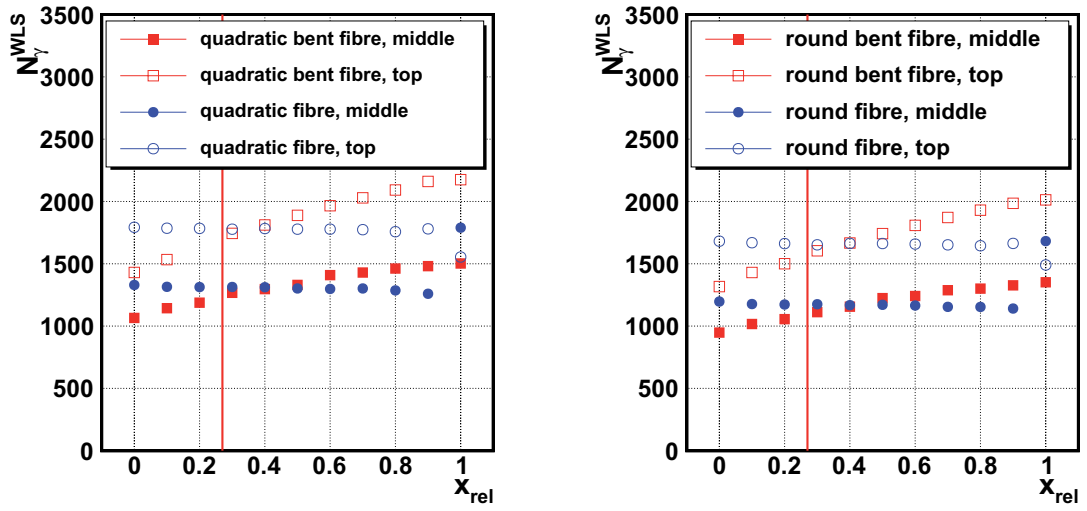

(a) MPV of number of photons arriving at the WLS fibre for different quadratic fibres.

(b) MPV of number of photons arriving at the WLS fibre for different round fibres.

Figure 9.42: Photons at fibre for bent and straight fibres. The red line shows the break-even point.

The figure shows clearly the increase of photons arriving at the fibre with increasing bending radius. This is obvious because the fibre length and with it the total volume increases with increasing bending radius.
The number of SiPM photons is also regarded. The results are shown in fig. 9.43.

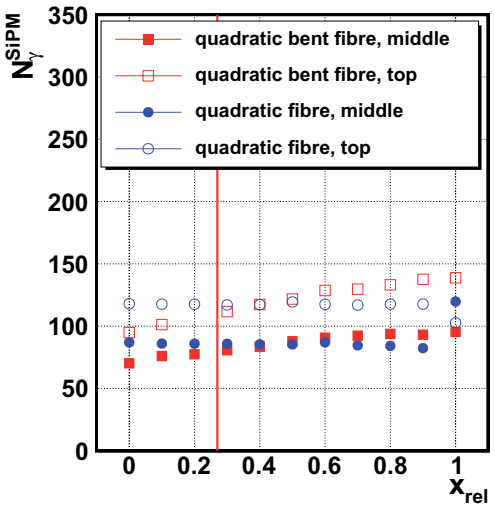

(a) Number of photons arriving at the SiPMs for a quadratic fibre.

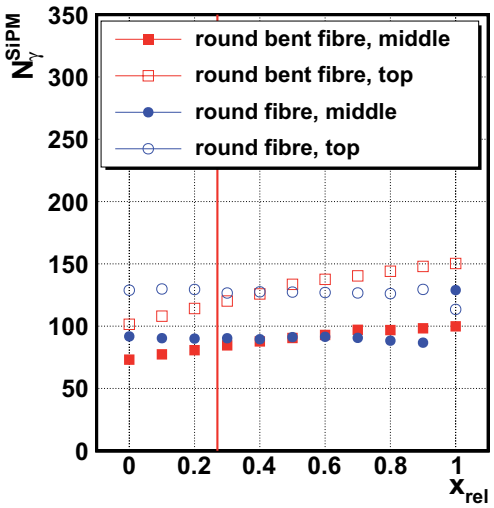

(b) Number of photons arriving at the SiPMs for a round fibre.

Figure 9.43: Number of photons at the SiPMs for different fibres .The red line shows the break-even point.

Remarkable at this point that despite the fact that less photons arrive at the WLS fibre, the number of photons at the SiPMs is higher for a round fibre. The photons are trapped in a round fibre with higher efficiency than in a quadratic one, with geometries as described in sec. 8.2.3. The photon yield at the fibre is about 10 % smaller than in the quadratic fibre but the number of photons arriving at the SiPM is the same or even higher.

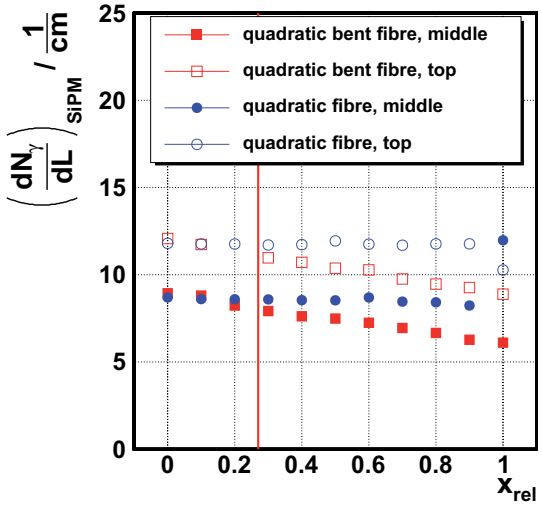

(a) Number of photons arriving at the SiPMs per length of the WLS fibre for quadratic fibres.

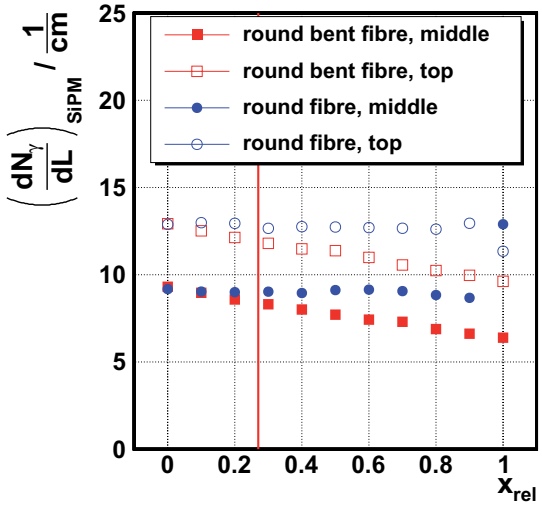

(b) Number of photons arriving at the SiPMs per length of the WLS fibre for round fibres.

Figure 9.44: Number of photons per fibre length for different setups. The red line denotes the point of same fibre length for bent and straight fibres.

The fact that the number of photons in the fibre and at the SiPMs becomes larger with increasing

bending radius does not qualify a bent fibre exclusively. There are several reasons why a bent fibre has disadvantages. First of all: the fibre has to be bent. This is a mechanical effort that is not trivial. When going to smaller bending radii the fibre has to be heated in order not to be damaged by the bending process. The groove in the scintillator has to be milled with high precision in a curved way.
Additionally, fig. 9.44 shows that the number of photons per fibre length arriving at the SiPMs is basically always smaller for a bent fibre.
These results disfavour a readout with help of a bent fibre, so the focus is put further on the properties of round straight fibres.

9.3.4 External Reflectors

As could be shown in the last sections, a setup with a bent fibre is disfavoured due to the limited increase in the photon yield and due to additional mechanical effort. The comparison between round and quadratic fibres shows that indeed the number of photons absorbed in the fibre is bigger for quadratic ones but the light yield at the SiPMs is nevertheless higher with a round fibre. It has also been shown that the fibre in the top position suffers significantly less from the absorption in the optical cement. The photon numbers are basically independent from x_{rel} except for the extreme value $x_{\text{rel}} = 1$ where the fibre is embedded in the side of the scintillator.

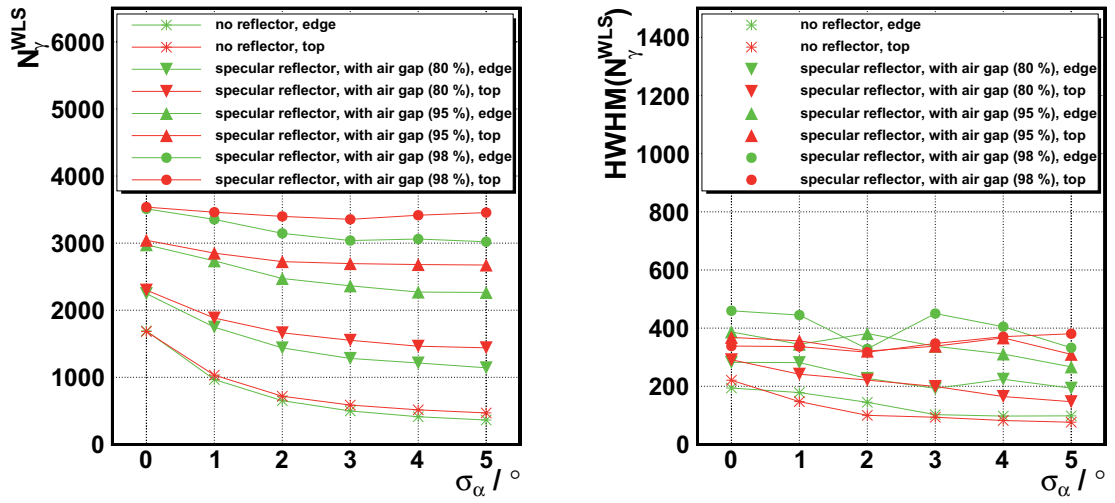

(a) MPV of the number of photons for different reflectors.

(b) HWHM of the number of photons for different reflectors.

Figure 9.45: MPV and HWHM of the distribution of photons arriving at the WLS fibre vs. σ_α for two different fibre setups.

So the favoured setup is that with a straight round fibre in the top position with values of $x_{\text{rel}} = 0$ (top) or $x_{\text{rel}} = 1$ (edge). For these setups the behaviour under the application of an external reflector has been studied. The results are shown in fig. 9.45.
The plots demonstrate again that a reflector has a major impact on the photon yield. That is also clearly visible when looking on the number of photons at the SiPMs that is shown in fig. 9.46.
There is an increase in the photon yields up to about a factor of three, depending on the reflectivity, but also the widths scale with a comparable factor. Additionally it is clear that the fibre in the top position allows a better yield than that in the edge position, although this effect is only in the order of 10 %.

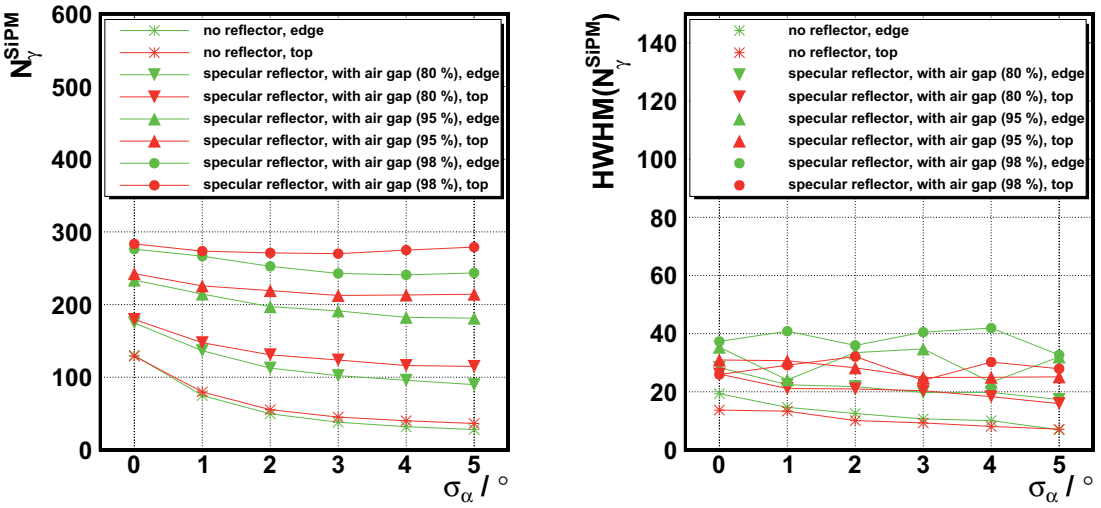

(a) MPV of the number of photons for different reflectors.

(b) HWHM of the number of photons for different reflectors.

Figure 9.46: MPV and HWHM of the distribution of photons hitting the SiPMs vs. σ_α for two different fibre setups (there is a small air gap between the SiPMs and the fibre).

Timing

Again one very interesting property of the setup is the dependence of the timing on the distance of the traversing muon. The results for two example setups are shown in fig. 9.47. Again (compare fig. 9.35) the timing of the setup is not correlated with the muon incoming point, what is especially very clearly visible for the straight fibre setup (fig. 9.47a).

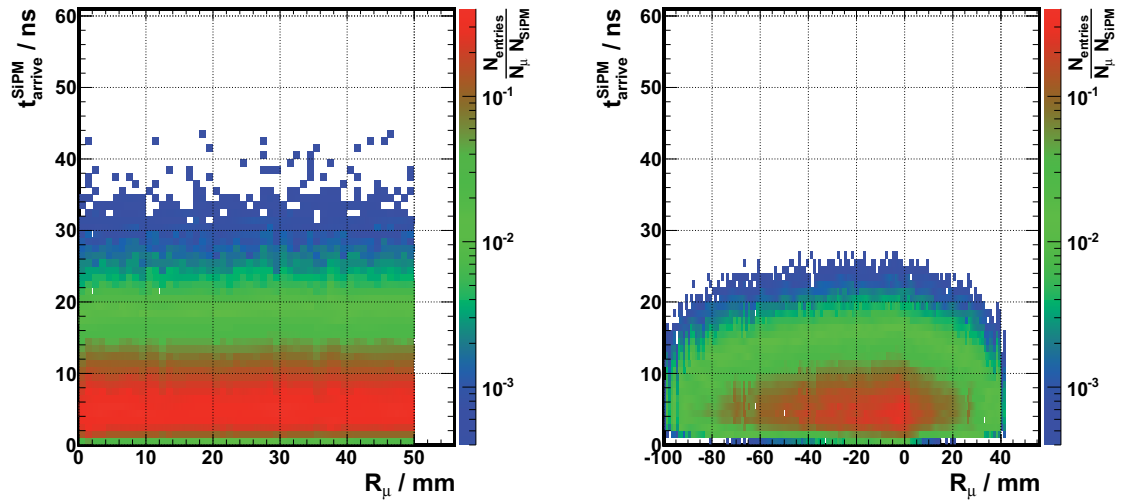

(a) Photon arriving time at the SiPMs for a straight fibre in the middle position ($x_{rel} = 0, y_{rel} = 0$).

(b) Photon arriving time at the SiPMs for a bent fibre with $y_{rel} = 0, r_{rel} = 1$.

Figure 9.47: Photon arriving time vs. the muon distance for two different fibre setups.

While the fibre itself has an additional decay time, the timing properties have been studied in detail for this preferred setup. Results are shown in fig. 9.48.
The figure shows clearly that the peak time for photon arrival is ≈ 6 ns in the worst case while the HWHM increases by a factor of two. It is clear that the WLS readout is considerably slower than the direct readout (by approx. a factor of two) but still provides enough time for the processing

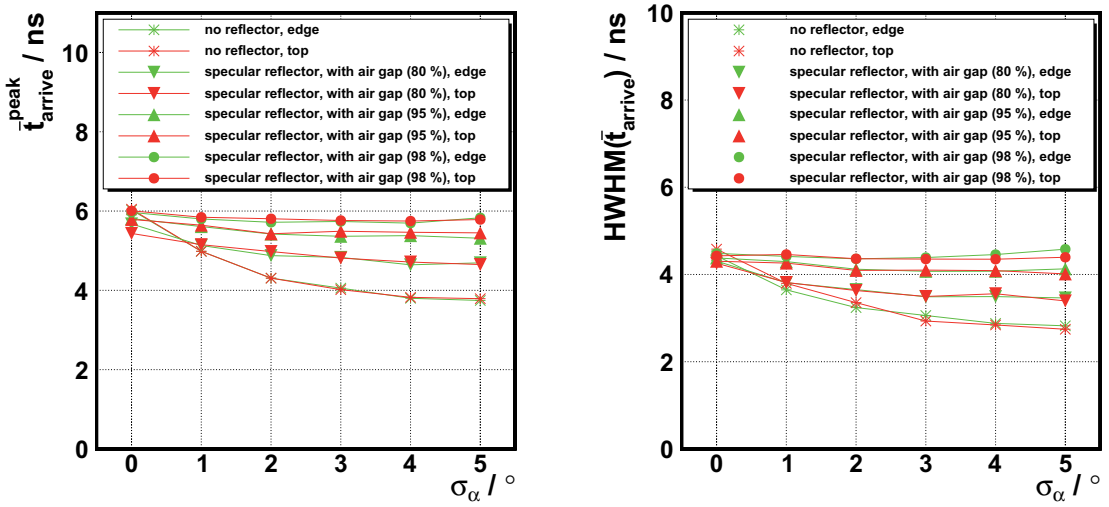

(a) Peak value of the arrival time of photons at the SiPMs.

(b) HWHM of the arrival time distribution of photons at the SiPMs.

Figure 9.48: Peak and HWHM of the time distribution of photon arriving at the SiPMs for different fibres and reflectors.

of the created signal. Fig. 9.49 shows additionally the time of the first photon arrival and the rise time, i. e. the difference between the point in time when 10 % and 90 % of the photons arrived. Here it also shows up that the WLS setup is slower in comparison to the direct redout. $\bar{t}_{90-10}$ is in the order of 3 ns in comparison to 1.5 ns as it was in the direct readout setups.

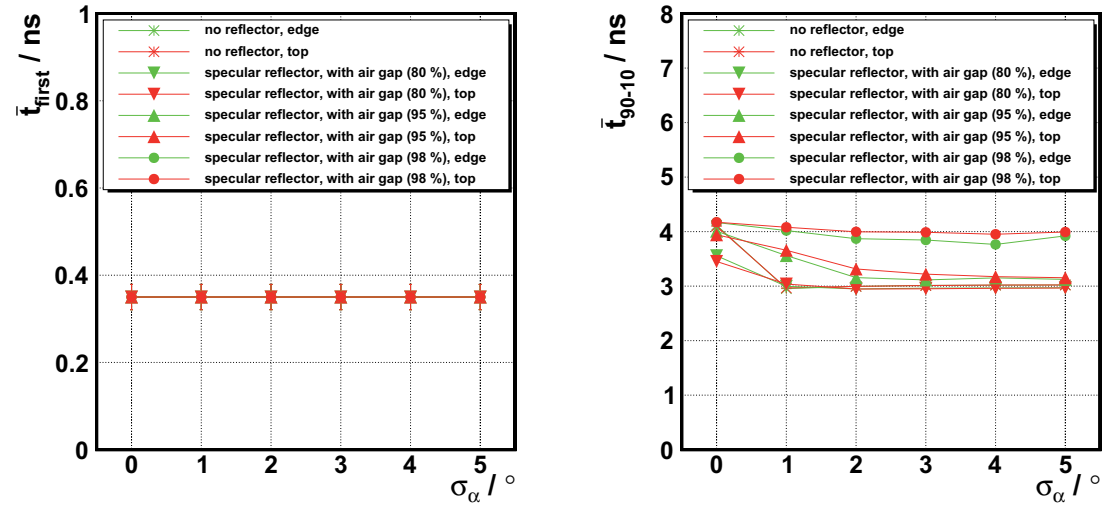

(a) Point in time of the first arrival of photons an the SiPMs.

(b) Rise time of the photons at the SiPMs

Figure 9.49: Time of the first incoming photons and the rise time for different fibres and reflectors.

One final timing consideration, regarding the fibre readout, is the point in time when 90 % of the total number of photons have reached the SiPMs, denoted as $\bar{t}^{90}$. The results are shown in fig. 9.50.
In most of the setups this time is between 11 ns and 15 ns after the muon passed the scintillator. Only for setups with high reflectivity this value increases up to $\approx$ 17 ns. This is by trend higher than for the setup with direct readout but is still in the same order of magnitude.

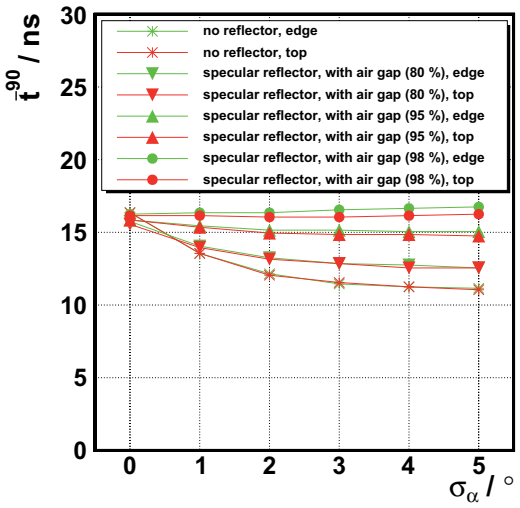

Figure 9.50: The point in time, when 90 % of the photons have arrived at the SiPMs ($\bar{t}^{90}$) vs. σ_α for different reflectors.

9.3.5 Other Geometries

As mentioned in sec. 9.2.6 there are also approaches with different geometries to realise the MTT. For the same setups as described in sec. 9.2.6 the simulations have been performed with a WLS fibre at two positions. Fig. 9.51 shows the number of photons absorbed in the WLS for $x_{\text{rel}} = 0$, $y_{\text{rel}} = 1$ (top position) and $x_{\text{rel}} = 1$, $y_{\text{rel}} = 0$ (edge position). It is clearly visible that

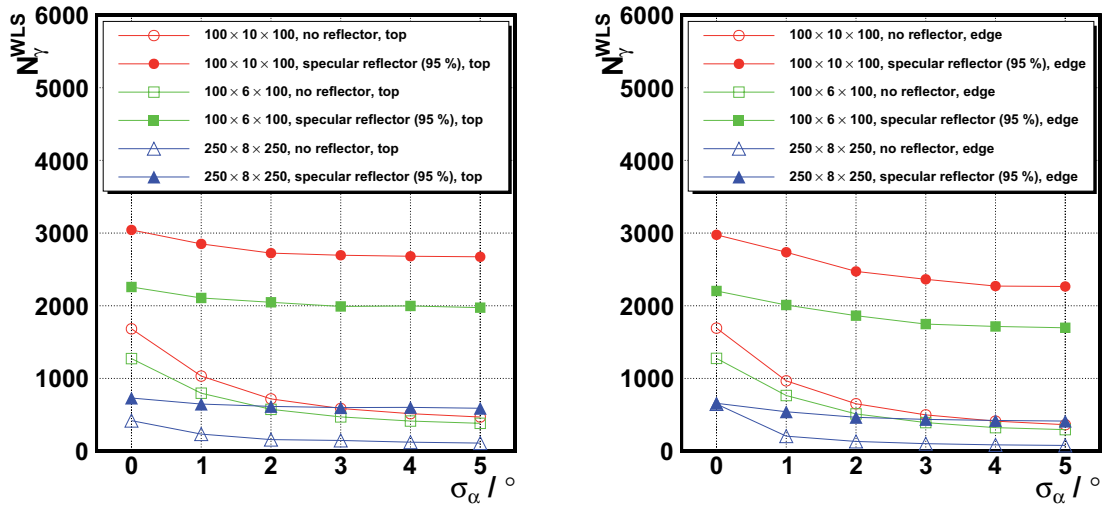

(a) Number of photons absorbed in the WLS fibre for different setups with the fibre in the top position.

(b) Number of photons absorbed in the WLS fibre for different setups with the fibre in the edge position.

Figure 9.51: MPV of the number of photons absorbed in the WLS fibre vs. σ_α for different fibre setups. There is always an air gap of 100 µm between scintillator and reflector. The widths of these distributions are shown in the appendix, see fig. B.3.

again (compare sec. 9.2.6) the setup with the big scintillator ($250 \times 8 \times 250$ mm^3) is disfavoured for basically all parameter settings.
This also reflects in the number of photons arriving at the SiPMs. It strictly follows the number of photons that hit the fibre and the results can be seen in fig. 9.52.
It becomes clear that the number of photons hitting the SiPMs is up to five times smaller for

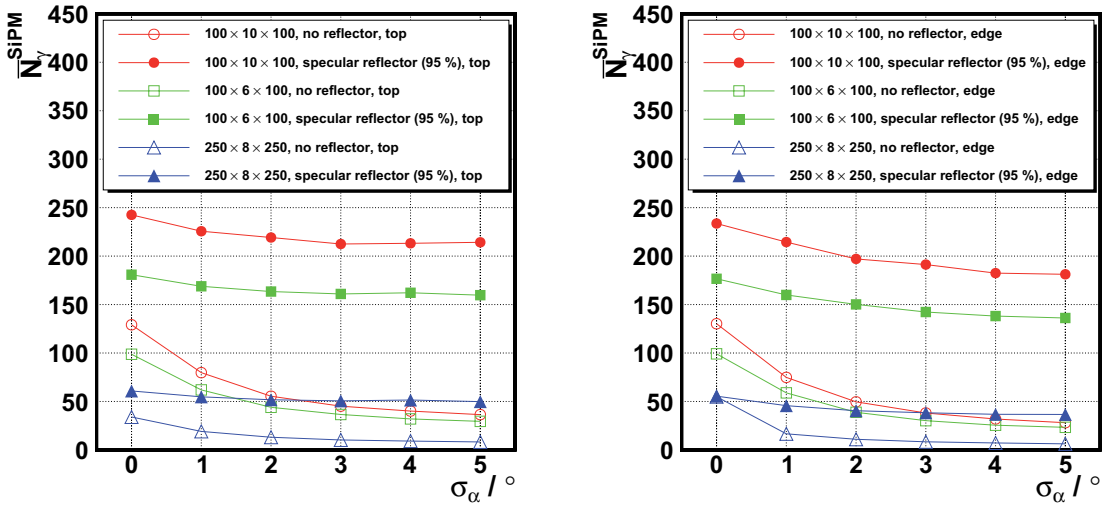

(a) Number of photons hitting the SiPMs for different setups with the fibre in the top position.

(b) Number of photons hitting the SiPMs for different setups with the fibre in the edge position.

Figure 9.52: MPV of the number of photons arriving at the SiPMs vs. σ_α for different fibre setups. There is always an air gap of 100 µm between scintillator and reflector. The widths of these distributions are shown in the appendix, see fig. B.4.

the big scintillator. Nevertheless, this number could suffice to reach a reasonable signal to noise ratio in the a final setup, especially with a wrapping with high reflectivity. The results for the scintillator with $100 \times 6 \times 100$ mm^3 lie in between the other two setups.
The timing properties are comparable for the different setups as can be seen in fig. 9.53.

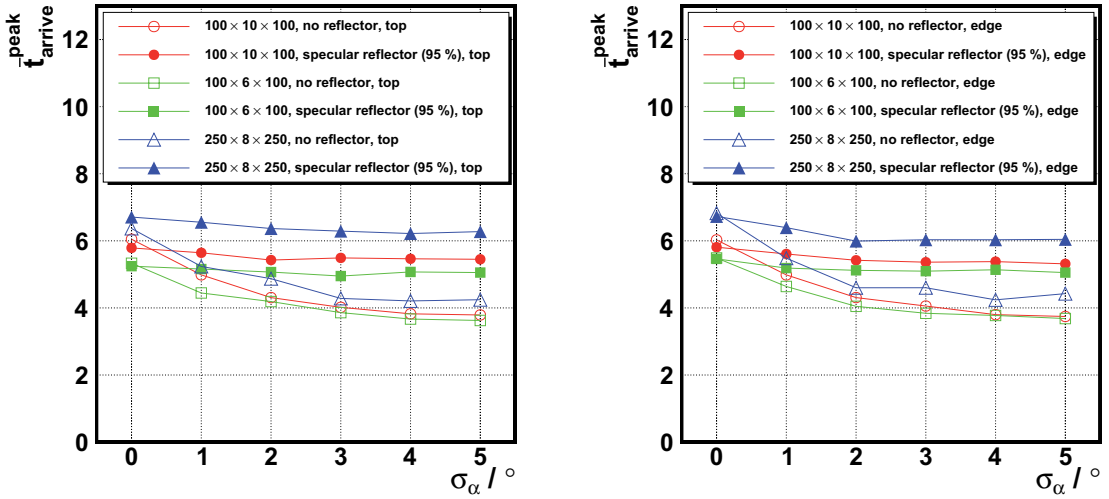

(a) Peak value of the arrival time of the photons at the SiPMs for the fibre in top position.

(b) Peak value of the arrival time of the photons at the SiPMs for the fibre in edge position.

Figure 9.53: Peak value of the arrival time of the photons at the SiPMs vs. σ_α for different scintillator and fibre setups. There is always an air gap of 100 µm between scintillator and reflector. The widths of these distributions are shown in the appendix, see fig. B.5.

The peak values are between ≈ 3 ns and ≈ 4.5 ns for all setups.

9.4 Summary of the results

As could be shown in the foregoing sections, the photon yield at the SiPMs in setups with and without a WLS fibre is strongly dependent on the surface roughness, characterised by the parameter σ_α. It has also been shown that the negative effects of an increased roughness can be compensated by a wrapping with preferably very high reflectivity. Reflectors directly attached to the scintillator (without an air gap) are completely disfavoured by the simulations.
The timing properties are very encouraging when regarding the proposed bunch crossing rates at the SLHC as the peak values of the photon arrival time are typically at less than 6 ns and most of the photons arrive within $15 - 17$ ns at the SiPMs.
A summary of the photon numbers and peak arrival times at the SiPMs is given in tab. 9.1.

Table 9.1: Summary of the photon number and arrival times for setups with direct readout. The summary distinguishes between a perfectly polished ($\sigma_\alpha = 0°$) and a 'realistic' scintillator surface ($\sigma_\alpha = 1° - 5°$).

direct readout					
size / mm^3	reflector (reflectivity)	$\sigma_\alpha = 0°$		$\sigma_\alpha = 1° - 5°$	
		$\overline{N}_\gamma$	$\bar{t}^{\text{peak}}$/ns	$\overline{N}_\gamma$	$\bar{t}^{\text{peak}}$/ns
$100 \times 10 \times 100$	-	16.2	3.7	$5.7 - 1.2$	$2.3 - 1.2$
	G4 diffuse, no air gap (80 %)	2.6	1.4	$2.6 - 2.5$	$1.3 - 1.4$
	G4 diffuse, no air gap (95 %)	11.0	2.3	$11.0 - 10.0$	$2.3 - 2.2$
	G4 diffuse, air gap (80 %)	17.6	3.1	$9.8 - 4.9$	$2.4 - 1.9$
	G4 diffuse, air gap (95 %)	21.7	2.9	$15.9 - 13$	$2.7 - 2.6$
	diffuse, air gap (80 %)	17.7	2.9	$9.8 - 5.4$	$2.3 - 1.7$
	diffuse, air gap (95 %)	22.6	2.6	$18.1 - 14.6$	$2.5 - 2.5$
	specular, air gap (80 %)	17.8	2.9	$10.1 - 5.4$	$2.3 - 1.8$
	specular, air gap (95 %)	22.6	2.7	$17.4 - 14.6$	$2.6 - 2.5$
	specular, air gap (98 %)	28.4	3.0	$25.9 - 22.9$	$3.0 - 2.9$
$100 \times 6 \times 100$	-	15.7	3.3	$4.5 - 1.5$	$1.7 - 0.9$
	specular, air gap (95 %)	20.5	2.7	$14 - 11.5$	$2.3 - 2.3$
$250 \times 8 \times 250$	-	2.5	4.3	$1.5 - 0.5$	$1.9 - 1.1$
	specular, air gap (95 %)	3.5	2.7	$2.5 - 2.5$	$2.7 - 2.3$

It could be shown that setups with a WLS readout provide significantly more photons than those with direct readout. An increase of up to a factor 10 is possible. It became clear that bent fibres only slightly increase the photon yield in comparison to straight fibres. The preferred position of the fibre inside the scintillator is at $y_{\text{rel}} = 1$, i. e. in the top position. This minimises the amount of optical cement and with it the non-scintillating volume. There seems to be no preferred positioning in x_{rel} as long as the fibre is not at one of the outer edges ($x_{\text{rel}} = 1$). Nevertheless, $x_{\text{rel}} = 1$ is one of the preferred scenarios because it is comparably easy to assemble. A round fibre is slightly favoured by the simulation as its photon trapping efficiency is higher than of a quadratic fibre.

Table 9.2: Summary of the photon number and arrival times for setups with WLS readout. The summary distinguishes between a perfectly polished ($\sigma_\alpha = 0°$) and a 'realistic' scintillator surface ($\sigma_\alpha = 1° - 5°$).

WLS readout						
size / mm^3	fibre	reflector (reflectivity)	$\sigma_\alpha = 0°$		$\sigma_\alpha = 1° - 5°$	
			$\overline{N}_\gamma$	$\bar{t}^{\text{peak}}_{\text{arrive}}$	$\overline{N}_\gamma$	$\bar{t}^{\text{peak}}_{\text{arrive}}$
$100 \times 10 \times 100$	edge	-	130	6.0	$75 - 28$	$5.0 - 3.7$
		specular, air gap (80 %)	175	5.7	$136 - 90$	$5.1 - 4.7$
		specular, air gap (95 %)	234	5.8	$214 - 181$	$5.6 - 5.3$
		specular, air gap (98 %)	276	6.0	$267 - 243$	$5.8 - 5.7$
	top	-	129	6.0	$80 - 36$	$5.0 - 3.7$
		specular, air gap (80 %)	180	5.4	$147 - 115$	$5.2 - 4.7$
		specular, air gap (95 %)	242	5.8	$225 - 214$	$5.6 - 5.5$
		specular, air gap (98 %)	283	6.0	$273 - 279$	$5.8 - 5.7$
$100 \times 6 \times 100$	edge	-	99	5.5	$59 - 23$	$5.2 - 5.1$
		specular, air gap (95 %)	177	5.5	$160 - 136$	$4.6 - 3.7$
	top	-	99	6.8	$62 - 29$	$4.4 - 3.6$
		specular, air gap (95 %)	181	6.7	$169 - 160$	$5.2 - 5.1$
$250 \times 8 \times 250$	edge	-	55	5.2	$17 - 6$	$6.4 - 6.0$
		specular, air gap (95 %)	56	5.3	$45 - 37$	$5.5 - 4.4$
	top	-	34	6.4	$19 - 9$	$5.2 - 4.2$
		specular, air gap (95 %)	61	6.7	$65 - 63$	$6.8 - 6.6$

The simulation results show that a scintillator with both, direct and WLS readout, has the capability to handle the requirements of the MTT. Nevertheless, detailed measurements are needed to confirm or falsify the simulation results.

Chapter 10

Preparation of the Test Stand

As there are some uncertainties in the adjustment of the parameters used in the simulations (e. g. absorption in the fibre, surface parameters) the results should be confirmed or falsified with help of measurements with comparable test setups. Furthermore the simulation results can only give a guideline for a detector development and measurements are essential to understand the detector parts.
For these reasons a test stand for cosmic muons is in preparation so that systematical measurements at various scintillator/WLS setups can be performed. This test stand is presented in the following sections.

10.1 Readout Electronics

The readout of the setups happens with SiPMs (see fig. 10.1) as described in sec. 8.2.2, i. e. Hamamatsu `S10362-11-100C`. The SiPM's power supply, signal readout and amplification are provided by a front end board developed in the electronics workshops of the IIIrd Physics Insitute A and B, it is shown in fig. 10.2. The basic readout principle of this board is similar to that shown in fig. 5.16. Additionally, it has a sophisticated bias voltage stabilisation that also allows an individual fine tuning of the voltage applied to the SiPM.

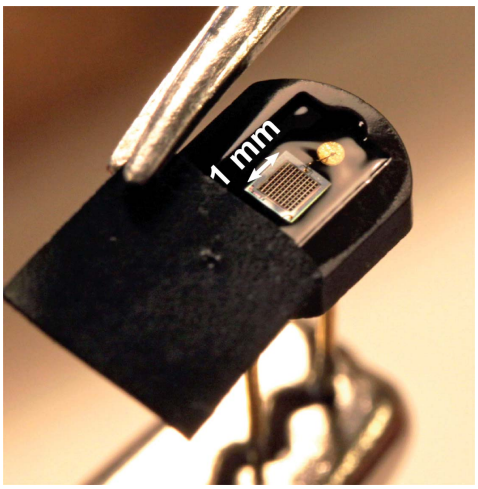

Figure 10.1: Picture of one of the used SiPMs (Hamamatsu `S10362-11-100C`) [Heb10].

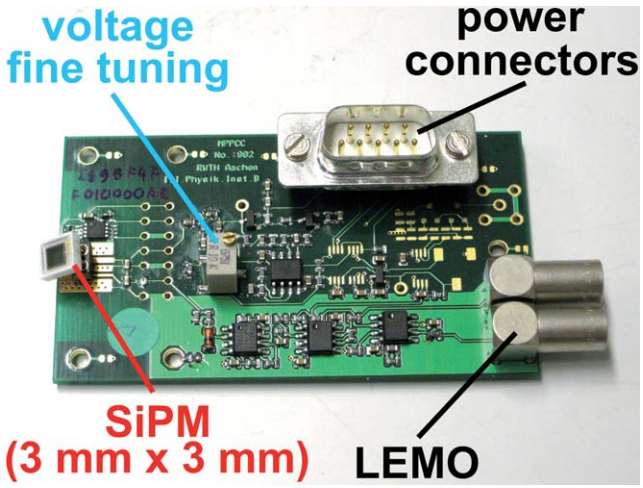

Figure 10.2: Front end board developed in Aachen shown with a 3×3 mm^2 SiPM (`S10362-33-100C`).

The characteristics of the noise pulses of an SiPM read out with help of this front end board are exemplarily shown in fig. 10.3. This oscilloscope sketch illustrates that the one photon equivalent pulse (p.e.) has an amplitude of roughly 30 mV and that higher pulses have amplitudes that are basically a multiple of that.

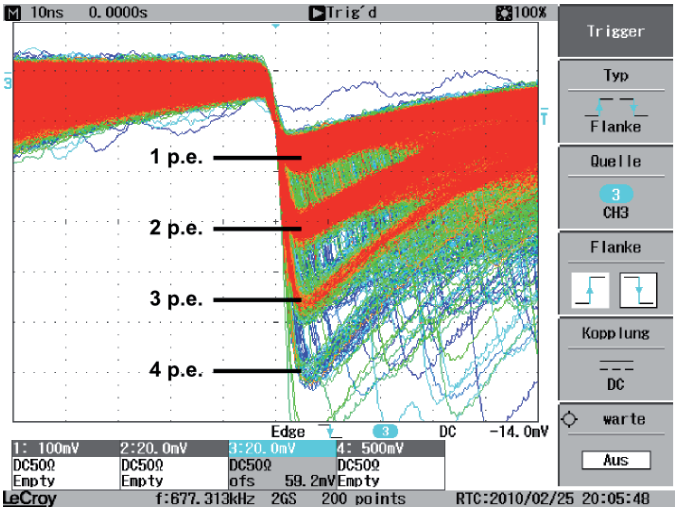

Figure 10.3: Typical noise characteristics for one SiPM. The pulses are accumulated and displayed according to their entrance time, i. e. red colour denotes recent events and blue colour denotes older events. The different between two p.e. is ≈ 30 mV.

10.2 Hodoscope

To be able to trigger on cosmic muons independently from the setup to be investigated, a simple hodoscope has been built of four fishtail scintillator tiles with a size of $300 \times 100 \times 5$ mm^3 that are read out by conventional PMTs. Fig. 10.4 shows this setup. The scintillator tiles are mounted

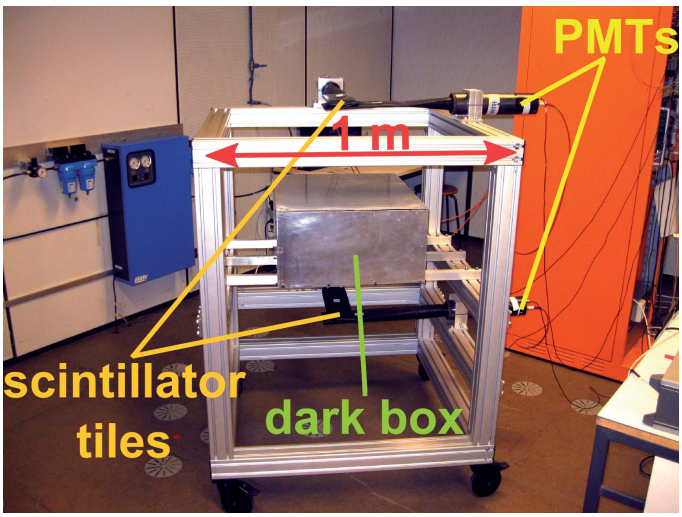

(a) Hodoscope setup built of four fishtail scintillator tiles and PMTs with a dark box in between the trigger scintillators.

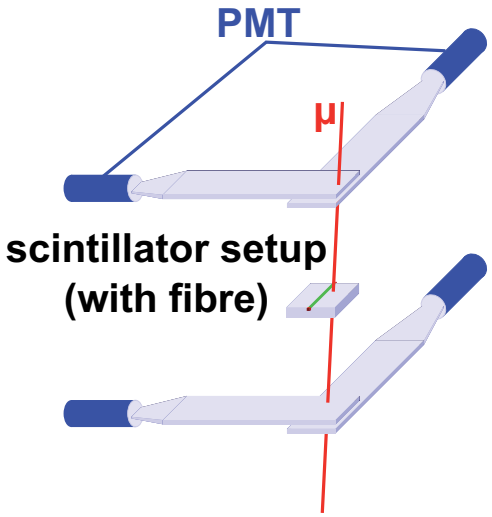

(b) Schematic view of the hodoscope setup. The scintillator setup, as described in sec. 10.3, is positioned in between the hodoscope scintillators (inside the dark box).

Figure 10.4: Hodoscope setup used in the test stand.

at the top and the bottom of the hodoscope frame and are aligned perpendicularly with respect to each other. This allows to define two areas of 100×100 mm^2 above and below the dark box with a distance of ≈ 1 m (adjustable). The scintillator setup of interest is positioned inside the dark box parallel to the areas (fig. 10.4b). If a coincidence of all four PMTs is claimed, muons travelling through the small corridor, defined by the two areas of the crossed scintillators, can be triggered. These muons are almost perpendicular and it is almost sure that they have also passed the scintillator setup in the dark box.

10.3 Scintillator setups

A very first test with a direct readout, has been performed with a $1 \times 1\,\mathrm{mm}^2$ SiPM. One SiPM has been mounted directly onto the scintillator without optical coupling and with optical gel between it and the scintillator. In both cases no signal could have been measured from cosmic muons. An additional wrapping realised by simple aluminium foil could not improve this setup.

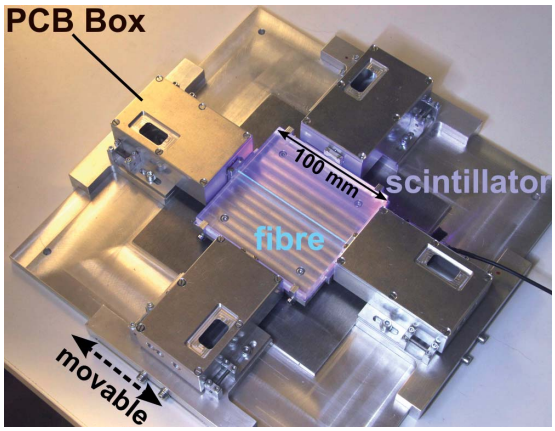

(a) Scintillator setup with readout possibilities from four sides (PCB boxes) [Heb10].

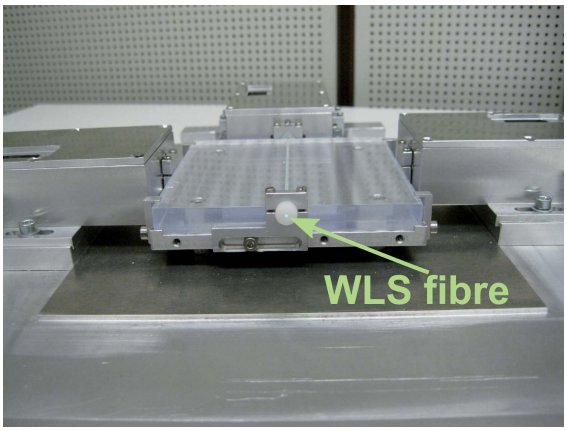

(b) The same setup as (a) but with one PCB box disassembled to make the WLS fibre visible.

Figure 10.5: Flexible scintillator setup with readout possibilities from different points. For example able to handle a scintillator with a bent fibre or with two straight fibres.

This result does not refuse the simulation results because it has been shown (fig. 9.15) that less than three photons are expected to hit an SiPM (in the relevant σ_α-region) in the direct readout setup with no reflector (without optical coupling this number is basically zero). Even with a reflector of low quality (80 % reflectivity or less) a vanishing photon yield is not surprising because also in this case the results predict only very small photon numbers. As these numbers are small and additional absorption processes inside the scintillator cannot be excluded, e. g. caused by impurities inside the scintillator or of the surface, more detailed measurements have to be performed, especially with larger SiPMs.

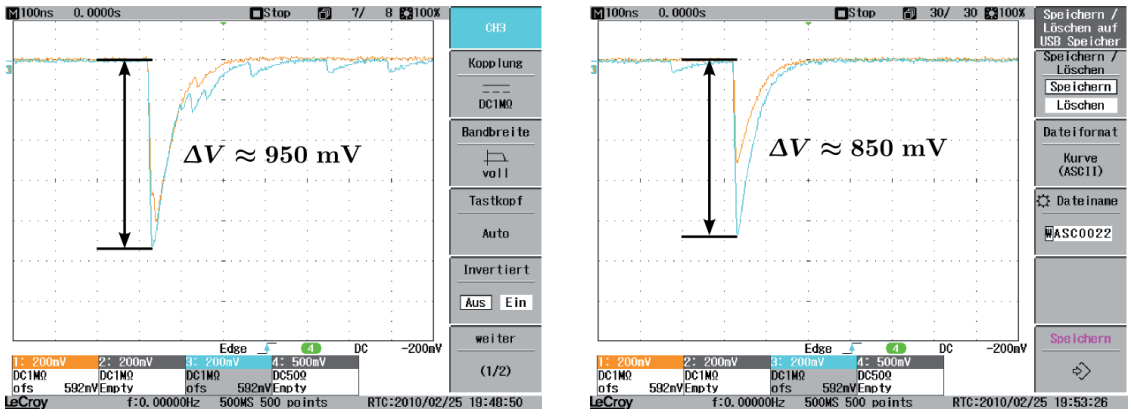

Figure 10.6: Two examples of SiPM pulses triggered by the hodoscope. It is clearly visible that the two pulses (orange and cyan) in each picture created at the same time. Typical pulse heights are in the order of several hundred mV.

Another test setup is shown in fig. 10.5. This setup is built-up accordingly to the simulated setup with a straight, round fibre in the top position (i. e. $x_{\mathrm{rel}} = 0$, $y_{\mathrm{rel}} = 1$) and is glued with optical cement `BC-600` that is equivalent to the one used in the simulations (`EJ-500`).

For the WLS readout a very first estimate of the photon number can be done with a simple measurement. As described above, a trigger for the oscilloscope is generated with help of the hodoscope setup and the SiPM pulses are recorded. Two examples are shown in figure 10.6.
It is clearly visible that the pulses from the two SiPMs are created at the same time and have a comparable height, i. e. the photons arrive simultaneously and at both SiPMs a comparable number of photons are detected.
Assuming that the pulse height scales linearly with the number of photons detected, and that one p.e. creates a pulse height difference of 30 mV, the number of photons detected per SiPM can be estimated to roughly 30 for this setup. Comparing this number with the simulation results shown in fig. 9.46 (red stars) it becomes clear that these number are very compatible, especially when considering the fact that the detection efficiency of the SiPMs has not been applied in the results shown.

10.4 Summary

The very first measurements show that a direct readout setup with $1 \times 1\,\mathrm{mm}^2$ SiPMs has a vanishing light yield. Nevertheless, a suitable detector could result from the usage of larger SiPM (e. g. $3 \times 3\,\mathrm{mm}^2$ active surface). Additionally a wrapping with a very high reflectivity ($> 90\,\%$) could make this kind of setup very attractive.
The first results with the WLS readout are much more promising. Muon passages are clearly measurable and distinguishable from noise pulses. The first estimates show that the number of photons at the SiPMs is compatible with simulation results.

Chapter 11

Conclusion and Outlook

In this thesis detailed simulations on the photon yield and the timing of scintillator based detectors have been presented. The scintillation light is read out with help of SiPMs that are also simulated in detail. The aim of these studies it to identify a most feasible detector that can take the role of a potentially new detector component in the CMS detector, the MTT.
The planned upgrade of the LHC to SLHC will make it necessary to improve the resolution of the muon momentum measurement to keep the amounts of date manageable without a significant increase in threshold.
The tools provided by the C++-framework GEANT4 have been used to create a stand-alone programme capable to simulate the light creation and propagation inside a plastic scintillator. Two fundamental setups were studied. One uses a direct readout, where the SiPMs are mounted directly onto the scintillator surface, the other setup uses SiPMs attached to a multi-cladding wavelength shifting fibre, where every layer of the fibre has been simulated.

One important input parameter for the simulations is the roughness of the surface expressed by the width of the distribution of the local surface normals denoted by σ_α, according to the theoretical background of the UNIFIED model used in GEANT4 to describe the reflections of optical photons. To obtain the value of the parameter, a typical piece of scintillator has been scanned in an AFM by the II$^{\text{nd}}$ Physics Institute A (RWTH Aachen University).

It could be shown that basically all results strongly depend on the surface roughness and dominate the behaviour of the light propagation, e. g. the number of reflection or the reflection angle. It has been shown that many of the investigated setups provide enough photons to be qualified for the MTT. The results also show that the WLS readout allows a photon yield that is more that one order of magnitude larger than for the direct readout. Nevertheless, also the direct readout setup can provide enough photons to realise a reliable detector if there is a wrapping with high reflectivity surrounding the scintillator. Additionally, SiPMs with an active area larger than 1×1 mm^2 should be used for the direct readout to provide a signal that is large enough to be distinguishable from noise.

A test stand for cosmic muons has been prepared that allows studying a variety of different scintillator setups, especially with straight or bent fibres. Very first measurements have been performed that show results that are compatible with the simulations. To further investigate the predictive abilities of the GEANT4 simulations, systematic measurements with different setups have to be performed.

Also additional simulations should be performed to take different setups into account, e. g. with SiPMs distributed in a different way on the scintillator. Another approach that has not been considered in this thesis, is to put the SiPMs on the side faces of the scintillator.

Appendix A

Additional AFM Results

A.1 Height distributions

Additionally to the results shown in sec. 7.3.1 a distribution of the heights of another area is shown in fig. A.1. The different areas show very similar distributions.

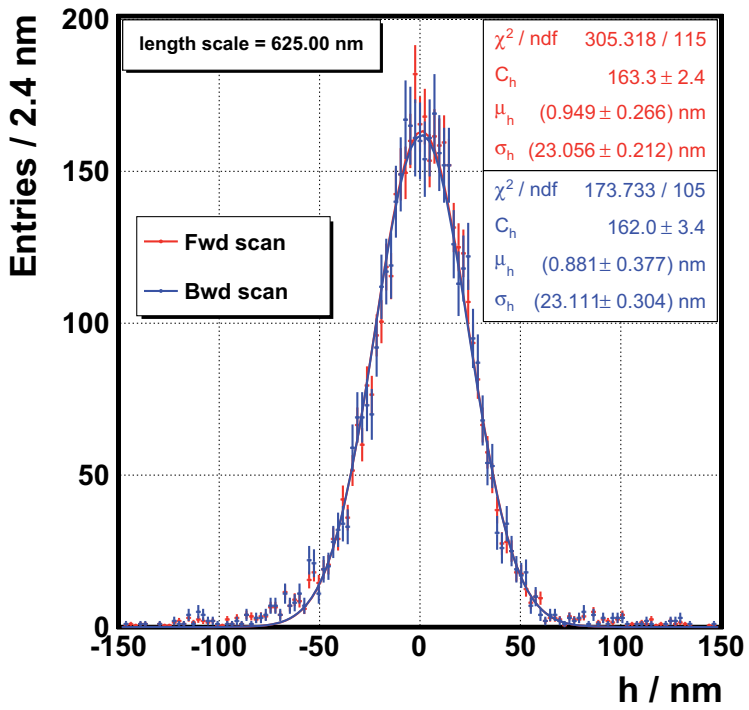

Figure A.1: The height distribution of another area ($40 \times 40\ \mu m^2$). The results are compatible with those shown in fig. 7.5b.

Appendix B

Additional Simulation Results

B.1 Energy loss in the scintillator

To ensure, the simulation meets the demand, that the energy loss of the muons traversing the scintillator follows a Landau distribution, the energy loss of muons in a piece of scintillator with a thickness of 1 mm to 20 mm has been studied.
Two example distributions with fitting results are shown in fig. B.1a and fig. B.1b. The Landau distribution is reproduced for every scintillator thickness and the fits match very well. The results

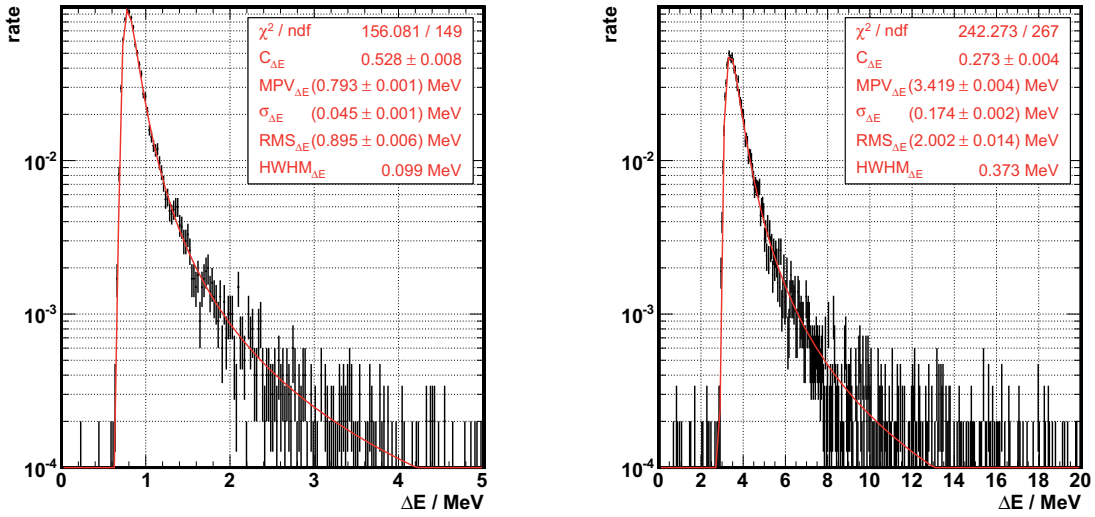

(a) Example of the energy loss distribution of muons in a piece of scintillator with a thickness of 5 mm. Results of a Landau fit are also shown.

(b) Example of the energy loss distribution of muons in a piece of scintillator with a thickness of 20 mm. Results of a Landau fit are also shown.

Figure B.1: Energy loss in scintillators with different thickness (example plots).

of the variation of the scintillator thickness are shown in fig. B.2. The plot shows clearly that the increase of the thickness of the scintillator leads to a linear increase in energy loss. Thus, the focus is put onto a setup with a particular thickness, see also sec. 9.1.2.

B.2 WLS setups

B.2.1 Different geometries

In sec. 9.3.5 different approches for the MTT with WLS readout have been shown. To complete the analysis the widths of the distributions are shown. Fig. B.3 shows the width for the number of photons arriving at the WLS fibre and fig. B.4 the number of photons hitting the SiPM.
The width of the photon arrival time at the SiPMs are shown in fig. B.5.

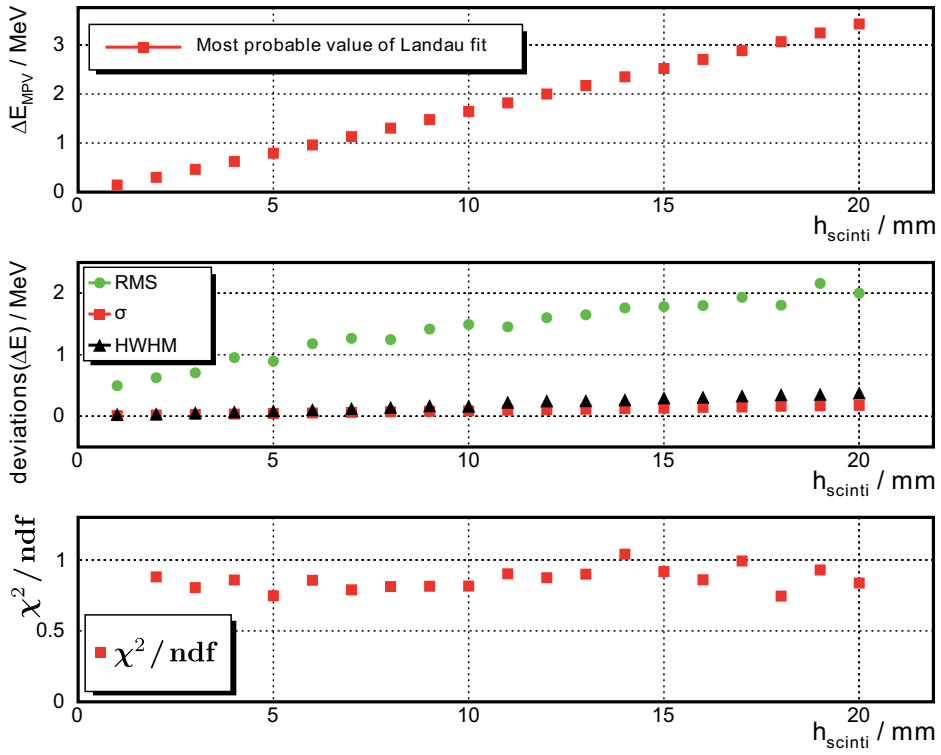

Figure B.2: Summary plot of energy loss in scintillators with different thickness. The upper plot shows the MPV, the middle plot the fitting parameter called σ, the RMS and the HWHM. In the lower part the corresponding fit's χ^2/ndf are shown. h_{scinti} is the height of the scintillator, i. e. its thickness.

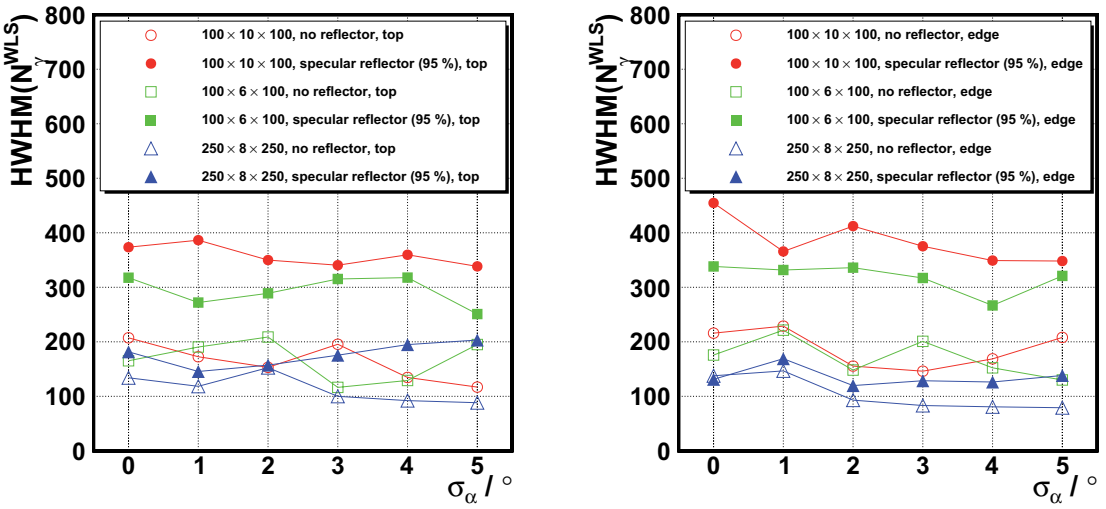

(a) HWHM of the number of photons absorbed in the WLS fibre for different setups with the fibre in the top position.

(b) HWHM of the number of photons absorbed in the WLS fibre for different setups with the fibre in the edge position.

Figure B.3: HWHM of the number of photons absorbed in the WLS fibre vs. σ_α for different setups with the fibre.

B.2.2 Photons in the scintillator

Photons created by scintillation in a material should have momenta isotropically distributed in the solid angle, this means uniformly distributed in the azimuth angle φ and in $\cos\vartheta$ (ϑ = polar angle). Fig. B.6 shows the distributions as obtained from the simulation.

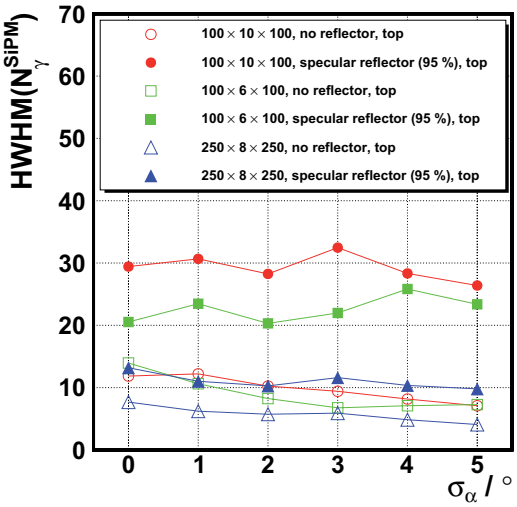

(a) HWHM of the number of photons hitting the SiPMs for different setups with the fibre in the top position.

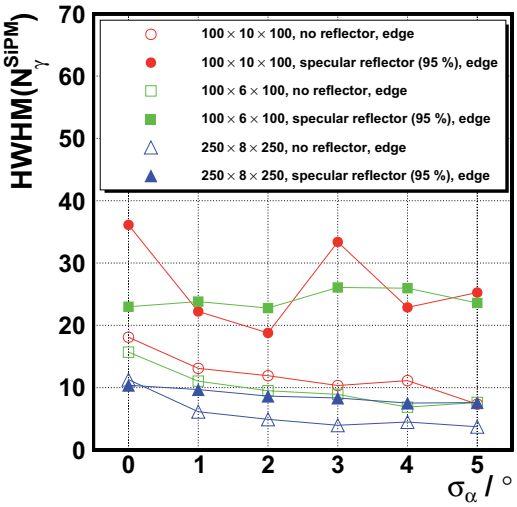

(b) HWHM of the number of photons hitting the SiPMs for different setups with the fibre in the edge position.

Figure B.4: HWHM of the number of photons arriving at the SiPMs vs. σ_α for different fibre setups.

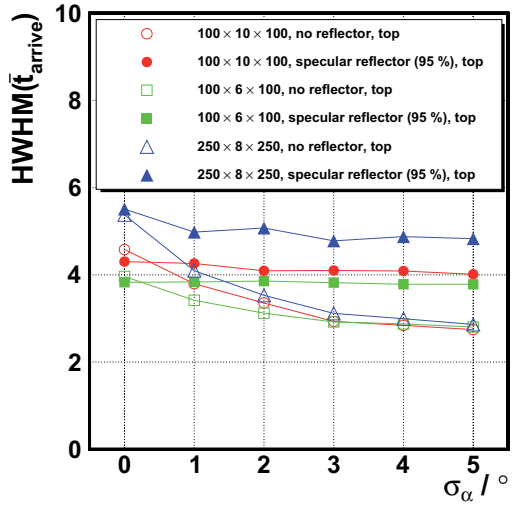

(a) HWHM of the photon arrival time distribution at the SiPM for different setups with the fibre in the top position.

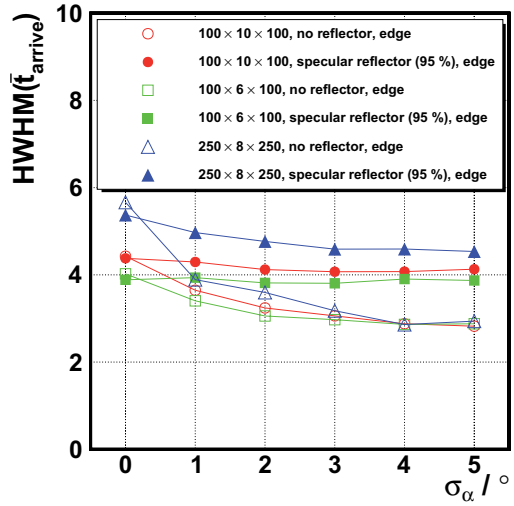

(b) HWHM of the photon arrival time distribution at the SiPM for different setups with the fibre in the top position.

Figure B.5: HWHM of the photon arrival time distribution vs. σ_α for different scintillator and fibre setups.

B.2.3 Photons in the fibre

Photons created in the fibre have momenta isotropically distributed in the solid angle. Fig. B.7 show the distributions as obtained from the simulation.

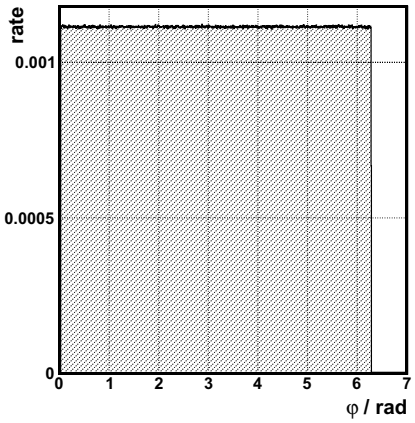

(a) Distribution of the azimuth angle of the initial momentum direction of photons created inside the scintillator. The decline in the last bin can be explained by the fact, that photons are never created with $\varphi = 2\pi$ but with $\varphi = 0$ instead.

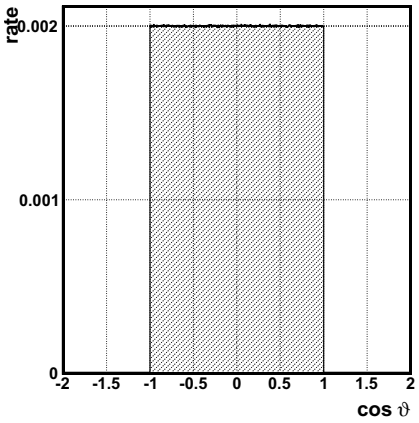

(b) Distribution of the cosine of the polar angle of the initial momentum direction of photons created inside the scintillator.

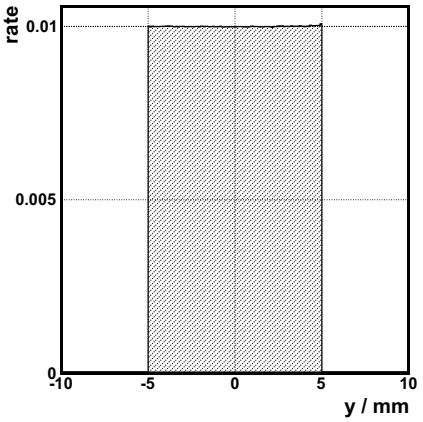

(c) Distribution of the y-coordinate of the creation position of photons inside the scintillator.

Figure B.6: Initial distributions of photons inside a scintillator. Examples for a scintillator with $100 \times 10 \times 100\ \mathrm{mm}^3$.

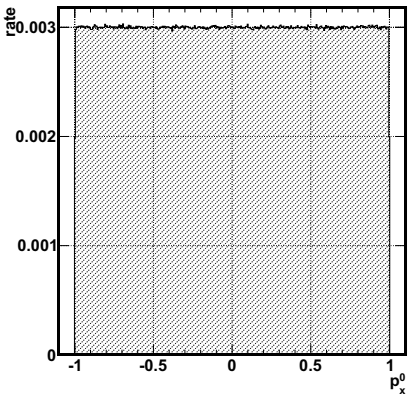

(a) Distribution of the x component of the initial photon momenta.

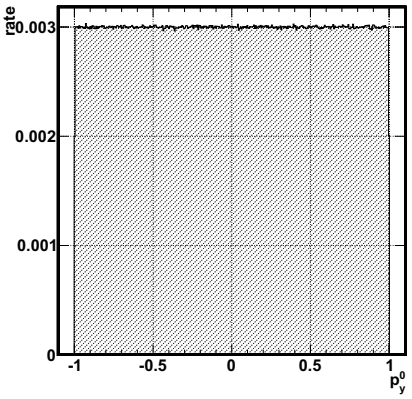

(b) Distribution of the y component of the initial photon momenta.

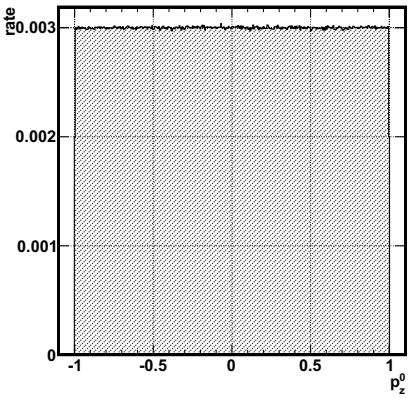

(c) Distribution of the z component of the initial photon momenta.

Figure B.7: Distribution of the initial momenta of the WLS-photons. p_i^0 denotes the ith component of the normalised momentum vector.

List of Figures

List of Tables

Bibliography

[Ago03] S. Agostinelli et al. 'GEANT4–a simulation toolkit'. In: *Nuclear Instruments and Methods in Physics Research* A 506 (2003) (2003), pp. 250 –303. (Cit. on pp. 49, 53).

[All06] J. Allision et al. 'Geant4 Developments and Application'. In: *IEEE TRANSACTIONS ON NUCLEAR SCIENCE* 53 (2006). (Cit. on p. 49).

[Anf09] Anfatec Instruments AG. 'Anfatec Webpage'. `http://www.anfatec.de/`. 2009. (Cit. on p. 57).

[Bet30] H. Bethe. 'Zur Theorie des Durchgangs schneller Korpuskularstrahlen durch Materie'. In: *Annalen der Physik* (1930). (Cit. on p. 33).

[BIC98] Saint-Gobain Industrial Ceramics Inc. BICRON. *Premium Plastic Scintillators*. 1998. (Cit. on pp. 65, 66).

[Bir64] J. B. Birks. *The Theory and Practice of Scintillation Counting*. Pergamon Press, 1964. (Cit. on pp. 18, 37, 38, 126).

[BQ86] G. Binnig and C. F. Quate. 'Atomic Force Microscope'. In: *Physical Review Letters* 56 (1986). (Cit. on p. 57).

[Brü04a] O. S. Brüning et al. *LHC Design Report Volume I*. `http://lhc.web.cern.ch/LHC/LHC-DesignReport.html`. 2004. (Cit. on p. 15).

[Brü04b] O. S. Brüning et al. *LHC Design Report Volume II*. `http://lhc.web.cern.ch/LHC/LHC-DesignReport.html`. 2004. (Cit. on p. 15).

[Brü04c] O. S. Brüning et al. *LHC Design Report Volume III*. `http://lhc.web.cern.ch/LHC/LHC-DesignReport.html`. 2004. (Cit. on p. 15).

[Bro78a] F.A. Brockhaus. *Der Grosse Brockhaus (in zwölf Bänden)*. Vol. Dritter Band. F.A. Brockhaus, 1978. (Cit. on p. 1).

[Bro78b] F.A. Brockhaus. *Der Grosse Brockhaus (in zwölf Bänden)*. Vol. Zweiter Band. F.A. Brockhaus, 1978. (Cit. on p. 1).

[Bro79] F.A. Brockhaus. *Der Grosse Brockhaus (in zwölf Bänden)*. Vol. Siebter Band. F.A. Brockhaus, 1979. (Cit. on p. 1).

[Bro80a] F.A. Brockhaus. *Der Grosse Brockhaus (in zwölf Bänden)*. Vol. Elfter Band. F.A. Brockhaus, 1980. (Cit. on p. 1).

[Bro80b] F.A. Brockhaus. *Der Grosse Brockhaus (in zwölf Bänden)*. Vol. Neunter Band. F.A. Brockhaus, 1980. (Cit. on p. 1).

[CD10] T. Aaltonen et al. 'Combination of Tevatron searches for the standard Higgs boson in the W+W- decay mode'. In: (2010). eprint: `1001.4162`. (Cit. on p. 11).

[CDF95] F. Abe et al. 'Observation of Top Quark Production in $\overline{p}p$ Collisions with the Collider Detector at Fermilab'. In: *Phys. Rev. Lett.* 74.14 (1995), pp. 2626–2631. DOI: `10.1103/PhysRevLett.74.2626`. (Cit. on p. 2).

[CER09] webpage CERN. *Document server*. `http://cdsweb.cern.ch`. 2009. (Cit. on pp. 13, 15, 125).

[CMS00a] The CMS Collaboration. 'Addendum to the CMS Tracker TDR'. In: *CERN/LHCC 2000-016* (2000). (Cit. on p. 16).

[CMS00b] The CMS Collaboration. *The Trigger and Data Acquisition project – The Level-1 Trigger, Vol. I.* TDR. 2000. (Cit. on pp. 16, 27, 125).

[CMS02] The CMS Collaboration. *The Trigger and Data Acquisition project – Data Acqusition & High-Level Trigger.* TDR. 2002. (Cit. on pp. 28, 29, 125).

[CMS06a] The CMS Collaboration. 'CMS Physics: Technical Design Report, Vol. I'. In: *CERN/LHCC 2006-001* (2006). (Cit. on pp. 16, 17, 19, 20, 24, 25, 125).

[CMS06b] The CMS Collaboration. 'CMS Physics: Technical Design Report, Vol. II'. In: *CERN/LHCC 2006-021* (2006). (Cit. on pp. 12, 125).

[CMS07] The CMS Collaboration. 'Expression of Interest in the SLHC'. In: *CERN/LHCC 2007-014* (2007). (Cit. on p. 30).

[CMS08] The CMS Collaboration. *The CMS experiment at the CERN LHC.* Tech. rep. Journal of Instrumentation, 2008. (Cit. on pp. 16, 18, 21–23, 26, 125).

[CMS97a] The CMS Collaboration. 'CMS Muon Technical Design Report'. In: *CERN/LHC 97-32* (1997). (Cit. on pp. 16, 24, 125).

[CMS97b] The CMS Collaboration. 'The CMS hadron calorimeter project: Technical Design Report'. In: *CERN/LHCC 97-031* (1997). (Cit. on pp. 16, 21).

[CMS98] The CMS Collaboration. 'CMS Tracker Technical Design Report'. In: *CERN/LHCC 98-6* (1998). (Cit. on pp. 16–18).

[D095] S. Abachi et al. 'Observation of the Top Quark'. In: *Phys. Rev. Lett.* 74.14 (1995), pp. 2632–2637. DOI: 10.1103/PhysRevLett.74.2632. (Cit. on p. 2).

[Deh88] H. Dehmelt. 'A Single Atomic Particle Forever Floating at Rest in Free Space: New Value for Electron Radius'. In: *Physica Scripta* T22 (1988), pp. 102 –110. (Cit. on p. 2).

[DeS97] R. DeSalvo. 'Why people like the Hybrid PhotoDiode'. In: *Nuclear Instruments and Methods in Physics Research* (1997). (Cit. on p. 20).

[DON01] K. Kodama et al. 'Observation of tau neutrino interactions'. In: *Physics Letters B* 504.3 (2001), pp. 218 –224. ISSN: 0370-2693. DOI: DOI:10.1016/S0370-2693(01)00307-0. URL: http://www.sciencedirect.com/science/article/B6TVN-42NY3K6-15/2/6aade3e03ecc53fcbf8986e79c267b29. (Cit. on p. 2).

[EB08] L. Evans and P. Bryant. 'LHC Machine'. In: *Insitute of Physics Publishing and SISSA* (2008). (Cit. on p. 15).

[Elj07] Eljen Technology. *EJ-500 OPTICAL CEMENT.* 2007. (Cit. on pp. 69, 70).

[Elj09] Eljen Technology. 'Eljen Webpage'. http://www.eljentechnology.com/. 2009. (Cit. on p. 69).

[Eva07a] L. Evans. 'Preparatory Phase of the Large Hadron Collider Upgrade'. In: *FP7-INFRASTRUCTURES-2007-1* (2007). (Cit. on p. 29).

[Eva07b] L. Evans. 'The Large Hadron Collider'. In: *New Journal of Physics* 9 (2007) 335 (2007). (Cit. on pp. 14, 15, 125).

[Fey69] R. P. Feynman. 'Very High-Energy Collisions Of Hadrons'. In: *Physics Review Letters* 23.24 (1969). (Cit. on p. 2).

[G408] Geant4 Collaboration. *Physics Reference Manual.* http://geant4.web.cern.ch/geant4/UserDocumentation/UsersGuides/PhysicsReferenceManual/fo/PhysicsReferenceManual.pdf. 2008. (Cit. on p. 49).

[G409] Geant4 Collaboration. *Geant4 User's Guide for Application Developers*. `http://geant4.web.cern.ch/geant4/UserDocumentation/UsersGuides/ForApplicationDeveloper/html/index.html`. 2009. (Cit. on p. 49).

[Göb06] H Göbel. *Einführung in die Halbleiter-Schaltungstechnik*. 2. Auflage. Springer, 2006. (Cit. on p. 43).

[GM64] M. Gell-Mann. 'A Schematic Model Of Baryons And Mesons'. In: *Physics Letters* 8.3 (1964). (Cit. on p. 2).

[GS08] C. Grupen and B. Shwartz. *Particle Detectors*. Cambridge, 2008. (Cit. on p. 36).

[Ham08a] Hamamatsu. *New type of Si Photon-counting Device*. 2008. (Cit. on pp. 45–47, 126).

[Ham08b] Hamamatsu. *Photodiode Technical Information*. `http://sales.hamamatsu.com/assets/applications/SSD/photodiode_technical_information.pdf`. 2008. (Cit. on pp. 42–44, 126).

[Ham09] Hamamatsu. *New type of Si photon-counting device, Active area: 1 x 1 mm*. 2009. (Cit. on pp. 45, 67, 69, 71, 126, 127).

[HBG01] E. Hering, K. Bressler, and J. Gutekunst. *Elektronik für Ingenieure*. Springer, 2001. (Cit. on pp. 43, 45, 47).

[Heb10] T. Hebbeker. *private communications*. III. Physikalisches Institut A. 2010. (Cit. on pp. 111, 113, 130).

[HM84] F. Halzen and A. D. Martin. *Quarks & Leptons*. Wiley, 1984. (Cit. on pp. 10, 11).

[KKP81] P. Klasen, K. Kleinknecht, and D. Pollmann. 'Application Of Wavelength-Shifter Techniques To Position Measuring Counters'. In: *Nuclear Instruments and Methods* 185 (1981). (Cit. on p. 68).

[Kle05] K. Kleinknecht. *Detektoren für Teilchenstrahlung*. Teubner Verlag, 2005. (Cit. on pp. 19, 36, 39, 51).

[Kor04] V. Korbel. 'Optimization studies for a scintillator-tile to wavelength-shifter fibre light readout for the TESLA-Calice Tile-HCAL'. In: *LC-DET-2004-28* (2004). (Cit. on p. 102).

[KS83] K. S. Kölbig and B. Schorr. 'A Programm Package For The Landau Distribution'. In: *Computer Physics Communications 31* 97-111 (1983). (Cit. on p. 78).

[Leo87] W. R. Leo. *Techniques for Nuclear and Particle Physics Experiments*. Springer, 1987. (Cit. on pp. 19, 34–37, 126).

[LM96] A. Levin and C. Moisan. 'A More Physical Approach to Model the Surface Treatment of Scintillation Counters and its Implementation into DETECT'. In: *TRI-PP-96-64* (1996). (Cit. on pp. 54, 55, 59, 127).

[Lut07] G. Lutz. *Semiconductor Radiation Detectors*. Springer, 2007. (Cit. on p. 42).

[MAB07] A. Montanari, G. Abbiendi, C. Battilana, A. Benvenuti, H.M. Dalavalla, and Perrotta. 'Muon Trigger Upgrade at SLHC: Muon Track fast Tag'. In: *CMS IN 2007/058* (2007). (Cit. on pp. 30, 31, 71, 125, 126).

[Mer09] M. Merschmeyer. *private communications*. III. Physikalisches Institut A. 2009. (Cit. on p. 46).

[Mon09] A. Montanari. *private communications*. 2009. (Cit. on pp. 30, 32).

[Nan09] Nanotec Electronica S.L. 'Nanotec Webpage'. `http://www.nanotec.es`. 2009. (Cit. on p. 58).

[NHH07] J. Ninkovic et al. 'The Avalanche drift diode – A backilluminated Silicon Photomultiplier'. In: *Nuclear Instruments and Methods in Physics Research Section A: Accelerators, Spectrometers, Detectors and Associated Equipment* 572.1 (2007), pp. 454 –455. (Cit. on p. 46).

[NIK89] S. K. Nayar, K. Ikeuchi, and T. Kanade. 'Surface Reflection: Physical and Geometrical Perspectives'. In: *CMS-RI-TR-89-7* (1989). (Cit. on pp. 54, 55, 59, 127).

[Nol04] W. Nolting. *Grundkurs Theoretische Physik 3 (Elektrodynamik)*. Springer, 2004. (Cit. on p. 8).

[OMO08] H. Oide, T. Muras, H. Otono, and S. Yamashita. 'Studies on multiplication effect of noises of PPDs, and a proposal of a new structure to improve the performance'. In: *arXiv* (2008). (Cit. on pp. 46, 47, 126).

[PDG08] C. Amsler et al. Particle Data Group. 'The Review of Particle Physics'. In: *Physics Letters* B667, 1 (2008). (Cit. on pp. 6, 7, 11, 14, 15, 33, 35, 38, 39, 126, 131).

[POF08] O. Ziemann, J. Krauser, P. E. Zamzow, and W. Daum. *POF Handbook*. Second Edition. Springer, 2008. (Cit. on p. 99).

[Ren06] D. Renker. 'Geiger-mode avalanche photodiodes, history, properties and problems'. In: *Nuclear Instruments and Methods in Physics Research* A 567 (2006) (2006), pp. 48 –56. (Cit. on p. 46).

[RY09] G. Roper Yearwood. *private communications*. I. Physikalisches Institut B. 2009. (Cit. on p. 99).

[Sch95] P. Schmüser. *Feynman-Graphen und Eichtheorien für Experimentalphysiker*. Springer, 1995. (Cit. on p. 9).

[Sen07] SensL. *Introduction to the Silicon Photomultiplier*. 2007. (Cit. on p. 46).

[SG05a] Saint-Gobain Ceramics & Plastics Inc. *BC-600 Optical Cement*. 2005. (Cit. on p. 69).

[SG05b] Saint-Gobain Ceramics & Plastics Inc. *Premium Plastic Scintillators*. 2005. (Cit. on pp. 65, 66).

[SG05c] Saint-Gobain Ceramics & Plastics Inc. *Scintillation Products, Scintillating Optical Fibers*. 2005. (Cit. on pp. 67–69, 71).

[Sil97] D. Silber. 'Optoelektronische Komponenten für Energieumwandlung, Nachrichtenübertragung und Sensorik'. Script by Lars Rinze. 1997. (Cit. on pp. 43–45).

[SL00] A. W. Snyder and J. D. Love. *Optical Waveguide Theory*. Kluwer, 2000. (Cit. on p. 99).

[TS02] U. Tietze and C. Schenk. *Halbleiter-Schaltungstechnik*. 12. Auflage. Springer, 2002. (Cit. on p. 43).

[Wik09a] Wikipedia. 'The Free Encyclopedia'. `http://wikipedia.org`. 2009. (Cit. on pp. 36, 42, 126).

[Wik09b] Wikipedia. 'The Free Encyclopedia'. `http://upload.wikimedia.org/wikipedia/commons/a/ab/Photomultiplier_schema_de.png`. 2009. (Cit. on pp. 39, 126).

[Wik09c] Wikipedia. 'The Free Encyclopedia'. `http://upload.wikimedia.org/wikipedia/commons/7/7c/Atomic_force_microscope_block_diagram.svg`. 2009. (Cit. on p. 57).

[Ynd95] F.J. Yndurin. 'Limits on the mass of the gluon'. In: *Physics Letters* B 345 (1995), pp. 524 –526. (Cit. on p. 6).

Danksagung

Zunächst möchte ich mich bei Prof. Dr. Hebbeker bedanken, dass er mir ermöglicht hat, diese Arbeit im III. Physikalischen Institut anzufertigen, und mich dabei betreut hat.
Vielen Dank auch an Prof. Dr. Wiebusch, der sich bereiterklärt hat diese als Zweitgutachter zu bewerten.
Ich danke auch meinen Eltern die durch ihre Unterstützung mein Studium überhaupt erst möglich gemacht haben.
Ich danke den Mitarbeitern und Kollegen des III. Physikalischen Instituts A und B für eine freundliche und offene Arbeitsatmosphäre in den vergangenen Monaten. Vor allem bei meinen Bürokollegen und -nachbarn bedanke ich mich für die angenehme Zeit. Zu nennen sind hier Michael Sowa, Gerrit Fieling und Jan-Frederik Schulte, aber auch Metin Ata, Michael Bontenackels, Carsten Hof, Carsten Magaß, Clemens Zeidler, Philipp Biallass, Erik Dietz-Laursonn, Andreas Güth, Walter Bender und Jens Frangenheim.
Ich möchte mich auch bei den Mitarbeitern der mechanischen und elektronischen Werkstätten für die Hilfe bei kleinen und großen Problemen und die Realisierung verschiedener Ideen bedanken. Besonders sind hier G. Hilgers, F. Adamczyk, B. Philipps, H. Frohn und J. Grooten zu nennen.
Für das Korrekturlesen bedanke ich mich bei Arnd Meyer und Stefan Schmitz, der auch immer für eine Diskussion zum Thema Datenauswertung zu haben war. Ein ganz besonderer Dank gilt Markus Merschmeyer, der sich nicht nur immer wieder Zeit für Korrekturen genommen hat, sondern mich zudem auch ausgezeichnet betreut hat und mit vielen Ideen und Anregungen zur Seite stand.
Ich bedanke mich sehr bei Marcus Liebmann vom II. Physikalischen Institut B der bereitwillig seine Zeit und sein Fachwissen zur Verfügung gestellt hat, um mit dem Rasterkraftmikroskop die Szintillatorproben zu untersuchen.
Für die vielen interessanten und anregenden Gespräche möchte ich mich bei Carsten Mai bedanken, der auch immer einen Rat bei Computerproblemen zur Hand hatte.
Ich danke auch bei allen "Bewohnern des Tanzsaals" für die nette Zusammenarbeit, besonders bei Jörg Rennefeld und Sven Lotzen, mit denen ich immer Erfahrungen austauschen konnte und Oxana Grünwald, die für Diskussionen zum Thema GEANT4 immer offen war.

Letzter und wichtigster Dank geht an meine Freundin Sonja Fischer, die mir in den letzten Jahren in allen Lebenslagen zur Seite stand, mich in jeder erdenklichen Form unterstützt hat und die immer sehr viel Verständnis für mein zeitaufwendiges Studium gezeigt hat.

Selbstständigkeitserklärung

Ich, Paul Papacz, erkläre hiermit, dass ich die Diplomarbeit ohne fremde Hilfe und ohne Benutzung anderer, als der angegebenen Quellen und Hilfsmittel angefertigt habe. Alle Ausführungen, die wörtlich oder sinngemäß übernommen wurden, sind als solche gekennzeichnet.

Aachen, den 01.03.2010

(Paul Papacz)